Investigations of Water-Based Liquid Antennas for Wireless Communications

by

Lei Xing

Submitted in accordance with the requirements for the award of the degree of Doctor of Philosophy of the University of Liverpool

September 2015

Copyright

To my husband and my parents: Thank you for your support.

Table of Contents

Acronyms

APCAP	Asia-Pacific Conference on Antennas and Propagation
AUT	Antenna under Test
CEMS	Computational Electromagnetics
Co-pol	Co-polarisation
CWGM	Conventional Waveguide Model
DDPA	Dense Dielectric Patch Antenna
DR	Dielectric Resonator
DRA	Dielectric Resonator Antenna
DVB-H	Digital Video Broadcasting to Handheld
DWM	Dielectric Waveguide Model
EDC	Effective Dielectric Constant
EGaIn	Eutectic Gallium 75% Indium 25%
FDTD	Finite Difference Time Domain
FEM	Finite Element Method
GaAs	Gallium Arsenide
GTD	Geometrical Theories of Diffraction
HF	High Frequency
HRAT	Hybrid Resonator Antenna Technique
IFFT	Inverse Fast Fourier Transform
IRE	Institute of Radio Engineers
LAPC	Loughborough Antenna & Propagation Conference

MoM	Method of Moments
MUT	Material under Test
MWM	Magnetic Wall Model
MWGM	Modified Waveguide Model
OATS	Open Area Test Site
PDMS	Polydimethylsiloxane
PG	Propylene Glycol
PICA	Planar Inverted Cone Antenna
PPT	Parts per Thousand
PVC	Polyvinyl Chloride
RC	Reverberation Chamber
RCS	Radar Cross Section
REF	Reference Antenna
RX	Receiving Antenna
SSC Pacific	Space and Naval Warfare Systems Center Pacific
SSM/I	Special Sensor Microwave Imager
2D	Two Dimensional
3D	Three Dimensional
TLM	Transmission Line Model Method
TX	Transmitting Antenna
UHF	Ultra High Frequency
UWB	Ultrawideband
VHF	Very High Frequency

VNA	Vector Network Analyser
X-pol	Cross-polarisation

Acknowledgements

Looking back to the four years of my PhD studies, I am grateful to many people. First and foremost, I would like to express my sincere appreciation and thanks to my research supervisor Professor Yi Huang. I thank you for giving me the opportunity to be one of your PhD students. I learned so much from you both academically and personally. Thank you for the invaluable comments and advice on my research. I also thank you for the generous support you have provided for to me. I will always treasure your support, encouragement, and guidance.

I would also like to thank my parents and parents in law. Your continuous support and understanding have made my life full of love and I am grateful for everything you have done. I would also like to express my gratitude to my husband. Without you, I wouldn't be who I am today. I think I am lucky to have you, providing me with inspirations, courage and love. I will always cherish the trust you gave me both on research and daily life.

Special thanks are also paid to my brilliant and lovely colleagues; in particular to Saqer S. Alja'afreh, Dr. Neda Khiabani, Dr Jingwei Zhang, Dr Ping Cao and Dr. Stephen J. Boyes as well as Zhihao Tian, Sheng Yuan, Chaoyun Song and Zhouxiang Fei, Muayad Kod, Rula Alrawashdeh, Muaad Hussein, Aznida Abu Bakar Sajak, Amir Kotb, Abed Pour Sohrab, Anqi Chen, Yuan Zhuang, Umniyyah Ulfa, Saidatul Izyanie, for many fruitful discussions and enjoyable moments.

Finally, I would also like to acknowledge Tingting Liu, Dr Wei Huang, Dr Tao Jin for always unconditionally providing me all kinds of samples. I have enjoyed getting to know you all personally and share such successful collaborations with you all. Particular thanks to Alan Roby from the Electrical Workshop for always being very kind to me and fabricating my antennas very quickly.

Last but not the least, the financial support from China Scholarship Council (CSC) and University of Liverpool is gratefully acknowledged.

List of Publications

Journal Publications

[1] **L. Xing**, Y. Huang, Q. Xu and S. Alja'afreh, "A transparent dielectric loaded reconfigurable antenna with a wide tuning range," submitted to IEEE Antennas Wireless Propag. Lett..

[2] **L. Xing**, Y. Huang, Q. Xu, S. Aljaafreh, T. Liu, "Complex permittivity of water-based liquids for liquid antennas," IEEE Antennas Wireless Propag. Lett. (In Revision).

[3] **L. Xing**, Y. Huang, Q. Xu and S. Alja'afreh, "A compact water loaded reconfigurable antenna for DVB-H applications," Electron. Lett. to be published.

[4] **L. Xing**, Y. Huang, Q. Xu, S. Alja'afreh, "A wideband hybrid water antenna with an F-shaped monopole," IEEE Access, vol. 3, pp. 1179-1187, 2015.

[5] **L. Xing**, Y. Huang, Q. Xu, S. Aljaafreh, T. Liu, "A broadband hybrid water antenna for hand-portable applications," IEEE Antennas Wireless Propag. Lett. [Online]. Available: http://ieeexplore.ieee.org/stamp/stamp.jsp?tp=&arnumber=7112462.

[6] **L. Xing**, Y. Huang, Q. Xu, S. Aljaafreh, "Wideband, hybrid rectangular water antenna for DVB-H applications," Microw. Opt. Technol. Lett., vol. 59, no. 9, pp. 2160-2164, 2015.

[7] **L. Xing**, Y. Huang, Y. Shen, S. Alja'afreh, Q. Xu, R. Alrawashdeh, "Further investigation on water antennas," IET Microw., Antennas Propag., vol. 9, no. 8, pp. 735-741, 2015.

[8] S. Alja'afreh, Y. Huang, **L. Xing**, Q. Xu and X. Zhu, "A low profile and wideband PILA-based antenna for handset diversity applications," IEEE Antennas Wireless Propag. Lett., vol. 14, pp. 923-926, 2015.

[9] S. Alja'afreh, Y. Huang, **L. Xing**, "A low profile and wideband PIFA antenna with polarisation and pattern diversities," IET Microw., Antennas Propag. to be published.

[10] Q. Xu, Y. Huang, X. Zhu, S. Alja'afreh, **L. Xing** and Z. Tian, "Diversity gain measurement in a reverberation chamber without extra antennas," IEEE Antennas Wireless Propag. Lett., vol. 14, pp. 1666-1669, 2015.

[11] Q. Xu, Y. Huang, X. Zhu, **L. Xing**, Z. Tian and C. Song, "A modified two-antenna method to measure the radiation efficiency of antennas in a reverberation chamber," IEEE Antennas Wireless Propag. Lett. [Online]. Available: http://ieeexplore.ieee.org/stamp/stamp.jsp?tp=&arnumber=7122231&isnumber=4357943

[12] Q. Xu, Y. Huang, X. Zhu, S. Alja'afreh and **L. Xing**, "A new antenna diversity gain measurement method using a reverberation chamber," IEEE Antennas Wireless Propag. Lett., vol. 14, pp. 935-938, 2015.

[13] Q. Xu, Y. Huang, **L. Xing**, Z. Tian, Z. Fei and L. Zheng, "A fast method to measure the volume of a large cavity," IEEE Access, vol. 3, pp. 1555-1561, 2015.

[14] Q. Xu, Y. Huang, X. Zhu, **L. Xing**, Z. Tian and C. Song, "Shielding effectiveness measurement of an electrically large enclosure using one antenna," IEEE Trans. Electromagn. Compat. to be published.

Conference Publications

[1] **L. Xing**, Y. Huang, Q. Xu, S. Aljaafreh, "Overview of water antenna designs for wireless communications," in Proc. IEEE Asia-Pacific Conf. on Antennas and Propag., 2015, pp. 242-243.

[2] **L. Xing**, Y. Huang, S. Alja'afreh, Q. Xu, M. Kod, C. Y. Song, "Reconfigurable 3D folded monopole antenna design for DVB-H applications," in Proc. Loughborough Antennas Propag. Conf., 2014, pp. 530-532.

[3] **L. Xing**, Y. Huang, Y. Shen, S. Alja'afreh, Q. Xu, R. Alrawashdeh, "Broadband U-shaped water antenna for DVB-H applications," in Proc. IEEE Int. Symp. on Antennas and Propag., 2014, pp. 1930-19311.

[4] **L. Xing**, Y. Huang, S. Alja'afreh, and S. J. Boyes, "A monopole water antenna," in Proc. Loughborough Antennas Propag. Conf., 2012, pp. 1-4.

[5] S. Alja'afreh, Y. Huang, **L. Xing**, "A new dual-feed PIFA diversity antenna," in Proc. European Conf. on Antennas and Propag., 2014, pp. 2800-2803.

[6] S. Alja'afreh, Y. Huang, **L. Xing**, "A compact wideband and low profile planar inverted-L antenna," in Proc. European Conf. on Antennas and Propag., 2014, pp. 3283-3286.

[7] S. Alja'afreh, Y. Huang, **L. Xing**, "A compact dual-feed water-based diversity antenna," in Proc. Loughborough Antennas Propag. Conf., 2013, pp. 182-185.

[8] S. Alja'afreh, Y. Huang, **L. Xing**, "A small U-shaped dielectric resonator antenna," in Proc. Loughborough Antennas Propag. Conf., 2012, pp. 1-4.

[9] Q. Xu, Y. Huang, X. Zhu, **L. Xing** and Z. Tian, "Antenna radiation efficiency measurement in a reverberation chamber without the need for calibration," in Proc. of the IEEE Int. Symp. on Antennas and Propag., 2015, pp. 1178-1179.

[10] Q. Xu, Y. Huang, J. Zhou, C. Song and **L. Xing**, "Field-circuit co-simulation of the Marx generator," in Proc. European Conf. on Antennas and Propag., 2015, pp. 1-5 .

[11] Q. Xu, Y. Huang, X. Zhu, **L. Xing** and Z. Tian, "Permittivity measurement of spherical objects using a reverberation chamber," in Proc. Loughborough Antennas Propag. Conf., 2014, pp. 44-47.

[12] Q. Xu, Y. Huang, X. Zhu, **L. Xing**, P. Duxbury and J. Noonan, "NSA simulation in semi-anechoic chamber using ray tube tracing method," in Proc. Int. Conf. on Computation in Electromagnetics, 2014, pp. 1-2.

[13] Q. Xu, Y. Huang, X. Zhu, **L. Xing**, P. Duxbury and J. Noonan, "An efficient method for the field uniformity analysis of anechoic chambers," in Proc. IEEE Int. Symp. on Antennas and Propag., pp. 2236-2237, 2014.

[14] Q. Xu, Y. Huang, X. Zhu, **L. Xing** and A. A. B. Sajak, "Statistical electromagnetic analysis of PEC sphere scattering," in Proc. Int. Conf. on Engineering Technology & Technopreneurship, 2014, pp. 94-98.

Abstract

Water-based liquid antennas are a new type of antennas, which have attracted increasing attention in recent years. They have emerged as promising alternatives to traditional antennas for many applications. The purpose of this thesis is to present a comprehensive study into water-based liquid antennas, aiming at gaining a better understanding of water-based liquid antennas from the liquids used to the antenna designs. This thesis is comprised of two main research areas.

The first area under investigation focuses on water-based liquid property characterisation. In water-based liquid antenna designs, a precise knowledge of the complex permittivity of the liquid is essential. Three water-based liquids, namely pure water, water with propylene glycol (PG) and salty water, are carefully studied from an antenna design point of view. A liquid measurement software package is developed to automatically record the liquid complex permittivity data under different temperatures, and measurements are conducted. The experimental data are processed to obtain accurate mathematical expressions for the complex permittivity of these liquids over a temperature range 0 ~ 70^{o}C (for pure water and salty water) and -10^{o}C ~ 70^{o}C (for water with PG), frequency range 0 ~ 18 GHz, PG concentration 0 ~ 70% and salinity 0.1 ~ 50 ppt. Water with PG is proposed as an alternative candidate for pure water in cold climates. It is demonstrated that the performance of the antenna will not be changed significantly by using water with PG.

The second area concerns water-based liquid antenna designs and is divided into three sections:

The first section deals with the water antenna working as a conducting antenna. A water monopole antenna with a dielectric layer is designed. Salty water is used to replace the conducting material (usually copper) in traditional designs. A comprehensive parametric study is performed and the physical insights behind the design are studied. A close relationship between the salty water conductivity and antenna radiation efficiency is explored.

The second section investigates the hybrid water antenna for hand-portable applications. By combining the resonance from the water dielectric resonator antenna (DRA) and that from the feeding structure, a wideband response can be achieved. Three hybrid water antennas are developed with low profiles and high efficiency. The unique features of water, namely liquidity and transparency are effectively utilised. A complex feeding structure is placed

inside the water dielectric resonator (DR) to feed the water DR and also work as a radiating element.

The third section relates to the water loaded reconfigurable antennas. Two water loaded reconfigurable antennas with special 3D folded structures are designed. Different technologies are applied in the reconfigurable designs such as the special folded 3D monopole structure, the use of water and its holder as a transparent dielectric loading, and the integration of an active component. The results show that the designs have compact sizes, reasonable efficiency and bandwidths.

This thesis has successfully demonstrated the attractive features and great potential of water-based liquid antennas. The knowledge gained in this work is very valuable for future water-based liquid antenna development.

Chapter 1: Introduction

1.1 Background

1.1.1 Antenna Definition

The IEEE Standard Definitions of Terms for Antennas (IEEE Std 145-1983) defines the antenna or aerial as "a means for radiating or receiving radio waves". In other words the antenna is the transitional structure between free-space and a guiding device [1].

Antennas are essential components of any wireless communication system. They are the devices that allow for the transfer of a signal to waves that, in turn, propagate through space and can be received by another antenna. The receiving antenna is responsible for the reciprocal process, i.e. that of turning an electromagnetic wave into a signal or voltage at its terminals that can subsequently be processed by the receiver [2]. The transmitting and receiving antennas can form a typical radio communication system as shown in Fig. 1.1.

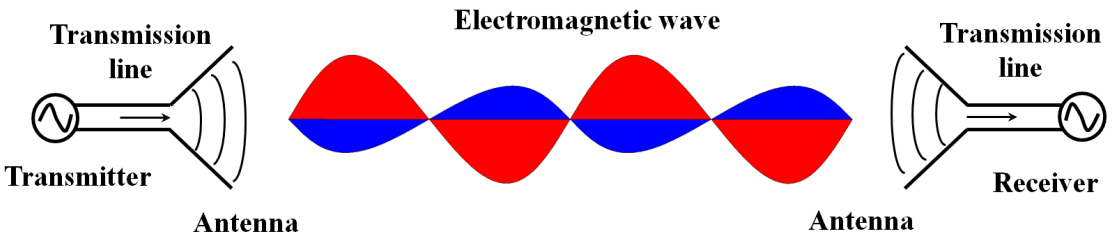

Fig. 1.1. A typical radio system [3].

1.1.2 Antenna History

The history of antenna theory dates back to James Clerk Maxwell who formulated the classical theory of electromagnetic radiation, bringing together for the first time electricity, magnetism, and represented their relations through a set of profound equations best known as Maxwell's Equations. He showed that light is an electromagnetic (EM) wave, and that all EM waves propagate through space with the same speed, the speed of light [4]. In 1886, Professor Heinrich Rudolph Hertz built the very first wireless system in his laboratory. The transmitter was a dipole which was connected to a variable voltage source with two conducting balls at the ends; while the receiver was a simple loop with two identical conducting balls. In the experiment, when a spark was generated at the transmitter,

a spark at the receiver was observed at the same time. This proved that the signal from location A (transmitter) was transmitted to location B (the receiver) in a wireless manner - by electromagnetic waves [3]. In 1892, Tesla delivered a presentation at the institute of radio engineerers (IRE) of London about “transmitting intelligence without wires”. In 1895, he transmitted signals detected 50 miles away. In 1895, a telegraph communication link was demonstrated by the Russian scientist, Alexander Popov. A message was sent from a Russian Navy ship 30 miles out at sea, all the way to his lab in St. Petersburg, Russia [2]. Later, Guglielmo Marconi developed and commercialised the wireless technology by introducing a radiotelegraph system. In 1901, he performed the first transatlantic transmission from Poldhu in UK to St. John’s, Newfoundland in Canada. He used several vertical wires attached to the ground as a transmitting antenna. Across the Atlantic Ocean, the receiving antenna was a 200 m wire held up by a kite. This experiment opened a new era for antennas. From 1901 to the 1940s, antenna technology was primarily focused on wire-type antennas and frequencies up to ultra high frequency (UHF). One of the most famous wire geometry antennas was the Yagi-Uda antenna (typically seen on the roof of most houses for television receptions) designed in early 1920s. It was considered as a breakthrough in antenna technology because compared with a half wavelength dipole, it provided a much higher gain. During and after World War II, with the need for detecting enemy aeroplanes, ships or submarines from hundreds of miles away, high frequency radar antennas were extensively developed [3]. New elements such as aperture antennas, horn antennas and reflector antennas were primarily introduced [1]. In the 1950s, frequency independent antennas were designed, with the geometries specified by curves, flares and angles instead of linear dimensions. They were regarded as a breakthrough in antenna evolution, which extended the maximum bandwidth to as great as 40 : 1 or more. Slot spiral antennas and log-periodic antennas are typical frequency independent antennas [5, 6]. In the early 1970s, microstrip or patch antennas were reported. Extensive research of microstrip antennas was devoted to explore their advantages such as light weight, low profile, low cost, conformal configuration and compatibility with integrated circuits [7]. In the 1970s and 1980s, a new antenna array referred to smart antenna received enormous interest worldwide, which combined antenna technology with that of digital signal processing (DSP) [1]. By using the signal processing, the beam pattern can be shaped to certain conditions. In the 1980s, the idea of using dielectric resonator (DR) as a practical antenna was materialised and Long *et al* published a paper on the cylindrical dielectric resonator antenna (DRA) [8]. Since then, extensive investigations were carried out on various aspects of DRAs [9-11]. Besides the mentioned antennas, many other types were subsequently developed for various applications.

With great developments in antennas, computer technology also embraced large advances, which had a major impact on the modern antenna technology. Since the early 1960s, numerical analysis methods were introduced, allowing unpredictable antenna performance to be modelled and analysed accurately.

After that, various computational electromagnetics (CEMs) methods were explored and studied, such as the method of moments (MoM), finite element method (FEM), finite difference time domain (FDTD), transmission line model method (TLM), geometrical theories of diffraction (GTD), which significantly improved the design convenience of antennas. Previously, the design of the antennas mainly relied on a "cut and try" operation, which was a very expensive and time-consuming procedure. Today, it is standard practice to employ software to aid antenna design. Many designs now proceed directly from the initial design stage to the prototype fabrication without intermediate testing.

1.1.3 Antennas Classifications

Since the start of radio communications over 100 years ago, thousands of antennas have been developed and studied. They can be categorised by different criteria [3]:

From the bandwidth point of view, antennas can be classified as narrowband or broadband;

From the polarisation point of view, they can be divided into linearly, circularly or elliptically polarised antennas;

From the resonance point of view, they can be organised as resonant (standing wave) or travelling wave antennas;

From the number of elements, they can be grouped as single element antennas or antenna arrays;

From the construction point of view, they can be categorised as solid antennas, liquid antennas, and gas antennas. Solid antennas refer to those made of conducting materials (such as dipoles, loops and horns), dielectric materials (such as DRAs) or a combination of both (such as patch antennas). Liquid antennas are mainly made of two types of liquids, namely liquid metals and water-based liquids. A plasma antenna is one example of gas antennas, which uses a plasma element as the conductive medium. By applying bursts of power to a tube filled with a low pressure gas, the power supplied ionises the gas providing the conductive medium for the RF signal to be radiated. Liquid antennas are promising candidates for wireless communications. Compared with solid antennas, liquid antennas are more conformable and reconfigurable; while compared with gas antennas, liquid antennas are much easier to be accessed and generated.

1.1.4 Liquid Antennas

Liquid antennas are a type of antenna utilising fluid to transmit and receive radio signals. They have a range of attractive features such as: conformability, reconfigurability, and small radar cross section

(RCS). Two types of liquid antennas are widely investigated: liquid metal antennas and water-based liquid antennas.

Liquid metal antennas are typically fabricated by injecting liquid metal (such as mercury) or liquid metal alloys (such as eutectic gallium 75% indium 25% (EGaIn)) into an elastomeric substrate (e.g., polydimethylsiloxane, PDMS) and are therefore flexible and mechanically durable. They have been recently used in a variety of reconfigurable microwave components and antennas [12-15]. EGaIn is a commercially available liquid metal alloy, which is electrically conductive (the resistivity of EGaIn is around 29.4×10-6 Ω·cm). According to CRC Handbook of Chemistry and Physics (CRC stands for "Chemical Rubber Company"), the components of EGaIn have "low orders of toxicity" [16]. For most applications requiring a liquid metal, EGaIn is superior to mercury (a common liquid metal), for three reasons: 1) EGaIn rapidly flows into and fills microchannels at room temperature when a critical pressure is applied; 2) EGaIn forms a thin oxide skin that provides mechanical stability to the liquid after it is injected into microchannels [16]; 3) mercury is toxic and forms unstable structures. Some designs using EGaIn were proposed, such as a mechanically flexible patch antenna incorporated with a liquid metal encased in an elastomer, this antenna could be flexed without significant change in performance [12]; a liquid metal alloy injected planar inverted cone antenna (PICA) for ultra-wideband (UWB) application, the antenna allowed stretching up to 40% along any axis, as well as folding and twisting, all without mechanical damage [13]; a frequency reconfigurable edge-fed microstrip patch antenna by using liquid metal as switches, two states of the antenna were achieved which designated the antenna to operate in either the 2.4 GHz ISM band or the 1.6 GHz GPS band [14]; and a pressure-driven liquid metal monopole antenna with a wide frequency tuning range from 2 to 9.5 GHz [15]. Another popular liquid metal is known as Galinstan, which consists of 68.5% gallium, 21.5% indium and 10% tin. Galinstan is a liquid from −19 to 1300°C. It is non-toxic and has an RF conductivity of $3.83 \pm 0.16 \times 10^6$ S/m. Some designs were produced by using this material, such as a liquid-metal frequency reconfigurable slot antenna, a continuous frequency tuning range from 1.42 to 1.84 GHz was achieved by controlling the liquid metal position and motion [17]; a tunable liquid metal monopole antenna, the resonant frequency can be tuned from 2 to 9.5 GHz by using pressure driven actuation [18]. The challenges associated with designing liquid metal antennas include: the need for the nontoxic liquid metal with stable structure, fabrication of microfluidic channels and high cost.

Water-based liquid antennas are a kind of antennas using water as the radiating element. By using water-based liquids with different conductivity, water-based liquid antennas can be considered as either DRAs or conducting antennas. They have attractive features such as: a) low-cost and readily accessible; b) compact size - water is a high permittivity material. When it is used as a DRA, the

antenna size can be reduced by a factor of $\sqrt{\varepsilon_r}$; c) conformability - it is easy to make the antenna to the desired shape; d) reconfigurability (physically, electrically and chemically) - the operational frequency and bandwidth may be controlled by the height and width of the liquid stream as well as the chemical composition; e) a small RCS - it can be drained when not in use; f) comparatively easy to transport - especially for a large antenna and g) transparency. All these benefits open up new revenue for water-based liquid antennas. The state of art of the water-based liquid antennas will be reviewed in Chapter 2.

1.2 Motivation of the Work

Water-based liquid antennas are becoming more and more popular in recent years. The first recorded paper on water-based liquid antenna (pure water) was published in 1999. The publications are very limited compared with other types of antennas; however, the trend is on the rise. It is believed that in the next couple of years, the number of publications will be noticeably increased. The published work mainly exists from the University of Liverpool, U. S. Navy, Nanyang Technological University, Heriot-Watt University and some groups in Hong Kong and the China mainland. Currently, most of the published work is focused on single water-based liquid antenna designs. It has not been found a comprehensive investigation on water-based liquid antennas, which provides a thorough discussion from the state of the art of water-based liquid antenna designs to the liquid characteristic analysis under different working mechanisms which has not yet been found. This thesis fills that gap.

In the published papers on water-based liquid antennas, pure water and salty water are most commonly used. The characteristics of pure water (distill water is the most common form of pure water) and salty water are well documented in the open literature [19-22]; however, most of them are focused on the physical or chemical behaviour of the liquids. The information of pure and salty water from antenna design point of view has not been considered. As the properties of pure and salty water are temperature, concentration and frequency dependent, there is a great need to find out the variations of complex permittivity of water-based liquids according to different temperatures, concentrations and frequencies. This is extremely useful in practical antenna design for a given application and it is one motivation for this study.

There are some concerns regarding to water-based liquids for antenna applications, such as the dielectric loss and temperature variations, and these limit the developments of water-based liquid antennas. Among these concerns, one of the most challenging one is how to guarantee the performance under extremely low temperature ($< 0^oC$). Pure water will be frozen when temperature is lower than 0^oC, in this case, water antennas will become solid antennas and the dielectric properties of

ice will be totally different from pure water in liquid state (ice antennas will not be discussed in this thesis). Some researchers have used the salty water antennas to avoid the frozen case, however, the problem is not fundamentally solved. The absence of knowledge for alternative liquids for cold climates and the lack of detailed measurement procedures concerning how to measure the temperature effects of liquid samples are interesting topics, which supplies the motivation to investigate this area.

Water is a kind of material with great design flexibility. When pure water is used as the main radiator, the water antenna will be a DRA. By adding salt into pure water, the dielectric response (real and imaginary) will be decreased and modified, making the antenna a conducting antenna. In the first few years of water antenna designs, cylindrical shape water antennas were very popular [23-27]. The idea originates from the monopole antenna and is straightforward to implement in practice. However, the physical insights behind the antenna design are not carefully studied, and the effects of each part of the antenna are not examined. It is still at a stage of cut and try. Thus it is necessary to study the antenna parameters comprehensively and improve the antenna performance accordingly. Besides, by tuning the conductivity of the salty water, the antenna efficiency will be varied. Therefore, it is realised that a conducting water monopole antenna with a better performance can be achieved based on the extensive parametric studies and a close relationship between the conductivity and the antenna radiation efficiency can be explored, which motivate the study on the conducting water monopole antenna.

In most of the water antenna designs, the resonances of water itself have been used. Two different scenarios are essentially considered: conducting water antennas and water DRAs. For conducting water antennas, salty water is the main radiator. In this case, the antennas are primarily designed for the very high frequency (VHF) band (as the water loss is relatively low), which means quite large antenna dimensions. Some interesting designs based on this idea are proposed, such as [24] and [28]. For water antennas working as DRAs, the antenna size can be reduced by a factor of $\sqrt{\varepsilon_r}$, however, the high permittivity of water will make the antenna bandwidth very narrow [23]. To overcome these limits, the idea of a hybrid resonator antenna technique (HRAT) can be employed. Some existing DRAs designs based on the HRAT are reported [29-36]. To the best of author's knowledge, no sample of such work exists in water antenna designs, which provides the motivation to develop new wideband hybrid water antennas by effectively utilizing the resonances from the water DR and that from the feeding probe. Moreover, the liquidity and transparency of water make it an excellent candidate for hybrid antenna designs. The difficulties of using the resonance of the probe in a solid DRA are either the probe length is limited by the DRA size or the matching is sometimes difficult to achieve [37]. However, by using the water as a DR, a complex feeding structure (more than one element) can be placed and easily tuned inside the water, which would be difficult and expensive to

realise in conventional solid dielectric materials such as ceramics.

With the rapid growth of digital technology, the personal consumption of media has been greatly encouraged. As part of this trend, the Digital Video Broadcasting to Handheld (DVB-H) standard makes it possible to deliver live broadcast television to a mobile handheld device, which aims to provide a generic way to serve handheld terminals in various parts of the world [38]. This is a new standard for delivering broadcast television to a mobile terminal or handheld device, ranging from 470 to 862 MHz. Research into the antenna designs for DVB-H applications has attracted a lot of interest [39-50]. Dedicated small size, reconfiguruable antennas such as folded monopole antennas [41, 43-45] integrated with varactor diodes widely exist in the open literature, whose purpose is to continuously tune the resonant frequency across the whole frequency band. To further minimise antenna size, the use of magneto dielectric material is reported and some promising designs are recorded [47-49]. However, the fabrication of magneto-dielectric material is complex, and needs special shaping and appropriate thermal treatments. The magnetic losses quickly increase with the frequency from about 700 MHz, which will affect the antenna efficiency. This has provided a natural motivation to design reconfigurable antennas with dielectric loading not only has a compact size but also high efficiency and easy fabrication process.

As a summary, the main objectives of this research are as follows:

To investigate the variation of complex permittivity of water-based liquids according to different temperatures, concentrations and frequencies, from the antenna design point of view.

To study alternative liquids for extremely low temperatures ($T < 0^{o}$C).

To study the parameters of the conducting water monopole antenna comprehensively and improve the antenna performance.

To explore the close relationship between the salty water conductivity and antenna radiation efficiency.

To develop new wideband hybrid water antennas based on HRAT.

To design dielectric loaded compact reconfigurable antennas with high efficiency and simple fabrication process.

1.3 Organisation of the Thesis

The contents of this thesis are organised in the following manner.

Chapter 1 provides the background to the project, the motivations of the work and layout of the thesis.

Chapter 2 is to review the previous work on water-based liquid antennas and the state of the art of water-based liquid antenna designs. Moreover, this chapter presents the measurement techniques that are used to characterise all antennas developed in the project. This chapter is important as many of the measurement details introduced later are based on this chapter.

Chapter 3 presents the water-based liquid complex permittivity estimations. The chapter is divided into two parts.

The first part of this chapter deals with the dielectric properties measurements. The liquid measurements carried out for our studies are explained and shown in detail. A locally developed liquid complex permittivity measurement software package is introduced and the setup of the liquid measurement system is displayed.

The second part of the chapter concerns the water-based liquid characterisations. Three water-based liquids namely pure water, water with propylene glycol (PG) and salty water are investigated using both measurement and numerical simulation approaches. New formulae for the approximation of the complex permittivity of the water-based liquids are derived. The complex permittivity of these liquids at various temperatures and substance concentrations are investigated. New comprehensive knowledge of these liquid materials with simple and accurate expressions is gained. In particular, the complex permittivity of water with PG at various conditions is reported.

In Chapter 4, a salty water antenna working as a conducting antenna is studied. The relationship between the salty water conductivity and antenna radiation efficiency is explored. And a broadband monopole water antenna with a dielectric layer is proposed, designed, optimised and evaluated. The characteristics of the antenna and the performance dependency on each part of the antenna are carefully examined.

Chapter 5 introduces the idea of HRAT. By combining the resonance of the water DRA and that of the feeding structure, a wideband response can be achieved. Three hybrid water antennas are designed. The performances of these designs are improved in terms of size and bandwidth. The unique features of the water DR, namely transparency, reconfigurability and liquidity are utilised, allowing complex structures (including the antenna feeding line) to be placed and tuned inside the water easily.

Chapter 6 describes two designs of water loaded reconfigurable antennas for DVB applications. By integrating varactor diodes, the operating frequency of the antennas can be continuously tuned across a wide frequency range. A transparent dielectric loading with a mixture of water and its holder is effectively employed to reduce the antenna size. The radiating element of the designs occupies a very

compact volume. It is demonstrated that these two designs are excellent candidates for UHF and DVB-H applications.

Finally, Chapter 7 draws the conclusion of the work. The main objectives are reviewed, and the contributions are highlighted. Furthermore, the challenges and possible extensions worthwhile to investigate as future research topics are presented.

1.4 References

[1] C. A. Balanis, *Antenna theory analysis and design*, John Wiley & Sons, Inc., 2005.

[2] J. L. Volakis, *Antenna engineering hand book*, McGraw-Hill Education, 2007.

[3] Y. Huang and K. Boyle, *Antennas from theory and practice*, John Wiley & Sons, Ltd, 2005.

[4] C. A. Balanis, "Antenna theory: a review," IEEE Proc., vol. 80, no.1, pp. 7-23, 1992.

[5] D. S. Filipouic and J. L. Volakis, "Novel slot spiral antenna designs for dual-band/multiband operation," IEEE Trans. Antennas Propag., vol. 51, no. 3, pp. 430-440, 2003.

[6] R. H. DuHamel and D. E. Isbell, "Broadband logarithmically periodic antenna structures," 1975 IRE National Convention Record, pt. 1, pp. 119-128.

[7] R. Garg, P. Bhartia, I. Bahl, A. Ittipiboon, *Microstrip antenna design handbook*, Artech House, Inc., 2001.

[8] S. A. Long, M. McAllister, and L. C. Shen, "The resonant cylindrical cavity antenna," IEEE Trans. Antennas Propag., vol. AP-31, 1983.

[9] R. K. Mongia and A. Ittipiboon, "Theoretical and experimental investigations on rectangular dielectric resonator antennas," IEEE Trans. Antennas Propag., vol. 45, no. 9, 1997.

[10] K. M. Luk and K. W. Leung, *Dielectric resonator antennas*, Research Studies Press Ltd., 2003.

[11] A. Petosa, *Dielectric resonator antenna handbook*, Artech House, Inc. 2007.

[12] G. J. Hayes, J. H. So, A. Qusba, M. D. Dickey, G. Lazzi, "Flexible liquid metal alloy (EGaIn) microstrip patch antenna," IEEE Trans. Antennas Propag., vol. 60, no. 5, pp. 2151-2156, 2012.

[13] S. Cheng, Z. Wu, P. Hallbjorner, K. Hjort, A. Rydberg, "Foldable and stretchable liquid metal planar inverted cone antenna," IEEE Trans. Antennas Propag., vol. 57, no. 12, pp. 3765-3771, 2009.

[14] M. Kelley, C. Koo, H. McQuilken, B. Lawrence, S. Li, A. Han and G. Huff, "Frequency reconfigurable patch antenna using liquid metal as switching mechanism," Electron. Lett., vol. 49, no. 22, pp. 1370-1371, 2013.

[15] A. M. Morishita, C. K. Y. Kitamura, A. T. Ohta and W. A. Shiroma, "Two-octave tunable liquid-metal monopole antenna," Electron. Lett., vol. 50, no. 1, pp. 19-22, 2014.

[16] M. D. Dickey, R. C. Chiechi, R. J. Larsen, E. A. Weiss, D. A. Weitz, and G. M. Whitesides, "Eutectic gallium-indum (EGaIn): A liquid metal alloy for the formation of stable structures in microchannels at room temperature," Adv. Funct. Mater., vol. 18, pp. 1097-1104, 2008.

[17] J. H. Dang, R. C. Gough, A. M. Morishita, A. T. Ohta and W. A. Shiroma, "Liquid-metal frequency-reconfigurable slot antenna using air-bubble actuation," Electron. Lett., vol. 51, no. 21, pp. 1630-1632, 2015.

[18] A. M. Morishita, C. K. Kitamura, A. T. Ohta and W. A. Shiroma, "Two-octave tunable liquid-metal monopole antenna," Electron. Lett., vol. 50, no. 1, pp. 19-20, 2014.

[19] L. Klein, C. T. Swift, "An improved model for the dielectric constant of sea water at microwave frequencies," IEEE Trans. Antennas Propag., vol. 25, no. 1, pp. 104-111, 1977.

[20] H. J. Liebe, G. A. Hufford, T. Manabe, "A model for the complex permittivity of water at frequencies below 1 THz," Int. J. of Infrared and Millimeter Waves, vol. 12, no. 7, pp. 659-675, Jul. 1991.

[21] W. Ellison, A. Balana, G. Delbos, K. Lamkaouchi, L. Eymard, C. Guillou, C. Prigent, "New permittivity measurements of seawater," Radio Sci., vol. 33, no. 3, pp. 639-648, 1998.

[22] T. Meissner, F. J. Wentz, "The complex dielectric constant of pure and sea water from microwave satellite observations," IEEE Trans. Geosci. Remote Sens., vol. 42, no. 9, pp.1836-1849, 2004.

[23] S. P. Kingsley, S. G. O'Keefe, "Beam steering and monopulse processing of probe-fed dielectric resonator antennas," Proc. IEE Radar, Sonar and Navigation, vol. 146, no. 3, pp. 121-125, 1999.

[24] H. Fayad and P. Record, “Broadband liquid antenna,” Electron. Lett., vol. 42, no. 3, pp. 133-134, 2006.

[25] S. G. O'Keefe, S. P. Kingsley, “Tunability of liquid dielectric resonator antennas,” IEEE Antennas Wireless Propag. Lett., vol. 6, pp. 533-536, 2007.

[26] L. Xing, Y. Huang, S. Alja'afreh, and S. J. Boyes, “A monopole water antenna,” in Proc. Loughborough Antennas Propag. Conf., 2012, pp. 1-4.

[27] R. Zhou, H. Zhang, H. Xin, “Liquid-based dielectric resonator antenna and its application for measuring liquid real permittivities,” IET Microw., Antennas & Propag., vol. 8, no. 4, pp. 255-262, 2014.

[28] C. Hua, Z. Shen, and J. Lu, “High-efficiency sea-water monopole antenna for maritime wireless communications,” IEEE Trans. Antennas Propag., vol. 62, no. 12, pp. 5968-5973, 2014.

[29] M. Lapierre,Y. M. M. Antar, A. Ittipiboon, A. Petosa, “Ultra wideband monopole/dielectric resonator antenna,” IEEE Microw. Compon. Lett., vol. 15, no. 1, pp. 7-9, 2005.

[30] K. Lan, S. K. Chaudhuri, S. Safavi-Naeini, “Design and analysis of a combination antenna with rectangular dielectric resonator and inverted L-plate,” IEEE Trans. Antennas and Propag., vol. 53, no. 1, pp. 495-501, 2005.

[31] Q. Rao, T. A. Denidni, A. R. Sebak, and R. H. Johnston, “Compact independent dual-band hybrid resonator antenna with multifunctional beams,” IEEE Antennas Wireless Propag. Lett., vol. 5, pp. 239-242, 2006.

[32] Y. Gao, B. L. Ooi, W. B. Ewe, A. P. Popov, “A compact wideband hybrid dielectric resonator antenna,” IEEE Microw. Compon. Lett., vol. 16, no. 4, pp. 227-229, 2006.

[33] T. H. Chang, J. F. Kiang, “Broadband dielectric resonator antenna with metal coating,” IEEE Trans. Antennas and Propag., vol. 55, no. 5, pp. 1254-1259, 2007.

[34] L. Huitema, M. Koubeissi, M. Mouhamadou, E. Arnaud, C. Decroze, T. Monediere, “Compact and multiband dielectric resonator antenna with pattern diversity for multistandard mobile handheld devices,” IEEE Trans. Antennas and Propag., vol. 59, no. 11, pp. 4201-4208, 2011.

[35] D. Guha, B. Gupta, and Y. M. M. Antar, "New pawn-shaped dielectric ring resonator loaded hybrid monopole antenna for improved ultrawide bandwidth," IEEE Antennas Wireless Propag. Lett., vol. 8, pp. 1178-1181, 2009.

[36] Y. M. Pan, S. Y. Zheng, W. W. Li, "Dual-band and dual-sense omnidirectional circularly polarised antenna," IEEE Antennas Wireless Propag. Lett., vol. 13, pp. 706-709, 2014.

[37] A. Buerkle, K. Sarabandi, H. Mosallaei, "Compact slot and dielectric resonator antenna with dual-resonance, broadband characteristics," IEEE Trans. Antennas and Propag., vol. 53, no. 3, pp. 1020-1027, 2005.

[38] "DVB-H Implementation Guidelines," ETSI TR 102 377 V1.1.1 (2009-02) European Telecommunications Standards Institute.

[39] L. Huitema, M. Koubeissi, C. Decroze, T. Monediere, "Ultrawideband dielectric resonator antenna for DVB-H and GSM applications," IEEE Antennas Wireless Propag. Lett., vol. 8, pp.1021-1027, 2009.

[40] L. Xing, Y. Huang, Q. Xu, S. Aljaafreh, T. Liu, "A broadband hybrid water antenna for hand-portable applications," IEEE Antennas Wireless Propag. Lett. [Online]. Available: http://ieeexplore.ieee.org/stamp/stamp.jsp?tp=&arnumber=7112462

[41] D. H. Choi, H. S. Yun, and S. O. Park, "Internal antenna with modified monopole type for DVB-H applications," Electron. Lett., vol. 42, pp. 1436-1438, 2006.

[42] X. L. Bao, M. J. Ammann, S. V. Shynu, "Design of a tunable compact antenna for digital video broadcasting handheld terminals," in Proc. Loughborough Antennas Propag. Conf., 2009, pp. 461-464.

[43] Y. Li, Z. Zhang, W. Chen, Z. Feng, M. F. Iskander, "A compact DVB-H antenna with varactor-tuned matching circuit," Microw. Opt. Technol. Lett., vol. 52, no. 8, pp. 1786-1789, 2010.

[44] D. H. Choi, Y. T. Im, Y. J. Cho, S. O. Park, "A tunable antenna for DVB-H applications," IEEE Antennas Wireless Propag. Lett., vol. 6, pp. 515-517, 2007.

[45] M. Komulainen, M. Berg, H. Jantunen, E. Salonen, "Compact varactor-tuned meander line monopole antenna for DVB-H signal reception," Electron. Lett., vol. 43, no. 24, pp. 1324-1326, 2007.

[46] M. Abdallah, F. Colombel, G. Le Ray, and M. Himdi, "Frequency tunable antenna for digital video broadcasting hand-held application," Prog. Electromagn. Res. Lett., vol. 24, pp. 1-8, 2011.

[47] F. Ferrero, A. Chevalier, J. M. Ribero, R. Staraj, J. L. Mattei, Y. Queffelec, "A new magneto-dielectric material loaded, tunable UHF antenna for handheld devices," IEEE Antennas Wireless Propag. Lett., vol. 10, pp. 951-954, 2011.

[48] F. Canneva, F. Ferrero, A. Chevalier, J. M. Ribero, J. L. Mattei, P. Queffelec and R. Staraj, "Miniature reconfigurable antenna with magneto dielectric substrate for DVB-H band," Microw. Opt. Technol. Lett., vol. 55, no. 9, pp. 2007-2011, 2013.

[49] L. Huitema, T. Reveyrand, J. L. Mattei, E. Arnaud, C. Decroze, T. Monediere, "Frequency tunable antenna using a magneto-dielectric material for DVB-H application," IEEE Trans. Antennas Propagat., vol. 61, no. 9, pp. 4456-4466, 2013.

[50] L. Xing; Y. Huang; S. Alja'afreh, Q. Xu, M. Kod, C. Y. Song, "Reconfigurable 3D folded monopole antenna design for DVB-H applications," in Proc. Loughborough Antennas Propag. Conf., 2014, pp. 530-532.

Chapter 2: Overview of Water-Based Liquid Antennas and Antenna Measurement Techniques

2.1 Introduction

This chapter has two parts.

In the first part, an overview of the research carried out on water-based liquid antennas over the past few years is presented chronologically. Major designs are highlighted. The state of the art of water-based liquid antenna technology is reviewed. The achieved performances of water-based liquid antennas are illustrated. It is going to give readers a sense of the design flexibility offered by water-based liquid antennas and their potential advantages compared to traditional antennas. The knowledge provided in this chapter will help antenna designers to gain a better understanding of their potential, and perhaps consider them as alternatives in future new antenna designs. It can also serve as a reference and a comprehensive review of the achievements up to now.

In the second part, the antenna measurement techniques, particularly used in the thesis, are reviewed. The physical insights into the techniques are illustrated; the derivation processes are provided and the measurement procedures are stated. It will give readers a clear picture of how and why these measurements are performed.

2.2 Overview of Water-Based Liquid Antennas

As a special type of liquid antennas, water-based designs have attracted increasing interest in recent years. Since 1999 to the present, more researchers have started to investigate water-based liquid antennas [1- 30].

The study of water-based liquids as radiating elements was first carried out in 1999 [1]. A cylindrical DRA with multi-probe was proposed, as shown in Fig. 2.1. It consisted of a water-filled cylindrical plastic tube, having a diameter of 550 mm and a height of 200 mm, mounted on an octagonal ground plane (800 mm across the flat edges). The distilled water was chosen as the dielectric medium mainly for three reasons [1]: as a liquid dielectric, 1) water could be easily constrained to the desired shape; 2) there were no air-gaps between the probe and dielectric, or between the dielectric and conducting plane; 3) when dealing with physically large DRAs at low frequencies, distilled water was a low cost

and readily accessible material with a high dielectric constant. The azimuth radiation pattern direction can be changed by exciting different probes within the dielectric when other probes are open-circuited. In some combinations, a pair of probes had a greater bandwidth than a single probe. It was demonstrated that the design had obvious applications for radar system where control of the radiation pattern was desirable.

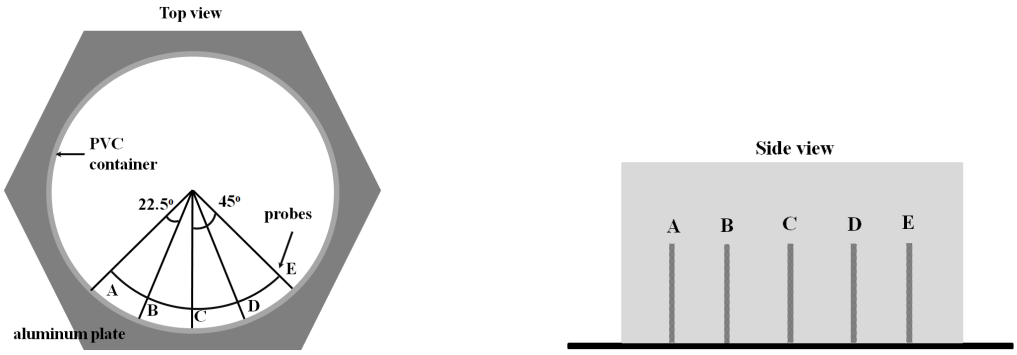

Fig. 2.1. Structure of water-filled multi-probe cylindrical VHF DRA [1].

In 2005 and 2006, Fayad *et al* designed a wideband saline water antenna, based on a monopole structure [2-4]. It can be regarded as a first salty water antenna reported in the open literature. The antenna was constructed from a polyvinyl chloride (PVC) tube mounted on a 25 × 25 cm^2 ground plane as shown in Fig. 2.2. Two monopole diameters of 25 and 50 mm were measured with water samples of different salinity. By increasing the salinity, the bandwidth increased.

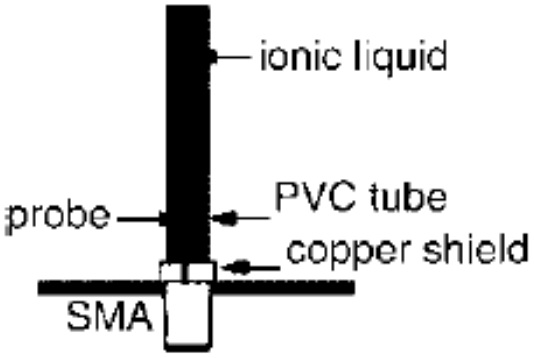

Fig. 2.2. Geometry of the proposed liquid antenna [4].

Later in 2007, a cylindrical 50 MHz DRA using water as the dielectric was presented, as shown in Fig. 2.3(a) [5]. By altering the level of water in the DRA from 276 to 95 mm, the resonant frequency of the antenna was shifted upwards from 50 to 96.8 MHz. A folded monopole probe with 3 varicap diodes in parallel at the top was employed to replace the single monopole probe as the feed for the DRA, as shown in Fig. 2.3(b), which could be tuned to give the best match as the water level was altered.

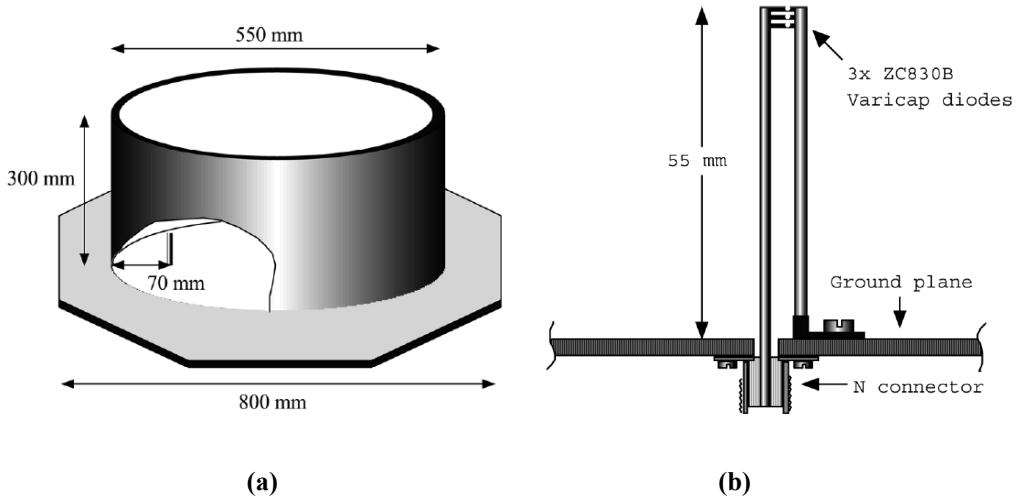

Fig. 2.3. (a) The structure to contain the water to form the DRA. (b) Tunable DRA probe [5].

In 2008, a bracelet-type liquid antenna was proposed for wearable or implantable bio-monitoring applications [6]. It consisted of salty water inside a very think flexible plastic tubing container with a tube radius of 2.5 mm, as shown in Fig. 2.4. The bracelet was mounted on various positions of an inhomogeneous multilayer cylinder emulating the human body. The liquid antenna worked at a central frequency of 1.7 GHz. The simulated results showed that this bracelet liquid antenna had higher efficiency and directivity in the direction transverse to the arm than a metal antenna of the same physical size at the same position. The antenna was very easy reconfigured by changing the salinity levels.

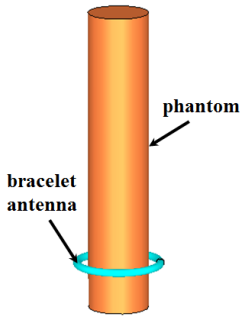

Fig. 2.4. Wearable liquid antenna bracelet around a lower-arm phantom [6].

In 2009, a rectangular liquid DRA with a compact size was reported, as shown in Fig. 2.5 [7]. Distilled water was used as the dielectric material. The water DRA had dimensions of 161 ×162.6 ×161 mm^3, which was placed on a metal plate with dimensions of 172 × 318 mm^2. Owing to the feed orientation and the symmetry of the antenna configuration, the $TE^{Z}_{21\delta}$ mode was excited as the main radiating mode with a resonant frequency at 242 MHz, a 10 dB bandwidth of 2.5%, and a gain of -2.5 dBi. The radiation patterns of the antenna were very similar to those of a monopole antenna. Based on this design, a method for measuring real permittivity of liquids was developed [8]. As the relative

permittivity ε_r' of the contained liquid with fixed configuration was directly linked to the antenna resonant frequency *f*, an analytical model ε_r' as a function of *f* was derived and applied to evaluate the liquid ε_r' with the measured antenna resonant frequency. The drawback of this method was that it only worked for materials with low losses (e.g. $\tan\delta < 0.1$).

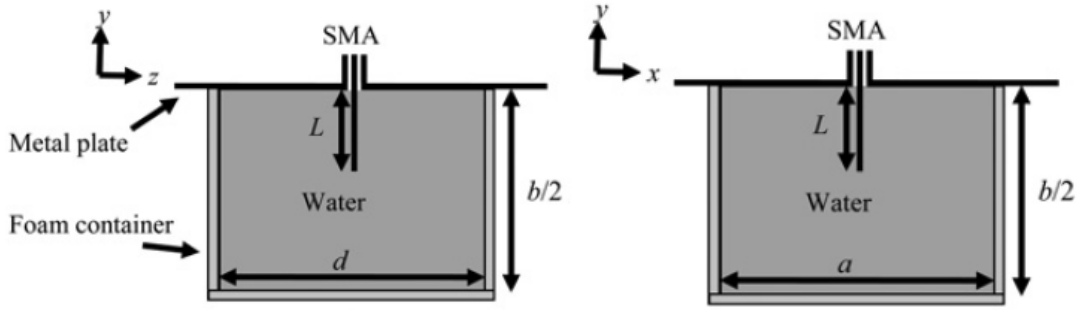

(a) **(b)**

Fig. 2.5. The configuration of the rectangular liquid dielectric resonator antenna (DRA) [8]. (a) Y-z plane. (b) X-y plane.

In 2011, a US patent on an electrolytic fluid antenna with a relatively small foot print was published [9]. It consisted of a current probe, a pump with a nozzle wherein the pump was configured to pump electrolytic fluid out the nozzle, and a transceiver operatively coupled to the current probe. The working mechanism behind the design was that the electrolytic fluid (24 in Fig. 2.6(a)) was pumped out the nozzle (20 in Fig. 2.6(a)) and through the aperture (22 in Fig. 2.6(a)) created a continuous stream which acted as the antenna element, thereby effectively forming an antenna capable of receiving and/or transmitting electromagnetic signals [9]. The length determined the frequency of the antenna and the thickness of the antenna determined the bandwidth. The reconfigurability of the antenna was also demonstrated. Fig. 2.6(b) shows stream 24 with multiple sub-streams of different lengths L_1 to L_n (n is an index). Different sub-stream lengths produced different electrical lengths that caused different resonant frequency responses [9].

Following [9], a patent on an improved electrolytic fluid antenna with signal enhancer was proposed [10], where the enhancer was required to improve the antenna performance. The signal enhancer (46 in Fig. 2.7) was placed inside the aperture (22 in Fig. 2.7) of the current probe (12 in Fig. 2.7). The signal enhancer comprised an inlet (48 in Fig. 2.7), an outlet (50 in Fig. 2.7) and a non-conductive housing (52 in Fig. 2.7) having an internal volume (54 in Fig. 2.7). When the antenna was working, the pump (14 in Fig. 2.7) was configured to pump electrolytic fluid through the internal volume so that the fluid filled the internal volume and then exited the outlet in a stream.

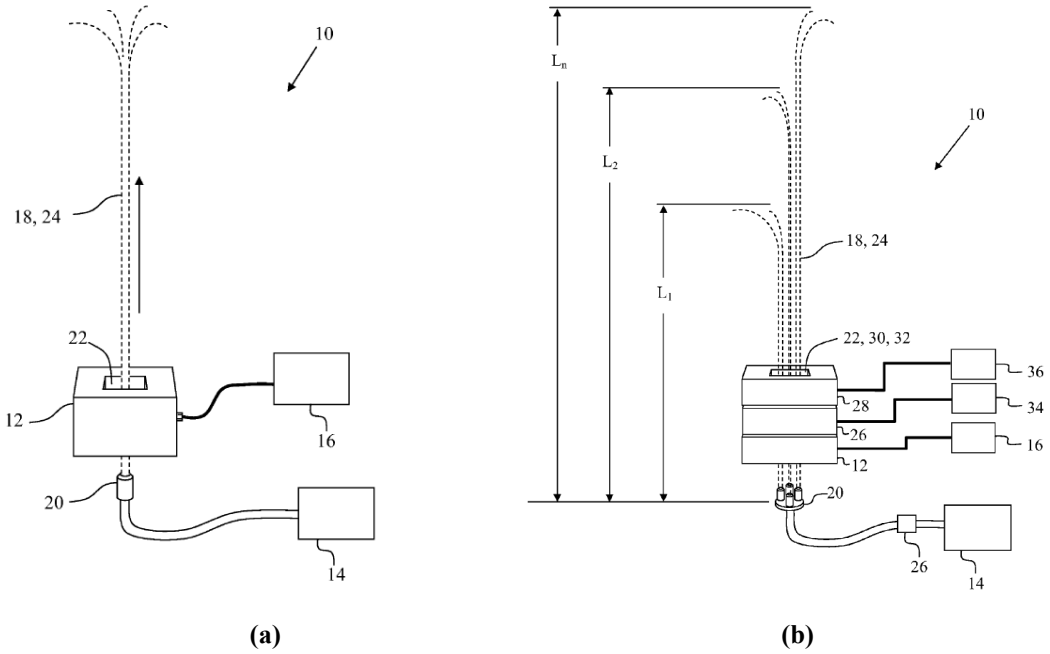

Fig. 2.6. (a) Perspective view of the electrolytic fluid antenna [9]. (b) Embodiment of the multi-band electrolytic fluid antenna with varying electrolytic fluid lengths [9].

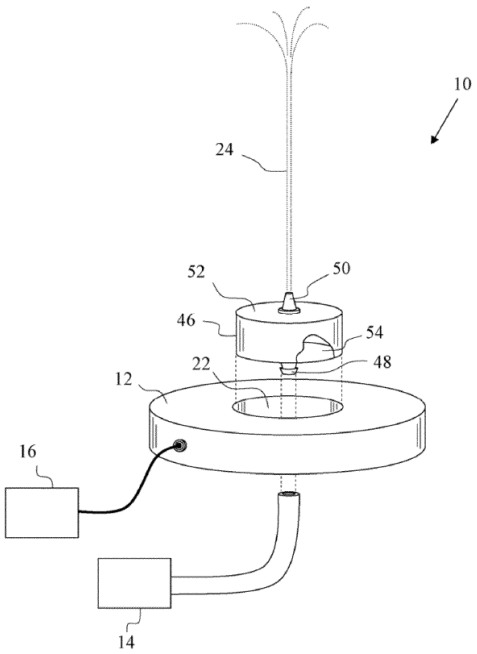

Fig. 2.7. An expanded perspective view of the electrolytic fluid antenna with a signal enhancer [10].

Based on patents [9, 10], Space and Naval Warfare Systems Center Pacific (SSC Pacific) developed a sea water antenna device, as shown in Fig. 2.8. The patented antenna was tested at a distance of over 30 miles at frequencies ranging from 2 to 400 MHz. The antenna required a relatively small footprint and can be modified to accommodate multiple frequencies and bandwidths by stacking current probes

and adding additional spray nozzles. It can be turned off when not in use, allowing antennas to "disappear" from the landscape [11].

Fig. 2.8. A salty water antenna produced by SSC Pacific [11].

The top view of the U-shaped water DRA proposed in [13] is shown in Fig. 2.9. The U-shaped water DR had dimensions of 25 × 14.4 × 9 mm^3 (a = 25 mm, g_4 = 1.4 mm, g_1 = 2.5 mm, g_3 = 1 mm, d = 13 mm, d_2 = 14 mm in Fig. 2.11) and was placed at the corner of a rectangular ground plane with dimensions of 40 × 90 mm^2 (L_g = 90 mm, W_g = 40 mm in Fig. 211). Three different modes, namely TE^{y}_{111}, TE^{y}_{211} and TE^{x}_{111}were excited. The antenna covered a frequency band from 2.4 to 3 GHz with a fractional bandwidth 22% for S_{11} < -10 dB.

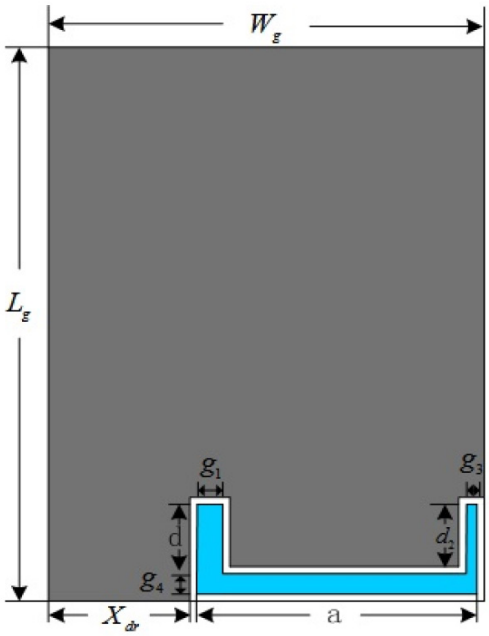

Fig. 2.9. Top view of the U-shaped water DRA antenna [13].

In 2014, a reconfigurable leaky-wave antenna using periodic water grating on the top of a grounded glass slab was designed [15] and the prototype is shown in Fig. 2.10. The coaxial probe protruded into

the glass slab with a certain heightlying at the focus of the parabolic reflecting wall and excited cylindrical electromagnetic waves in the slab. The direct forward waves were suppressed by the reflecting post and the backward waves were reflected by the parabolic reflecting wall and transformed into plane waves propagating in the glass slab. Water grooves were cut into the glass slab from the top surface with a certain depth. By properly choosing the water flow among grooves, a number of water grating antennas were obtained as shown in Fig. 2.11. A set of parameters $\{W_g, P_g\}$ was used to represent the water grating structure, where W_g represented the width of the water grating and P_g denoted its period. The antennas in Fig. 2.11(b) and (c) can be coded as $\{2d_g, 4(d_g + d_s)\}$ and $\{2d_g, 5(d_g + d_s)\}$, respectively. The antenna beam-point angle can be tuned by varying the period of the grating. The bandwidth of the antenna can be slightly adjusted by modifying the width of the grating, which related to the number of water-filled grooves. The simulated and measured E-plane patterns of the water grating antenna at 5.5 GHz was shown in Fig. 2.12. It was observed that the beam-pointing angle can be tuned from -32° to 18° at 5.5 GHz.

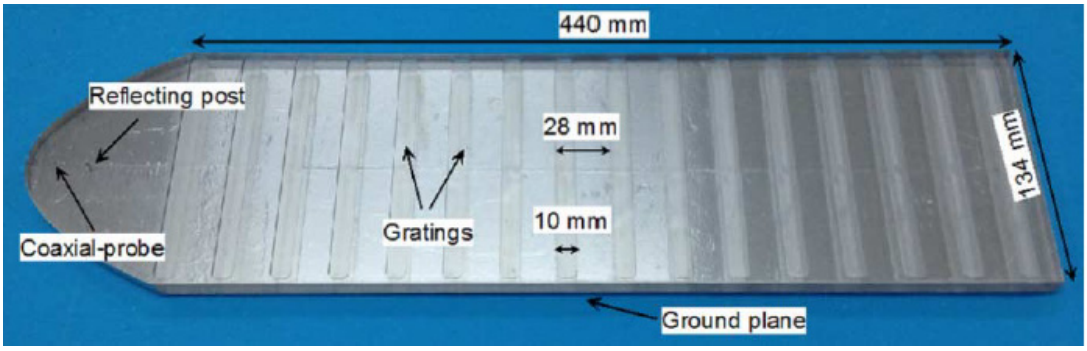

Fig. 2.10. Fabricated water grating leaky-wave antenna [15].

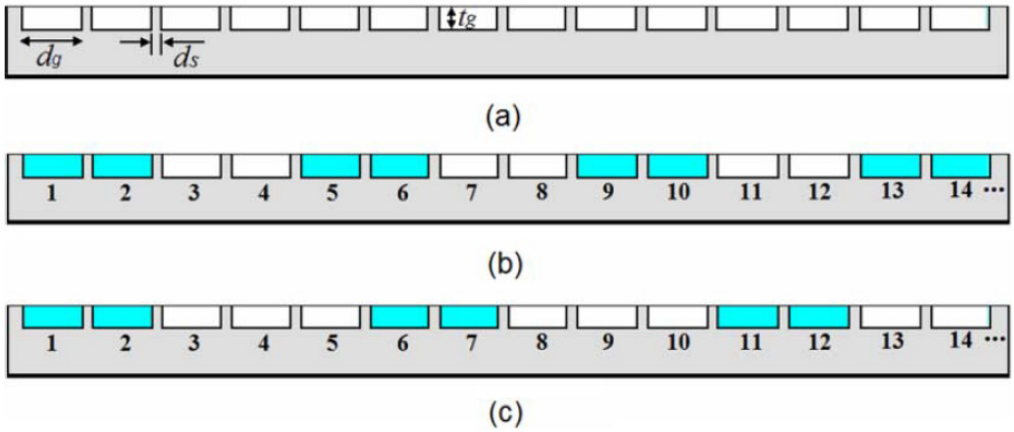

Fig. 2.11. Side view of the periodic grating structures [15]. (a) Slab with empty grooves. (b) Water grating antenna $\{2d_g, 4(d_g + d_s)\}$. (c) Water grating antenna $\{2d_g, 5(d_g + d_s)\}$.

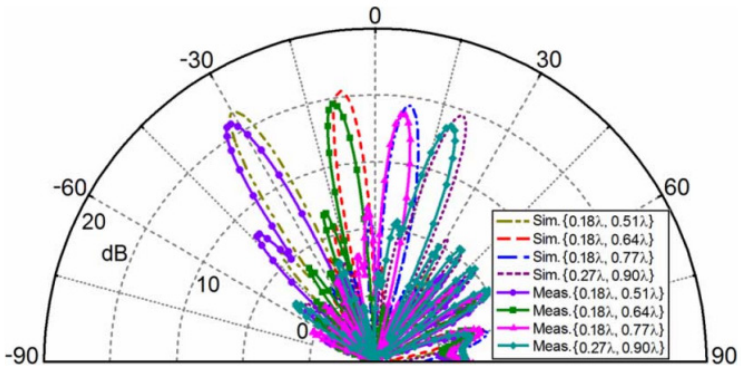

Fig. 2.12. Simulated and measured E-plane patterns at 5.5 GHz (d_g = 5 mm, d_s = 2 mm, h = 12.7 mm, h_c = 10 mm, h_s = 12.7 mm, C = 15mm, C_1 = 16 mm, C_2 = 34 mm, w_s = 124 mm, t_g = 1.7 mm, L = 440 mm) [15].

Also in 2014, a high efficiency seawater monopole antenna for maritime wireless communications was proposed [17], as shown in Fig. 2.13. A disk loaded feeding probe was employed instead of the ordinary feeding probe to improve the radiation of the antenna. A theoretical study based on the three-term theory was carried out to examine the antenna performance. The measured results showed that this water antenna had a -10 dB bandwidth of 28% (53.8 - 71.2 MHz), and the center frequency can be tuned over a frequency of 62.5 to 180.2 MHz by changing the water height from 1000 to 300 mm.

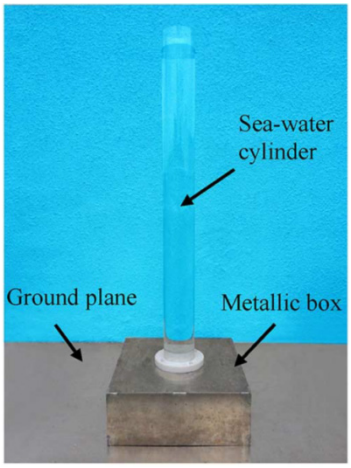

Fig. 2.13. The fabricated monopole sea-water antenna in [17].

In [18], compact dual-band directional/ omni-directional DRAs were proposed. The resonant mode of the water filled glass bottle was employed to cover the higher band around 2.2 GHz and a resonant frequency of the slot under the glass bottle was introduced to cover the lower band around 1. 75 GHz, thus the dual-band operation can be realised. The directional and omni-directional radiation patterns were achieved by using one DRA shown in Fig. 2.14(a) and two closely spaced dual-band antennas as shown in Fig. 2.14(b), respectively.

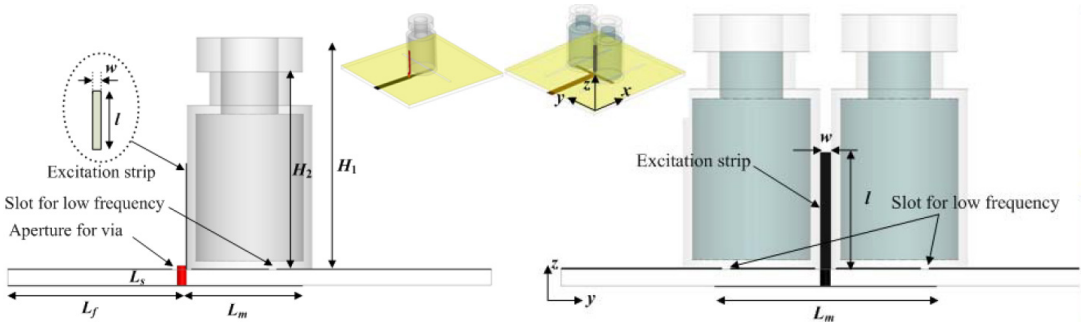

(a) **(b)**

Fig. 2.14. (a) Dual-band DRA with directional radiation pattern. (b) Dual-band DRA with omni-directional radiation pattern [18].

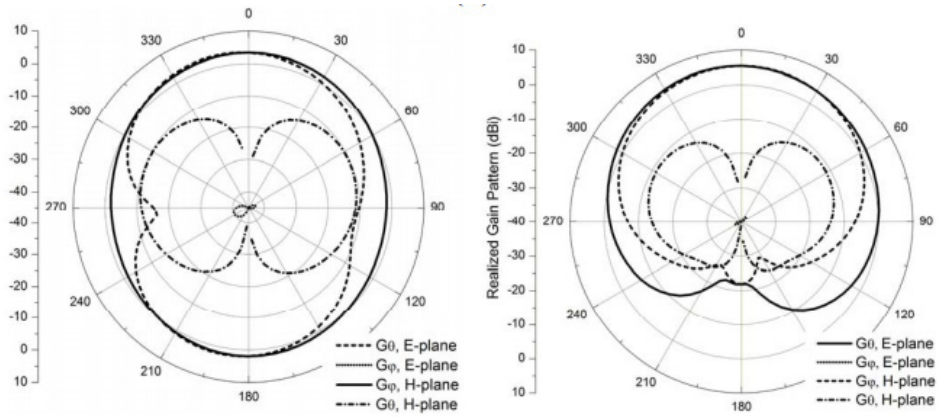

(a) **(b)**

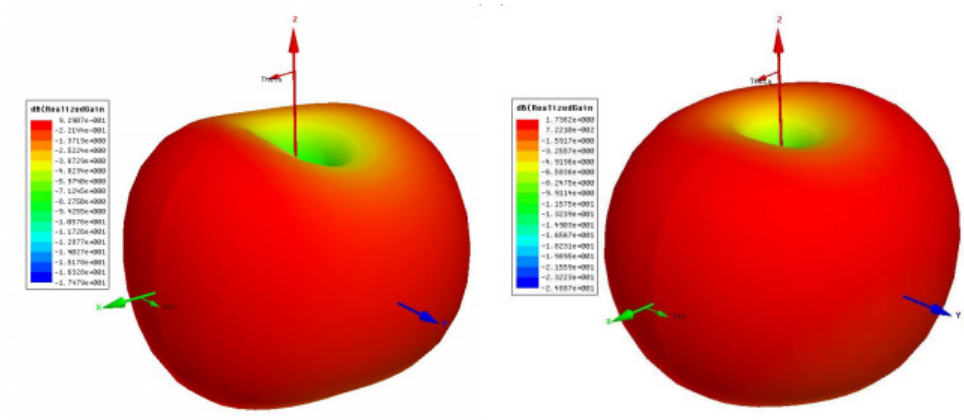

(c) **(d)**

Fig. 2.15. (a) Dual-band DRA with directional radiation pattern at 1.75 GHz [18]. (b) Dual-band DRA with directional radiation pattern at 2.275 GHz [18]. (c) Dual-band DRA with omni-directional radiation pattern at 1.775 GHz [18]. (d) Dual-band DRA with omni-directional radiation pattern at 2.2 GHz [18].

In 2015, more publications were produced. The antennas were not limited to the basic shapes such as rectangular and cylindrical. Modified geometries were explored. The antenna types were not only conducting antennas or DRAs, some hybrid antennas combining both metal antenna and DRA were reported.

Ref. [19] presented a water dense dielectric patch antenna (DDPA) fed by an L-shaped probe as shown in Fig. 2.16, which developed from the DDPA introduced in [20]. Two boxes made of plexiglass were stacked together. The top smaller rectangular box with a width of W_P, a length of L_P, and a height of H_P was filled with pure water to construct the water dielectric patch, while the bottom larger square box with a height of H_A was empty and was used as a supporting structure [19]. Therefore, the substrate between the water patch and the ground plane was air in this design. A square metallic ground plane of length W_G was installed at the bottom surface of the large box, where the L-shaped probe was mounted [19]. The operation mechanism of the water DDPA was similar to the conventional metallic patch antenna, and the antenna was excited in a mode like the TM_{01} mode of the rectangular patch antenna. The water patch in this antenna worked as neither a conductor for current flow nor a DR, it was used for providing a boundary condition similar to an electrical wall. The measurement results showed that the antenna had an impedance bandwidth 8% for S_{11}< -10 dB, maximum gain of 7.3 dBi, and radiation efficiency up to 70%. Besides, the transparency of the water was utilised and a dual-function of the water antenna was realised by integrating solar cells under the water patch as shown in Fig. 2.17. Luckily, the performance of the antenna was not changed significantly.

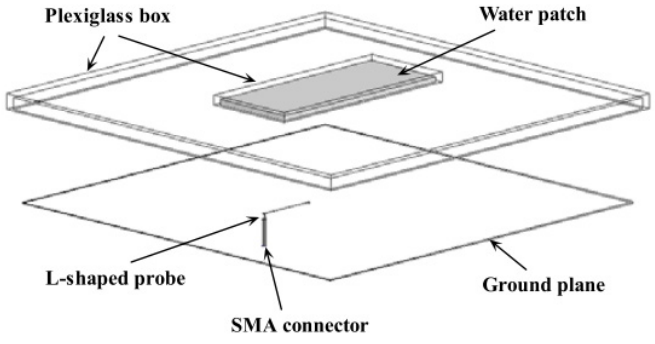

(a)

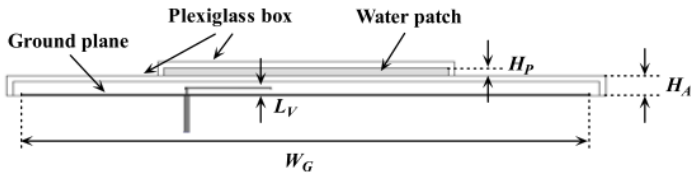

(b)

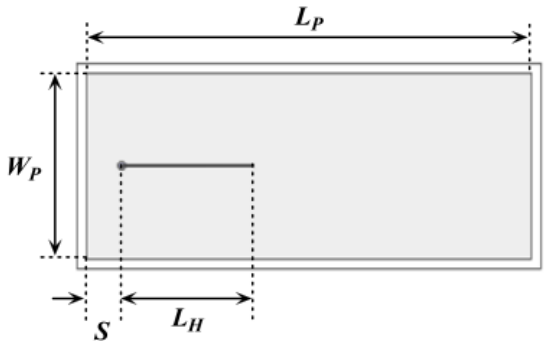

(c)

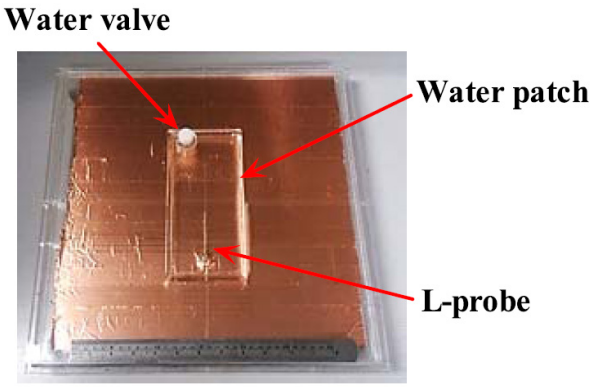

(d)

Fig. 2.16 Geometry of the proposed L-probe fed water dielectric patch antenna [19]. (a) Overall geometry. (b) Side view. (c) Top view of the water patch with L-probe. (d) Fabricated water dielectric patch antenna.

Fig. 2.17. Fabricated water dielectric patch antenna integrated with solar cells [19].

As the water-based liquid antennas have attracted increasing attention, a special section for liquid antennas was organised at the IEEE 4th Asia-Pacific Conference on Antennas and Propagation (APCAP 2015), a number of the more-recent designs were published [24-27].

Ref. [25] presented a hybrid water antenna at UHF band as shown in Fig. 2.18(a). It was composed of a seawater monopole and a distilled water ring antenna. The combination of the seawater antenna and distilled water antenna can be regarded as a hybrid conducting monopole and a DR ring antenna. Different liquids and different types of antennas were effectively combined to form a hybrid structure. The antenna covered a frequency range from 52.5 to 162.5 MHz (a fractional bandwidth of 102%). To further broaden the bandwidth, a conical DRA was used instead of the ring antenna as shown in Fig. 2.18(b), with a very wide frequency range from 54.5 to 251.4 MHz (a fractional bandwidth of 129%).

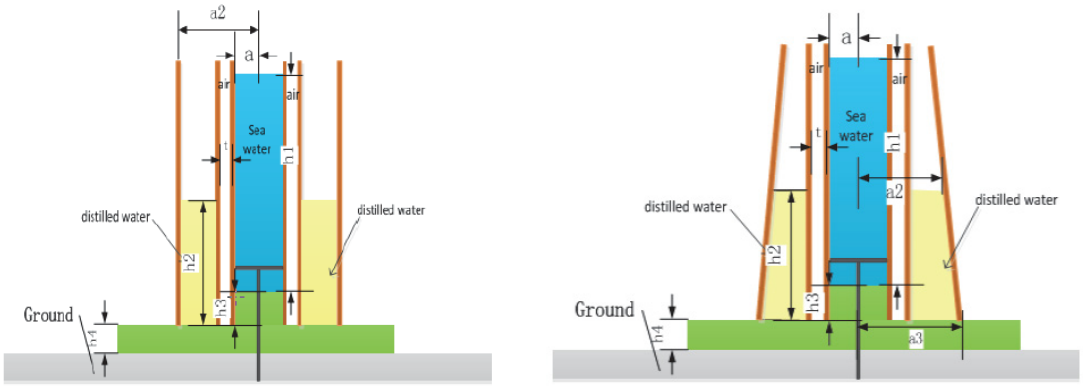

Fig. 2.18. (a) Geometry of the hybrid water monopole-ring antenna [25]. (b) Geometry of the hybrid water monopole-conical antenna [25].

In [26], a 2 × 2 water dielectric patch antenna array was designed for Wi-Fi communication application as shown in Fig. 2.19. The antenna element was based on the design proposed in [19] and the pure water layer was used to replace the top metallic patch of the traditional microstrip antenna. The H-shaped slots were employed to couple the feeding network. The simulated results show that the antenna array covered a frequency range from 2.23 to 2.65 GHz for S_{11}< -10 dB, and the gain was between 11 to 12.8 dBi across the operating frequency.

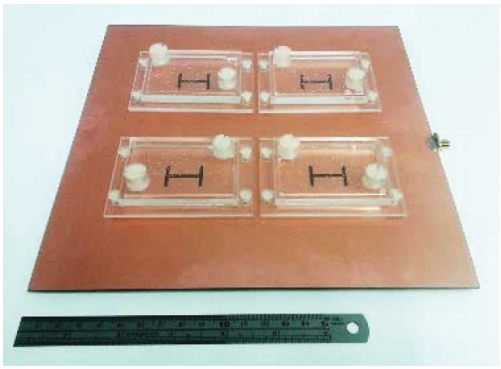

Fig. 2.19. Fabricated water dielectric patch antenna array [26].

In [27], a seawater half-loop antenna was developed at the VHF band for maritime wireless communications. A capacitive coupling feeding structure in Fig. 2.20(a) was designed to efficiently excite the half-loop seawater stream. When the antenna was activated, the seawater was first pumped into metallic tube and then the water stream shot out from the tube to form a half loop. The resonant frequency can be tuned by changing the capacitive feeding or the power of the water pump. A fabricated antenna is displayed in Fig. 2.20(b). It should be mentioned that the use of this antenna is restricted in complex and poor marine environments such as a storm [27].

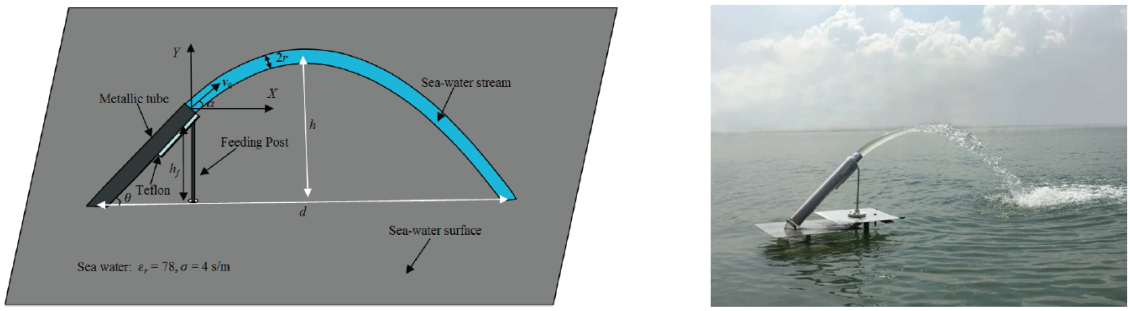

(a) **(b)**

Fig. 2.20. (a) Geometry of the seawater half-loop antenna. (b) Fabricated seawater half-loop antenna [27].

In [28], a pure water Yagi monopole antenna was designed, which comprised a probe-fed water monopole as the driven element and a water cylinder as the parasitic element, as shown in Fig. 2.21. A unidirectional far field pattern can be achieved, by varying the diameter and radius of the parasitic element and the spacing between the two water cylinders [28]. The antenna covered a wide frequency range from 1.42 to 1.82 GHz for S_{11} < -10 dB (a fractional bandwidth of 25%), with a maximum gain of 9.3 dBi.

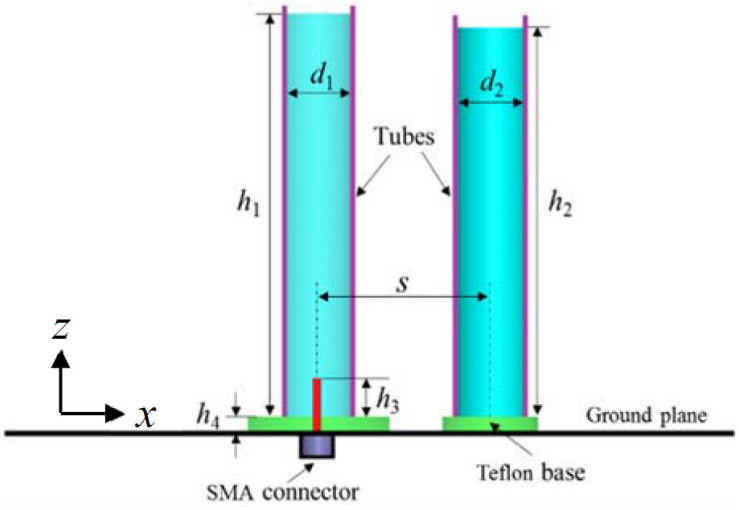

Fig. 2.21. Configuration of the proposed pure water Yagi antenna [28].

In [29], a dynamic type seawater monopole antenna was proposed, as shown in Fig. 2.22. The design was improved from the seawater monopole antenna reported in [17]. A water pump was employed to provide the dynamic water stream. A shunt feeding structure formed by a conducing tube and a Gamma-shape feeding arm connected to the conducting tube was used to excite the antenna. A matching network was placed in a waterproof plastic box to improve impedance matching. Both static and dymatic types of seawater monopole were fabricated and measured. Measured results showed that these two prototypes were in reasonably good agreement. It was found that by tuning the water height from 0.6 to 1 m, the center frequency of the antenna could be tuned over a frequency range of 65.1 to 98.5 MHz [29].

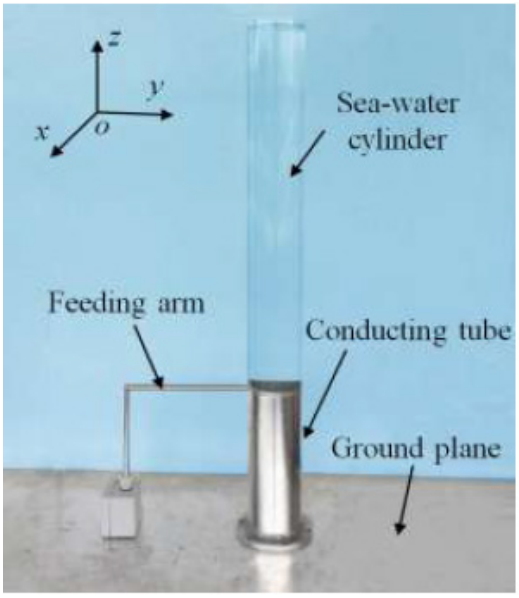

Fig. 2.22. Photograph of the static type seawater monopole antenna [29].

In this section, the published water-based liquid antenna designs have been carefully covered. A summary is given in Table 2.1, which shows a high degree of flexibility and versatility that water-based liquid antennas can offer.

Table 2.1 Summary of water-based liquid antennas

Ref.	Antenna Figure	Antenna Structure	Size (mm^3)	Working Mechanism	Frequency Band (MHz)
[1]	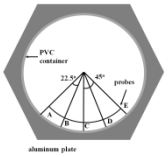	Cylindrical DRA	800 × 800 × 200	Frequency reconfigurable	58.6 - 60.8 (S_{11} < -10 dB)

[4]	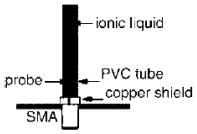	Conducting monopole	250 × 250 × 20.7	Single band	1440 - 1560 (S_{11} < -10 dB)
[5]	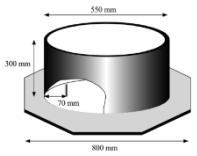	Cylindrical DRA	800 × 800 × 300	Frequency reconfigurable	50 - 96.8 (S_{11} < -10 dB)
[6]		Bracelet-type conducting loop	48 × 48 × 5	Single band	Resonant at 1700
[8]	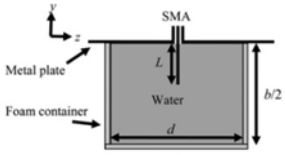	Cylindrical DRA	318 × 318 × 162.6	Single band	Resonant at 236
[11]		Conducting monopole	N/A	Frequency reconfigurable	2 - 400
[13]	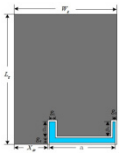	U-shaped DRA	40 × 90 × 9	Wideband	2400 - 3000 (S_{11} < -10 dB)
[15]	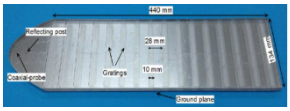	Leaky wave antenna	514 × 134 × 12.7	Beam reconfigurable	4020 - 6780 (S_{11} < -10 dB)
[17]	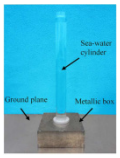	Conducting monopole	106 × 106 × 1050	Frequency reconfigurable	62.5 - 180.2 (S_{11} < -10 dB)
[18]	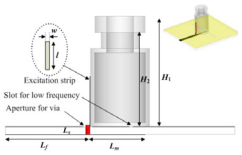	Cylindrical DRA	N/A	Multiband	Resonant at 1750 and 2200
[19]	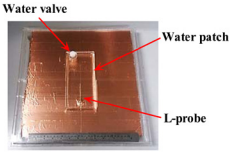	Water DDPA	350 × 350 × 40	Single band	880 - 960 (S_{11} < -10 dB)

[25]	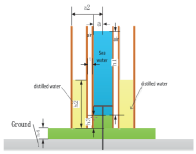	Hybrid antenna	320 × 320 × 1050	Wideband	52.5 - 162.5 (S_{11} < -10 dB)
[26]	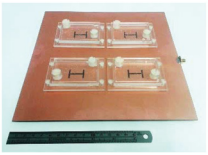	Water DDPA	N/A	Wideband	2230 - 2650 (S_{11} < -10 dB)
[27]	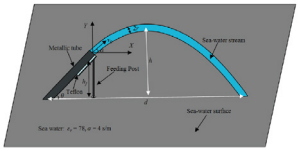	Water half-loop antenna	N/A	Wideband	96 - 130 (S_{11} < -10 dB)
[28]	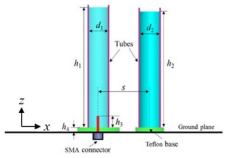	Yagi monopole	N/A	Wideband	1220 - 2080 (S_{11} < -10 dB)
[29]	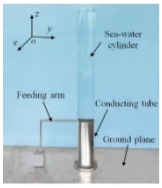	Conducting monopole	1285 (height)	Frequency reconfigurable	65.1 - 95.8 (S_{11} < -10 dB)

2.3 Overview of Antenna Measurement Techniques

Once the antenna is designed and constructed, it is essential to validate the design with proper measurements, which is a crucial element of the development process. In this section, we are going to explain antenna measurements used in this thesis and how they are performed.

The antenna performance can be evaluated according to many parameters, such as the reflection coefficient, bandwidth, radiation patterns, polarisation, directivity, gain, and efficiency. This section will present the measurement techniques in terms of reflection coefficient S_{11}, radiation patterns, gain and efficiency, which will be used in later chapters. This section is important, as the measurements later used will be based on the theories established in this part. The antenna measurements facilities will be based on the anechoic and reverberation chamber at the University of Liverpool, where all of the work in this thesis was completed.

2.3.1 S_{11} Measurements

The measurements of the reflection coefficient S_{11} are relatively straightforward. The antenna under test (AUT) is connected to one port of the vector network analyser (VNA), and record the data. The antenna impedance and return loss can be obtained from the measured S_{11}.

The standard measurement procedures are as follows [31]:

1. Select a suitable cable (low loss and phase stable) for the measurement and ensure that it is properly connected to the VNA. Sometimes to avoid cable effects, an RF choke is added.

2. Select the measurement frequency range and suitable number of measurement points over the frequency.

3. Perform the one-port calibration and ensure that the cable is not moved or errors could be generated.

4. Conduct the measurements in an environment with little reflection such as an open area or an anechoic chamber.

5. Record the measured results.

2.3.2 Radiation Pattern Measurements

The radiation pattern of an antenna is a plot of the radiated field or power as a function of the angle at a fixed distance which should be large enough to be considered as far field [31]. It is one of the most important parameters to characterise the antenna radiation. Compared with the S_{11} measurement, radiation pattern measurements are more difficult and time-consuming. There are a few methods to measure the antenna radiation patterns. They can be classified as indoor ranges (anechoic chamber) and outdoor ranges (open area test site). They can also be categorised as near-field and far-filed measurement methods. Which method is chosen primarily depends on antenna size and location [31].

In this thesis, an anechoic chamber is used to make the far field antenna pattern measurements. The chamber is a metallic room whose internal walls and ceiling are lined with material (made of carbon-loaded polyurethane foam) that absorbs electromagnetic energy in the frequency range of interest. It is intended to simulate an open area test site (OATS). A picture of an anechoic chamber at the University of Liverpool is shown in Fig. 2.23, which has dimensions of $6 \times 3.5 \times 3$ m^3. The source antenna is placed at one end of the chamber acting as a transmitting antenna (TX), and the AUT is put at the other end as a receiving antenna, a separation of 3 m is set to promise the far field criteria. The AUT is usually mounted on a positioner, rotating in the azimuth plane to obtain a two-dimensional (2D)

radiation pattern [31]. Some chambers may be equipped with positioners that are also capable of moving in the elevation plane, allowing measurement of the full three-dimensional (3D) radiation pattern. The source antenna may be rotated about its axis for polarisation measurements [31]. An automatic control system has been set up to record the data, which is given in Fig. 2.24. The turntable positioner, plotter, VNA are all under PC's control. Each time, the PC instructs the positioner to rotate, and triggers a sweep in the VNA, then records the data. This process is repeated until the measurement is finished [31]. Usually, the chamber is arranged to transmit from the source antenna and receive at the AUT. For a passive antenna system, the radiator is reciprocal which is the case for most practical antennas; the pattern information could be obtained by either the transmitter or receiver. This is in contrast to an active antenna system, in which transmitting and receiving behaviour may be considerably different, thus both relative patterns are required [32].

In general, the radiation pattern of an antenna is 3D. Sometimes, it is difficult to acquire the 3D pattern, thus in many papers, at least two orthogonal 2D patterns are necessary in order to obtain a good 3D pattern approximation. A 2D pattern is obtained by fixing one of the angles (θ or φ) while varying the other [32].

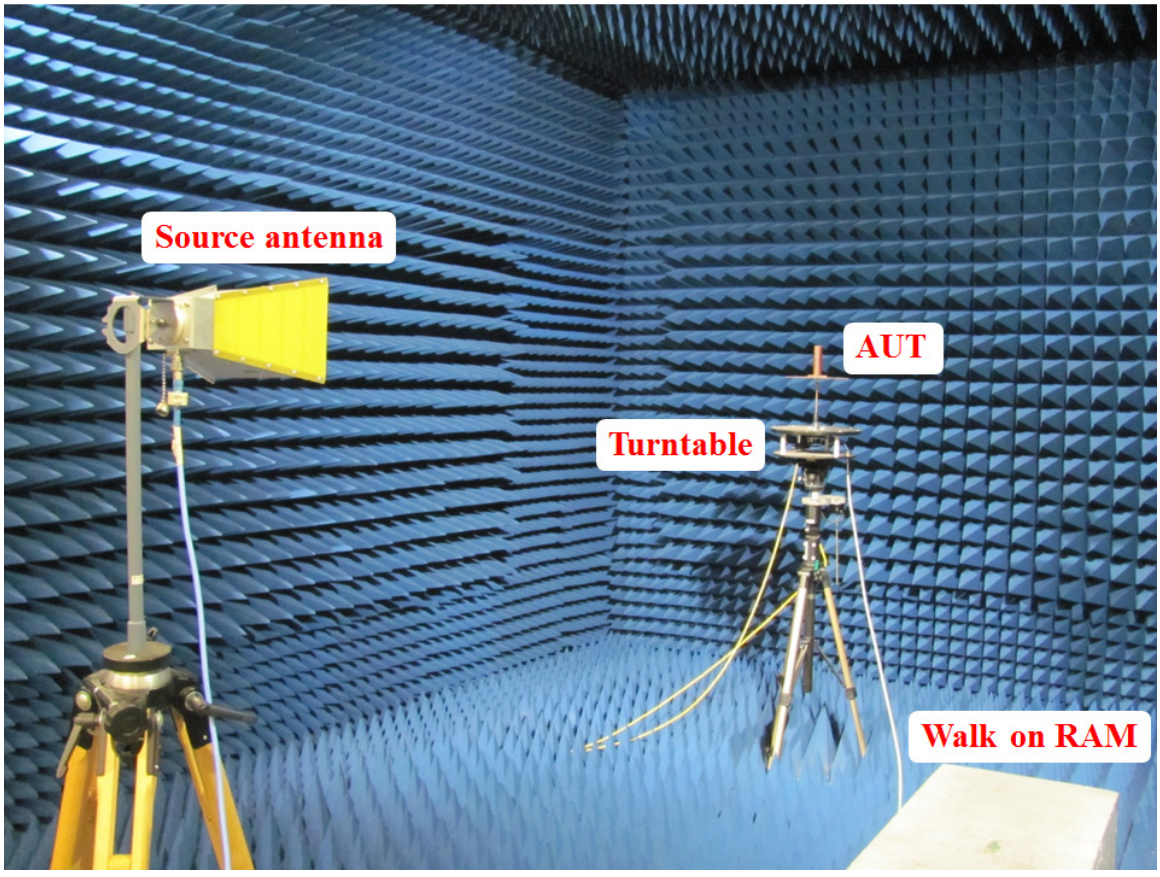

Fig. 2.23. The anechoic chamber at the University of Liverpool

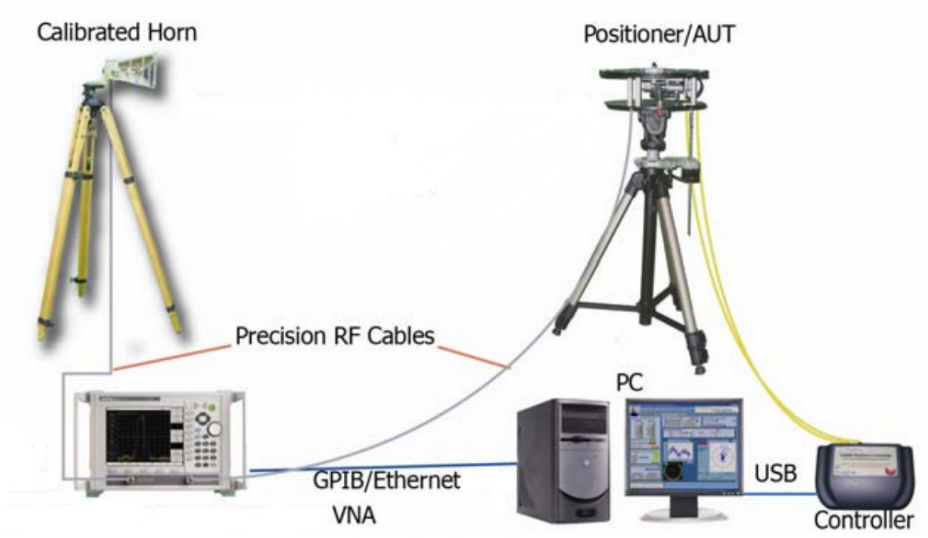

Fig. 2.24. Typical measurement layout [33].

2.3.3 Gain Measurements

The most important figure of merit that describes the performance of a radiator is the gain. It is a measure that considers both the antenna efficiency and its directional capabilities. It can be defined as the ratio of the radiation intensity in a given direction, to the radiation intensity that would be obtained if the power accepted by the antenna is radiated isotropically. The radiation intensity corresponding to the isotropically radiated power is equal to the power accepted (input) by the antenna divided by 4π [34]. In equation, it can be expressed as

$$G = 4\pi \frac{raidation\ internsity}{total\ input\ (accepted)\ power} = 4\pi \frac{U(\theta,\varphi)}{P_{in}} \tag{2.1}$$

where $U(\theta,\varphi)$ is the radiation intensity in W/unit, and P_{in} is the input power accepted by the antenna in W.

The gain is linked to the directivity and the antenna efficiency [31]:

$$G = \eta\, D \tag{2.2}$$

where η is the radiation efficiency of the antenna, and D is the directivity of the antenna.

In most cases, the realised gain is frequently used, which takes the impedance matching into account.

$$G_{realised} = \eta_{total} D \tag{2.3}$$

where D is again the directivity of the antenna, η_{total} is the total efficiency of the antenna.

There are two basic methods to measure the gain of an antenna: absolute-gain method and gain-transfer method, they are both based on Friis transmission equation. The measurement environment is essentially the same as the radiation pattern measurements. The absolute-gain method needs no a prior knowledge of the gains for the antennas. However, they require either two identical antennas or three different antennas by performing the measurements for three times, also, the knowledge of the pathloss between the source and test end of the chambers. The gain-transfer method requires an antenna whose gain is exactly known (also called reference antenna (REF)) and a TX whose gain does not need to be known. The advantage of this method is that it does not require the knowledge of the pathloss.

The method for the antenna gain measurement in the thesis is the gain- transfer method at an anechoic chamber. Two sets of measurements are performed:

1. The test antenna is in receiving mode, and its received power P_{AUT} is measured.

2. The antenna with known gain is in receiving mode in the exactly the same arrangement (the distance R and the transmitted power P_0 are kept the same), and its received power P_{REF} is measured.

According to Friis transmission equation in dB,

$$G_{AUT\ dB} + G_{TX\ dB} = 20\,log_{10}\left(\frac{4\pi R}{\lambda}\right) + 10\,log_{10}\left(\frac{P_{AUT}}{P_0}\right) \tag{2.4}$$

$$G_{REF\ dB} + G_{TX\ dB} = 20\,log_{10}(\frac{4\pi R}{\lambda}) + 10\,log_{10}\left(\frac{P_{REF}}{P_0}\right) \tag{2.5}$$

where $G_{AUT\ dB}$ is the gain of the AUT, $G_{REF\ dB}$ is the gain of the REF and $G_{TX\ dB}$ is the gain of the transmitting antenna.

$$G_{AUT\ dB} = G_{REF\ dB} + 10log_{10}\left(\frac{P_{AUT}}{P_{REF}}\right) \tag{2.6}$$

2.3.4 Efficiency Measurements

According to IEEE definition of antenna efficiency [35], the radiation efficiency is defined as the ratio of total radiated power to the power accepted by the antenna port; and the total efficiency is referred to the ratio of the power radiated to the power available at the antenna port. Mathematically, the total efficiency is a product of the radiation efficiency and mismatching efficiency of an antenna.

In the area of antenna efficiency measurements, there have been a variety of techniques proposed in the past few years. The reverberation chamber is one of the most popular approaches. A reverberation

chamber is basically a shielded room (metallic walls) with an arbitrarily-shaped metallic rotating paddle (stirrer or tuner). The paddle is designed to create a continuously changing boundary condition of the electromagnetic fields in the chamber. Rotating the paddle creates a statistical environment in a reverberation chamber which offers a unique test facility for a wide range of electromagnetic applications. Particularly, the reverberation chamber is ideally suited for performing radiated power measurements of an antenna or device under test, thus, it is possible to determine the efficiency of an antenna.

The antenna efficiency measurements based on the reverberation chamber technique can be categorised as measuring the unknown efficiency of an antenna with and without the use of a known efficiency reference antenna. In the following sections, these two approaches will be reviewed in details.

2.3.4.1 Efficiency Measurements with a Reference Antenna

The measurement setup is illustrated in Fig. 2.25. The stirrers in the reverberation chamber are driven by stepper motors, for each stirrer position, the S parameters are collected by a VNA and a computer. Port 1 of the VNA in our case is connected to TX with reflection coefficient S_{11TX}; port 2 is connected to the antenna on the receiving side (REF or AUT) with reflection coefficient S_{22REF} or S_{22AUT}. The radiation efficiency of the transmitting antenna and reference antenna is η_{TX} and η_{REF}, respectively.

The measurement procedures are summarised as follows:

1. Boot up the computer and turn on the stirrer motors.

2. Configure the PC and the VNA to talk together.

3. Calibrate the VNA (the reference plane is calibrated at the end of the cable).

4. Place all the antennas inside the reverberation chamber to ensure that the chamber Q factor does not change during the whole measurement, and no line-of-sight between each antenna.

5. Connect TX to Port 1 of the VNA and AUT to Port 2 of the VNA, REF is loaded with 50 Ohm termination. Record the complex S parameters (S_{21AUT}, S_{22AUT}) for each stirrer position.

6. Connect REF to Port 2 of the VNA, AUT is loaded with 50 Ohm termination. Collect the complex S parameters (S_{21REF}, S_{22REF}) for each stirrer position.

7. Change the TX polarisation and repeat the step 5 and 6.

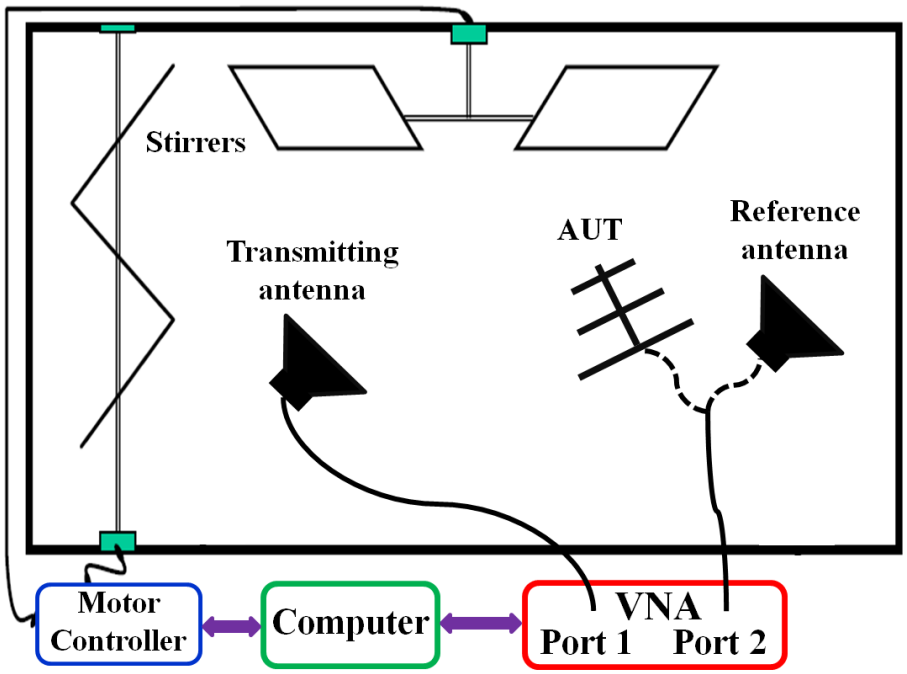

Fig. 2.25. Reverberation chamber setup for the efficiency measurement with a reference antenna.

The transfer function between the TX and AUT is:

$$T_{TA} = \frac{\langle |S_{21AUT}|^2 \rangle}{(1 - |\langle S_{11TX} \rangle|^2)(1 - |\langle S_{22AUT} \rangle|^2)\eta_{TX}\eta_{AUT}} \tag{2.7}$$

The transfer function between the TX and REF is:

$$T_{TR} = \frac{\langle |S_{21REF}|^2 \rangle}{(1 - |\langle S_{11TX} \rangle|^2)(1 - |\langle S_{22REF} \rangle|^2)\eta_{TX}\eta_{REF}} \tag{2.8}$$

where $\langle \cdot \rangle$ means the average value of the S parameters (complex average) using any stirring method (mechanical stir, frequency stir, source stir, etc). The average value of the complex S parameters ($\langle S_{11TX} \rangle$ or $\langle S_{22REF} \rangle$) is the unstirred part of the S parameters, which is equal to the S parameters measured in the anechoic chamber.

If the reverberation chamber is well-stirred and has a good field uniformity, $T_{TA} = T_{TR}$, thus we can get:

$$\eta_{AUT} = \frac{\langle |S_{21AUT}|^2 \rangle}{\langle |S_{21REF}|^2 \rangle} \times \frac{(1 - |\langle S_{22REF} \rangle|^2)}{(1 - |\langle S_{22AUT} \rangle|^2)} \times \eta_{REF} \tag{2.9}$$

To avoid confusion, η means the radiation efficiency, while the total efficiency includes the mismatch and is denoted as:

$$\eta_{totalAUT} = (1 - |\langle S_{22AUT}\rangle|^2) \times \eta_{AUT} \quad (2.10)$$

Please note that we have $\langle S_{22}\rangle$ in both (2.9) and (2.10), it can be measured in an anechoic chamber or in a reverberation chamber since $S_{22freesapce} = \langle S_{22}\rangle$ [36].

The equation (2.9) indicates that the efficiency of the AUT can be obtained by the S parameters and the radiation efficiency of the reference antenna.

2.3.4.2 Efficiency Measurements without a Reference Antenna

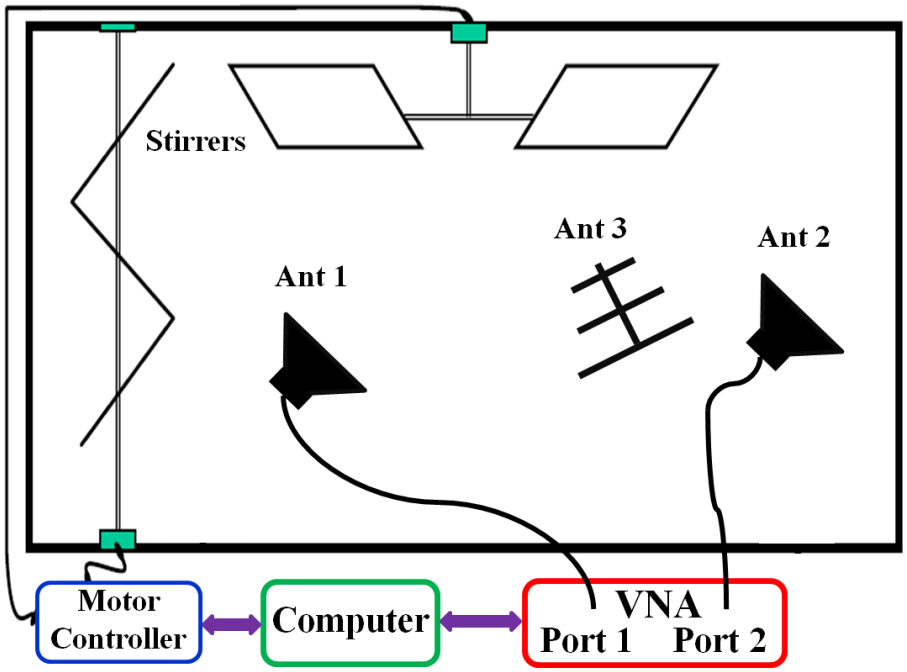

Fig. 2.26. Efficiency measurement without a reference antenna.

In this section, the techniques for determining the efficiency (the radiation and total efficiency) of an unknown antenna without using a reference antenna (i.e. an antenna with a known efficiency) are reviewed. The methods are based on the idea proposed by Holloway *et al* in [37]. The physical insights of these methods are based on the differences of the chamber quality factor (Q) in the time domain and frequency domain, which is directly related to the efficiency of the antennas used in the measurements. The measurement setup is shown in Fig. 2.26, it is seen that, no reference antenna is needed.

The chamber quality factor Q is a parameter often used to characterise a reverberation chamber and it is defined as:

$$Q = \frac{\omega U}{P_d} \tag{2.11}$$

where U is the energy stored in the chamber, P_d is the power dissipated in the chamber, and $\omega = 2\pi f$ (where f is the frequency). It can be obtained from both the time-domain and frequency-domain data.

In the frequency domain, for a chamber with ideal antennas (well-matched, 100% total efficiency) and no line of sight, the Q can be expressed as [37]:

$$Q_{FD} = C_{RC}\langle|S_{21}|^2\rangle \tag{2.12}$$

where the parameter C_{RC} is a chamber constant defined as [37]:

$$C_{RC} = \frac{16\pi^2 V}{\lambda^3} \tag{2.13}$$

where V is the volume of the chamber, and λ is the free-space wavelength.

It should be noted that (2.12) is only accurate, when both antennas are ideal antennas (well-matched, no line-of-sight, 100% total efficiency) [37, 38]. If we consider the antenna efficiency, and the line-of-sight component, the corrected Q_{FD}becomes [37, 38]:

$$Q_{FDCor} = \frac{C_{RC}\langle|S_{21,s}|^2\rangle}{\eta_{1tot}\eta_{2tot}} \tag{2.14}$$

where $S_{21,s}$ is the stirred part of the S-parameter [37], $S_{21,s} = S_{21} - \langle S_{21}\rangle$.

In the time domain, the Q is determined by [37, 38]:

$$Q_{TD} = \omega\tau_{RC} \tag{2.15}$$

where τ_{RC} is the chamber decay time and ω is the angular frequency.

As stated in [37], in the time domain, the power in the chamber decays exponentially and follows $P_0 e^{-t/\tau}$, where τ is the decay time constant. There are two ways to obtain the τ value [38]: 1) measure in the time domain directly; 2) measure the S parameters in the frequency domain and then apply the inverse fast Fourier transform (IFFT) to the S-parameters. The least-square fit is then applied to $ln(IFFT(S_{21})^2)$ or $ln(IFFT(S_{11})^2)$ to extract the slope k, and $\tau = -1/k$ can be obtained [38]. To reduce the measurement error, τ can be measured with different stirrer positions (source positions) and then averaging, thus τ can be replaced as $\langle\tau\rangle$. It should be noted that it is not necessary to measure it directly in the time domain since the time domain response can be obtained from the inverse Fourier transform from the frequency domain response [38].

If the chamber is well-stirred (the field in the chamber is statistically uniform), the two Q factors (2.14) and (2.15) are equal [37], $Q_{FDCor} = Q_{TD}$, thus we have:

$$\eta_{1tot}\eta_{2tot} = \frac{C_{RC}\langle|S_{21,s}|^2\rangle}{\omega\tau_{RC}} \tag{2.16}$$

Apply equation (2.15) to antenna 1, we have:

$$\frac{C_{RC}\langle|S_{11,s}|^2\rangle/e_b}{\eta_{1tot}\eta_{1tot}} = \omega\tau_{RC} \tag{2.17}$$

Apply equation (2.15) to antenna 2, we have:

$$\frac{C_{RC}\langle|S_{22,s}|^2\rangle/e_b}{\eta_{2tot}\eta_{2tot}} = \omega\tau_{RC} \tag{2.18}$$

The expressions in (2.16), (2.17) and (2.18) represent three equations and three unknowns (η_{1tot}, η_{2tot} and e_b), which can be solved to give the total efficiency for the two unknown antennas as [37]:

$$e_b = \frac{\sqrt{\langle|S_{11,s}|^2\rangle\langle|S_{22,s}|^2\rangle}}{\langle|S_{21,s}|^2\rangle} \tag{2.19}$$

$$\eta_{1tot} = \sqrt{\frac{C_{RC}}{\omega e_b\tau_{RC}}\langle|S_{11,s}|^2\rangle} \tag{2.20}$$

$$\eta_{2tot} = \sqrt{\frac{C_{RC}}{\omega e_b\tau_{RC}}\langle|S_{22,s}|^2\rangle} \tag{2.21}$$

where e_b refers to an enhanced backscatter constant.

If only one antenna is used (the one-antenna method in [37]), which means the TX and RX are the same, $\langle|S_{11,s}|^2\rangle = \langle|S_{22,s}|^2\rangle$, $e_b = 2$ [37].

$$\eta_{itot} = \sqrt{\frac{C_{RC}}{2\omega\tau_{RC}}\langle|S_{ii,s}|^2\rangle} \quad (i = 1\ or\ 2) \tag{2.22}$$

$$\eta_i = \frac{1}{(1-|\langle S_{ii}\rangle|^2)}\sqrt{\frac{C_{RC}}{2\omega\tau_{RC}}\langle|S_{ii,s}|^2\rangle} \quad (i = 1\ or\ 2) \tag{2.23}$$

If two antennas are used (the two-antenna method in [37]), it does not require $e_b = 2$, it does require e_b to be identical for two antennas placed in different positions within the chamber, the efficiency of these two antennas are:

$$\eta_{itot} = \sqrt{\frac{C_{RC}}{\omega e_b \tau_{RC}} \langle |S_{ii,s}|^2 \rangle} \quad (i = 1 \; or \; 2) \tag{2.24}$$

$$\eta_i = \frac{1}{(1 - |\langle S_{ii} \rangle|^2)} \sqrt{\frac{C_{RC}}{\omega e_b \tau_{RC}} \langle |S_{ii,s}|^2 \rangle} \quad (i = 1 \; or \; 2) \tag{2.25}$$

If three antennas are used (the three-antenna method in [37]), there is no requirement for e_b, the efficiency of these three antennas are:

$$\eta_{1tot} = \sqrt{\frac{C_{RC}}{\omega \tau_{RC}} \frac{\langle |S_{21,s}|^2 \rangle \langle |S_{31,s}|^2 \rangle}{\langle |S_{32,s}|^2 \rangle}} \tag{2.26}$$

$$\eta_{2tot} = \sqrt{\frac{C_{RC}}{\omega \tau_{RC}} \frac{\langle |S_{21,s}|^2 \rangle \langle |S_{32,s}|^2 \rangle}{\langle |S_{31,s}|^2 \rangle}} \tag{2.27}$$

$$\eta_{3tot} = \sqrt{\frac{C_{RC}}{\omega \tau_{RC}} \frac{\langle |S_{31,s}|^2 \rangle \langle |S_{32,s}|^2 \rangle}{\langle |S_{21,s}|^2 \rangle}} \tag{2.28}$$

$$\eta_1 = \frac{1}{(1 - |\langle S_{11} \rangle|^2)} \sqrt{\frac{C_{RC}}{\omega \tau_{RC}} \frac{\langle |S_{21,s}|^2 \rangle \langle |S_{31,s}|^2 \rangle}{\langle |S_{32,s}|^2 \rangle}} \tag{2.29}$$

$$\eta_2 = \frac{1}{(1 - |\langle S_{22} \rangle|^2)} \sqrt{\frac{C_{RC}}{\omega \tau_{RC}} \frac{\langle |S_{21,s}|^2 \rangle \langle |S_{32,s}|^2 \rangle}{\langle |S_{31,s}|^2 \rangle}} \tag{2.30}$$

$$\eta_3 = \frac{1}{(1 - |\langle S_{33} \rangle|^2)} \sqrt{\frac{C_{RC}}{\omega \tau_{RC}} \frac{\langle |S_{31,s}|^2 \rangle \langle |S_{32,s}|^2 \rangle}{\langle |S_{21,s}|^2 \rangle}} \tag{2.31}$$

2.3.4.3 Efficiency Measurements by using a Modified Two-Antenna Method

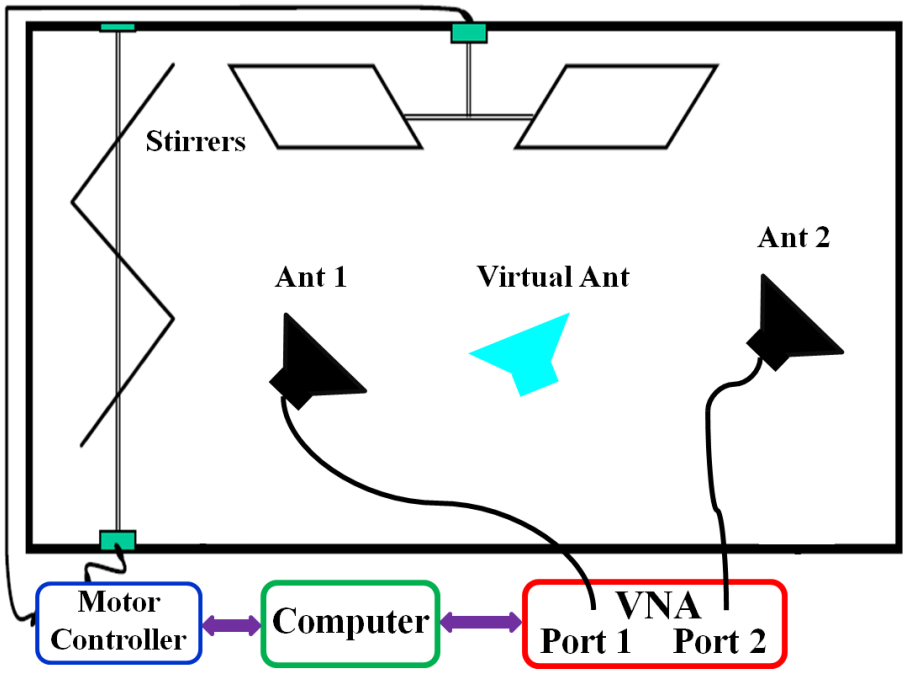

Fig. 2.27. Efficiency measurement set up by using modified two antenna method.

The two-antenna method works well for high efficiency antennas. However, when the AUT is very lossy (radiation efficiency is very small), the method can be problematic. Since $S_{11,s} = S_{11} - \langle S_{11} \rangle$, the attenuation of the antenna is very large, the contribution from the reverberation chamber is very small, S_{11} will be very close to $\langle S_{11} \rangle$, this will make $S_{11,s}$ very small or even below the noise level after calibration [39]. To solve this issue, a modified two-antenna method to measure the radiation efficiency of antennas in reverberation chamber is proposed [39]. By combing the conventional reference antenna method and the one-antenna method as well as introducing a virtual antenna, the efficiency of a highly lossy antenna can be obtained. This method is used to measure the efficiency of water loaded reconfigurable antennas in Chapter 6.

The measurement setup is illustrated in Fig. 2.27 [39]. Two antennas are placed in the chamber and at least one antenna should have high efficiency (τ_{RC} can be extracted from this antenna). In [39], antenna 2 is supposed to have high efficiency and antenna 1 is the AUT. A virtual antenna which is exactly the same as antenna 2 is introduced to understand the enhanced backscatter effect [39].

When the chamber is well-stirred (with a large number of modes and a large mode-density), the stirred S parameters between antenna 2 and virtual antenna has a relationship as follows [37]:

$$e_b = \frac{\sqrt{\langle |S_{22,s}|^2 \rangle \langle |S_{vv,s}|^2 \rangle}}{\langle |S_{2v,s}|^2 \rangle} = 2 \tag{2.32}$$

As the virtual antenna is exactly the same as antenna 2, $\langle |S_{22,s}|^2 \rangle = \langle |S_{vv,s}|^2 \rangle$, we have [39]:

$$\langle |S_{22,s}|^2 \rangle = 2 \langle |S_{2v,s}|^2 \rangle \tag{2.33}$$

The transfer function between antenna 2 and virtual antenna can be expressed as [39]:

$$T_{2v} = \langle |S_{2v,s}|^2 \rangle / [(1 - |\langle S_{22} \rangle|^2)(1 - |\langle S_{vv} \rangle|^2)\eta_2 \eta_v] \tag{2.34}$$

$$T_{2v} = \langle |S_{22,s}|^2 \rangle / 2[(1 - |\langle S_{22} \rangle|^2)^2 {\eta_2}^2] \tag{2.35}$$

The transfer function between antenna 2 and AUT can be expressed as [39]:

$$T_{21} = \langle |S_{21,s}|^2 \rangle / [(1 - |\langle S_{22} \rangle|^2)(1 - |\langle S_{11} \rangle|^2)\eta_2 \eta_1] \tag{2.36}$$

If the RC is well-stirred and has a good field uniformity, $T_{21} = T_{2v}$, thus we have [39]:

$$\eta_1 = 2 \langle |S_{21,s}|^2 \rangle (1 - |\langle S_{22} \rangle|^2)\eta_2 / \left[(1 - |\langle S_{11} \rangle|^2) \langle |S_{22,s}|^2 \rangle\right] \tag{2.37}$$

η_2 can be obtained according to equation (2.23)

$$\eta_2 = \frac{1}{(1 - |\langle S_{22} \rangle|^2)} \sqrt{\frac{C_{RC}}{\omega e_b \tau_{RC}} \langle |S_{22,s}|^2 \rangle} \tag{2.38}$$

Substitute (2.38) into (2.37), η_1 is achieved [39]:

$$\eta_1 = \frac{\langle |S_{21,s}|^2 \rangle}{(1 - |\langle S_{11} \rangle|^2)} \sqrt{\frac{2C_{RC}}{\omega \tau_{RC} \langle |S_{22,s}|^2 \rangle}} \tag{2.39}$$

$$\eta_{1tot} = \langle |S_{21,s}|^2 \rangle \sqrt{\frac{2C_{RC}}{\omega \tau_{RC} \langle |S_{22,s}|^2 \rangle}} \tag{2.40}$$

τ_{RC} can be extracted from the time domain response of antenna 2. As antenna 1 is very loss, it is very hard to extract τ_{RC} from the time domain response from the reverberation chamber may be smaller than the noise level by using antenna 1.

It is important to mention that there are two prerequisites for this modified two antenna method: 1) the reverberation chamber must be well-stirred that is $e_b = 2$; 2) at least one antenna should be highly efficient antenna to make sure $S_{*,s}$ ($*$ = 11 or 22) is in the dynamic range of the VNA to extract τ_{RC} [39].

This proposed method can also be generalised to nonreciprocal antennas such as active antennas. If the transmitting efficiency and receiving efficiency of the AUT are different (nonreciprocal), the total TX efficiency and total RX efficiency will be:

$$\eta_{1totTx} = \langle |S_{21,s}|^2 \rangle \sqrt{\frac{2C_{RC}}{\omega\tau_{RC}\langle |S_{22,s}|^2 \rangle}} \tag{2.41}$$

$$\eta_{1totRx} = \langle |S_{12,s}|^2 \rangle \sqrt{\frac{2C_{RC}}{\omega\tau_{RC}\langle |S_{22,s}|^2 \rangle}} \tag{2.42}$$

2.4 Summary

In this chapter, an overview of the state of the art of water-based liquid antenna has been presented. Water-based liquid antennas can be designed to suit a wide range of physical or electrical requirements of varied communication applications, from high frequency (HF) to UHF band. This will make the water-based liquid antennas excellent alternatives to traditional antennas.

The antenna measurement techniques used in the thesis have been clearly explained. The derivation process, the measurement settings as well as the physics behind the phenomenon have been reviewed, which set a solid foundation for the antenna performance validation in experiments.

2.5 References

[1] S. P. Kingsley, S. G. O'Keefe, "Beam steering and monopulse processing of probe-fed dielectric resonator antennas," Proc. IEE Radar, Sonar and Navigation, vol. 146, no. 3, pp. 121-125, 1999.

[2] E. Paraschakis, H. Fayad, and P. Record, "Ionic liquid antenna," in Proc. IEEE Int. Workshop Antenna Tech.: Small Antennas and Novel Metamaterials, 2005, pp. 552-554.

[3] H. Fayad, and P. Record, "Wideband saline-water antenna," in Proc. IEE Conf. on Wideband and Multi-band Antennas and Arrays, 2005, pp. 198-201.

[4] H. Fayad, P. Record, "Broadband liquid antenna," Electron. Lett., vol. 42, no. 3, pp. 133-134, 2006.

[5] S. G. O'Keefe, S. P. Kingsley, "Tunability of liquid dielectric resonator antennas," IEEE Antennas Wireless Propag. Lett., vol. 6, pp. 533-536, 2007.

[6] A. Traille, L. Yang, A. Rida and M. M. Tentzeris, "A novel liquid antenna for wearable bio-monitoring applications," IEEE MTT-S Int. Microw. Symp. Dig., pp. 923-926, 2008.

[7] R. Zhou, H. Zhang, and H. Xin, "A compact water based dielectric resonator antenna," in Proc. IEEE AP-S Int. Symp., 2009, pp. 1-4.

[8] R. Zhou, H. Zhang, and H. Xin, "Liquid-based dielectric resonator antenna and its application for measuring liquid real permittivities," IET Microw., Antennas Propag., vol. 8, no. 4, pp. 255-262, 2014.

[9] D. W. S. Tam, "Electrolytic fluid antenna," U. S. Patent No.: US7898484B1, 2011.

[10] D. W. S. Tam, "Electrolytic fluid antenna with signal enhancer," U. S. Patent No.: US8368605B1, 2013.

[11] http://www.public.navy.mil/spawar/Pacific/TechTransfer/ProductsServices/Documents/TIPSheets/Sea_Water_Antenna_System_98582_et_al_TIP_REV4_6_11.pdf

[12] L. Xing, Y. Huang, S. Alja'afreh, and S. J. Boyes, "A monopole water antenna," in Proc. Loughborough Antennas Propag. Conf., 2012, pp. 1-4.

[13] S. Alja'afreh, Y. Huang, and L. Xing, "A compact dual-feed water-based diversity antenna," in Proc. Loughborough Antennas Propag. Conf., 2013, pp. 182-185.

[14] L. Xing, Y. Huang, Y. Shen, S. Alja'afreh, Q. Xu, R. Alrawashdeh, "Further investigation on water antennas," IET Microw., Antennas Propag., vol. 9, no. 8, pp. 735-741, 2015.

[15] Z. Hu, Z. Shen, W, Wu, "Reconfigurable leaky-wave antenna based on periodic water grating," IEEE Antennas Wireless Propag. Lett., vol. 13, pp. 134-137, 2014.

[16] L. Xing, Y. Huang, S. Alja'afreh, Q. Xu, M. Kod, C. Y. Song, "Reconfigurable 3D folded monopole antenna design for DVB-H applications," in Proc. Loughborough Antennas Propag. Conf., 2014, pp. 530-532.

[17] C. Hua, Z. Shen, and J. Lu, "High-efficiency sea-water monopole antenna for maritime wireless communications," IEEE Trans. Antennas Propag., vol. 62, no. 12, pp. 5968-5973, 2014.

[18] Y. Chen, C. Wang, "Dual-band directional/omni-directional liquid dielectric resonator antenna designs using characteristic modes," in Proc. IEEE AP-S Int. Symp., 2014, pp. 848-849.

[19] Y. Li, K. M. Luk, "A water dense dielectric patch antenna," IEEE Access, vol.3, pp. 274-280, 2015.

[20] H. W. Lai, K. M. Luk, and K.W. Leung, "Dense dielectric patch antenna-A new kind of low-profile antenna element for wireless communications," IEEE Trans. Antennas Propag., vol. 61, no. 8, pp. 4239-4245, 2013.

[21] L. Xing, Y. Huang, Q. Xu, S. Aljaafreh, "Wideband, hybrid rectangular water antenna for DVB-H applications," Microw. Opt. Technol. Lett., vol. 59, no. 9, pp. 2160-2164, 2015.

[22] L. Xing, Y. Huang, Q. Xu, S. Aljaafreh, T. Liu, "A broadband hybrid water antenna for hand-portable applications," IEEE Antennas Wireless Propag. Lett. [Online]. Available: http://ieeexplore.ieee.org/stamp/stamp.jsp?tp=&arnumber=7112462.

[23] L. Xing, Y. Huang, Q. Xu, S. Alja'afreh, "A wideband hybrid water antenna with an F-shaped monopole," IEEE Access, vol. 3, pp. 1179-1187, 2015.

[24] L. Xing, Y. Huang, Q. Xu, S. Aljaafreh, "Overview of water antenna designs for wireless communications," in Proc. IEEE Asia-Pacific Conf. on Antennas and Propag., 2015, pp. 242-243.

[25] Y. Qian, Q. Chu, "Broadband hybrid water antennas," in Proc. IEEE Asia-Pacific Conf. on Antennas and Propag., 2015, pp. 244-245.

[26] J. Sun, K. M. Luk, "Design of a 2 × 2 water dielectric patch antenna array for Wi-Fi application," in Proc. IEEE Asia-Pacific Conf. on Antennas and Propag., 2015, pp. 246-247.

[27] C. Hua, Z. Shen, "Sea-water half-loop antenna for maritime wireless communications," in Proc. IEEE Asia-Pacific Conf. on Antennas and Propag., 2015, pp. 240-241.

[28] Z. Hu, W. Wu, Z. Shen and C. Hua, "A Yagi monopole antenna made of pure water," in Proc. IEEE AP-S Int. Symp., 2015, pp. 2241-2242.

[29] C. Hua, Z. Shen, "Shun-excited sea-water monopole antenna of high efficiency," IEEE Trans. Antennas Propag. [Online]. Available: http://ieeexplore.ieee.org/stamp/stamp.jsp?tp=&arnumber=7247644

[30] L. Xing, Y. Huang, Q. Xu, S. Alja'afreh, "A compact water loaded reconfigurable antenna for DVB-H applications," Electron. Lett. to be published.

[31] Y. Huang and K. Boyle, *Antennas from theory and practice*, John Wiley & Sons Ltd, 2005.

[32] M. D. Foegelle, "Antenna pattern measurement: concepts and techniques," in Compliance Engineering Annual Reference Guide 2002, Los Angeles, CA: Compliance Engineering Magazine, 2002, pp. 1-12.

[33] http://www.diamondeng.net/PDF/brochurelr.pdf

[34] C. A. Balanis, *Antenna theory analysis and design*, John Wiley & Sons, Inc., 2005.

[35] "IEEE Standard Definitions of Terms for Antennas," IEEE Std 145-1993, pp. 1-32, 2013.

[36] P. S. Kildal, C. Carlsson and J. Yang, "Measurement of free-space impedances of small antennas in reverberation chambers," Microw. Opt. Technol. Lett., vol. 32, pp. 112-115, 2002

[37] C. L. Holloway, H. A. Shah, R. J. Pirkl, W. F. Young, D. A. Hill, and J. Ladbury, "Reverberation chamber techniques for determining the radiation and total Efficiency of antennas," IEEE Trans. Antennas Propag., vol. 60, pp. 1758-1770, 2012.

[38] Q. Xu, Y. Huang, L. Xing, Z. Tian, Z. Fei and L. Zheng, "A fast method to measure the volume of a large cavity," IEEE Access, vol. 3, pp. 1555-1561, 2015

[39] Q. Xu, Y. Huang, X. Zhu, L. Xing, Z. Tian and C. Y. Song, "A modified two-antenna method to measure the radiation efficiency of antennas in a reverberation chamber," IEEE Antennas Wireless Propag. Lett. [Online]. Available: http://ieeexplore.ieee.org/stamp/stamp.jsp?tp=&arnumber=7122231.

Chapter 3: Complex Permittivity of Water-Based Liquids

3.1 Introduction

For water-based liquid antenna designs, a precise knowledge of the complex permittivity of the liquid is essential. The complex permittivity of the given material is a function of frequency *f*, temperature *T* and substance concentration *S*. Many models have been developed to estimate the complex permittivity $\varepsilon(f, T, S)$. In [1], a simple Debye expression for the seawater complex permittivity was used and polynomial fits were derived. In [2], the complex permittivity of pure water, tap water and water with 20% salty solution at 2.45 GHz were studied. The empirical formulae and analysis with the increase in temperature by microwave heating were also given. In [3], a double Debye model was introduced as a modified form of the traditional Debye model to improve the complex permittivity prediction of the freshwater at frequencies beyond 100 GHz. In 1998, Ellison *et al* developed new equations of complex permittivity of seawater based on their own measurement results [4]. It was found that organic contents of natural seawater had little effect on the permittivity measurement results. In [5], Meissner and Wentz proposed updated fits for both pure water and seawater. A validation using an extensive analysis of brightness temperatures from a special sensor microwave imager (SSM/I) was provided. The permittivity data of pure water and sea water are available, but the permittivity data linked to PG, is still very limited. If we would like to use such a liquid for electromagnetic applications (including antenna design), more information is required. Besides, the permittivity data of water-based liquids at various temperatures and concentrations will be a valuable guide for using water in a wide frequency range from 0 to 18 GHz or even higher bands such as millimetre wave frequencies.

In this chapter, three water-based liquids, namely pure water, water with PG and salty water are measured. The experimental data are processed to obtain accurate mathematical expressions for the complex permittivity of these liquids over a temperature range 0 ~ 70^{o}C (pure water and salty water) and -10^{o}C ~ 70^{o}C (water with PG), frequency range 0 ~18 GHz, PG concentration 0 ~ 70% and salinity 0 ~ 50 parts per thoudand (ppt). It is worth mentioning that, salt will be saturated at certain salinity for salty water. The saturation point of salty water is around 35 to 50 ppt, which is a function of temperature.

The main focus of this chapter will be on two aspects: 1) To gain more knowledge about water with PG; 2) To derive simple and accurate expression of the permittivity for pure water and salty water over a wide frequency, temperature and salinity range.

The organisation of this chapter is as follows:

Section 3.2 introduces the water-based liquid measurement software package and the dielectric properties measurement settings. Section 3.3 details the numerical analysis and derivation methodology used in this study. Section 3.4 compares the derived new fits with our measurement results and other models reported in the published papers. A summary is presented in section 3.5 to review all findings.

3.2 Complex Permittivity Measurements

Every material has a unique set of electrical characteristics depending on its dielectric properties. Accurate measurements of these dielectric properties can provide researchers with valuable information to properly incorporate the material into its intended application. Much work has been devoted to exploring the measurement techniques of dielectric properties [6]. The measurement methods relevant for any desired application depend on the nature of the dielectric material to be measured (both physically and electrically), the frequency of interest, and the degree of accuracy required. Thus, choosing a proper measurement method to obtain the dielectric properties of material both accurately and efficiently is challenging.

In this section, the complex permittivity of water-based liquids is measured by using Keysight (former Agilent) Dielectric Probe 85070E (performance probe), as shown in Fig. 3.1. The probe withstands a wide temperature range from -40^{o}C to +200^{o}C and covers a wide frequency range from 500 MHz to 50 GHz [8]. Before measuring the liquids, calibration at the tip of the probe should be performed. The three known standards: air, short circuit and distilled water are used to remove the systematic errors from the measurement. During the measurements, air bubbles on the tip of the probe should be avoided, as they can be a significant source of error.

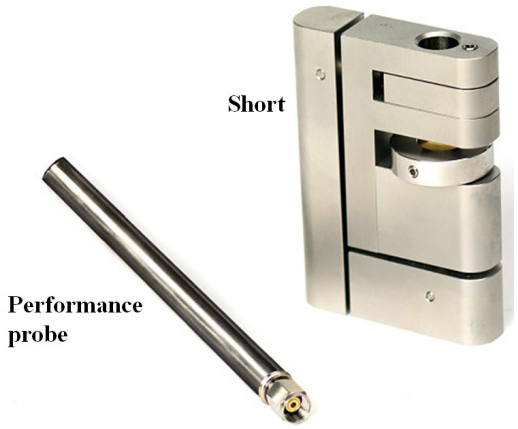

Fig. 3.1. Keysight 85070E dielectric probe kit [7].

The thermal characteristics of the liquids are investigated together with the frequency response. Real-time liquid complex permittivity measurement software is developed in house, as shown in Fig. 3.2. This software can automatically record the complex permittivity of liquids under different temperatures. A calibration should be performed before the measurement. For each measurement, the real-time complex permittivity response (real and imaginary part of the permittivity) is recorded by our software. A switch is used to triger the digital thermal probe. Every 60 seconds, a measurement is triggered, and a data file is saved after the measurement. This software significantly improves the complex permittivity measurement efficiency.

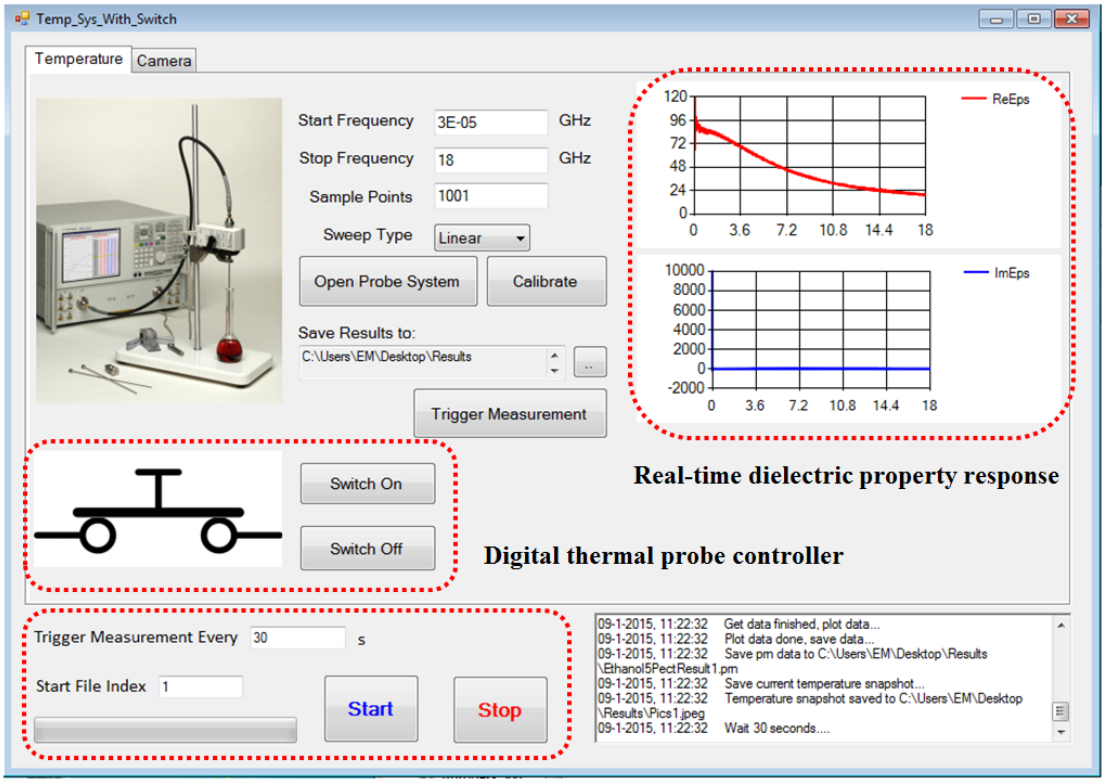

Fig. 3.2. Liquid complex permittivity measurement software.

Two scenarios are considered for the liquid permittivity measurements, these are high temperature and low temperature tests.

The setup of the high temperature permittivity measurement is presented in Fig. 3.3(a). The sample under test is placed in a water environment. The hot plate is used to tune the temperature of the water environment, thus the temperature of the sample will be slowly increased.

For low temperature permittivity measurement, the setup is similar as shown in Fig. 3.3(b) and (c), however, the hot plate is replaced by a foam chamber. The foam chamber can make the temperature

inside the foam chamber change very slowly. Instead of using a water environment, an ethanol environment is created, which can keep the sample in a very low temperature (< 0°C).

16 different substance concentrations, 321data files in total were prepared. Some liquid samples are displayed in Fig. 3.3(d). For each sample, the temperature is changed from 0 to 70°C (for pure water and salty water) and -10°C to 70°C (for water with PG). For a specific temperature and substance concentration, 1001 frequency points from 30 kHz to 18 GHz were recorded for the complex permittivity calculation.

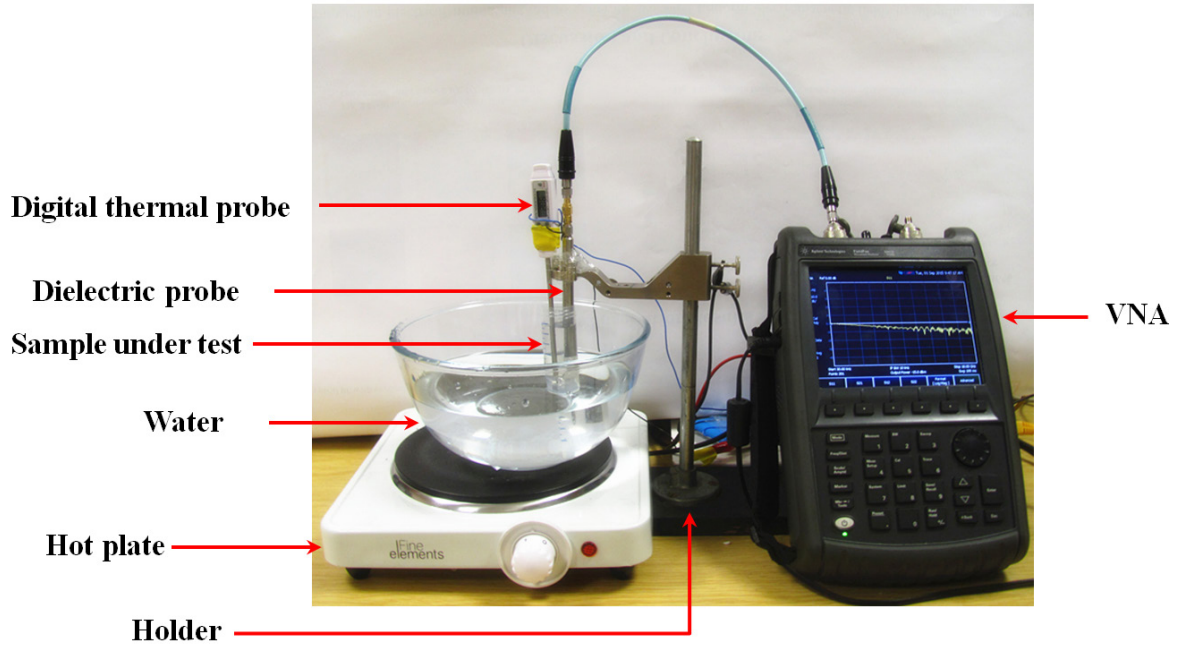

(a)

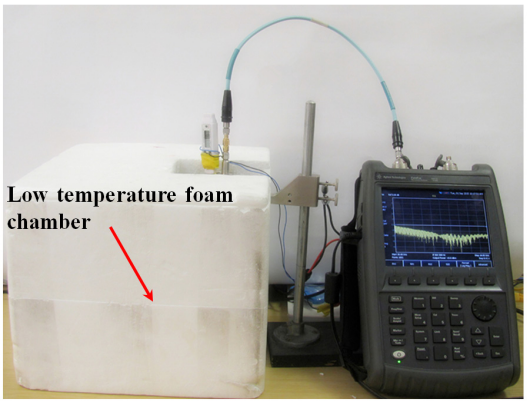

(b)

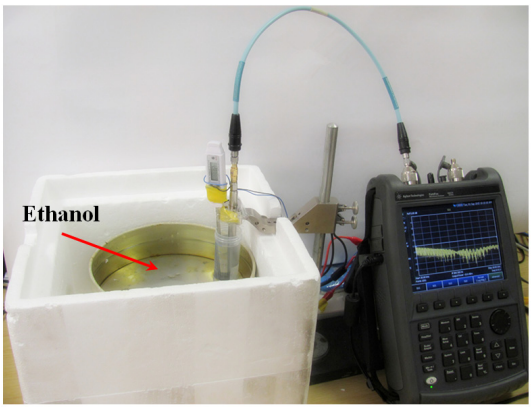

(c)

(d)

Fig. 3.3. (a) High temperature water-based liquids measurement setup. (b) Low temperature water-based liquids measurement setup. (c) Open view of low temperature water-based liquids measurement setup. (d) Liquid samples.

3.3 Numerical Analysis of Complex Permittivity Model

In the existing frequency and temperature range, both the first and second order Debye models were tried to describe the complex permittivity and it was found that the differences of these two models are small. For simplicity, the first order Debye model is used and the complex permittivity can be expressed as:

$$\varepsilon = \varepsilon_\infty + \frac{\varepsilon_s - \varepsilon_\infty}{1 + j2\pi f\tau} \tag{3.1}$$

where ε_s and ε_∞ are the static and high frequency dielectric constants, respectively [4]. τ is the relaxation time constant in seconds [4], and f is the frequency.

In order to take the temperature and material concentration into account, a general polynomial equation is proposed and shown in (3.2). The parameters/coefficients ε_∞, α_0 and β_0 are dependent on temperature T and substance concentration S. Thus, the complex permittivity is a function of frequency f, temperature T and substance concentration S.

$$\varepsilon(f,\ T,\ S) = \varepsilon_\infty(T,S) + \frac{\beta_0(T,S)}{\alpha_0(T,S) + j2\pi f} \tag{3.2}$$

where the temperature T is in degree Celsius (°C). The substance concentration S has different definitions for water with PG and salty water. For water with PG, S stands for the volume of PG over the volume of pure water, ranging from 0 to 70%. For salty water, S is the salinity of salt in water with unit parts per thousand (ppt), varying from 0 to 50 ppt.

To obtain the permittivity in (3.2), a flowchart is shown in Fig. 3.4 to illustrate the process. An objective function G is defined as the square of the difference between the experimental data and curve fitting function as given in (3.3). By minimizing G, a set of optimised values for ε_∞, α_0, β_0 are obtained. Each parameter can be expressed as polynomial functions of T and S using regression analysis. Substituting the polynomial functions of ε_∞,α_0, β_0 into (3.2), a new curve-fitting equation of $\varepsilon(f, T, S)$ is successfully produced. To evaluate the accuracy of the proposed $\varepsilon(f, T, S)$ equation, the averaged error rate (AER) is defined in (3.4): the smaller the AER, the better the accuracy.

$$G = \sum_i [Re(\varepsilon_i^{meas} - \varepsilon_i^{fit})]^2 + [Im(\varepsilon_i^{meas} - \varepsilon_i^{fit})]^2 \tag{3.3}$$

$$Average\ Error\ Rate = mean\left(\frac{\left|\varepsilon_i^{meas} - \varepsilon_i^{fit}\right|}{\left|\varepsilon_i^{meas}\right|} \times 100\%\right) \tag{3.4}$$

where i is the number of measured complex permittivity. *Re* and *Im* are the real and imaginary parts of the complex permittivity, respectively. *Mean* is the averaged value across the frequency band.

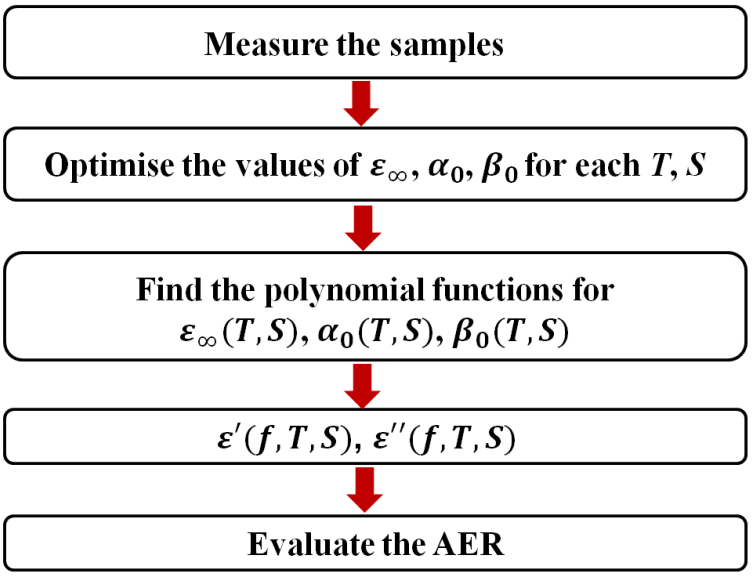

Fig. 3.4. Workflow of the parameters/coefficients derivation process.

3.4 Results Comparison

In this section, new equations of the complex permittivity for three water-based liquids are proposed. From an antenna design point of view, the characteristics of water with PG are carefully investigated. It is the first time, water with PG is considered as a promising candidate for liquid antenna design. New fits with simple and accurate expressions for pure water and salty water are derived. Compared with previous published results, our equations are based on more measured data with a wide temperature and salinity range (0 ~ 70°C and 0 ~ 50 ppt), as well as small frequency step size (≈ 20 MHz).

3.4.1 Pure Water (16 data files)

For pure water, the substance concentration $S = 0$. The approximated polynomial functions of ε_∞, α_0, β_0 are as follows:

$$\varepsilon_\infty(T,0) = \sum_{m=0}^{2} C_{\varepsilon m} T^m$$

$$\alpha_0(T,0) = \sum_{m=0}^{2} C_{\alpha m} T^m$$

$$\beta_0(T,0) = \sum_{m=0}^{2} C_{\beta m} T^m \tag{3.5}$$

where m is a non-negative integer. $m = 0, 1, 2$.

The coefficients $C_{\varepsilon m}$, $C_{\alpha m}$,$C_{\beta m}$ are calculated by using the least square regression analysis, and the values are listed in Table 3.1. To validate the derived formulae, comparisons have been made. For example, the complex permittivity at a temperature of 30°C for the new fits, the measured results and data from Ellison *et al* [9] are compared in Fig. 3.5. It is observed the predicted complex permittivity has a good agreement with our measured results and those from Ellison *et al*.

The complex permittivity variations as a function of frequency and temperature are shown in Fig. 3.6. From these plots, some conclusions can be drawn: 1) At the same temperature, with the increase of frequency, the real part of the permittivity ε'decreases and the imaginary part of the permittivity ε'' increases. 2) At the same the frequency, ε'' normally decreases as with temperature increases. But $\varepsilon'$is less straightforward: it may increase or decrease with the temperature.

To evaluate the accuracy of the new fits across the frequency band, the AER at different temperatures are plotted in Fig. 3.7. It is found that the AER of ε' and ε'' are less than 1% and 7%, respectively, indicating that the new fits can describe the measured results precisely.

Table 3.1: Parameters of the fit (3.5) for pure water

m	$C_{\varepsilon m}$	m	$C_{\alpha m}$	m	$C_{\beta m}$
0	0.0011	0	0.0131	0	-0.1216
1	-0.0588	1	2.0167	1	161.4882
2	5.0498	2	56.5955	2	4763.000

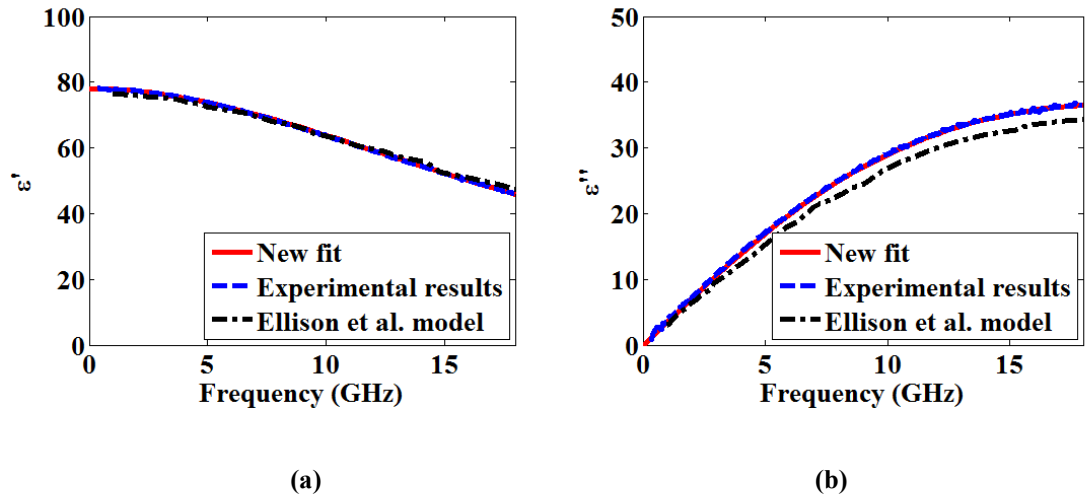

(a) **(b)**

Fig. 3.5. Complex permittivity of pure water with a temperature of 30°C as a function of frequency for different models. (a) ε'. (b) ε''.

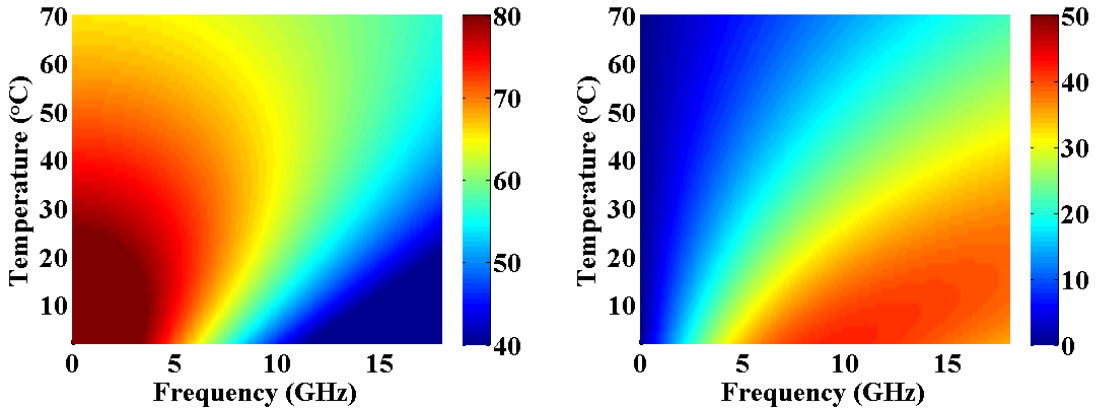

(a) (b)

Fig. 3.6. Complex permittivity variations of pure water as a function of frequency and temperature using the new formula. (a) ε'. (b) ε''.

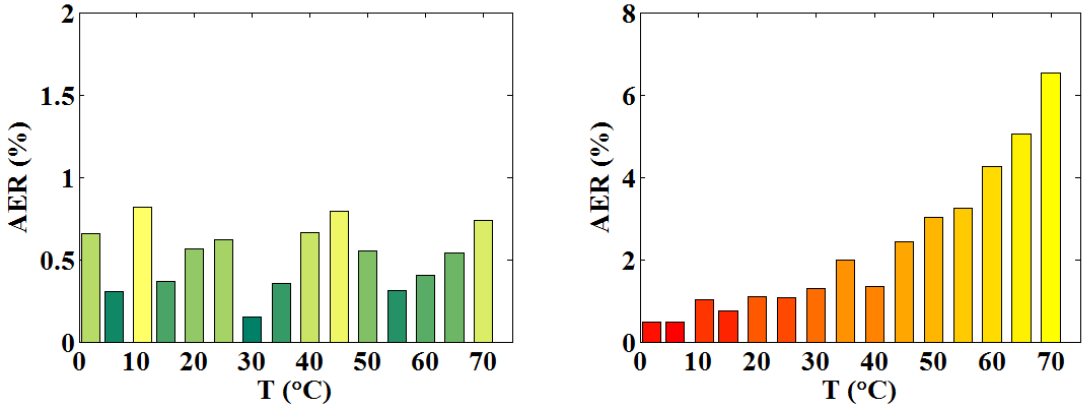

(a) (b)

Fig. 3.7. AER of pure water at different temperatures. (a) ε'. (b) ε''.

3.4.2 Water with PG (251 data files)

Water sometimes may not be considered as a good material for antenna designs, as it will be frozen when temperature is below 0°C, limiting the development of water antennas. Water with PG therefore is proposed as a solution to lower the freezing point of water in cold climates. Propylene glycol (PG) is a kind of antifreeze frequently used in applications such as food-processing systems, animal feed, cosmetics or in water pipes in homes. It is viscous, colorless, and has good solubility in water [10]. Fig. 3.8 shows the freezing point of water with PG in various solutions. The freezing point decreases with the PG solution increases. The freezing point of water with 5% PG ($Volume_{PG}$: $Volume_{water}$ = 5%

: 95%) is around -3°C, which meets the lower limit of commercial temperature grade for electronic devices (0 ~ 85°C).

In this section, water with PG concentration from 0 to 70% has been investigated. The parameters ε_∞, α_0, β_0 are T and S dependent and can be approximated by using polynomial functions:

$$\varepsilon_\infty(T,S) = \sum_{m+n=0}^{5} C_{\varepsilon mn} S^m T^n$$

$$\alpha_0(T,S) = \sum_{m+n=0}^{5} C_{\alpha mn} S^m T^n$$

$$\beta_0(T,S) = \sum_{m+n=0}^{5} C_{\beta mn} S^m T^n \tag{3.6}$$

where m, n are non-negative integers. $m + n = 0, 1, 2, 3, 4, 5$.

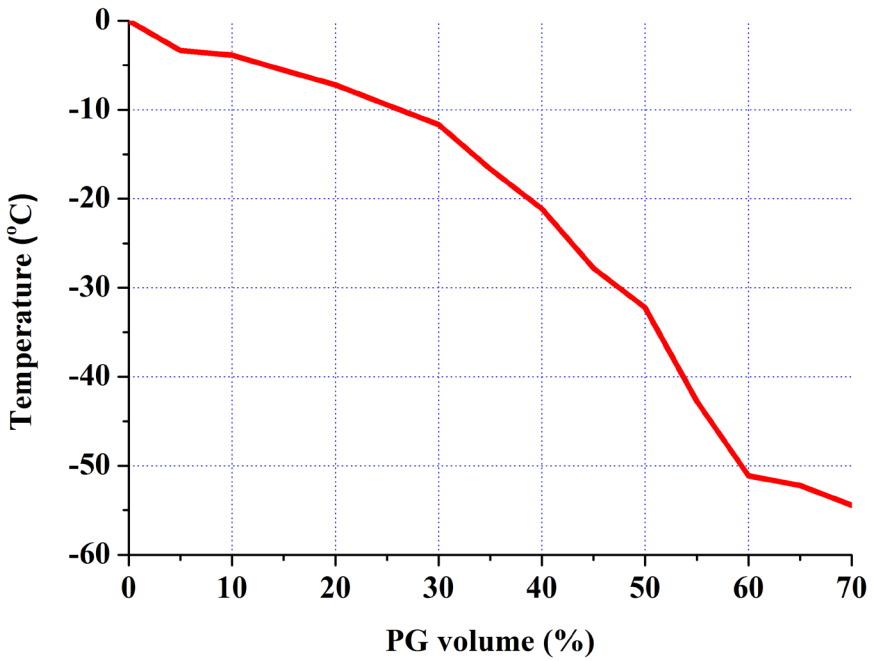

Fig. 3.8. Freezing point of PG solutions in volume [11].

By minimizing the objective function (3.3), the values for the coefficients $C_{\varepsilon mn}$, $C_{\alpha mn}$, $C_{\beta mn}$ are obtained and shown in Table 3.2. It should be mentioned that for different PG concentrations, the freezing point of the liquid is different. The derived formulae only work when the liquid is not frozen.

TABLE 3.2 Parameters of the fit (3.6) for water with PG

m, n	$C_{\varepsilon mn}$	m, n	$C_{\alpha mn}$	m, n	$C_{\beta mn}$
0, 0	5.8153	0, 0	57.0326	0, 0	4599.4
0, 1	0.0104	0, 1	2.7688	0, 1	241.3886
0, 2	-0.0049	0, 2	-0.0373	0, 2	-4.5624
0, 3	$1.1025e^{-4}$	0, 3	$7.4789e^{-4}$	0, 3	0.0586
0, 4	0	0, 4	0	0, 4	0
0, 5	$-9.6927e^{-9}$	0, 5	$-3.0092e^{-8}$	0, 5	$-1.401e^{-6}$
1, 0	0.6437	1, 0	-2.848	1, 0	-296.9865
1, 1	-0.0018	1, 1	-0.0525	1, 1	-5.8259
1, 2	$-2.5578e^{-4}$	1, 2	0.0020	1, 2	0.2509
1, 3	$2.426e^{-6}$	1, 3	$-2.4139e^{-5}$	1, 3	-0.0025
1, 4	$-7.4928e^{-9}$	1, 4	$5.7655e^{-8}$	1, 4	$2.9502e^{-6}$
2, 0	-0.00268	2, 0	0.0953	2, 0	10.3136
2, 1	$2.6816e^{-5}$	2, 1	-0.0027	2, 1	-0.1960
2, 2	$1.1304e^{-5}$	2, 2	$-3.6164e^{-5}$	2, 2	-0.0041
2, 3	$-2.4451e^{-8}$	2, 3	$1.6607e^{-7}$	2, 3	$2.2549e^{-5}$
3, 0	$3.3057e^{-4}$	3, 0	-0.0013	3, 0	-0.1417
3, 1	$-6.9713e^{-6}$	3, 1	$9.8514e^{-5}$	3, 1	0.008
3, 2	$-1.114e^{-7}$	3, 2	$2.2773e^{-7}$	3, 2	$2.0956e^{-5}$
4, 0	0	4, 0	0	4, 0	0
4, 1	$9.5183e^{-8}$	4, 1	$-8.0676e^{-7}$	4, 1	$-6.642e^{-5}$
5, 0	$-1.5283e^{-8}$	5, 0	$8.2905e^{-8}$	5, 0	$8.6078e^{-6}$

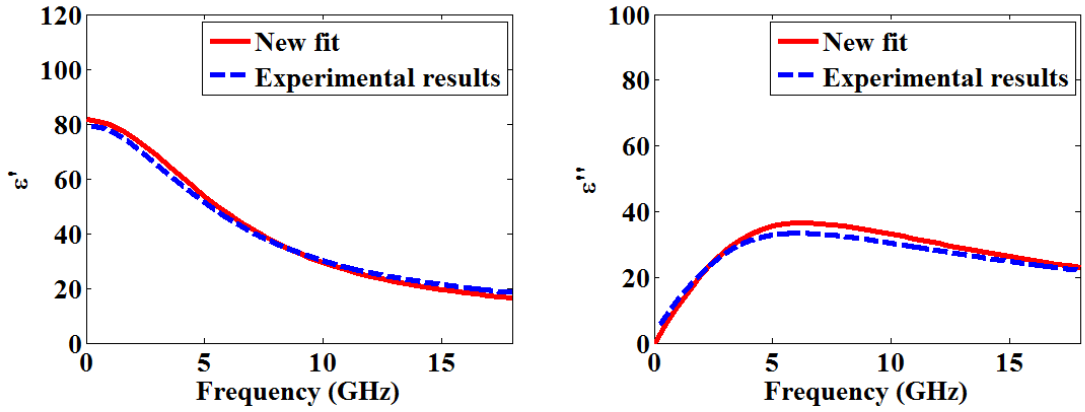

Fig. 3.9. Complex permittivity of water with PG for S = 5%, T = -2°C as a function of frequency for new fits and measured results. (a) ε'. (b) ε''.

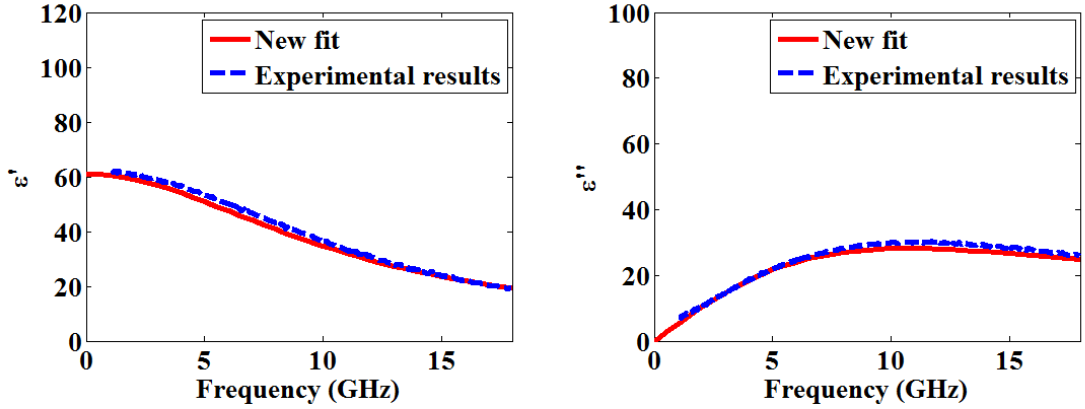

Fig. 3.10. Complex permittivity of water with PG for S = 30%, T = 45°C as a function of frequency for new fits and measured results. (a) ε'. (b) ε''.

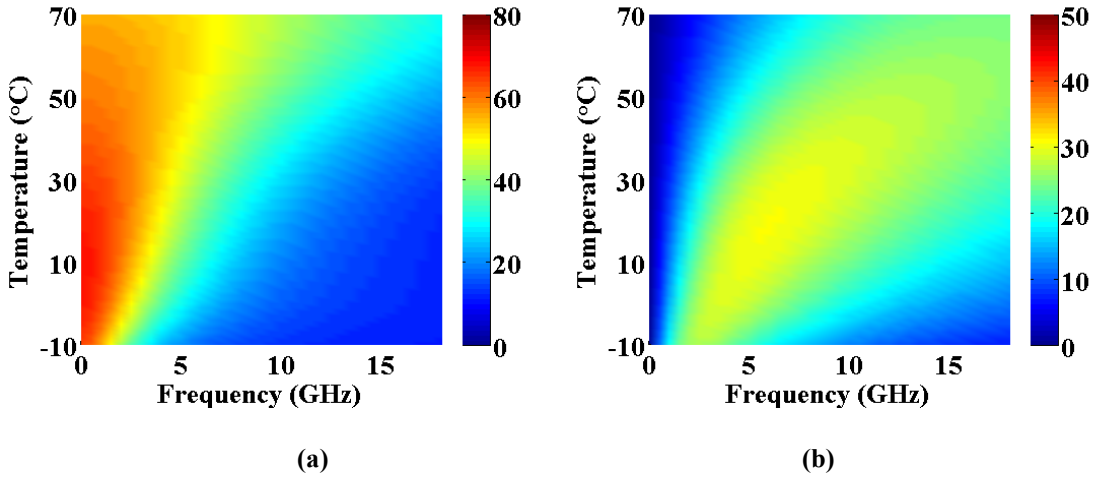

Fig. 3.11. Complex permittivity variations of water with 30% PG as a function of frequency and temperature using the new formula. (a) ε'. (b) ε''.

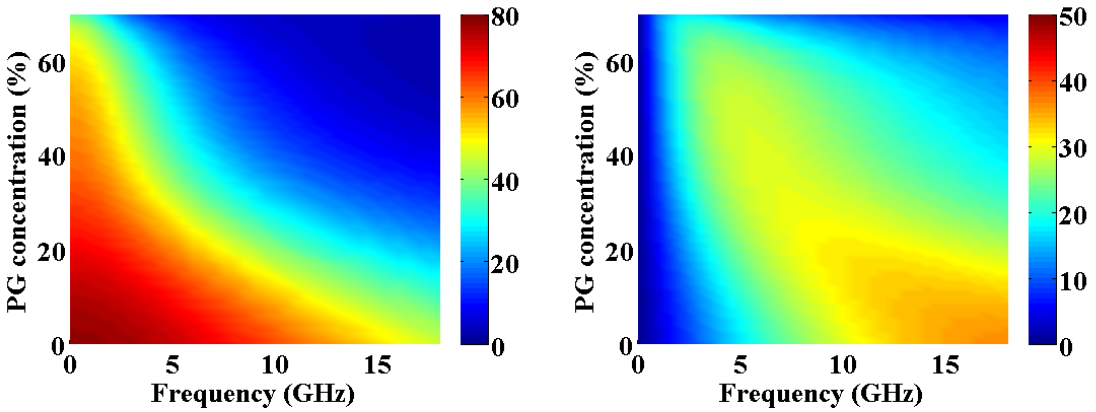

Fig. 3.12. Complex permittivity variations of water with PG at 30°C as a function of frequency and PG concentration using the new formula. (a) ε'. (b) ε''.

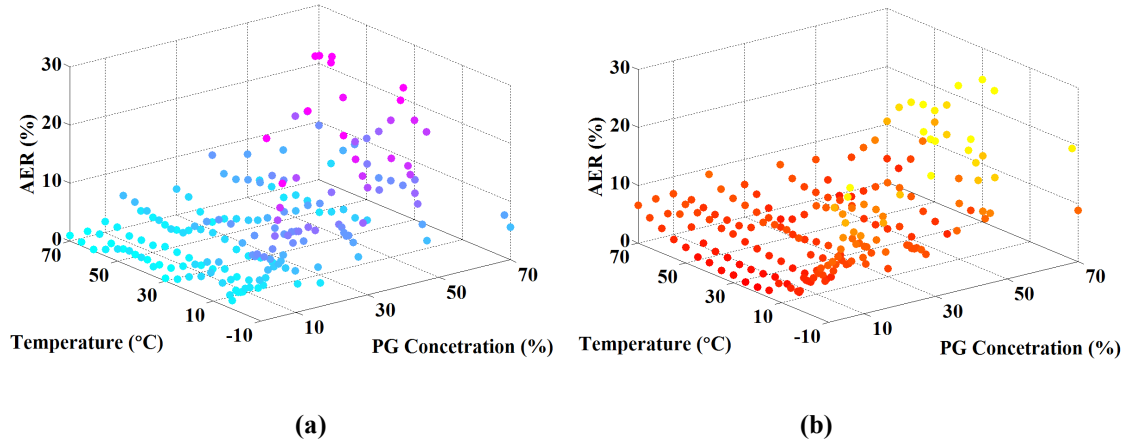

Fig. 3.13. AER of water with different PG concentrations at different temperatures and. (a) ε'. (b) ε''.

To validate the derived equations, the comparisons between the measured and calculated ε as a function of frequency for S = 5%, T = -2°C and S = 30%, T = 45°C are shown in Fig. 3.9 and Fig. 3.10, respectively. Good agreements are observed.

$\varepsilon(f,T,S)$ at S= 30% and T= 30°C is shown in Fig. 3.11 and Fig. 3.12, respectively. From these plots, the variations of $\varepsilon(f,T,S)$ according to different temperatures, concentrations and frequencies are shown clearly. It is very useful for choosing the right liquid with a given condition. For example, when designing a dielectric resonator antenna (DRA), a liquid with a high ε' and a low ε'' is normally needed; when designing a conducting antenna, a liquid with a high ε'' is preferred.

To evaluate the accuracy of the new fits across the frequency range, the AER at different temperatures and PG concentrations are shown in Fig. 3.13. Most of the AER values are around 8%,

which means the predicted fits agree with the measured results very well. Some lager AER values are mainly due to the inaccuracy of material properties that caused by the liquid solution changes and measurement errors.

A comparison between pure water, water with 5% and 10% PG as a function of frequency at $T = 2^{o}C$ is shown in Fig. 3.14. It is noted that the complex permittivity of these three liquids has a similar shape across the frequency band. Especially at frequencies lower than 2GHz, a very close agreement is observed, which means the water with 5% or 10% PG can be a very good alternative candidate for the water antenna design at lower temperatures. To validate the implementation of water with PG, a hybrid water antenna with pure water and 10% PG was fabricated and measured, the performances in terms of S_{11} and antenna efficiency are very similar for these two liquids, and the details will be presented in Chapter 5.

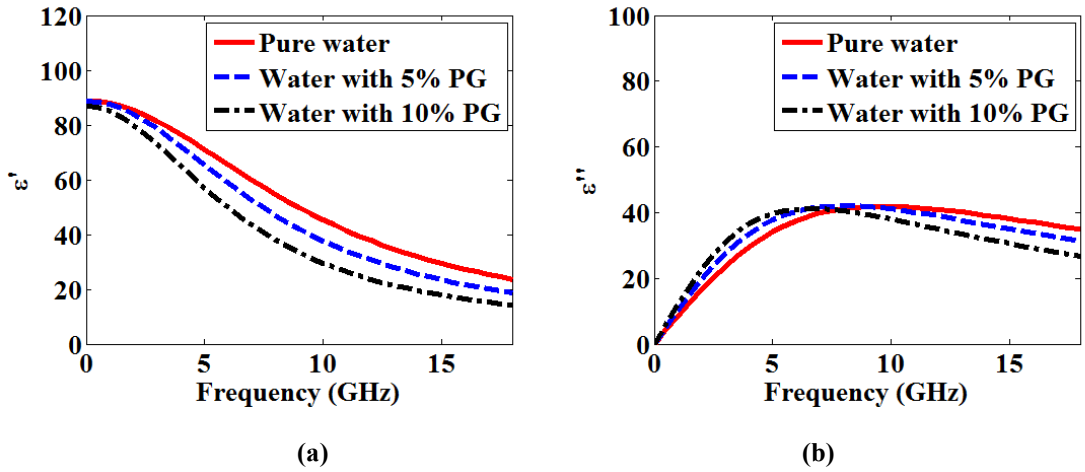

Fig. 3.14. Complex permittivity comparison of pure water, water with 5% PG and water with 10% PG as a function of frequency at $T = 2^{o}C$. (a) ε'. (b) ε''.

3.4.3 Salty Water (54 data files)

In this section, salty water with salinity from 0 to 50 ppt has been studied, the new fits for salty water have been derived. A new approximated polynomial function of the coefficients $C_{\varepsilon mn}$, $C_{\alpha mn}$, $C_{\beta mn}$, $C_{\gamma mn}$ is given in (3.7), and the last term in the permittivity equation is to take the conductivity of salt into account. Again, these coefficients are determined by minimizing the objective function (3.3), and the values are listed in Table 3.3.

$$\varepsilon(f,\ T,\ S) = \varepsilon_{\infty}(T,S) + \frac{\beta_0(T,S)}{\alpha_0(T,S) + j2\pi f} + j\frac{\gamma_0}{2\pi f} \tag{3.7}$$

$$\varepsilon_\infty(T,S) = \sum_{m+n=0}^{3} C_{\varepsilon mn} S^m T^n$$

$$\alpha_0(T,S) = \sum_{m+n=0}^{3} C_{\alpha mn} S^m T^n$$

$$\beta_0(T,S) = \sum_{m+n=0}^{3} C_{\beta mn} S^m T^n$$

$$\gamma_0(T,S) = \sum_{m+n=0}^{3} C_{\gamma mn} S^m T^n \tag{3.8}$$

where m, n are non-negative integers. $m + n = 0, 1, 2, 3$.

TABLE 3.3 Parameters of the fit (3.8) for salty water

m, n	$C_{\varepsilon mn}$	m, n	$C_{\alpha mn}$	m, n	$C_{\beta mn}$	m, n	$C_{\gamma mn}$
0, 0	4.5939	0, 0	76.038	0, 0	6796.9	0, 0	24.217
0, 1	0.3211	0, 1	0.56	0, 1	-52.421	0, 1	0.4458
0, 2	-0.0198	0, 2	0.0643	0, 2	7.9144	0, 2	-0.0557
0, 3	0.0002	0, 3	-0.0003	0, 3	-0.07	0, 3	-0.0009
1, 0	-0.1191	1, 0	-0.3546	1, 0	-38.357	1, 0	16.826
1, 1	-0.0036	1, 1	0.0509	1, 1	4.6429	1, 1	0.5059
1, 2	0	1, 2	-0.0006	1, 2	-0.058	1, 2	-0.0014
2, 0	0.0096	2, 0	-0.0374	2, 0	-5.3303	2, 0	-0.5289
2, 1	0	2, 1	-0.0001	2, 1	-0.0342	2, 1	-0.0021
3, 0	0.0001	3, 0	-0.0007	3, 0	0.1006	3, 0	0.0078

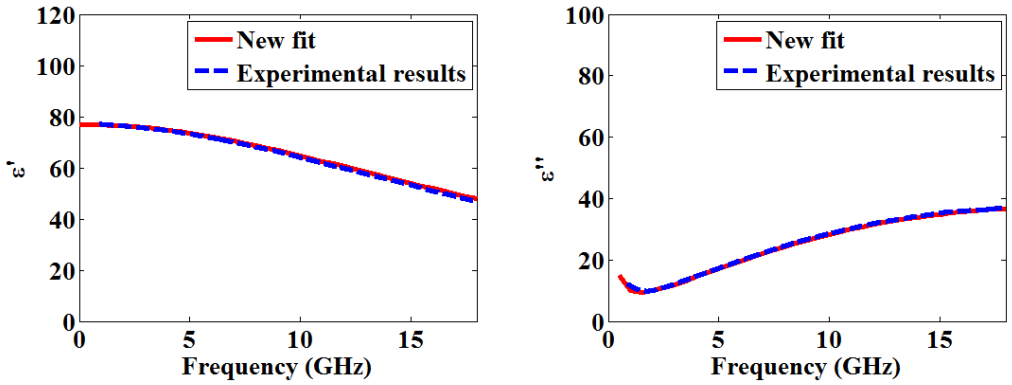

Fig. 3.15. Complex permittivity of salty water for *S*=1 ppt, *T*=30°C as a function of frequency for new fits and measured results. (a) ε'. (b) ε''.

The comparisons between the measured and calculated ε as a function of frequency for S = 1 ppt, T = 30°C are shown in Fig. 3.15, again good agreements are obtained. It is observed, with a specific S and T, by increasing the frequency, ε' decreases, while ε'' increases.

For specific salinity, $\varepsilon(f,T,S)|_{S=0.5}$ is shown in Fig. 3.16, and for a fixed temperature, $\varepsilon(f,T,S)|_{T=30}$ is given in Fig. 3.17. Similar to water with PG, we can choose salty water with specific salinity regarding to different applications.

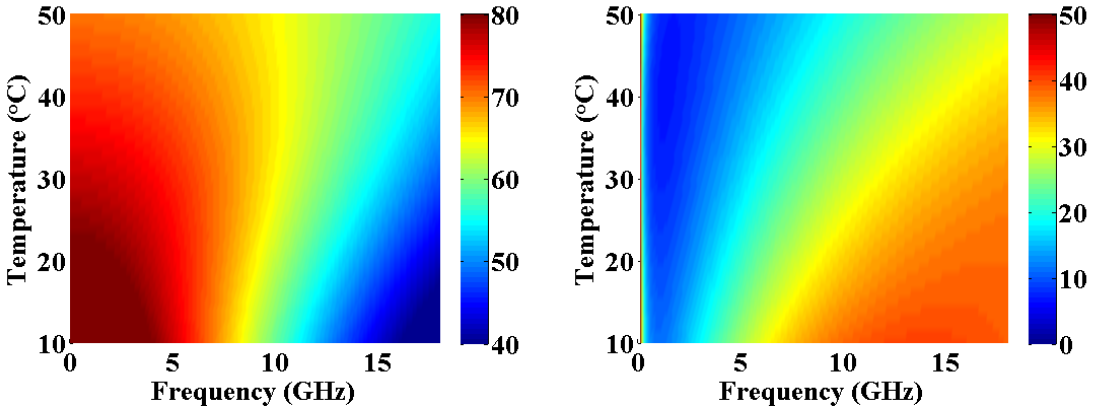

Fig. 3.16. Complex permittivity variations of salty water with 0.5 ppt as a function of frequency and temperature using the new formula. (a) ε'. (b) ε''.

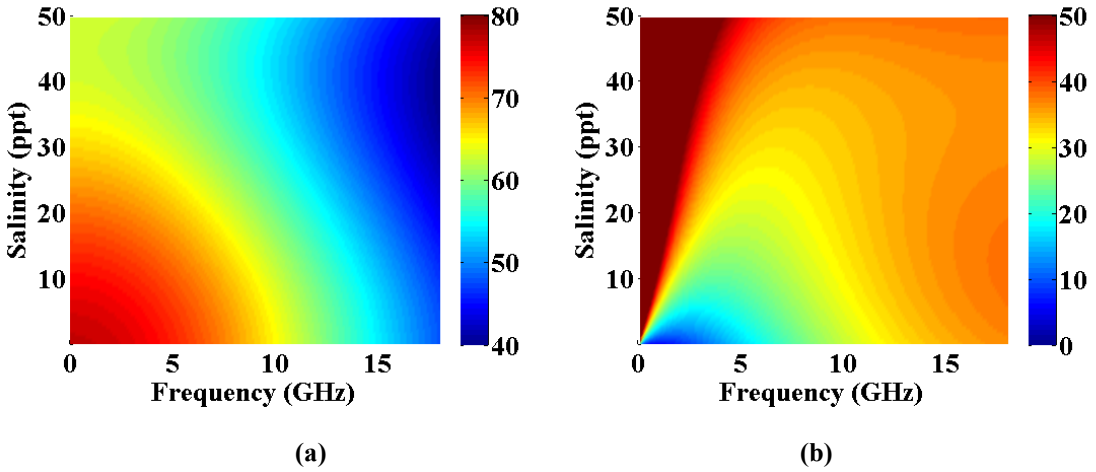

Fig. 3.17. Complex permittivity variations of salty water at 30°C as a function of frequency and salinity using the new formula. (a) ε'. (b) ε''.

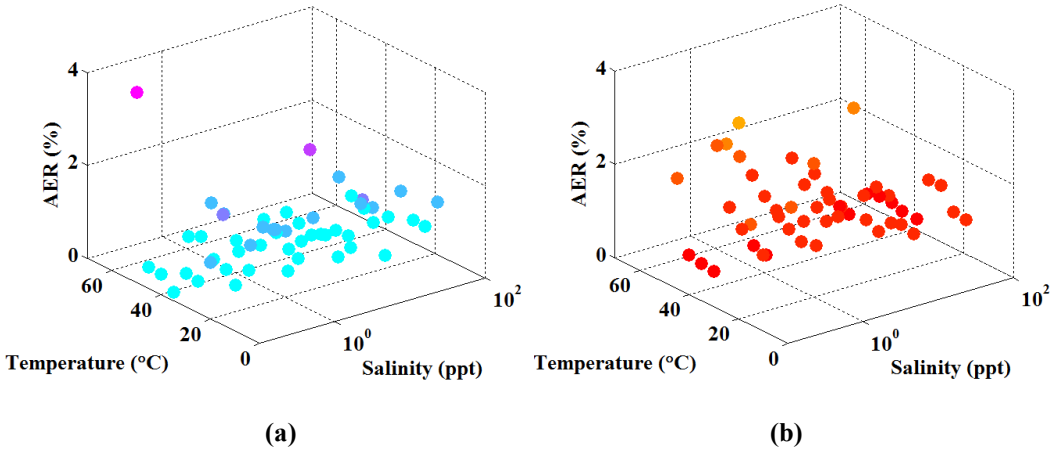

Fig. 3.18. AER of salty water for different temperatures and salinity. (a) ε'. (b) ε''.

The AER for different temperatures and salinity are displayed in Fig. 3.18. By using this simpler dielectric expression with fewer parameters and lower orders, the new fits achieve a maximum AER of 4% at different temperatures and salinity, with most of the AER values below 2%, which means the new fits have very close agreements with the measured results and can be used to obtain the material properties easily and accurately.

3.5 Summary

In this chapter, three water-based liquids namely water with PG, pure water and salty water have been investigated under various conditions. 321 data files at different temperatures with 16 different substance concentrations have been measured and recorded. A real-time liquid complex permittivity

measurement software package has been developed to automatically record the permittivity data, which has greatly improved the efficiency of the liquid measurements under different temperatures. Two different scenarios (high and low temperature) have been performed. New formulae/fits with lower orders and fewer parameters have been derived, which are simple and easy to use. Good agreements between the new fits and measured results are obtained. It has been shown that the new fits can accurately describe the complex permittivity, when $0< f \leq 18$ GHz, $0 < T \leq 70^{o}$C (for pure water and salty water) and $-10^{o}\text{C} < T \leq 70^{o}\text{C}$ (for water with PG), $0 \leq PG\ concentration \leq 70\%$, $0 \leq Salinity \leq 50$ ppt. These new curve fitting equations are of significant importance in predicting the complex permittivity of these water-based liquids at various frequencies, substance concentrations and temperatures. It has been found that water with 5% or 10% PG is similar to pure water at lower frequencies and temperatures, thus it is proposed as an alternative candidate for water antenna designs for cold climates, which has greatly increased the possibility of using the water-based liquid for antenna designs. The knowledge gained for water with PG is very valuable for overcoming the limitations of water-based antennas, such as temperature variations of the complex permittivity. The formulae for pure water and salty water are also derived, compared with published results, our new fits are based on more experiment data and smaller frequency step size with simpler expressions.

The main contributions of this research are new formulae with simple expressions for water-based liquids and a software pack developed for liquid measurements which can be generalised to deal with other types of liquids. Moreover, the novelty idea that mix water with other types of liuqids is very benifical for future liquid antenna designs.

3.6 References

[1] L. Klein, C. T. Swift, “An improved model for the dielectric constant of sea water at microwave frequencies,” IEEE Trans. Antennas Propag., vol. 25, no. 1, pp. 104-111, 1977.

[2] A. Kumar, “Complex permittivity and microwave heating of pure water, tap water and salt solution,” Int. J. Electron., vol. 47, no. 6, pp. 531-536, 1979.

[3] H. J. Liebe, G. A. Hufford, T. Manabe, “A model for the complex permittivity of water at frequencies below 1 THz,” Int. J. of Infrared and Millimeter Waves, vol. 12, no. 7, pp. 659-675, 1991.

[4] W. Ellison, A. Balana, G. Delbos, K. Lamkaouchi, L. Eymard, C. Guillou, C. Prigent, “New permittivity measurements of seawater,” Radio Sci., vol. 33, no. 3, pp. 639-648, 1998.

[5] T. Meissner, F. J. Wentz, "The complex dielectric constant of pure and sea water from microwave satellite observations," IEEE Trans. Geosci. Remote Sens., vol. 42, no. 9, pp.1836-1849, 2004.

[6] M. S. Venkatesh, G.S.V. Raghavan, "An overview of dielectric properties measuring techniques," Canadian Biosystems Engineering, vol. 47, pp. 7.15-7.30, 2005.

[7] "Basics of measuring the dielectric properties of materials," Keysight literature number 5989-2589EN, 2015.

[8] "Dielectric Probe Kit 200 MHz to 50 GHz," Keysight literature number 5989-0222EN, 2014.

[9] W. J. Ellison, "Permittivity of pure water, at standard atmospheric pressure, over the frequency range 0-25 THz and the temperature range 0-100^{o}C," J. Phys. Chem. Ref. Data, vol. 36, no. 1, pp. 1-18, 2007.

[10] M. Burr and L. Tice, "A study of the inhibitory concentration of glycerine-sorbito and propylene glycol-sorbitol combinations on the growth of microorganisms," J. Am. Pharm. Assoc., vol. 46, no. 4, pp. 217-218, Apr. 1957.

[11] Antifreeze Solutions in Home Fire Sprinkler Systems, Code Consultants Inc., St. Louis, MO, 2010.

Chapter 4: A Monopole Water Antenna

4.1 Introduction

Since the systematic study of dielectric resonators as radiating elements was conducted in the 1980s, the DRA has attracted a lot of attention over the past decades [1]. It can be regarded as a kind of resonator fabricated using low-loss microwave dielectric materials. The resonant frequency is predominantly a function of its size, shape, and material property. A considerable amount of work has been carried out to study DRAs with different shapes, resonant modes, excitation schemes, bandwidth enhancement techniques, polarisations, compact size techniques, magneto dielectrics, electromagnetic band-gap (EBG) structures and liquids [1-7].

Liquid (such as water and ionic liquid) antennas not only share the features of other DRAs but also offer the following advantages of conformability, reconfigurability, small RCS, easy transportation, low-cost and improvement in electromagnetic coupling. All these benefits open up new opportunities for liquid antenna designs. With water being one of the most popular, much effort has been made to explore the designs of water antennas.

In this chapter, salt is added to pure water to decrease and modify the dielectric response (real and imaginary part of the permittivity). The characteristic analysis in Chapter3 can be used as a guide for the salty water antenna design with the specific salinity. Our focus of this chapter is on salty water antennas: the resonant frequency, the radiation efficiency and the bandwidth.

The chapter invstigates a monopole water antenna and organised as follows:

In Section 4.2, the relationship between the conductivity and radiation efficiency is investigated. By varying the salty water conductivity, the radiation efficiency of the water antenna is obtained. In section 4.3, the configuration of a monopole water antenna with a dielectric layer between the water and ground plane is presented. In section 4.4, the characteristics of the antenna and the performance dependency on each part of the antenna are carefully examined. In section 4.5, the water with different salt concentrations (thus conductivity) are studied and evaluated. The temperature characteristics of the salty water are also investigated. In section 4.6, a Teflon based monopole water antenna is fabricated and evaluated. In section 4.7, a summary is drawn to review all the findings.

4.2 The Relationship between Conductivity and Radiation Efficiency

Salty water has variable relative permittivity and conductivity [8] which can be considered having a combination of two different properties: dielectric and conductive. Without considering the dielectric properties, salty water may be considered as a conductor and suitable for making normal conducting antenna. By changing the conductivity of water, the water antenna will show different performance. On the other hand, without considering the conductivity, water is a material with a high permittivity and can be used as a good alternative material for DRAs. From a circuit point of view, salty water can be equivalent to a capacitor and a resistor in parallel. Its permittivity properties can be viewed as capacitance and the loss introduced by the conductivity performs as resistance, which will influence the radiation efficiency of the water antenna. There is a close relationship between conductivity and antenna radiation efficiency (defined as is the ratio of the radiated power to the input power accepted by the antenna). When conductivity is nearly 0, the efficiency of the antenna is high. The antenna works as a DRA. As the conductivity increases, the dielectric response becomes weak and the conducting response becomes strong, and the efficiency of the antenna decreases. The antenna is a mixture of a DRA and a conducting antenna. When the conductivity goes to infinity (that is a perfect conducting antenna), the efficiency increases. The antenna becomes a conducting antenna. It is worth mentioning that the water antenna will be two different types of antenna when conductivity is nearly 0 or very high. Fig. 4.1 shows the radiation efficiency of a monopole water antenna as a function of the water conductivity at a specific frequency. CST Microwave Studio has been used for this investigation.

The lowest conductivity is $10^{-1.5}$ S/m and the radiation efficiency = 32%. From this figure, we can draw some interesting conclusions: when the conductivity increases from 10^{-6} to 10^{-3}, the efficiency decreases from about 100% to 80%, the antenna acts as a high permittivity DRA. When the conductivity is between 10^{-3} S/m and 10^{2} S/m, the antenna can be considered as a combination of dielectric and conducting antennas, the efficiency is below 80%. When the value of conductivity is over 10^{2}, the water antenna may be treated as a normal conducting antenna and the efficiency is well over 80%. In reality, the conductivity of salty water cannot be so high as 10^{2} S/m, as the salt will be saturated in the water. The maximum water conductivity reported is from the Dead Sea in Jordan (31.5000° N, 35.5000° E). The permittivity and conductivity of the Dead Sea water have been shown in Fig. 4.2 as a reference.

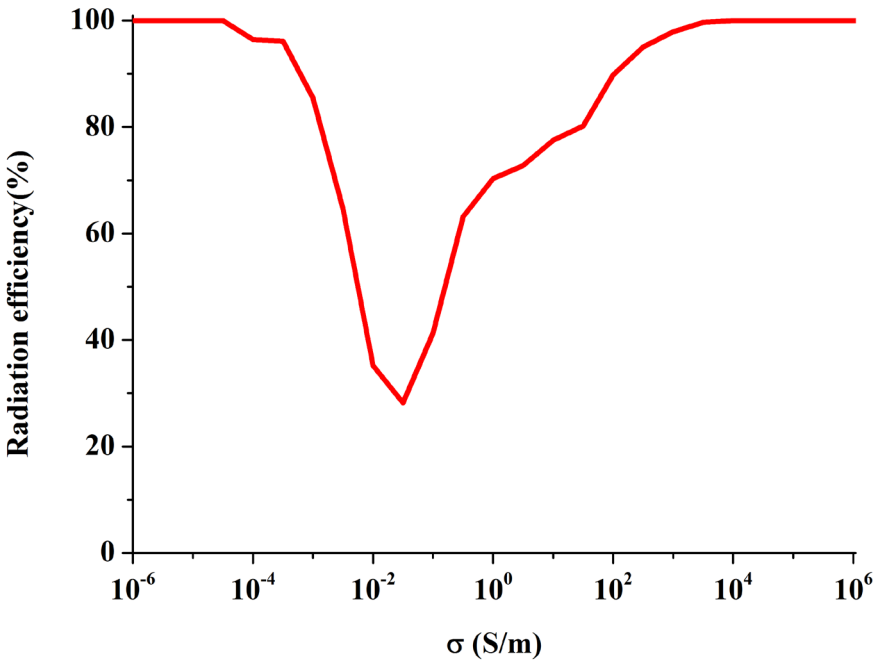

Fig. 4.1. Relationship between conductivity and radiation efficiency of a monopole antenna at 2 GHz

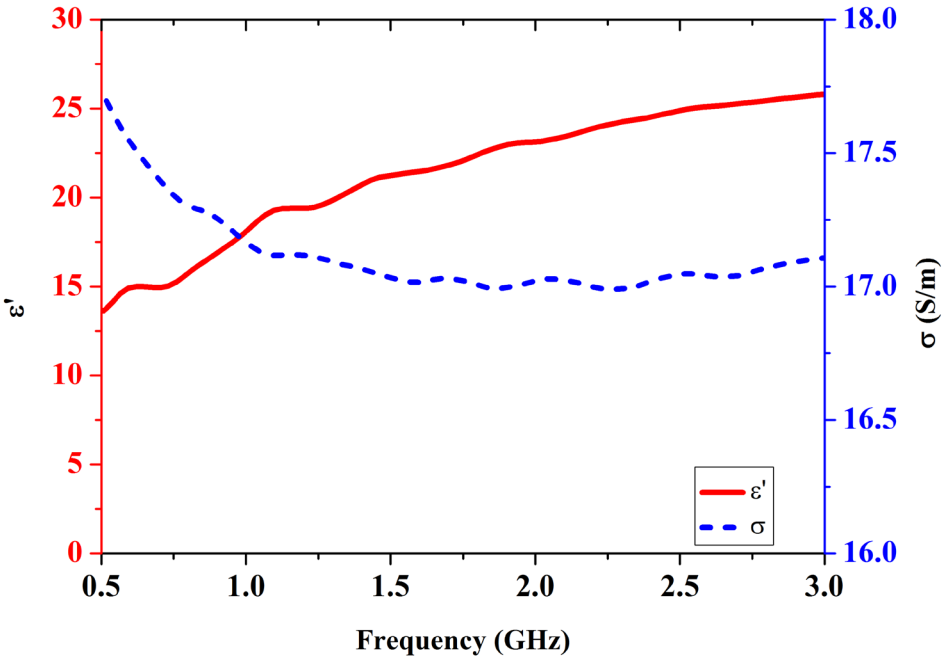

Fig. 4.2. $\varepsilon'$and σ of Dead Sea water as a function of frequency.

4.3 Antenna Configuration

In this section, a water monopole antenna with a dielectric layer is presented. The cross-section view is shown in Fig. 4.3. It consists of five parts: a ground plane, a dielectric layer, a SMA connector, the water and a tube [9]. The dielectric layer is needed to isolate the water from the ground plane and its effects on the antenna performance are studied in terms of the changes in the dimensions of the dielectric layer and the water tube, the position of the feed, the water height and the size of the ground plane. The square ground plane has dimensions of $L_g \times L_g \times H_g$. The circular dielectric layer has a radius R_d, height H_d and relative permittivity ε_r . The offset of the feed pin from the center of the tube is L_s (not shown in Fig. 4.3 since it is 0). The height of the feed pin in the water is L_p. The heights of the water and the tube are H_w and H_t, respectively. The inner diameter of the tube is D_w. The SMA connector acting as the feed of the antenna is considered in the simulation [10].

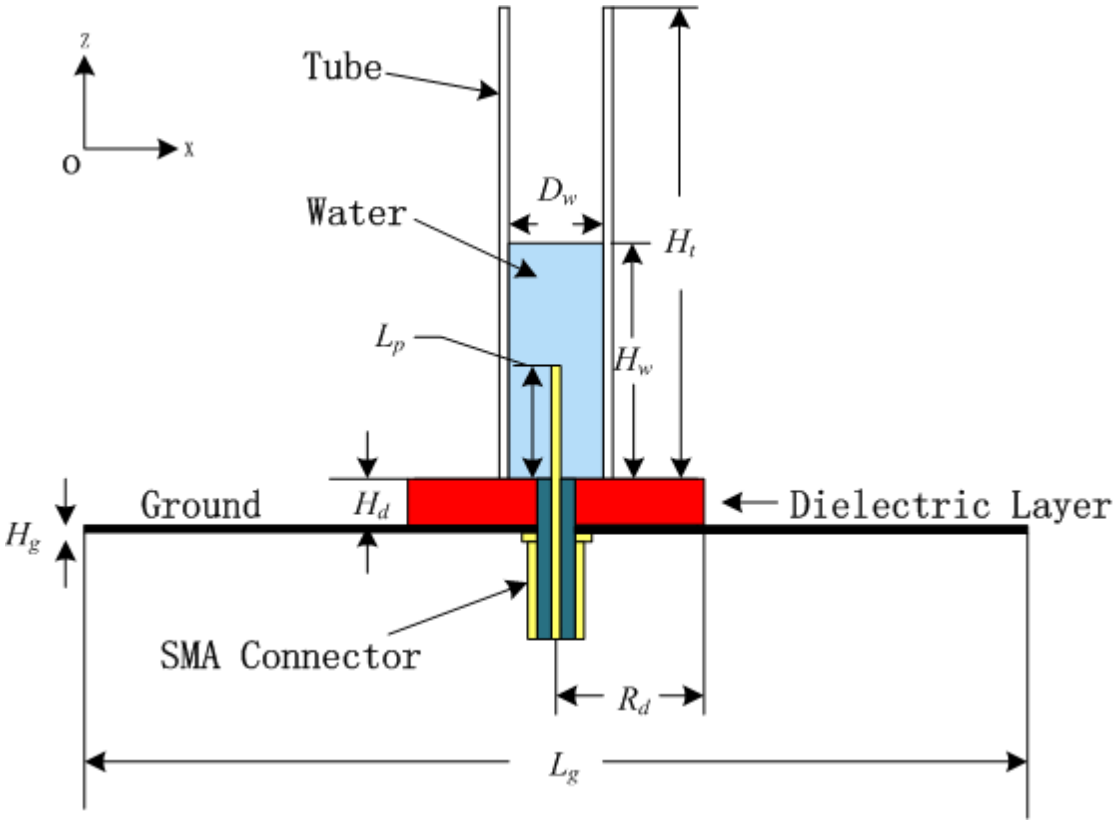

Fig. 4.3. Geometry of the water antenna.

The procedure adopted for this study is that only one parameter is changed at a time to observe its effects on the antenna performance while others are kept constant. Different sets of parameters are considered to cover a wide range of situations. The operational frequency is from 0.5 to 3 GHz to cover some popular frequency bands. The parameters of our reference water antenna are: L_g = 200

mm, H_g = 2 mm, H_d = 7 mm, R_d = 25 mm, D_w = 25 mm, H_w = 44 mm, L_p=8.9 mm, L_s = 0 mm, H_t = 100 mm. A foam is chosen as the dielectric layer with relative permittivity $\varepsilon_r \approx 1$ and the water relative permittivity and conductivity are set as 80 and 4.7 S/m (for sea water), respectively [11]. The fractional bandwidth (B_F) is calculated using equation:

$$B_F = \frac{(f_{high} - f_{low})}{(f_{high} + f_{low})/2} \times 100\% \quad (4.1)$$

where f_{low} and f_{high} are the lowest frequency and highest frequency, respectively, for the reflection coefficient S_{11}= -10 dB over the band of interest. The monopole water antenna has the first resonant frequency around 1.73 GHz (the reactance is zero) and a fractional bandwidth of 106.4%; under the same condition, the equivalent copper monopole antenna has the first resonant frequency around 1.81 GHz (> 1.73 GHz) and a fractional bandwidth of 82% (< 106.4%).

4.4 Comprehensive Study of Antenna Parameters

A number of parameters shown in Fig. 4.3 influence the antenna characteristics, including the dielectric layer and the water tube dimensions, the position of the feed, the water height and the size of the ground plane. To achieve the optimum antenna performance, a parametric study was carried out to investigate the performance of the antenna.

4.4.1 Dielectric Layer Effects

The dielectric layer is needed to isolate the water from the ground plane and avoid a short circuit, as the water in our study has variable conductivity. For this dielectric layer, three parameters are of interest: the dielectric layer relative permittivity ε_{rd}, the dielectric layer height H_d and the dielectric layer radius R_d. After extensive simulations, we can conclude that this water antenna performance is not very sensitive to the dielectric layer radius R_d but the effects of the relative permittivity ε_{rd} and the dielectric layer height H_d on the resonant frequency, the fractional bandwidth and the radiation efficiency of the antenna are significant. Some selected results are shown in Fig. 4.4. When the relative permittivity ε_{rd} is changed from 1 to 10, the resonant frequency and the fractional bandwidth as a function of ε_{rd} are illustrated in Fig. 4.4(a). Similarly the radiation efficiency as a function of frequency for ε_{rd} = 1, 5, and 10 are given in Fig. 4.4(b), respectively. It is apparent that the permittivity of the dielectric layer has great effects on the bandwidth and the radiation efficiency of the antenna. When the relative permittivity ε_{rd} is increased from 1 to 10, the resonant frequency of the water monopole is reduced from 1.73 to 1.11 GHz; the fractional bandwidth (which is much higher than that of its counterpart conductive antenna) is reduced from 106% to 14%, and the maximum radiation efficiency is decreased from 60% to 30%. Overall, the lower the relative

permittivity of the dielectric layer, the better the antenna performance. When the dielectric layer with a lower permittivity is used, the Q factor of the antenna will be small, which makes the antenna much easier to radiate, thus a wide bandwidth and high efficiency can be achieved. The foam with relative permittivity near 1 has the widest bandwidth and the highest radiation efficiency. However, in reality, the density of such foam could be too low to support the water, thus Teflon with relative permittivity 2.1 is chosen for our experiment.

When the thickness of the dielectric layer (with $\varepsilon_r \approx 1$) is varied from 2 to 9 mm, the simulated results are obtained and shown in Fig. 4.5(a) - (b). As the dielectric layer thickness H_d is increased, the resonant frequency of the antenna varies slightly, however, the fractional bandwidth first increases to the peak and then decreases. For the radiation efficiency at the center frequency, it increases with the dielectric layer thickness H_d. When this thickness is further increased, the dielectric layer will become the main radiator, and the antenna will be considered as a dielectric resonant antenna more than a conductive antenna whose bandwidth will be narrow. In some cases, the radiation efficiency is pretty high, but the fractional bandwidth is narrow. While in some other cases, the fractional bandwidth is very wide, but the radiation efficiency is low due to the loss in the water -the smaller the Q factor, the larger the bandwidth. Thus, there is a trade-off between the radiation efficiency and the fractional bandwidth. Our target is to achieve a relative broad bandwidth and acceptable radiation efficiency.

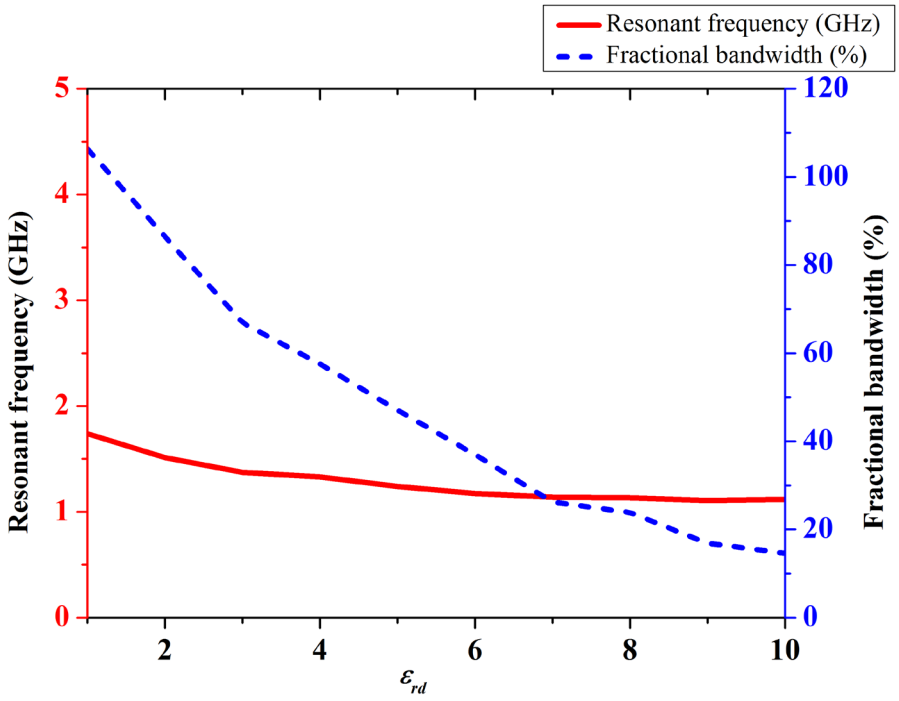

(a)

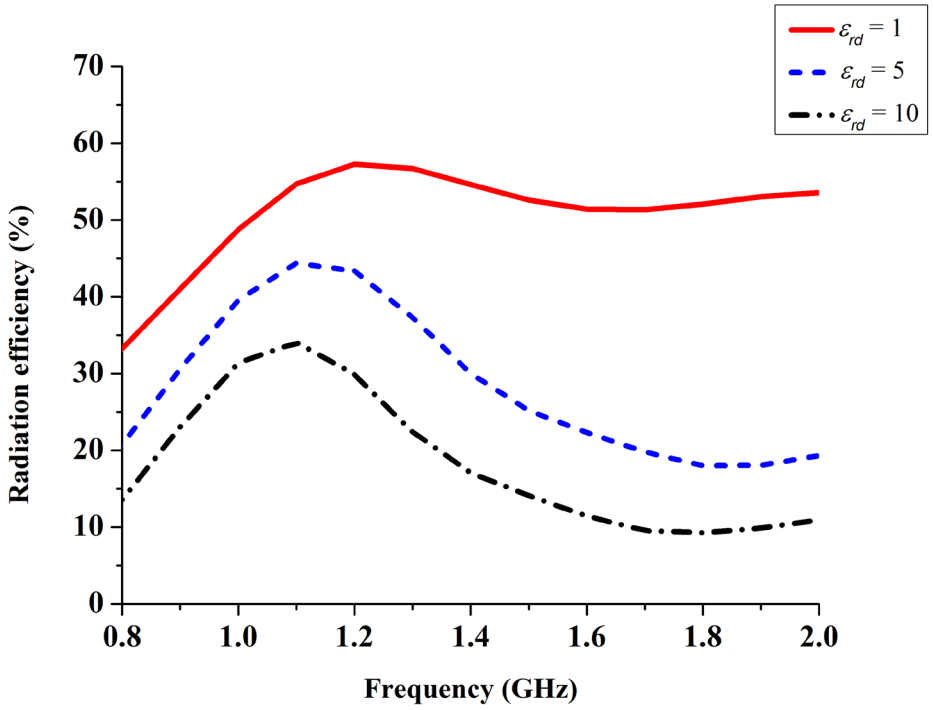

(b)

Fig. 4.4. (a) Resonant frequency (GHz) and fractional bandwidth (%) vs. dielectric layer relative permittivity. (b) Radiation efficiency vs. frequency (GHz) for different dielectric layer relative permittivity.

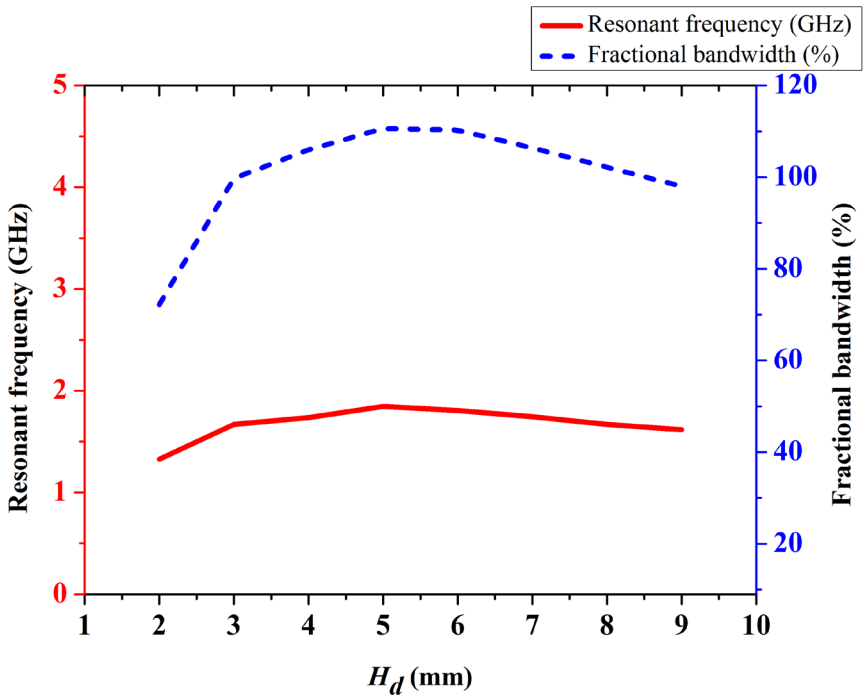

(a)

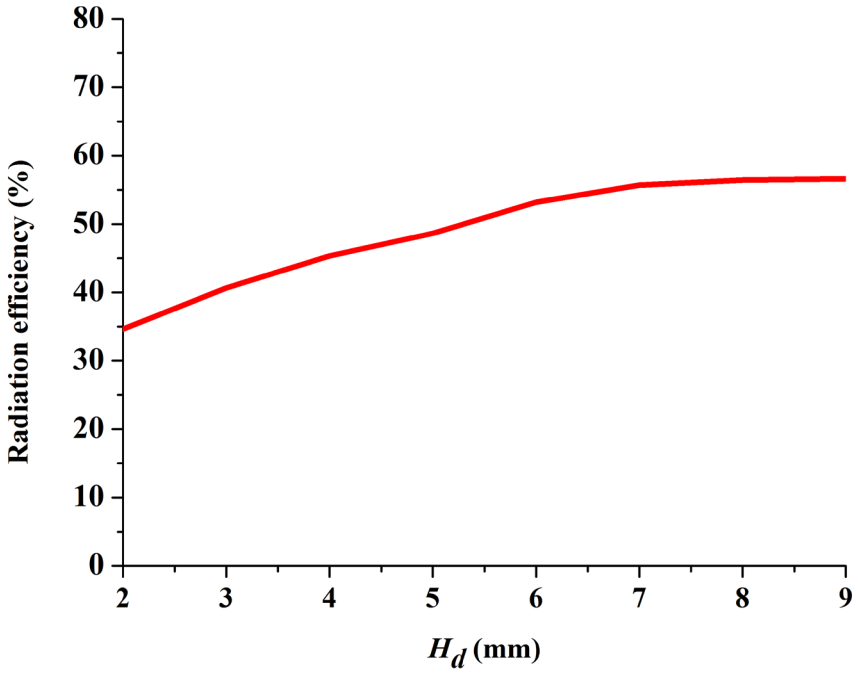

(b)

Fig. 4.5. (a) Resonant frequency (GHz) and fractional bandwidth (%) vs. dielectric layer thickness H_d (mm). (b) Radiation efficiency (%) at the center frequency vs. dielectric layer thickness H_d (mm).

4.4.2 Feeding Effects

As the antenna structure is symmetric, the feeding configuration is investigated by altering the feeding offset L_s (the position of the SMA connector to the center of the water) from 0 to 12 mm (limited by the tube diameter of 25 mm) and the probe length in the water L_p from 0 to 50 mm to explore their influences on the antenna characteristics while other parameters are kept the same as the reference antenna. The results indicate that the feeding effects are closely linked to the conductivity of the water. In particular: 1). When the water conductivity is greater than about 4 S/m (similar to seawater), the feeding offset L_s and the probe length in the water L_p do not significantly affect the resonant frequency and the fractional bandwidth. In this case, the water antenna mainly acts as a conducting antenna rather than a dielectric resonant antenna. The water antenna is not very sensitive to the feeding pin/probe. 2). When the water conductivity is much smaller than 4 S/m, the water antenna acts as a DRA. By changing the conductive probe length, impedance matching can be tuned; while changing the location of the feeding pin, different modes can be excited, thus the antenna performance is changed. This is an important issue for most DRAs, but not an issue for this monopole water antenna.

4.4.3 Water Tube Diameter Effects

As the water tube diameter D_w is altered from 4 to 40 mm, the antenna reflection coefficient is affected accordingly. Take water tube diameter D_w = 8 mm as an example. It is interesting to note that there are two resonant frequencies below 4 GHz for the antenna as shown in Fig. 4.6. The E-field distributions of the two frequencies are displayed in Fig. 4.7, which is similar to a conventional conductive monopole. When the water diameter D_w is increased, the second resonant frequency (resonant frequency 2 in the figure) shifts downwards and closer to the first resonant frequency (resonant frequency 1 in the figure), as depicted in Fig. 4.8(a). By increasing the water diameter D_w, the first resonant frequency and the second resonant frequency get closer and the antenna becomes a wideband antenna. The normalised current distributions at the resonant frequency in Fig. 4.8(b) - (c) can be used to further explain the process. The increase of the water tube diameter results in the change of the current distribution, which is significant for the second resonant frequency. The shape of the current distribution of the second resonant frequency becomes similar to that of the first resonant frequency when the water tube diameter is increased, and the antenna bandwidth becomes broad. Just like a conducing monopole, the fatter the antenna, the larger the bandwidth.

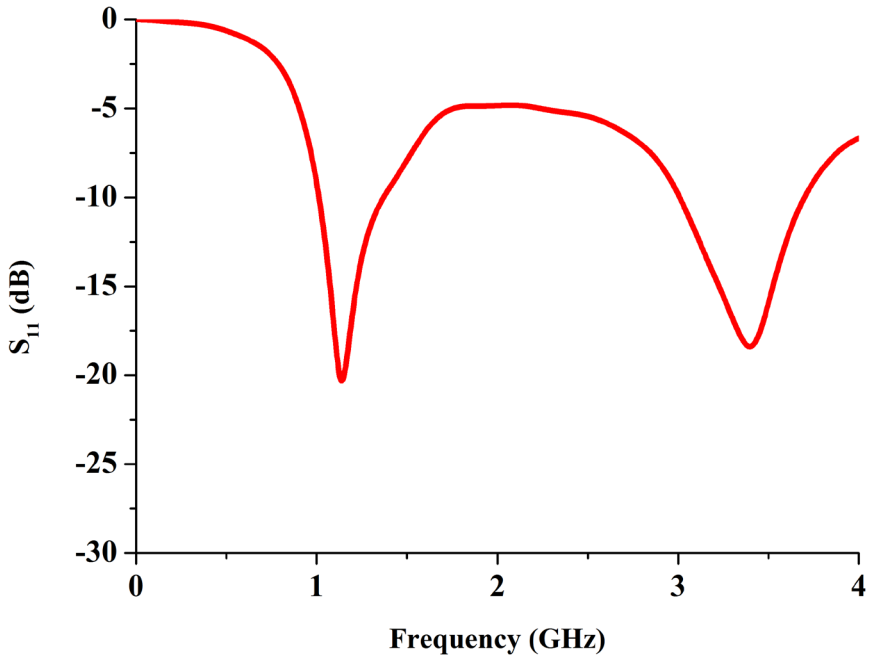

Fig. 4.6. S_{11} (dB) vs. frequency (GHz) for the water diameter of 8mm.

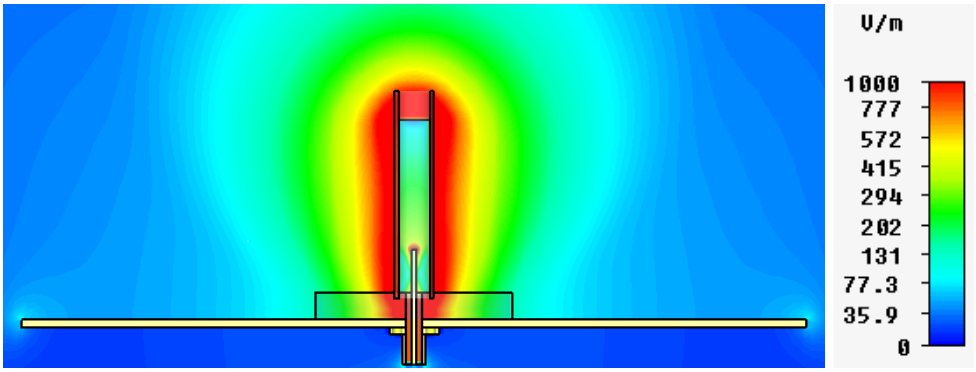

(a)

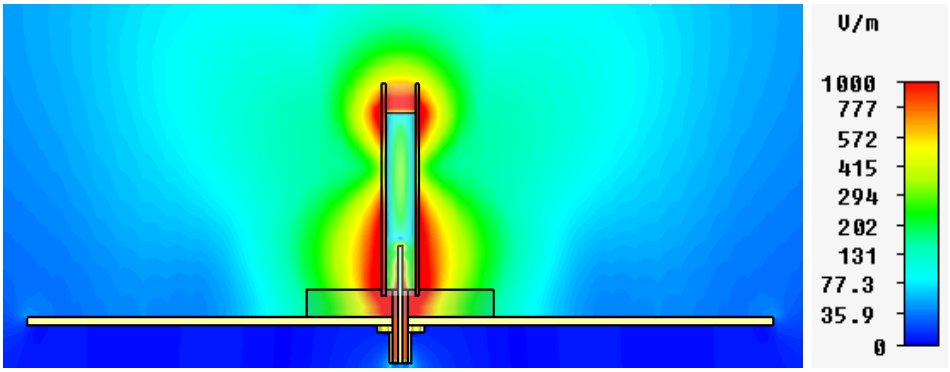

(b)

Fig. 4.7. E-field distribution of the water monopole. (a) 1.16 GHz. (b) 3.42 GHz.

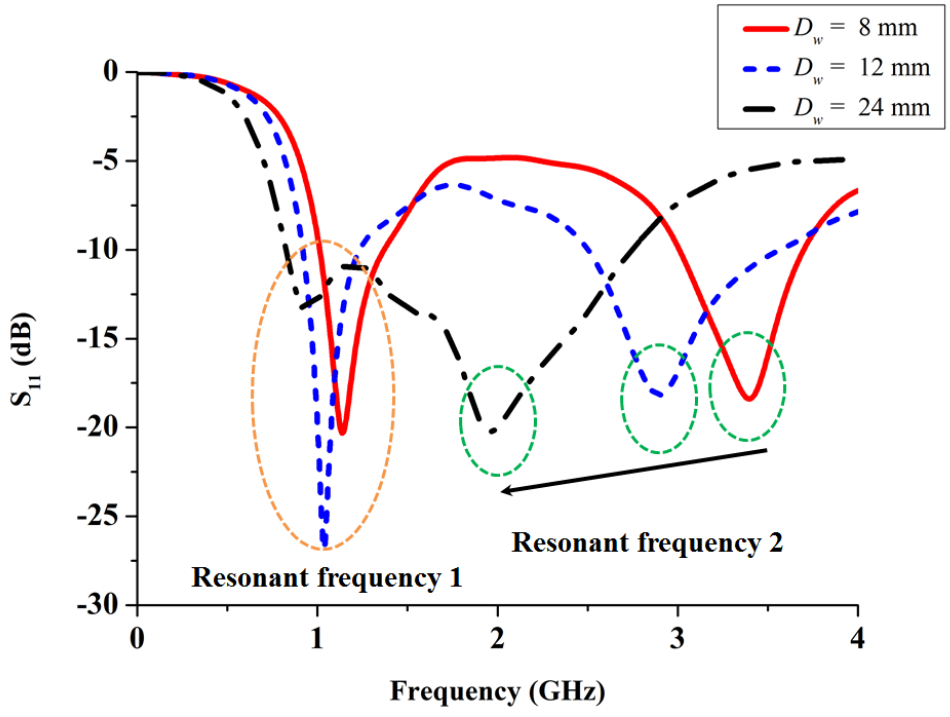

(a)

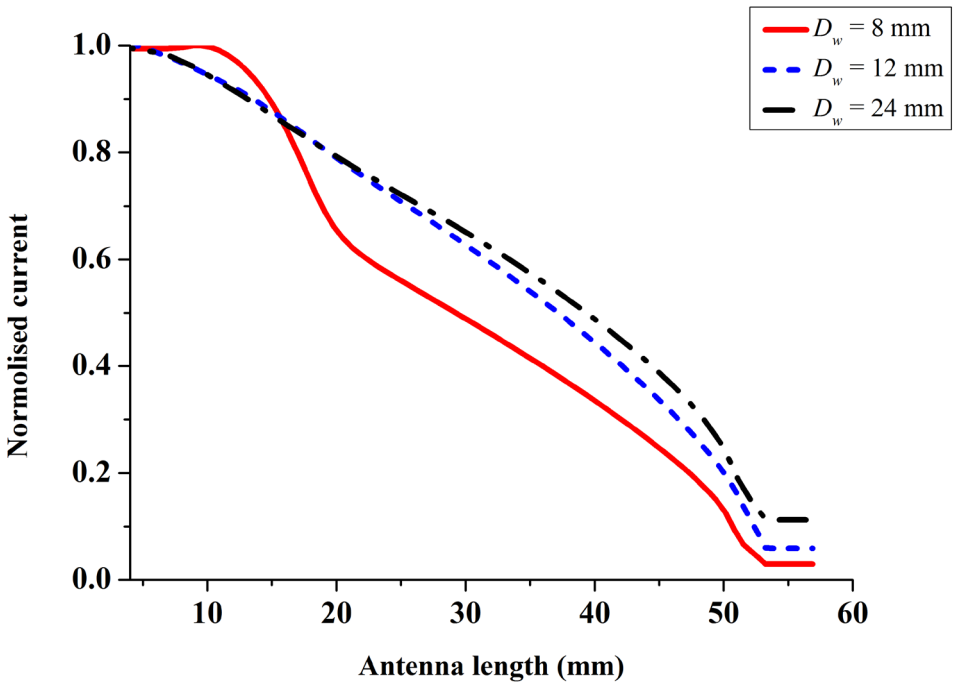

(b)

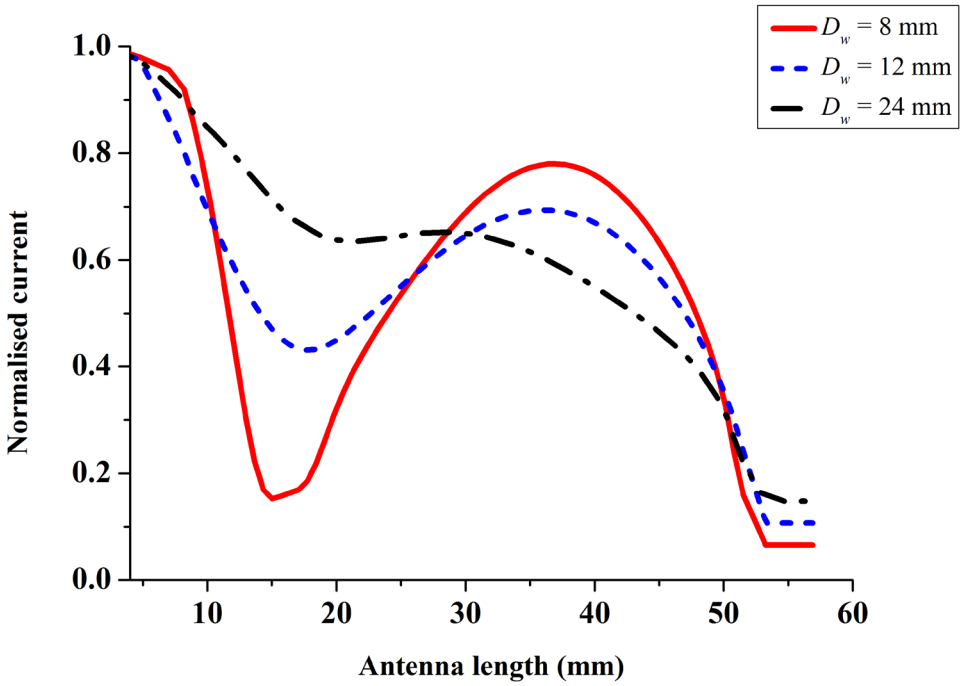

(c)

Fig. 4.8. (a) S_{11} (in dB) vs. frequency (GHz) for different water tube diameter. (b) The normalised current distribution of the first resonant frequency for different water tube diameter. (c) The normalised current distribution of the second resonant frequency for different water tube diameter.

When the water height H_w is changed from 35 to 75 mm, the simulated results are shown in Fig. 4.9, where we can see that the fractional bandwidth is not sensitive to the water height variation. However, the resonant frequency is reduced from 1.88 to 1.40 GHz (not 0.94 GHz as expected for a conductive antenna) and the radiation efficiency at the center frequency is decreased slightly from 58% to 47% (Fig. 4.9(b)). When the height of the water is doubled, the resonant frequency is not halved. The main reason is due to the loss of the material. When the wave propagates in the water, as shown in Fig. 4.9(c), for a fixed antenna length (100 mm), the current along the water antenna consumes more energy than a perfect conducting (PEC) antenna, thus the water antenna does not have the same linear relationship between the antenna length and the resonant frequency as the conducting antenna.

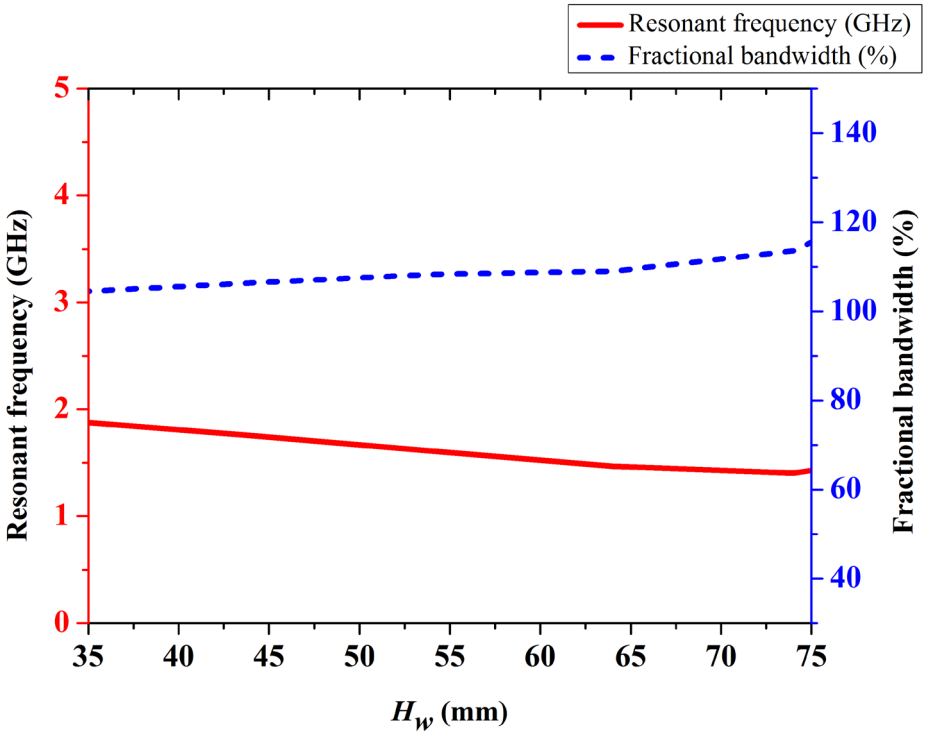

(a)

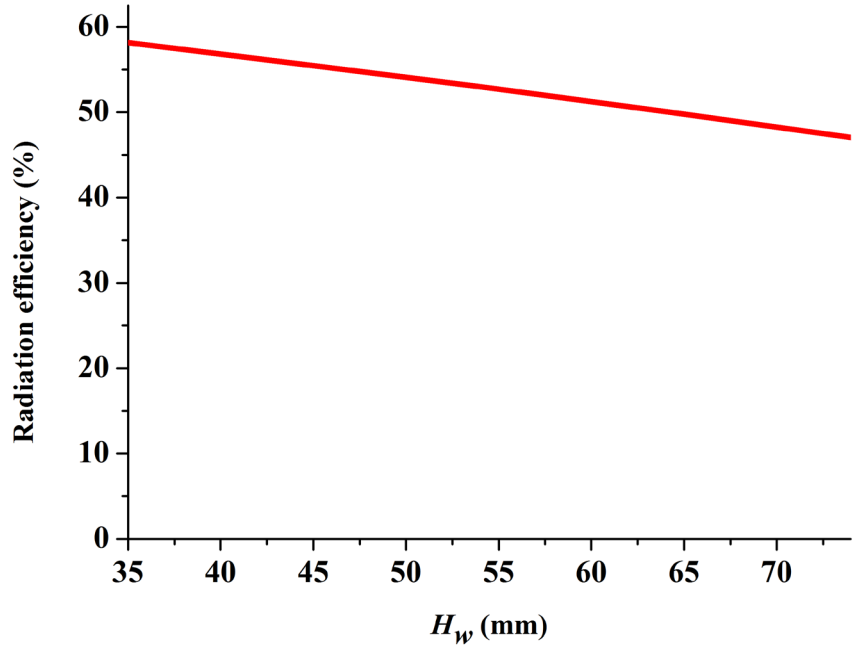

(b)

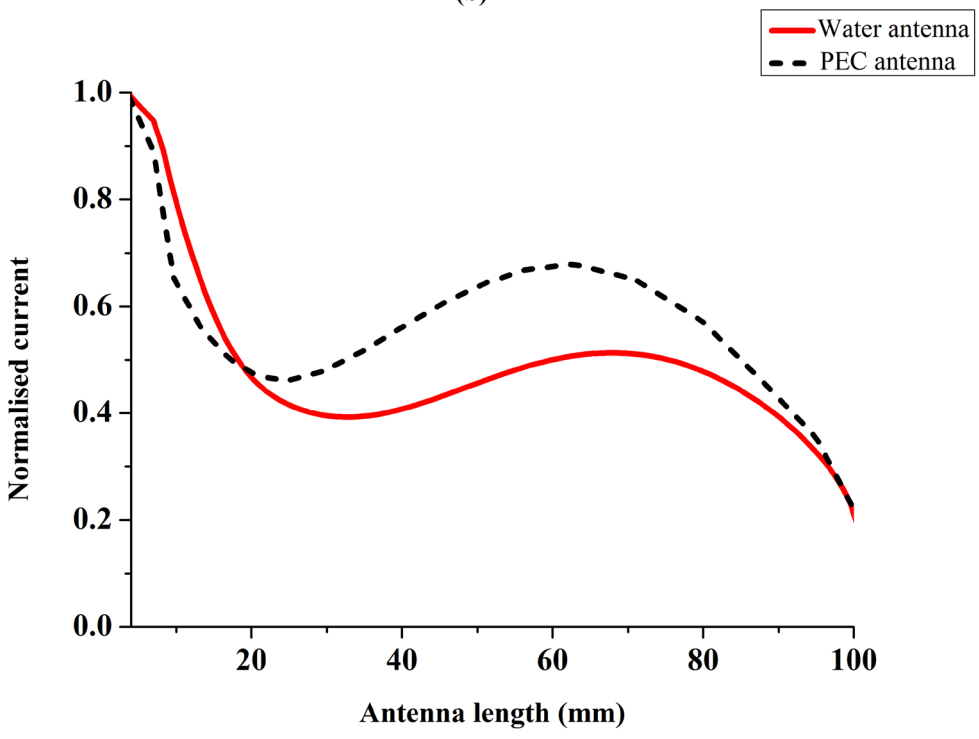

(c)

Fig. 4.9. (a) Resonant frequency (GHz) and fractional bandwidth (%) vs. water height H_w (mm). (b) Radiation efficiency (%) at the center frequency vs. water height H_w (mm). (c) Normalised current distribution comparison between the water antenna and the PEC antenna when the antenna length is 100 mm.

4.4.4 Ground Plane Effects

Now let us change the ground plane length L_g from 10 to 300 mm but keep other parameters the same as the reference antenna. The simulated results are shown in Fig. 4.10, which indicates the effects of the ground plane size on the resonant frequency and the fractional bandwidth. Initially, the increase of L_g results in a large decrease of the resonant frequency and significant increase of the fractional bandwidth. When L_g is larger than about 150 mm which is one wavelength of the resonant frequency at 2 GHz, the resonant frequency and fractional bandwidth become not sensitive to the ground plane size. As stated in [11], for the monopole structure, the ground plane length L_g should have at least one wavelength to minimise the radiated power leakage and the edge diffraction. Thus in our design, we have chosen the ground plane size to be 200 mm × 200 mm.

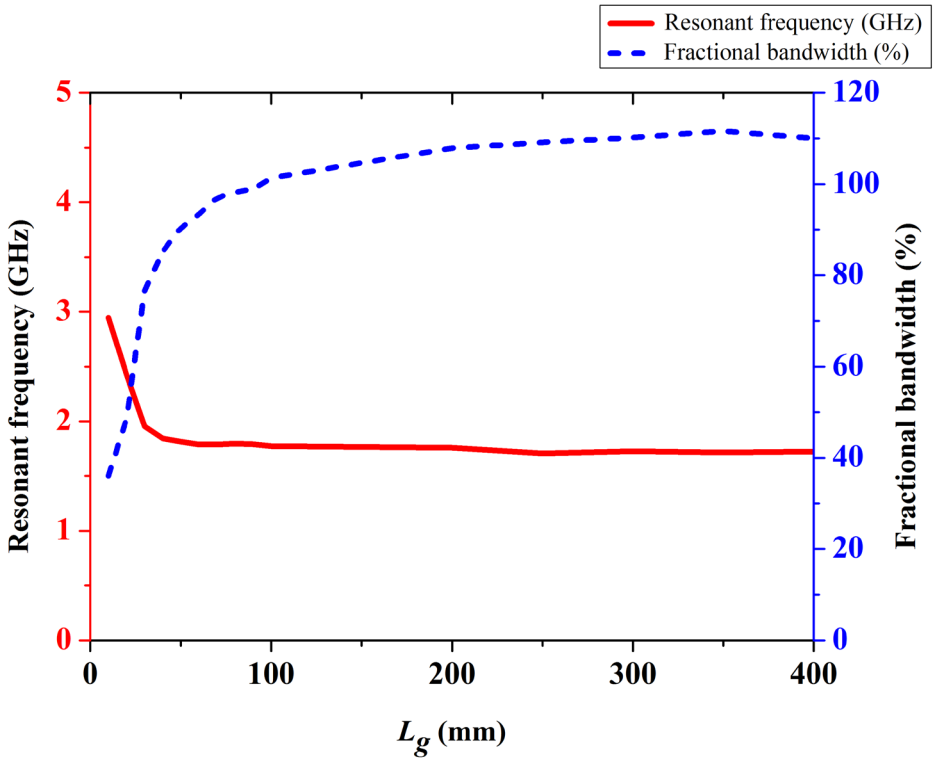

Fig. 4.10. Resonant frequency (GHz) and fractional bandwidth (%) vs. ground plane width L_g (mm).

The effects of various parameters on the water antenna performance have now been carefully examined. Some interesting conclusions can be summarised as follows:

1) The selection of the dielectric layer is very important in achieving broad bandwidth and high radiation efficiency. The water antenna has a much larger bandwidth, but smaller radiation efficiency than a PEC antenna. Increasing the relative permittivity of the dielectric layer will result in the decrease of the resonant frequency, the factional bandwidth and the radiation efficiency.

2) By increasing the thickness of the dielectric layer, the resonant frequency and the fractional bandwidth will first increase to the maximum value and then decrease. The radiation efficiency will increase with the dielectric layer thickness.
3) The position of the feeding pin and the probe length in the water are not an important factor when the water conductivity is greater than 4 S/m. But they become important when the water conductivity becomes very small.
4) The variation on the water tube diameter has great effects on the resonant frequency and the radiation efficiency. At certain water height and diameter, the fractional bandwidth and the radiation efficiency can be maximised.
5) The increase of the water height will reduce the resonant frequency, but not in a linear relationship.
6) The ground plane length L_g should be at least one resonant frequency wavelength in order to obtain a wide bandwidth.

4.5 Water Characteristics

In Chapter 3, the characteristics of salty water have already been carefully analysed, providing a solid foundation for salty water antenna design. Especially for water antenna designs, researchers care about the radiation efficiency of antennas, which is directly linked to the material loss determined by the imaginary part of the material properties. In this section, for our experimental investigation, salty water samples with different salinity are employed and their material properties are measured using a Keysight Dielectric Probe 85070 at room temperature (25˚C) and calculated using the equation of $tan\,\delta = \frac{\varepsilon''}{\varepsilon'} = \frac{\sigma}{\omega\varepsilon'}$ [11]. The sample salinity are 0.1 ppt, 0.5 ppt, 1 ppt, 5 ppt, 10 ppt, 50 ppt (0.0001 g/ml, 0.0005 g/ml, 0.001 g/ml, 0.005 g/ml, 0.01 g/ml, and 0.05 g/ml). Four sets of the results are shown in Fig. 4.11(a) - (b). The CST seawater model result (salinity 15 ppt) at 25˚C is also included in the figure as a reference for comparison. We can see that the measured results are comparable with the theoretical values. Besides the salinity, the water dielectric properties are also affected by temperature. The water sample with 0.01g/ml salinity is measured between 25˚C to 50˚C. The temperature is tuned by a hot plate as shown in Chapter 3 and three sets of the results are shown in Fig. 4.11(c) - (d). It is observed that from 0 to 3 GHz, at a given temperature, with the increase of the salinity, the relative permittivity decreases and the conductivity increases. For a given salinity, with the increase of the temperature, the relative permittivity decreases, however, the conductivity variation is less straightforward, it may decrease or increase with the frequency.

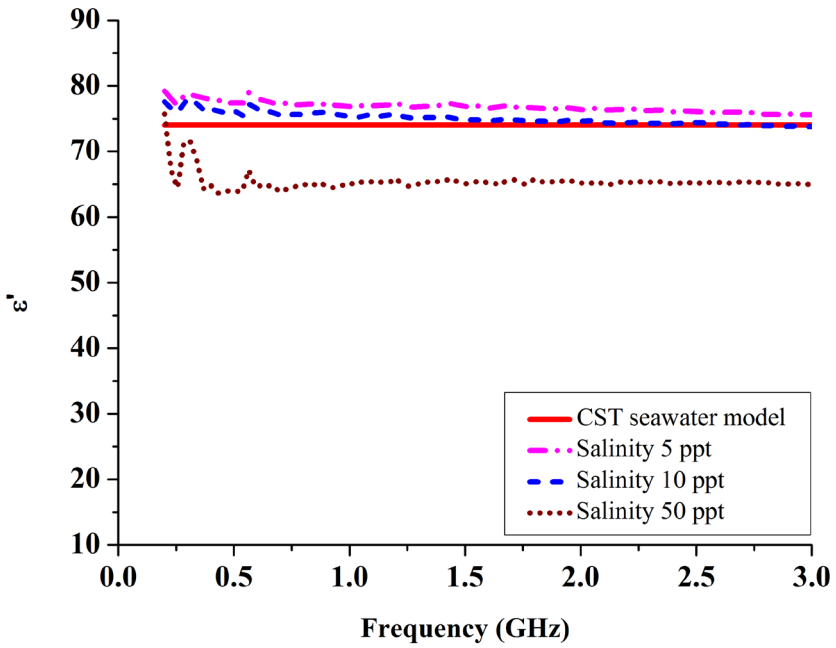
90
80
70
60
50
40
30
20
10
ε'
0.0
0.5
1.0
1.5
2.0
2.5
3.0
Frequency (GHz)
CST seawater model
Salinity 5 ppt
Salinity 10 ppt
Salinity 50 ppt

(a)

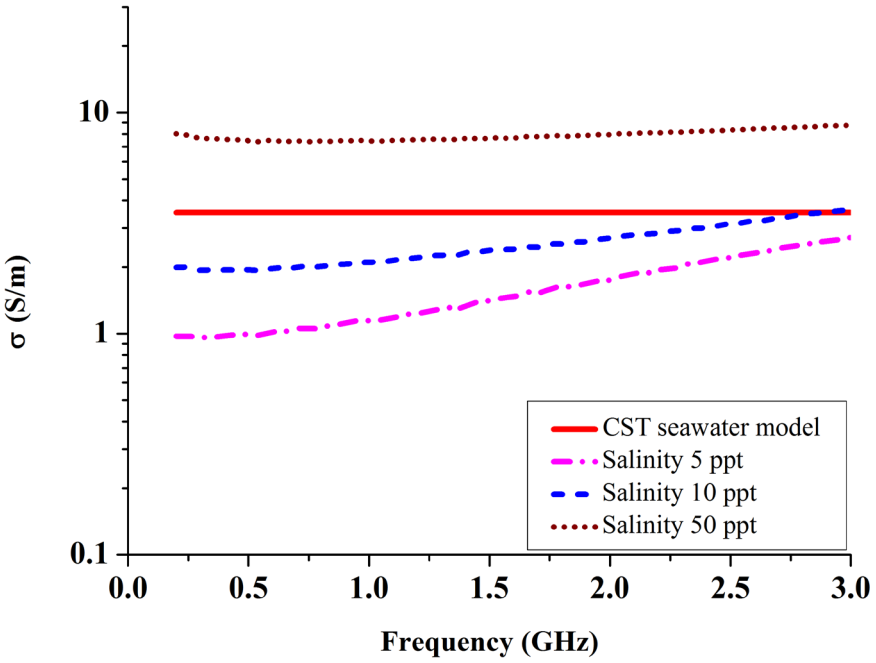
10
1
0.1
σ (S/m)
0.0
0.5
1.0
1.5
2.0
2.5
3.0
Frequency (GHz)
CST seawater model
Salinity 5 ppt
Salinity 10 ppt
Salinity 50 ppt

(b)

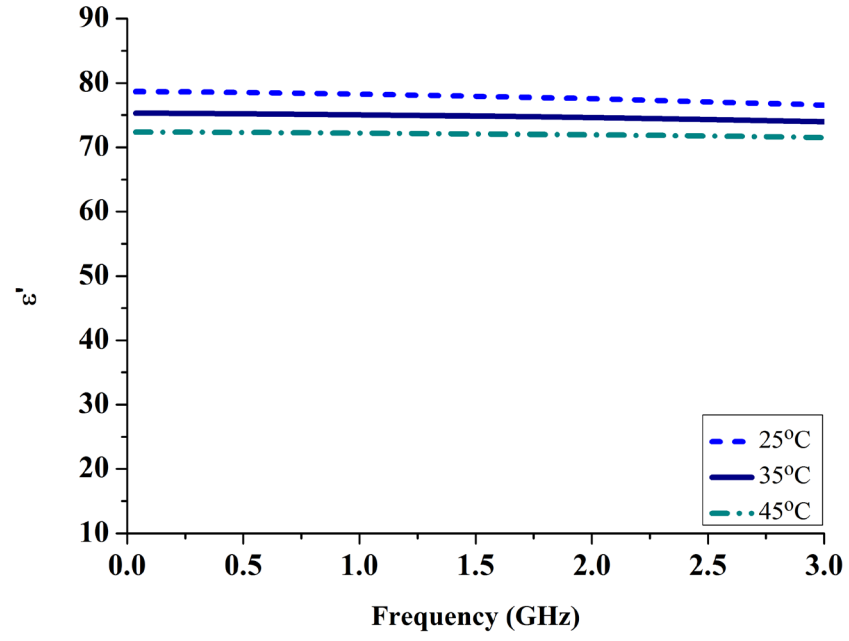

(c)

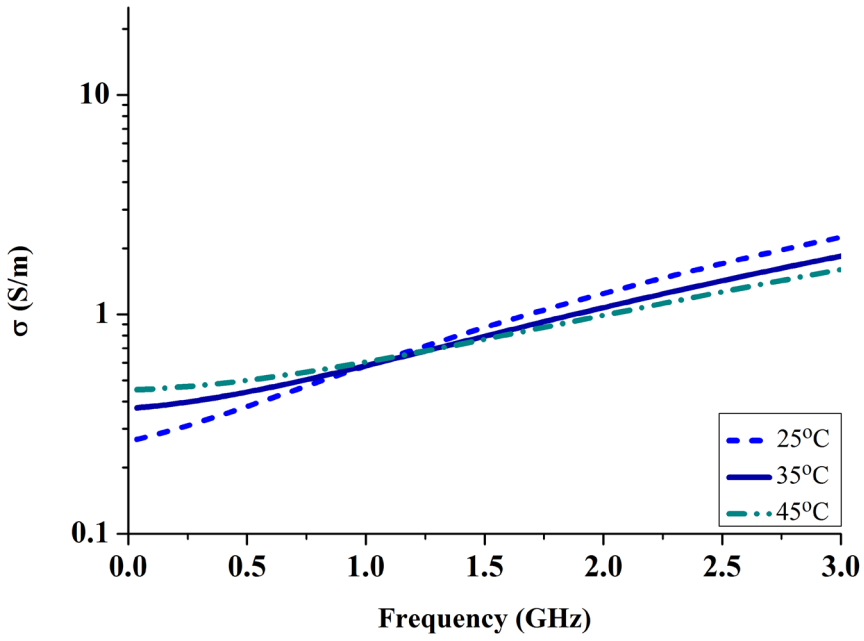

(d)

Fig. 4.11. (a) Measured relative permittivity of different salty water samples vs. frequency (GHz) at 25˚C. (b) Measured conductivity (S/m) of different salty water samples vs. frequency (GHz) at 25˚C. (c) Measured relative permittivity of the water sample with salinity 10 ppt vs. frequency (GHz) at different temperatures. (d) Measured conductivity (S/m) of the water sample with salinity 10 ppt vs. frequency (GHz) at different temperatures.

4.6 Monopole Water Antenna Measurements

From the extensive parametric study, it is clear that the water antenna characteristics are affected by a number of parameters and are much more complex than a metal antenna. If designed well, a water antenna with a broad bandwidth and acceptable radiation efficiency can be obtained. In the framework of this study, a first Paxolin (a phenolic paper laminate, relative permittivity around 5.5) based antenna prototype has been manufactured to corroborate simulated results. It has been presented in [9] and in order to further improve the antenna performance, based on the knowledge gained, a Teflon (with relative permittivity 2.1) based monopole water antenna is fabricated by integrating a circular Teflon layer between the water tube and the copper ground [10], the prototype antenna is shown in Fig. 4.12, the optimal parameters are L_g = 200 mm, H_g = 2 mm, H_d = 7 mm, R_d = 25 mm, D_w = 25 mm, H_w = 44 mm, L_p = 8.9 mm, L_s = 0 mm, H_t = 100 mm and the water salt salinity = 10 ppt or 0.01 g/ml (room temperature at 25˚C). The efficiency is measured in a reverberation chamber [12] and realised gain is measured in an anechoic chamber [11].

Fig. 4.12. Prototype of the seawater antenna and samples.

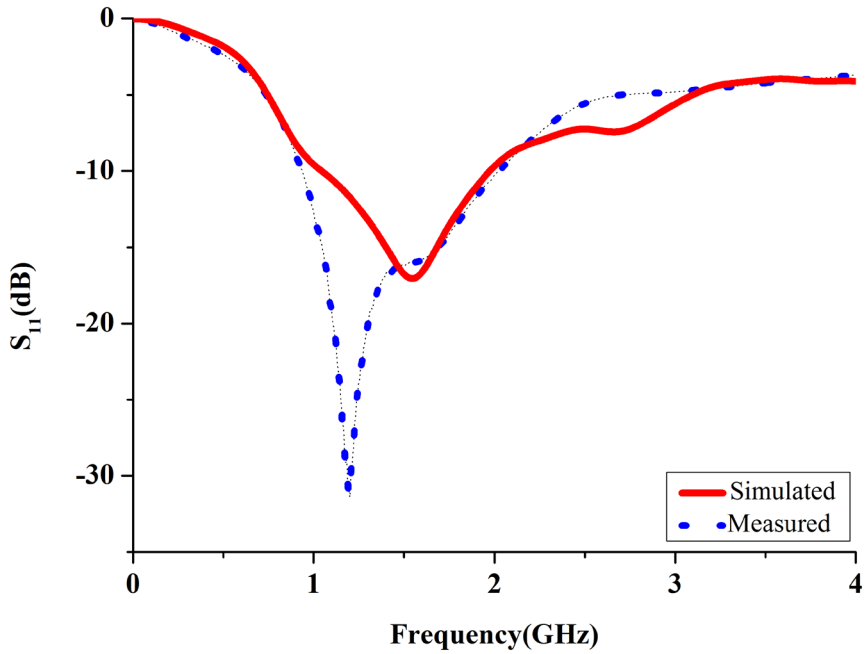
0
-10
-20
-30
S_{11}(dB)
0
1
2
3
4
Frequency(GHz)
Simulated
Measured

(a)

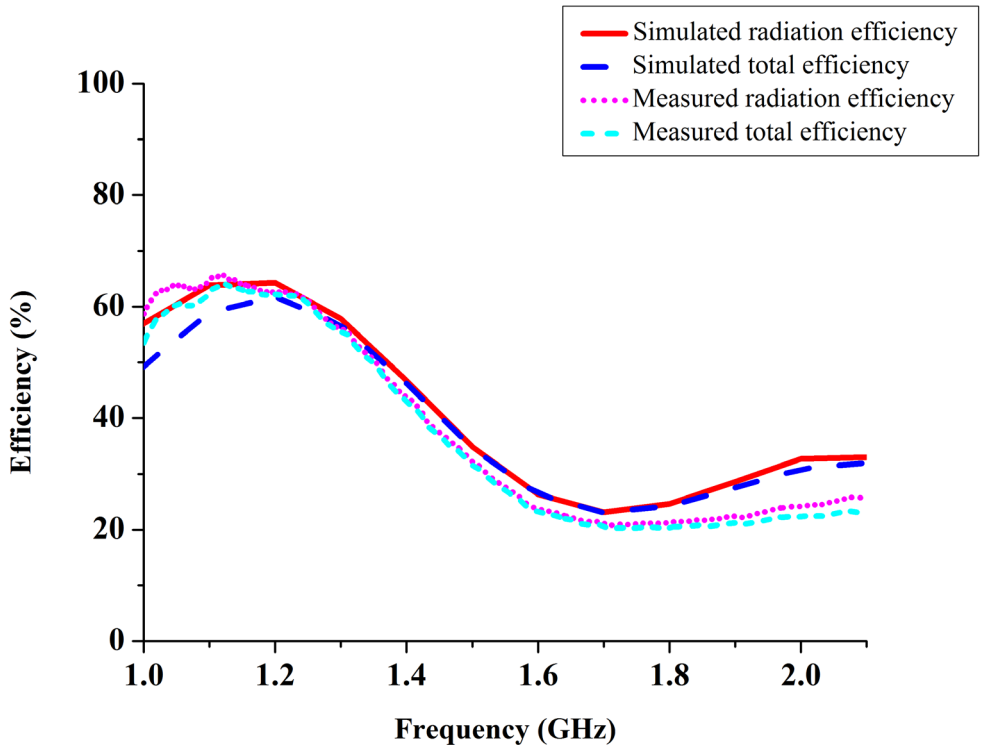
Simulated radiation efficiency
Simulated total efficiency
Measured radiation efficiency
Measured total efficiency
100
80
60
40
20
0
Efficiency (%)
1.0
1.2
1.4
1.6
1.8
2.0
Frequency (GHz)

(b)

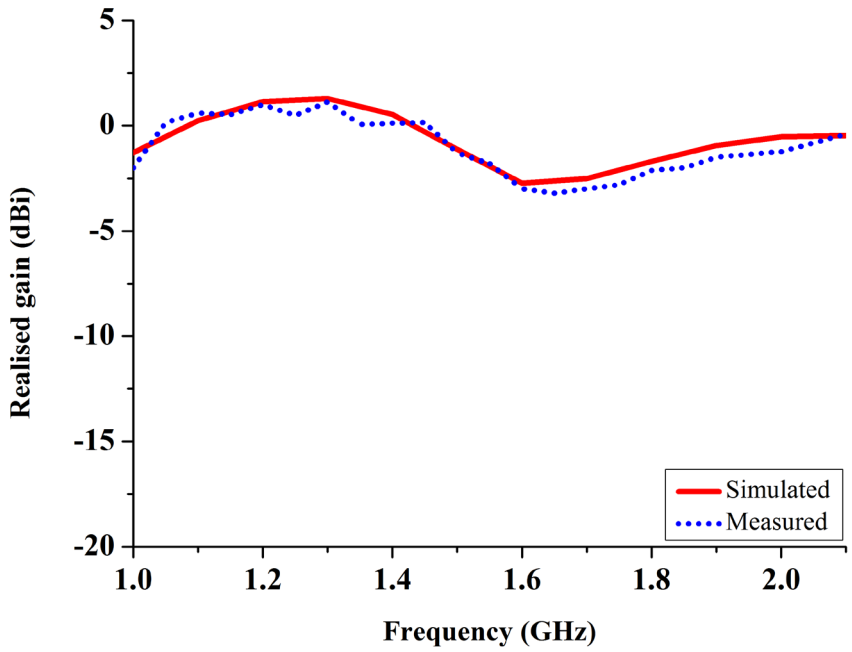

(c)

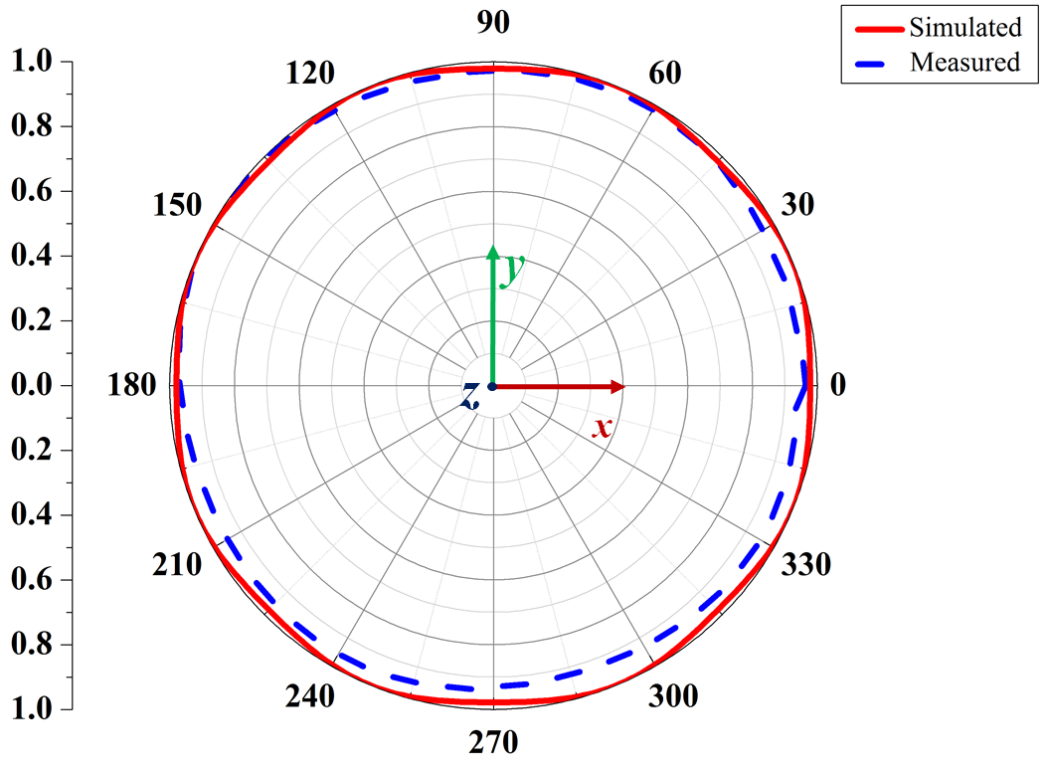

(d)

Fig. 4.13. Measured and simulated result comparison. (a) S_{11} (in dB). (b) Radiation and total efficiency. (c) Realised gain (maximum gain). (d) Xoy plane radiation pattern at 1.1 GHz .

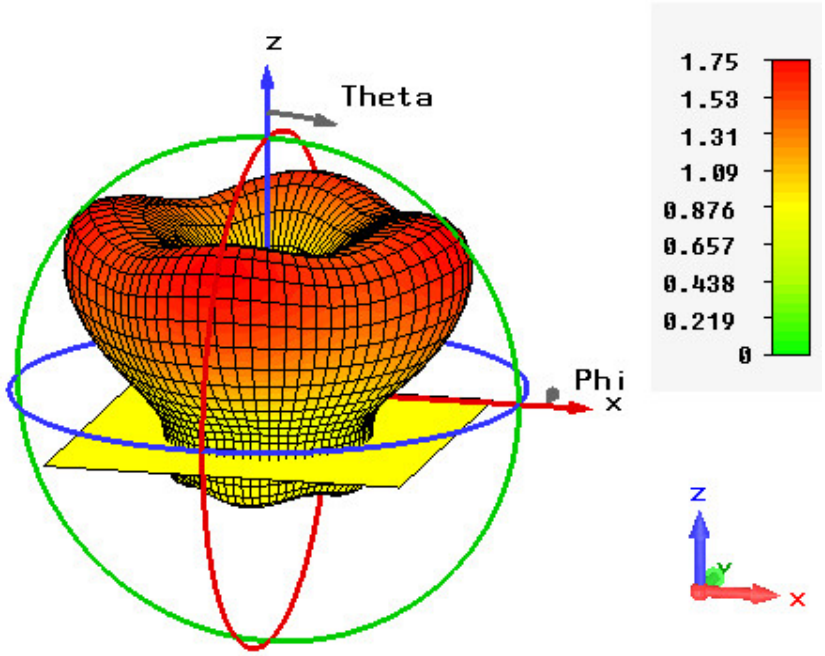

Fig. 4.14. 3D radiation pattern of the monopole water antenna at 1.1 GHz.

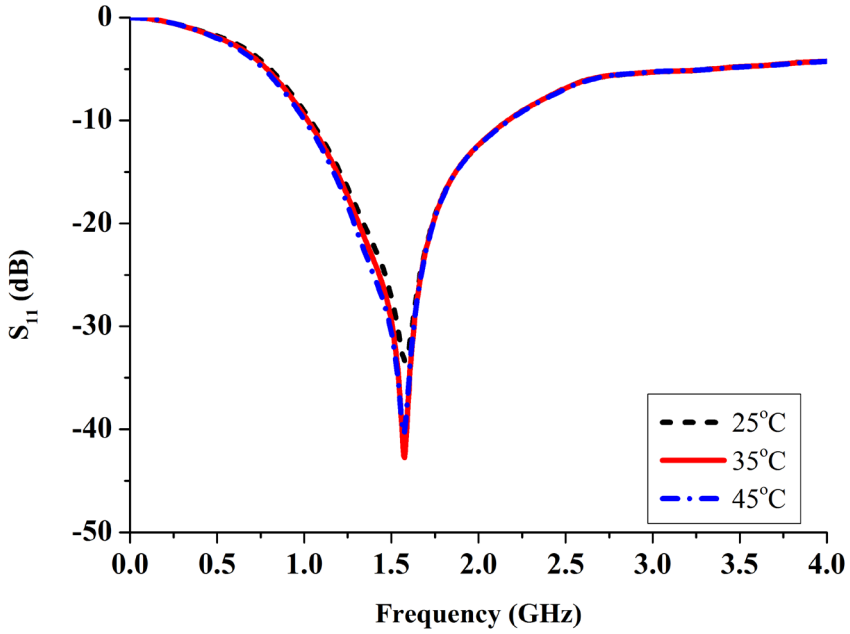

(a)

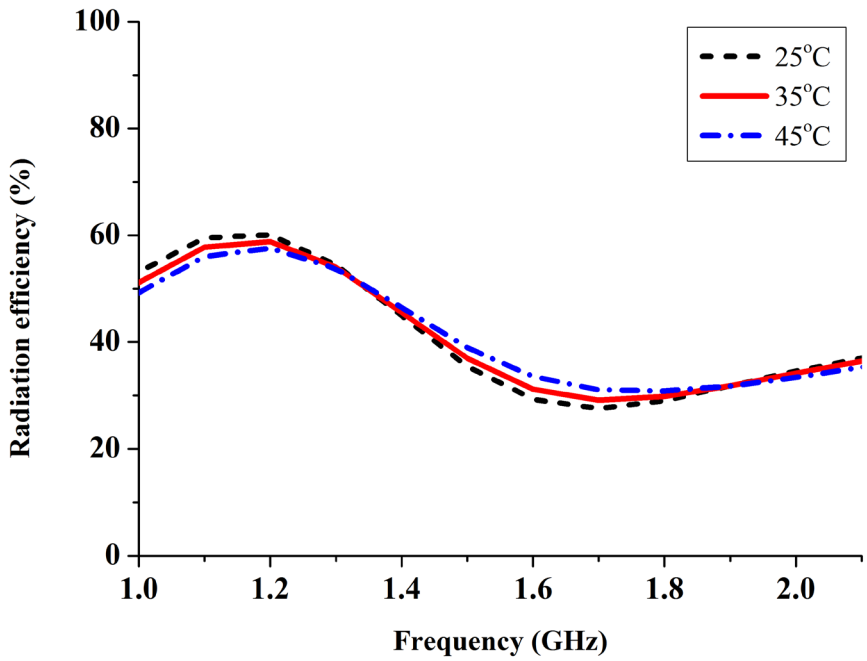

(b)

Fig. 4.15. Performance comparison of the proposed antenna for different temperatures. (a) Simulated S_{11} (in dB). (b) Simulated radiation efficiency.

The simulated and measured results are compared in terms of the S_{11}, efficiency, realised gain (maximum gain) and xoy plane radiation pattern at 1.1 GHz, as shown in Fig. 4.13. It is evident that the Teflon base water antenna has a very broad bandwidth: from 1 to 2.1 GHz for S_{11} < -10 dB (the fractional bandwidth > 70%). Very good agreements between the simulated and measured efficiency and realised gain are observed.

As water will leak from the water tube, only the xoy plane radiation pattern at 1.1 GHz was measured. As the cross-polarisation (X-pol) (the orthogonal radiation of the desired polarization of wave) of monopole antenna is very small, only the co-polarisation (Co-pol) (the desired polarization of the wave to be radiated by the antenna) is shown. To allow readers to fully understand the radiation of the monopole water antenna, the simulated 3D pattern is shown in Fig. 4. 14.

Since the complex permittivity of salty water varies with the temperature, the antenna performance will change correspondingly. To study the temperature effects on the antenna performance, the simulated S_{11} and radiation efficiency over different temperatures are compared as shown in Fig. 4. 15(a) and (b), where the measured permittivity data at these temperatures (25°C, 35°C and 45°C) were used in the simulations.

It is observed that when the temperature increases from 25°C to 45°C, the S_{11} curves are almost the same; while the radiation efficiency is slightly decreased at lower frequencies, which agrees with the conductivity plot in Fig. 4.11(d) (the conductivity at 45°C is smaller than the conductivity at 25°C when the frequency is lower than 1GHz). Overall, the simulated S_{11} and radiation efficiency have very similar shapes.

4.7 Summary

In this chapter, a monopole water antenna with a dielectric layer has been thoroughly investigated. The relationship between conductivity and antenna radiation efficiency has been studied. An extensive parametric study has been carefully carried out. The dependence of behaviour on various parameters has been explored.

The developed Teflon-based prototype antenna has a broad bandwidth (the fractional bandwidth > 70% for S_{11} < -10 dB) and exhibits good performance. Measurements have been conducted and the results agree well with the simulations. It has been demonstrated that the monopole water antenna with a dielectric layer is superior to the conventional antenna in the following aspects: 1) a broad bandwidth with reasonable efficiency, 2) low cost, 3) transparent, 4) frequency and conductivity reconfigurable characteristics.

This salty water antenna design is an example of a water antenna working as a conducting antenna. These characteristics make this antenna potentially very promising for wireless communications on the sea. The knowledge gained in this investigation is extremely valuable for the future research into more practical water antennas and it has a potential to be made as a broadband, cost effective, transparent, tunable or reconfigurable antenna.

4.8 References

[1] A. Petosa, A. Ittipiboon, Y. M. M. Antar, D. Roscoe, “Recent advances in dielectric-resonator antenna technology,” IEEE Antennas and Propag. Mag., vol. 40, no. 3, pp. 35-48, 1998.

[2] R. K. Mongia, P. Bhartia, “Dielectric resonator antennas - a review and general design relations for resonant frequency and bandwidth,” Int. J. Microw. Millim.-Wave Comput.-Aided Eng., vol. 4, no. 3, pp. 230-247, 1994.

[3] S. Long, M. McAllister, S. Liang, "The resonant cylindrical dielectric cavity antenna," IEEE Trans. Antennas Propag., vol. 31, no. 3, pp. 406-412, 1983.

[4] M. W. McAllister, S. A. Long, G. L. Conway, "Rectangular dielectric resonator antenna," Electron. Lett., vol. 19, no. 6, pp. 218-219, 1983.

[5] A. Ittipiboon, R. K. Mongia, Y. M. M. Antar, P. Bhartia and M. Cuhaci, "Aperture fed rectangular and triangular dielectric resonators for use as magnetic dipole antennas," Electron. Lett., vol. 29, no. 23, pp. 2001-2002, 1993.

[6] K. W. Leung, E. H. Lim, X. S. Fang, "Dielectric resonator antennas: from the basic to the aesthetic," in Proc. of the IEEE , vol.100, no.7, pp. 2181-2193, 2012

[7] K. S. Ryu and A. A. Kishk, "UWB dielectric resonator antenna having consistent omnidirectional pattern and low cross-polarization characteristics," IEEE Transactions on Antennas and Propag., vol. 59, pp. 1403-1408, 2011.

[8] W. Ellison, A. Balana, G. Delbos, K. Lamkaouchi, L. Eymard, C. Guillou, C. Prigent, "New permittivity measurements of seawater," Radio Sci., vol. 33, no. 3, pp. 639-648, 1998.

[9] L. Xing, Y. Huang, S. Alja'afreh, S. J. Boyes, "A monopole water antenna," in Proc. Loughborough Antennas Propag. Conf., 2012, pp. 1-4.

[10] L. Xing, Y. Huang, Y. Shen, S. Alja'afreh, Q. Xu and R. Alrawashdeh, "Further investigation on water antennas," IET Microw., Antennas Propag., vol. 9, no. 8, pp. 735-741, 2015.

[11] Y. Huang, and K. Boyle, *Antennas: from theory to practice*, John Wiley & Sons Ltd, 2008.

[12] S. J. Boyes, P. J. Soh, Y. Huang, G. A. E. Vandenbosch and N. Khiabani, "Measurement and performance of textile antenna efficiency on a human body in a reverberation chamber," IEEE Trans. Antennas Propag., vol. 61, no. 2, pp. 871-881, 2013.

Chapter 5: Broadband Hybrid Water Antenna Designs for Hand-Portable Applications

5.1 Introduction

In previous water antenna designs reported in the literature, only the radiator of water DRAs has been used which results in either low efficiency or narrow bandwidths. To overcome this problem, the hybrid resonator antenna technique (HRAT) could be used as a promising solution [1]. The hybrid DRA is the combination of two different types of radiators, and has two radiating bands: one from the DR, and the other due to the feeding structure. The resonance of the DRA is combined with that of the feeding structure, covering the required frequency band. Wideband DRAs taking advantage of this kind of hybrid structures have been reported in designs [2-5], including a dual-band circular disk DRA [2], a pawn-shaped DR loaded hybrid monopole antenna [3], a monopole antenna with an anisotropic metamaterial coating [4], and a monopole loaded rectangular DRA [5].

In the designs proposed in this chapter, the resonance of the feeding probe is utilised and it improves the radiation efficiency of the water antenna. This hybrid technique has previously been employed in wideband DRAs, but here it is used for a liquid antenna which has a new feeding structure.

The difficulties in using the resonance of the probe in a solid DRA are mainly composed of two aspects: 1) the probe length is limited by the DRA size; 2) the matching is sometimes difficult to achieve [6]. The liquidity and transparency of water allow a complex feeding structure (such as the L-shaped, F-shaped probes described in this chapter) to be placed and easily tuned inside water, which is difficult and expensive to realise in conventional solid dielectric materials such as ceramics.

In this chapter, three wideband, hybrid water antennas are proposed to cover the frequency band from 470 to 862 MHz, which is the typical frequency band for DVB-H (digital video broadcasting for hand-held devices) [7]. These three proposed hybrid water antennas are all based on the same physical insights, however, the performance of the antenna is improved in terms of small size and wide bandwidth, exhibiting the design variety of water antennas. In comparison with other designs for this band, the main contributions of our designs are observed in five aspects: 1) without using any active components and extra circuit, the antenna achieves a very wide bandwidth with a low profile (10 mm); 2) the hybrid antenna structure combines a monopole antenna and a metal coated DRA to produce a wideband response; 3) an efficient probe structure is placed inside the water which is difficult for

conventional ceramic dielectric materials; 4) the water DRA is coated with metal patches to reduce the antenna size; 5) the antenna is optically transparent. The design procedure mainly includes two parts: firstly, a DRA which is formed by a metal coated water DR is designed to work at the upper frequency band; then, a monopole antenna, which is the feeding probe, is designed to cover the lower band of interest. For the U-shaped hybrid water antenna design and the F-shaped probe fed hybrid water antenna design, a third step is required, which is a parasitic and a conducting stub are introduced to improve the impedance matching, respectively. The compactness and bandwidth can be adjusted by tuning the parameters of the hybrid structure. The antenna is studied using both the simulation and measurement approaches. CST Microwave Studio is employed for the numerical simulation.

The chapter is organised as follows:

In section 5.2, the rectangular DRA resonant mode theory is reviewed and investigated. In section 5.3, the pure water characteristics used in hybrid water antenna designs are evaluated and compared with the CST Debye model data. Thermal characteristics of pure water are studied. In section 5.4 to 5.6, three hybrid water antennas are proposed; the physical insights behind the designs are discussed. Comprehensive parametric studies are performed. The effects of each part of the antenna are carefully examined. Three water antennas prototypes with optimised parameters are fabricated. Experiments are conducted and the results are compared with simulation results. In section 5.7, a summary is presented to review all findings.

5.2 Rectangular Dielectric Resonator Antenna

The first systematic theoretical and experimental study of a specific dielectric resonator antenna configuration was carried out by Long *et al* in the 1980s, who examined the characteristics of DRAs of different shapes [8]. Their research demonstrated that DRAs could be considered to be attractive alternatives to traditional antennas, such as microstrip patches, monopoles and dipoles [8]. Since then, a considerable amount of work has been carried out on studies of this type of antennas and numerous papers have been published on this subject. Among the existing DRA designs, three basic shapes, namely hemispherical, cylindrical and rectangular are the most commonly used [9]. The hemispherical DRA is of limited practical value due to the difficulty involved in fabrication and the lack of any degree of freedom in choosing the design parameters. For a material with a given dielectric constant, the radius of the sphere will determine the resonant frequency and Q factor, leaving the designer no control of the antenna size or its impedance bandwidth [9]. The cylindrical DRA offers greater design flexibility, where both the dielectric constant and the ratio of radius/height

control the resonant frequency and Q factor. Various modes can be excited, resulting in different radiation patterns. The rectangular DRA offers the greatest design flexibility of the three basic shapes, having two degrees of freedom (length/width and depth/width) [9]. For a given dielectric constant, several aspect ratios can be chosen to resonate at the same frequency, while offering different Q factors [9, 10].

The isolated rectangular DRA and coordinate system has been shown in Fig. 5.1. The rectangular DR has three independent dimensions, i.e. its length b in the x direction, its height d in the y direction and its width a in the z direction. By using a combination of magnetic wall model (MWM) and dielectric waveguide model (DWM), perfect magnetic walls are assumed along the four surfaces parallel to the direction of propagation in the DR, while the tangential components of the electric and magnetic fields are assumed to be continuous across the two surfaces, perpendicular to the direction of propagation [9]. The modes of a rectangular DRA can be divided into TE and TM modes. The lowest order TE mode (also known as $TE_{11\delta}$ mode) has been employed in various circuit applications. In this section, the TE mode is discussed. Regarding to the rectangular dielectric waveguide model used by Marcatili [11], if the dimensions of DRA are $b > d > a$, the modes in the order of increasing resonant frequency are $TE^{z}_{111}, TE^{y}_{111}, TE^{x}_{111}$. These modes radiate like x-, y- and z-directed magnetic dipoles respectively. Since the analysis of $TE^{z}_{111}, TE^{y}_{111}, TE^{x}_{111}$ mode is similar, only the case of the TE^{z}_{111} mode is discussed.

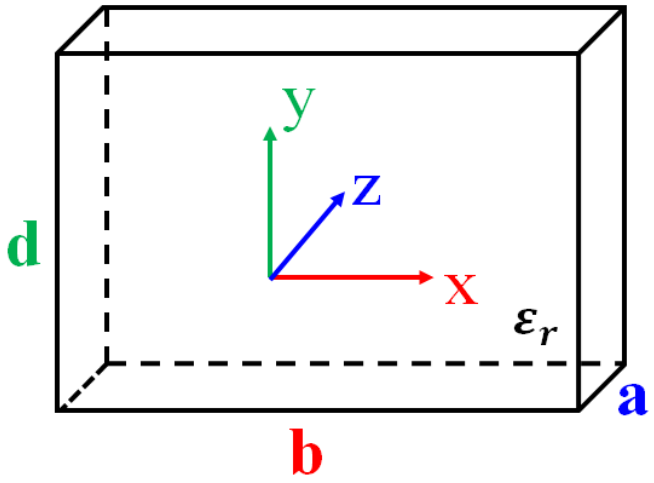

Fig. 5.1. Isolated rectangular DRA.

The lowest mode TE^{z}_{111} mode and its dimensions can be estimated by following equations [12], and the detailed derivation process is illustrated in Appendix A1:

$$k_z \tan(k_z a/2) = \sqrt{(\varepsilon_r - 1)k_0^2 - k_z^2} \tag{5.1}$$

$$k_x^2 + k_y^2 + k_z^2 = \varepsilon_r k_0^2 \tag{5.2}$$

$$k_x = \frac{\pi}{b},\ k_y = \frac{\pi}{d} \tag{5.3}$$

where k_x and k_y, are the wavenumbers in x and y directions, respectively. k_0 denotes the free space wavenumber, z direction is the wave propagating direction.

The radiation Q factor of the DRA is determined using [12, 13]:

$$Q = \frac{2\omega W_e}{P_{rad}} \tag{5.4}$$

where W_e and P_{rad} are the stored energy and radiated power, respectively.

$$W_e = \frac{\varepsilon_0 \varepsilon_r abd}{32}(1 + \frac{sin(k_z a)}{k_z a})(k_x^2 + k_y^2) \tag{5.5}$$

$$P_{rad} = 10k_0^4\ (|\overrightarrow{p_m}|)^2 \tag{5.6}$$

where $\overrightarrow{p_m}$ is the magnetic dipole moment of the DRA [12].

$$\overrightarrow{p_m} = \frac{1}{2}\int_V \vec{R} \times \overrightarrow{J_p}\ \ dV \tag{5.7}$$

$\overrightarrow{J_p}$ denotes the volume polarisation current density. $\vec{R}$ is a vector from origin [13].

It is known that a homogeneous dielectric body of dielectric constant ε_r placed in free space radiates like a volume electric current of density $\overrightarrow{J_p}$ [13].

$$\overrightarrow{J_p} = j\omega\varepsilon_0(\varepsilon_r - 1)\overrightarrow{E} \tag{5.8}$$

where $\overrightarrow{E}$ is the electric field intensity inside the resonator

Substituting the values of $\overrightarrow{J_p}$ in Eqn. (5.7) with Eqn. (5.8), the following closed form expression for $\overrightarrow{p_m}$ is obtained [13].

$$\overrightarrow{p_m} = \frac{j8\omega\varepsilon_0(\varepsilon_r - 1)}{k_x k_y k_z} sin(k_z a/2)\overrightarrow{a_z} \tag{5.9}$$

5.3 Dielectric Material Consideration

The dielectric material choice is one of the most important parameters in the DRA design, and has a significant influence on antenna characteristics such as impedance bandwidth, Q factor, resonant frequency and radiation efficiency. The dielectric material should be chosen according to different applications. If a wide bandwidth application is targeted, a relatively low permittivity material is preferred, the antenna size will be large or the efficiency of the antenna will be low. If the designer targets an ultra-miniature antenna, a high permittivity material will be of interest. However, the Q factor will be high, thus the bandwidth of the antenna will be narrow. Therefore, there exists a trade-off between the bandwidth and the Q factor. In this chapter, the idea of effective relative permittivity is employed. By mixing a high permittivity material (water) with a low permittivity material (holder, made of acrylic plastic), the effective permittivity of the mixture will be reduced to improve the bandwidth [14]. By tuning the height ratio of the water layer to water holder, different values of effective permittivity can be obtained, which is a smart way to obtain any desired permittivity. The loss of the water and holder mixture will be smaller than an equivalent water DRA of the same size.

The water discussed in this chapter is pure water. Its electrical properties are a function of temperature and frequency [15]. Sometimes, water is not considered as a good dielectric, as the loss normally increases with the frequency, especially at frequencies higher than 1 GHz. In this chapter, in order to have a compact size and acceptable radiation efficiency, the water antenna is designed to work below 1 GHz, as the water loss is not significant across the band. The properties of pure water were measured by using a Keysight Dielectric Probe 85070 at room temperature (25˚C) and the results are compared with CST Debye model as shown in Fig. 5.2. A very good agreement is obtained. The real part of the permittivity ε' is not sensitive to the frequency of interest. The temperature effects on its properties are also studied as shown in Fig. 5.3. The real part of the permittivity $\varepsilon'$and loss tangent $tan\delta$ decrease, as the temperature of the pure water increases, agreeing with the conclusions in [16].

By considering commercial applications such as a tablet PC or portable TV handset, the working temperature should be in the range of 0 - 85^{o}C (commercial grade). The antifreeze propylene glycol (PG) is added into the water to lower the freezing point. The freezing point of 10% PG ($Volume_{PG}$: $Volume_{water}$ = 10% : 90%) is around -6^{o}C. The water with 10% PG under different temperatures were measured and the results are given in Fig. 5.4. It is observed that the dielectric properties of the pure water and water with 10% PG are very similar. The loss of the 10% PG is slightly higher than the pure water, but not much. Water with PG can be a promising alternative to the pure water in some cold climates.

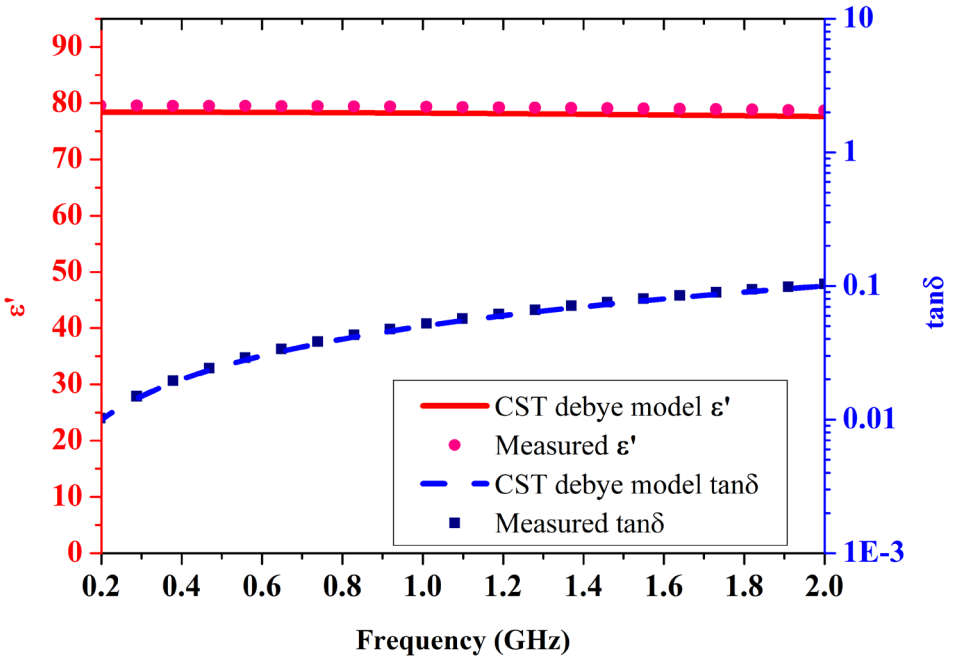

Fig. 5.2. The real part of permittivity and loss tangent of the pure water at 25°C from the measurement and CST Debye model.

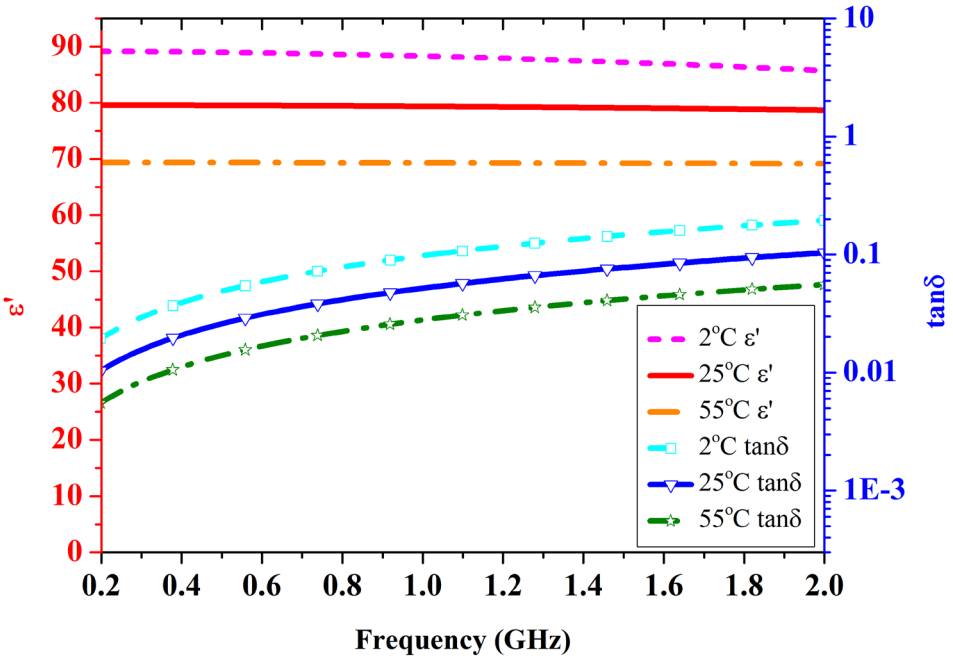

Fig. 5.3. Measured real part of the permittivity and loss tangent of the pure water at different temperatures over the frequency of interest.

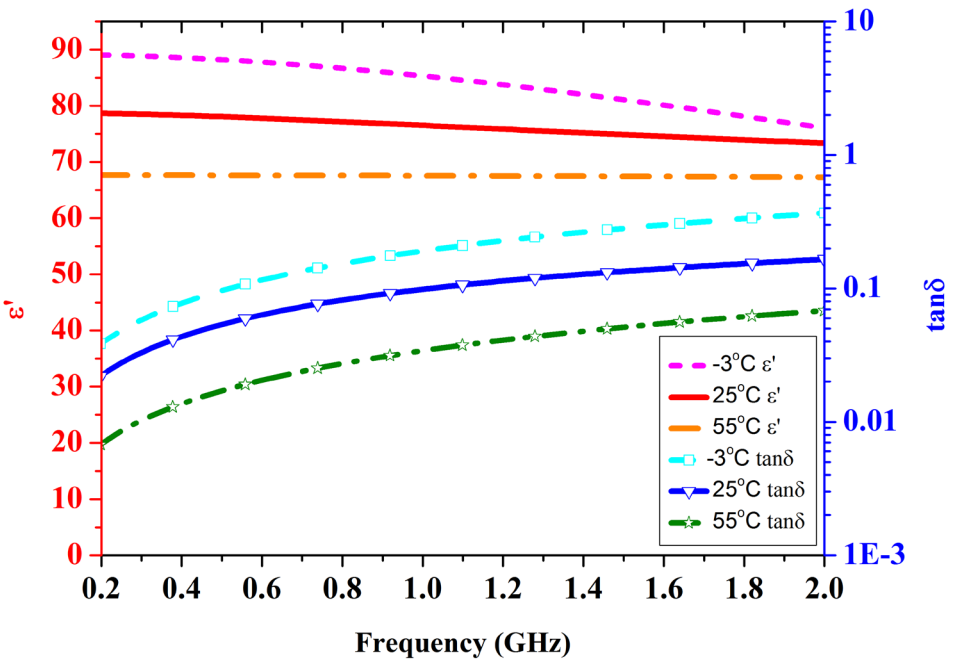

Fig. 5.4. Measured real part of the permittivity and loss tangent of the water with 10% PG at different temperatures over the frequency of interest.

5.4 Rectangular Hybrid Water Antenna Design

In this section, a wideband, hybrid rectangular water antenna is designed and optimised. The hybrid structure combines a rectangular DRA and a monopole antenna to effectively double the available bandwidth without compromising other characteristics. With a proper design, the resonance of the DRA and the resonance from the feeding probe are combined to produce a wideband response. The proposed antenna has an extremely wide bandwidth from 464 to 1017 MHz (for S_{11} < -6 dB), or a fractional bandwidth of 75%.

5.4.1 Antenna Configuration and Design

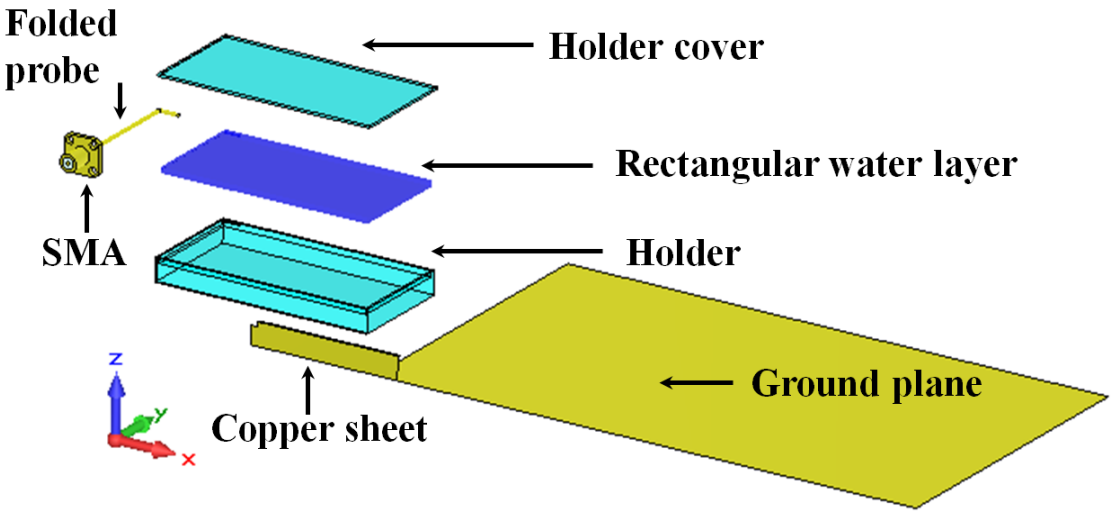

(a)

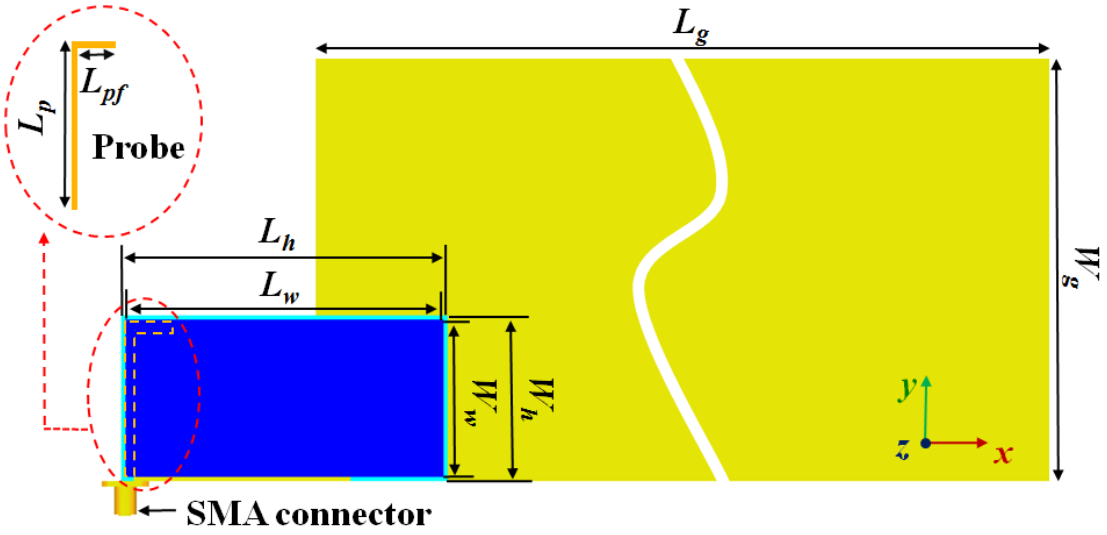

(b)

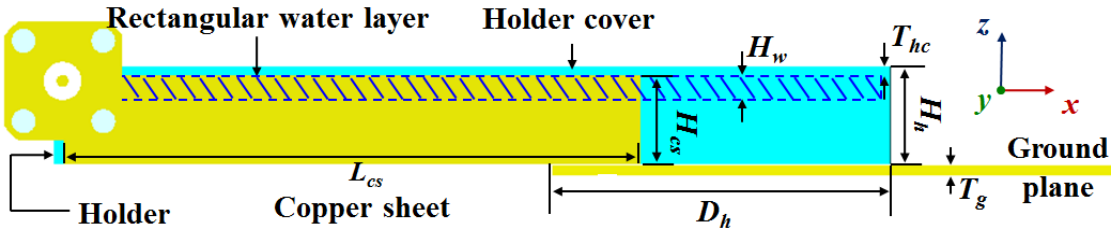

(c)

Fig. 5.5. Configuration of the proposed antenna. (a) Exploded view. (b) Top view (holder cover is hidden). (c) Front view.

The configuration of the proposed water antenna is shown in Fig. 5.5. It consists of a rectangular water holder with dimensions of $L_h \times W_h \times H_h$, a rectangular water layer (the dashed blue lines in Fig. 5.5(c)) with dimensions of $L_w \times W_w \times H_w$ inside the holder, and a rectangular ground plane (made of copper) with dimensions of $L_g \times W_g \times T_g$ ($230 \times 130 \times 1$ mm^3), corresponding to a standard DVB-H handheld receiver for a tablet PC or portable TV handset. The material of the water holder is set as acrylic plastic, with relative permittivity 2.7 ~ 3. The rectangular water layer and the water holder can form a mixed DR. In this design, by properly choosing the height ratio (H_h : H_w) of the water holder to the water layer, the effective permittivity of the mixed DR is around 20. A folded feeding probe with a diameter of 1.3 mm and a total length of $L_p + L_{pf}$ is inserted in the left corner of the water holder horizontally to excite the antenna. A copper sheet with dimensions of $L_{cs} \times H_{cs}$ is attached to the front face of the water holder which will reduce the resonant frequency of the mixed DR. The water holder has a displacement of D_h to the left edge of the ground plane.

The proposed antenna is designed to cover a frequency range from 470 to 862 MHz. To cover such a wide frequency band with this hybrid antenna, the following design procedure is proposed to achieve the broadband performance:

(1) A metal coated DRA is designed to produce a resonance around the upper end of the required frequency band (around 860 MHz). The rectangular metal coated DR is expected to resonant at the lowest mode - $TE_{11\delta}$ mode and the dimensions can be roughly estimated from Eqns (5.1)-(5.3) (the detailed optimisation procedure is similar to section 5.6.2, which is not repeated in this part). This mode is determined by the combined effects of the metal coated DR and the feeding probe. The feeding probe introduces a partially perfect electric conducting boundary which will disturb the field distribution inside the DR. The E field distribution of the probe fed DR mode is shown in Fig. 5.6(a). A clear $TE_{11\delta}$ mode pattern (a half cycle) is observed.

(2) A DR loaded monopole is designed to introduce a resonance around the lower end of the frequency band (around 550 MHz), where the feeding probe simultaneously acts as a monopole and the feeding structure of the DR. By loading the metal coated DR, the resonant frequency of the monopole can be reduced from 1.3 GHz (without the DR loading) to 550 MHz (with the DR loading). Fig. 5.6(b) shows that the E field is concentrated on the folded feeding probe which is similar to a monopole, it can be concluded that the main radiation at 550 MHz is from the feeding probe.

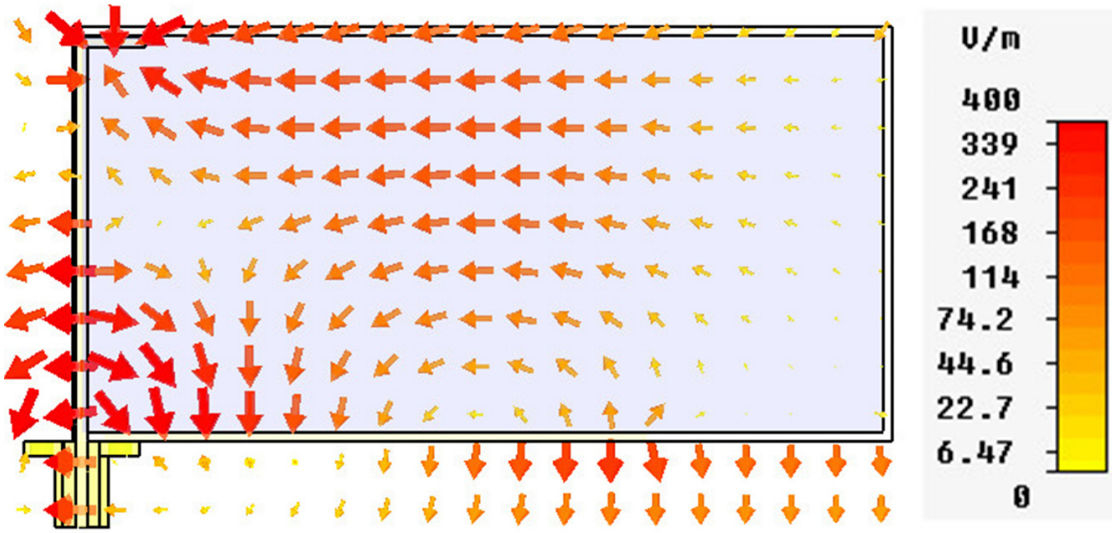

(a)

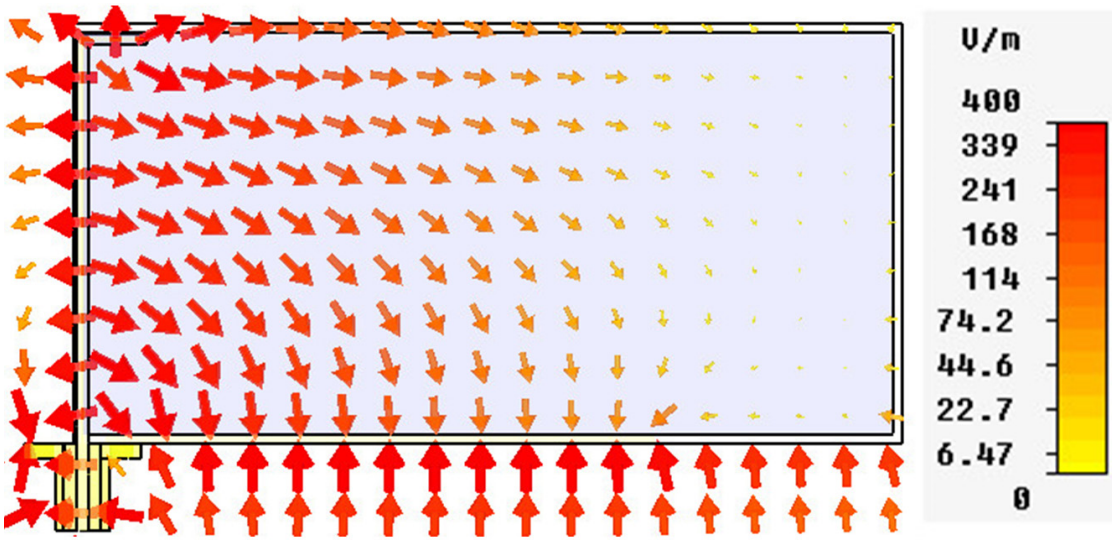

(b)

Fig. 5.6. (a) E field distribution of the probe fed DR mode of the proposed antenna (at 880 MHz). (b) E field distribution of the monopole mode of the proposed antenna (at 550 MHz).

(3) By optimizing the parameters, two resonances are combined to produce a wideband response which is much wider than the sum of the bandwidths of each individual antenna. The wideband response is sensitive to the position offset D_h between the DR and the ground plane. As shown in Fig. 5.7, when the displacement D_h is varied from 12 to 48 mm, the lower resonance which is caused by the monopole mode mainly stays stable while the upper resonance which is determined by the combined effects of the metal coated DR and the feeding probe shifts upwards. This is because the space DR covered by the ground plane changes lead to the DR boundary condition changes. When D_h is further increased, the upper resonance is shifted upwards to even outside the required frequency

band, thus the two resonances are separated. By fine-tuning the value of D_h, the optimal impedance matching for the required frequency band can be achieved.

Besides the position offset D_h, another parameter that affects the antenna performance is L_{cs}. After extensive simulations, we can conclude that the proposed antenna is not very sensitive to the length of the copper sheet L_{cs}, when $L_{cs} > L_h - D_h$ (that is the copper sheet can be connected to the ground plane).

The ground plane effects of this antenna are quite similar to the U-shaped hybrid water antenna and will be carefully examined in section 5.5.

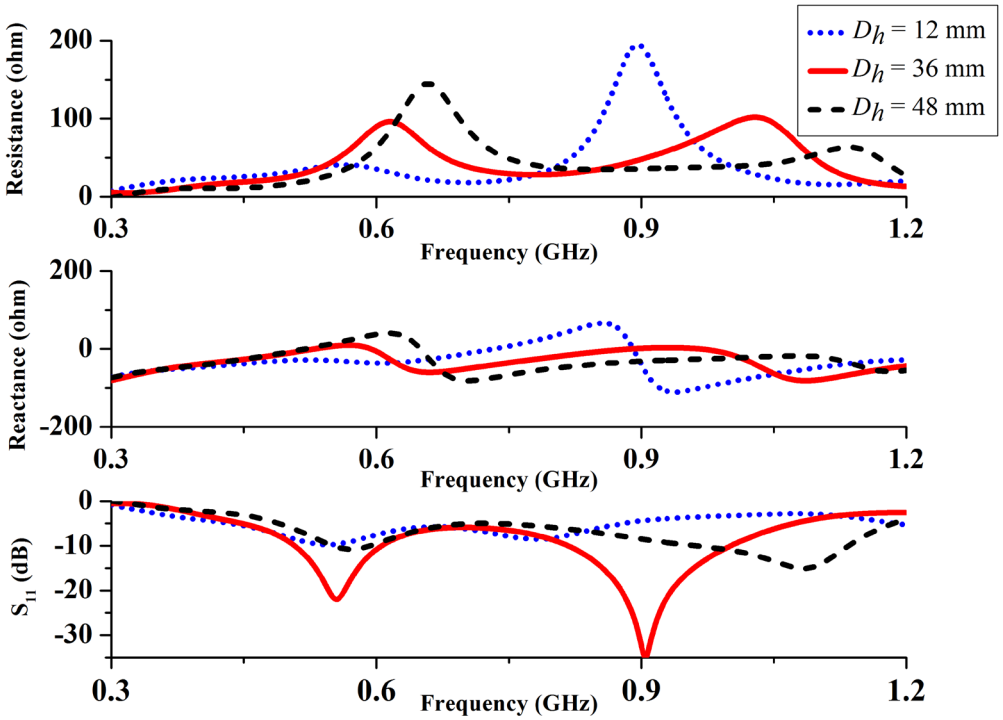

Fig. 5.7. Simulated input impedance and S_{11} with different D_h.

5.4.2 Measurement Results

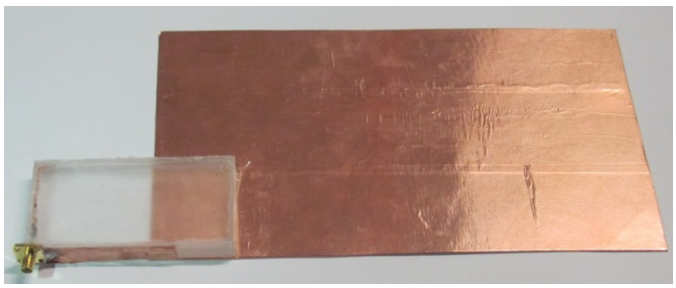

Fig. 5.8. Fabricated water antenna.

To validate the proposed design, a prototype of the proposed antenna is fabricated and shown in Fig. 5.8. The optimised antenna parameters are L_g =230 mm, W_g =130 mm, T_g = 1 mm, L_h = 90 mm, W_h = 45.6 mm, H_h = 10.6 mm, L_w = 88 mm, W_w = 43.6 mm, H_w = 2.5 mm, Th_c = 1 mm, L_p = 45.6 mm, L_{pf} = 7 mm, L_{cs} = 62.3 mm, H_{cs} = 9.6 mm, D_h = 36.4 mm. The DR occupies a size of 90 × 45.6 × 10.6 mm^3 which is roughly 0.15λ× 0.072λ× 0.017λ, at the lowest frequency 470 MHz. In Fig. 5.9, it can be seen that the -6 dB bandwidth (the industrial requirement) is about 553 MHz, ranging from 464 to 1017 MHz, which is well matched over a wide frequency band. The radiation efficiency (defined as the ratio of the power radiated to the power accepted by the antenna port) and the realised gain measurements were performed in a reverberation chamber by using the two-antenna approach described in [17] and an anechoic chamber, respectively. It is interesting to note that in Fig. 5.10, the radiation efficiency of the designed antenna across the working frequency is higher than 60%. At 800MHz, there is a 10% disagreement between the simulation and the measurement, which is probably due to the material difference and fabrication error. Overall, good agreement is achieved. Due to the limited measurement facilities, the maximum realised gain, a function of frequency, is hard to measure. Instead, the realised gain in the direction of $\theta = 90°$, $\varphi = 45°$ was measured and compared with the simulated result in Fig. 5.11. Again good agreement is observed. As a reference, the simulated maximum realised gain is added.

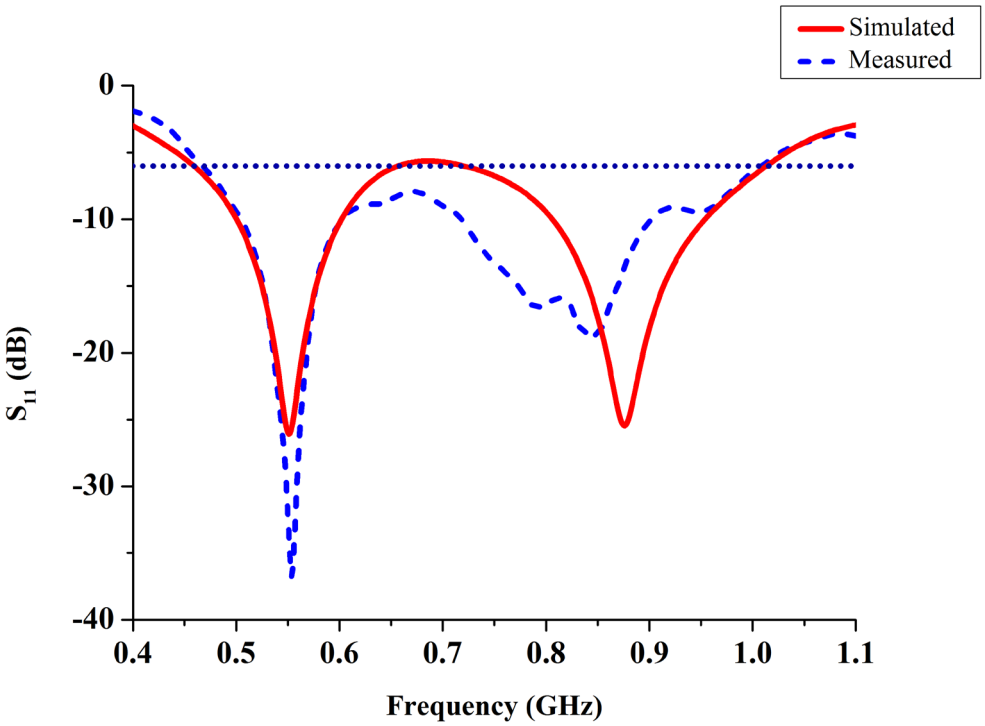

Fig. 5.9. Simulated and measured S_{11} (dB) of the proposed antenna.

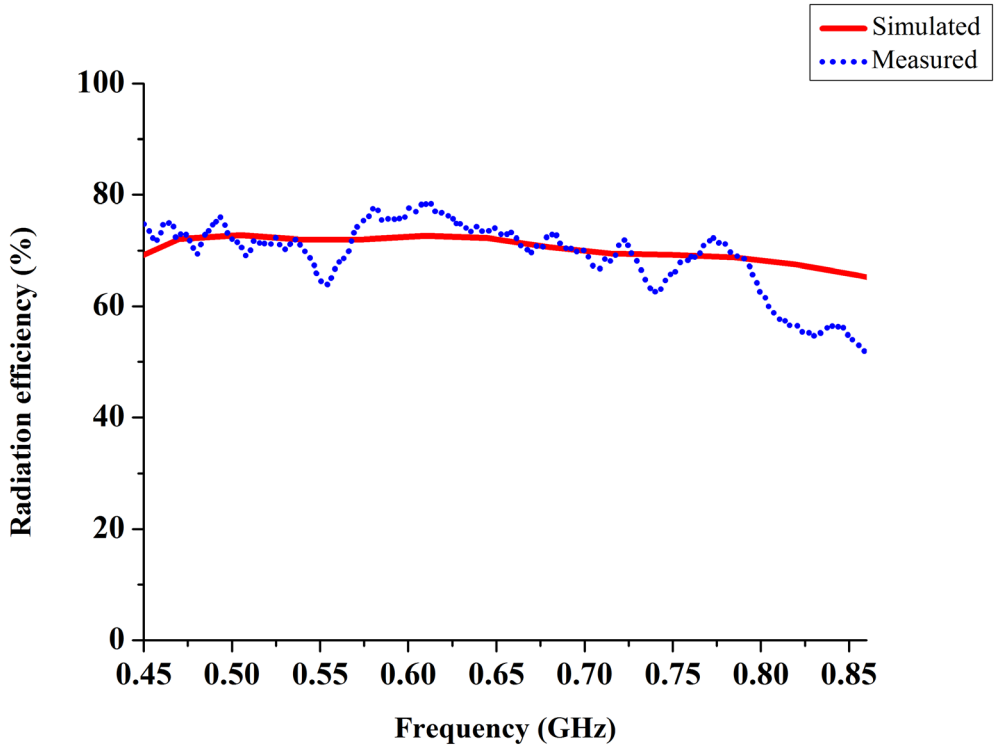

Fig. 5.10. Simulated and measured radiation efficiency of the proposed antenna.

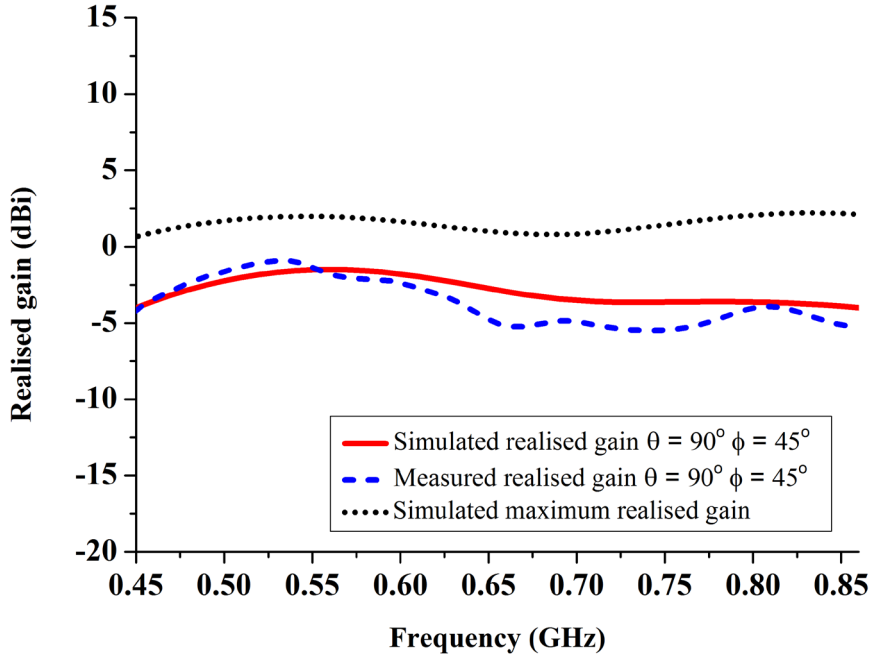

Fig. 5.11. Simulated and measured realised gain of the proposed antenna.

The radiation patterns were measured in an anechoic chamber. The simulated and the measured 3D and 2D radiation patterns (dual polarisations) at 550 MHz and 880 MHz are plotted in Figs. 5.12, respectively. Good agreement is obtained. These results demonstrate that the antenna operates at two different modes across the whole frequency band.

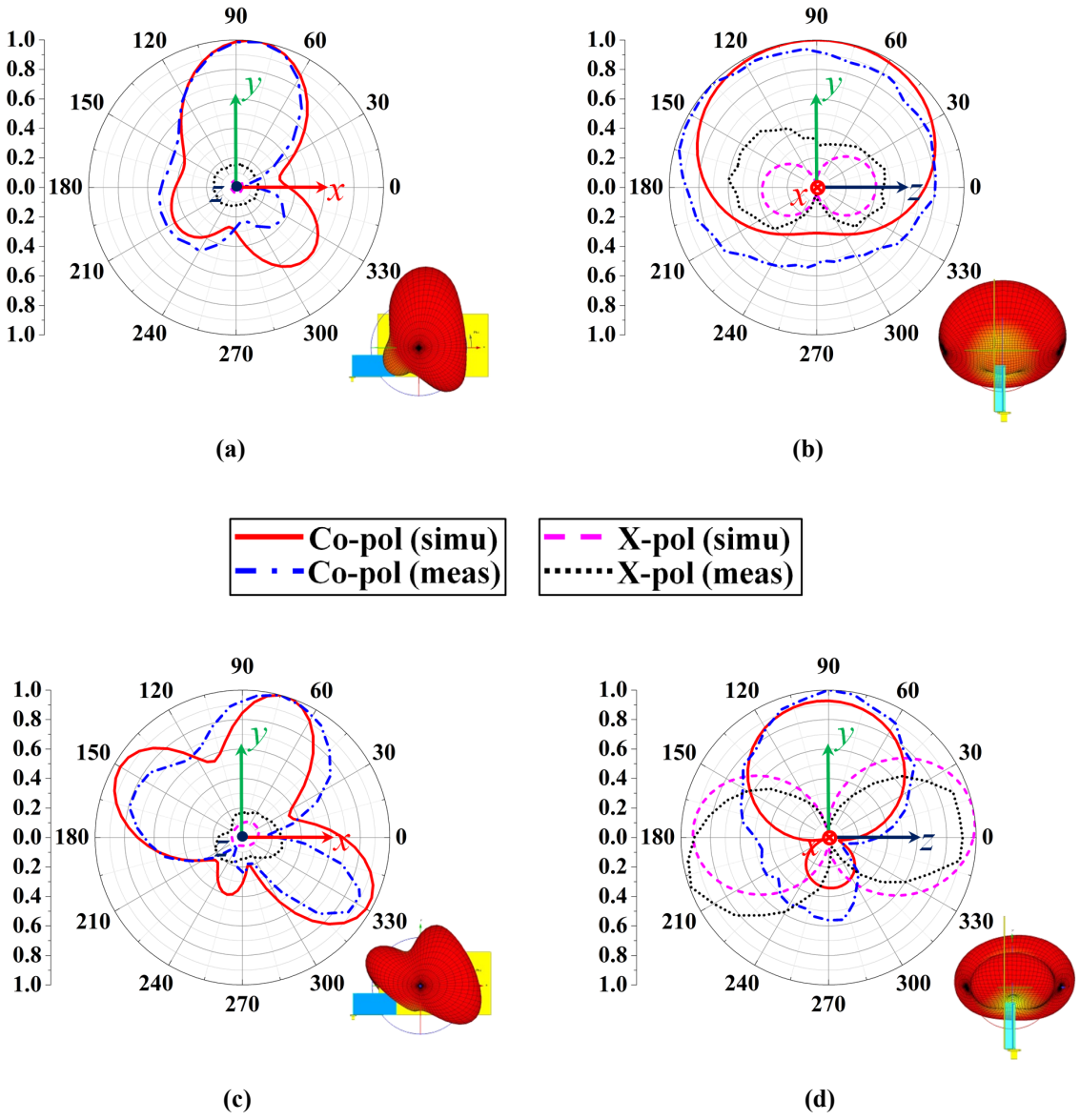

Fig. 5.12. Simulated and measured radiation pattern. (a) Xoy plane at 550 MHz. (b) Yoz plane at 550 MHz. (c) Xoy plane at 880 MHz. (d) Yoz plane at 880 MHz.

In this section, a wideband, hybrid rectangular water antenna has been proposed, designed, fabricated and measured. This hybrid antenna has a 75% bandwidth for S_{11}< -6 dB and a radiation efficiency > 60% across the whole band from 470 to 862 MHz. The DR occupies a compact size of 90 × 45.6 × 10.6 mm^3 which is roughly 0.15λ× 0.072λ× 0.017λ, at the lowest frequency 470 MHz.

5.5 U-Shaped Hybrid Water Antenna Design

In this section, a broadband, low profile, hybrid water antenna with a U-shaped water layer is proposed. This design is improved from the rectangular hybrid water antenna proposed in section 5.4, by modifying the rectangular water layer to a U-shaped water layer, which reduces the antenna size considerably. The working mechanism is similar to the rectangular hybrid water antenna, which combines the resonance of the water DRA and the resonance of the monopole to cover the required frequency band. The unique liquidity feature of the water DR allows complex structures (including the antenna feeding line) to be placed and tuned inside water easily. The proposed antenna has a -6 dB impedance bandwidth from 430 to 900 MHz (a fractional bandwidth of 70%). Compared with other antennas for this band, this new antenna has a wider bandwidth, more compact size and simpler structure.

5.5.1 Antenna Configuration and Design

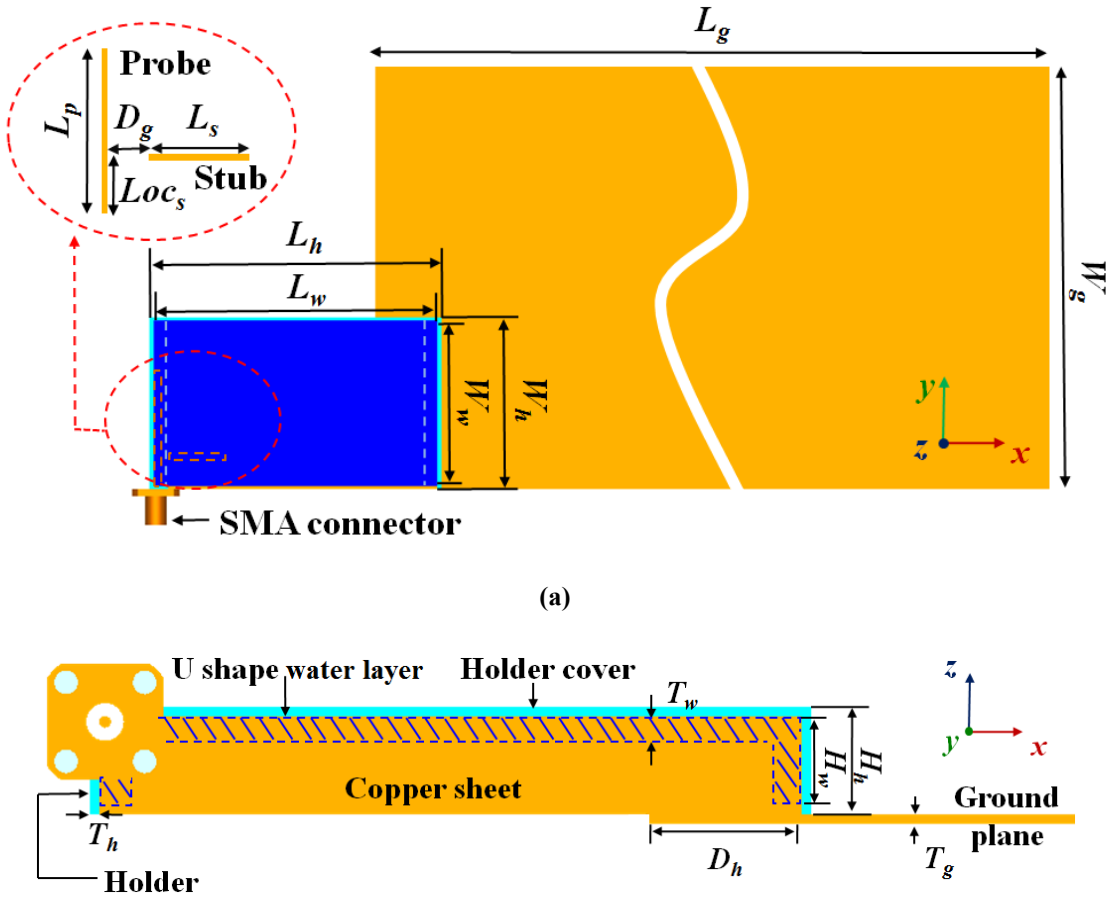

Fig. 5.13. Geometries of the proposed antenna. (a) Top view (holder cover is hidden). (b) Front view.

The proposed antenna is shown in Fig. 5.13. It consists of a rectangular water holder with dimensions of $L_h \times W_h \times H_h$ (thickness T_h), a U-shaped water layer (the dashed blue lines in Fig. 5.13(b)) inside the holder with length L_w, width W_w, thickness T_w and height H_w, and a rectangular ground plane (made of aluminum) with dimensions of $L_g \times W_g \times T_g$ ($230 \times 130 \times 1$ mm^3). The material of the water holder is set as acrylic plastic. The U-shaped water layer and the holder can form a mixed DR with effective relative permittivity around 20. A feeding probe with a glued parasitic stub is inserted into the water layer horizontally to excite the antenna. Matching can be improved by adjusting the locations and dimensions of the stub. This is a unique feature for using liquid (water) as the DR. It allows complex structures to be embedded and tuned inside water which is difficult and expensive for solid dielectrics. A copper sheet connected to the ground plane is attached to the front face of the water holder which acts as a metal coating to decrease the resonant frequency of the DR and also acts as the ground plane of the probe. The water holder has a displacement of D_h to the left edge of the ground plane.

The proposed antenna is developed to cover a wide frequency band. The technique is to combine two closely spaced resonant frequencies together.

Like the rectangular hybrid water antenna, one resonance is from the metal coated water DR, which is the $TE_{11\delta}$ mode resonates around 810 MHz. This mode is determined by the combined effects of the metal coated DR and the feeding probe. Without the probe, the mode cannot be excited properly. Another resonance is from the feeding probe, which acts as a monopole antenna to cover the lower frequency band. The metal coated DR performs as a load to reduce the frequency of the monopole. Without the metal coated DR, the monopole would work around 1.91 GHz which is much higher than the required frequency band. By loading the water DR, the resonant frequency can be reduced to around 520 MHz.

5.5.2 Parametric Study

The general behaviour of this hybrid water antenna is influenced by a number of parameters, including the length and location of the stub (L_s, Loc_s), the offset of the water holder (D_h) and the size of the ground plane (L_g, W_g). To achieve the optimal performance, a parametric study is performed.

A. Stub length and location

The liquidity and the transparency of water allow a parasitic conducting stub placed inside the water to improve the impedance matching, as shown in Fig. 5.13(a). The simulated S_{11} with different values of L_s and Loc_s are plotted in Fig. 5.14. It is noted that the values of L_s and Loc_s affect both the DR mode and the monopole mode. As the stub is placed in the water, tuning the values of L_s and Loc_s

will affect the modes inside the water DR, causing the DR mode change correspondingly. Moreover, the location and length of the stub also affect the impedance matching of the monopole, causing the monopole mode varies. By properly tuning the values of L_s and Loc_s, the frequencies can be shifted downwards, and the impedance matching can be improved. The optimal performance will be achieved when L_s = 20 mm, Loc_s = 20 mm.

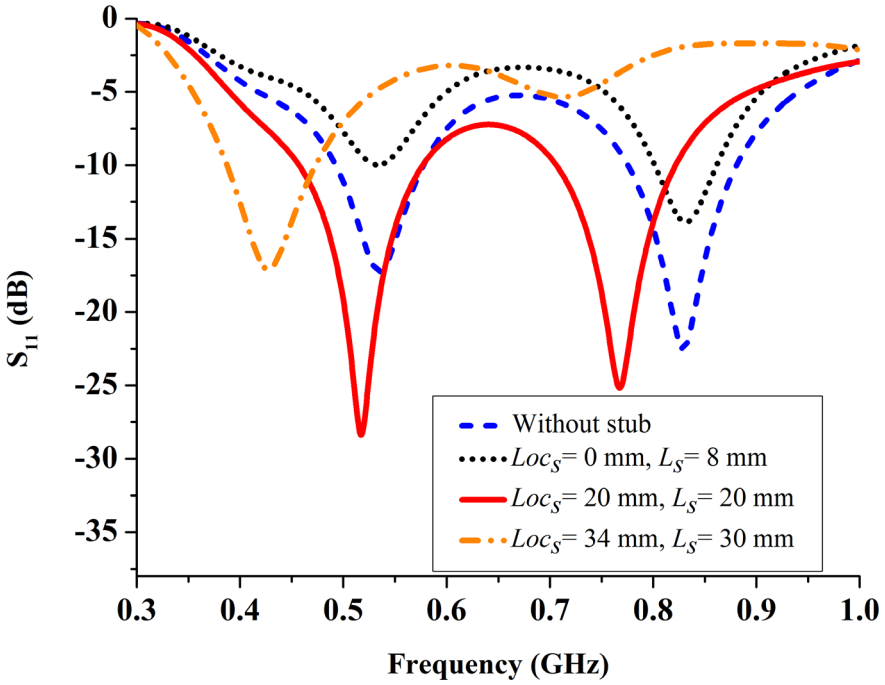

Fig. 5.14. Simulated S_{11} with different values of Loc_s and L_s.

B. Water holder offset

The wideband response of this hybrid water antenna is sensitive to the position offset D_h between the DR and the ground plane. As can be seen in Fig. 5.15, when D_h is varied from 4 to 36 mm, the lower resonance caused by the monopole mode mainly remains stable while the upper resonance determined by the metal coated DR shifts upwards. This is because the changing of the space DR covered by the ground plane leads to the changing of the DR boundary conditions. When D_h is further increased, the upper resonance is shifted upwards, the impedance matching becomes worse, leading the two resonant frequencies separate. By fine-tuning D_h, the optimal impedance matching for the target frequency band can be obtained.

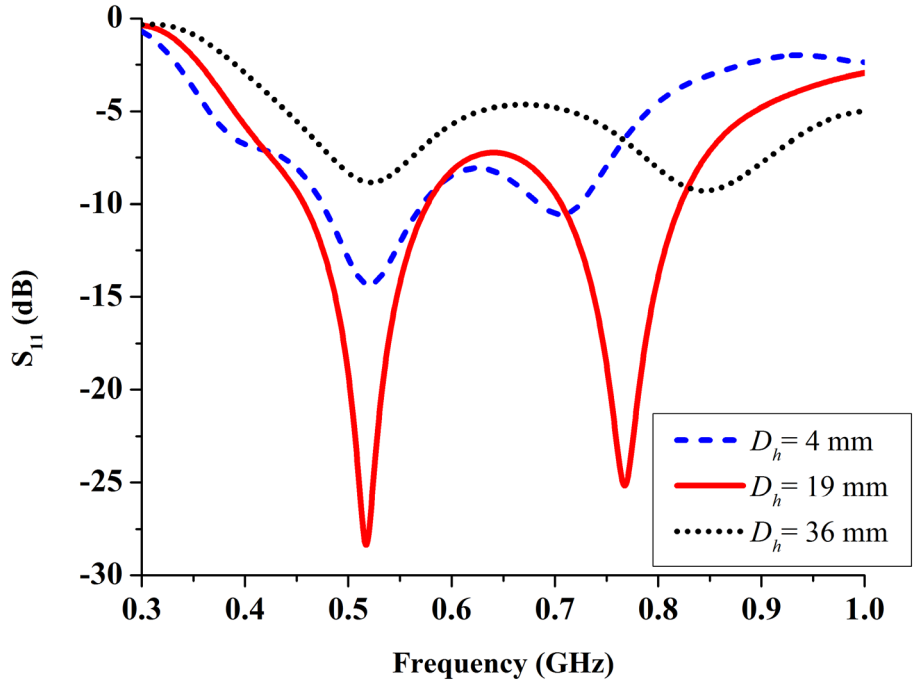

Fig. 5.15. Simulated S_{11} with different values of D_h.

C. Ground plane size

The ground plane size may affect the input impedance, hence the reflection coefficient S_{11} of the antenna. For a given ground plane width W_g= 130 mm, the S_{11} curves for three different values of L_g are presented as shown in Fig. 5.16. We can see that the first resonant frequency is affected (for frequency band around 500 MHz, the ground plane is part of the radiator, by changing the values of L_g, this band will be affected); however, the -6 dB bandwidth across the required band is stable. For some space limited applications, the ground plane can be further reduced to save more space for other components.

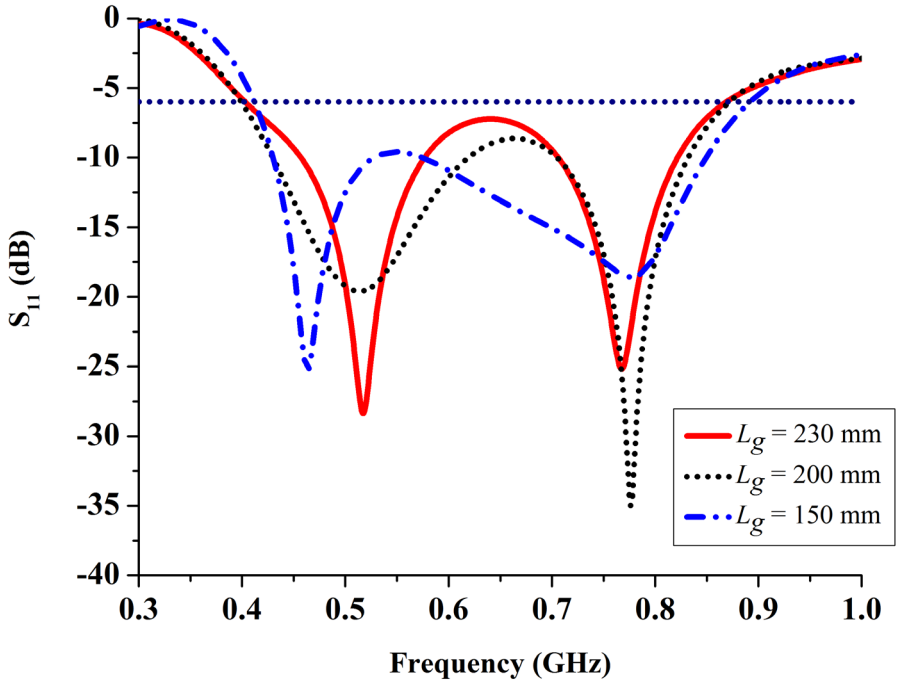

Fig. 5.16. Simulated S_{11} with different values of L_g.

5.5.3 Measurement Results

To validate the theoretical design and analysis, a prototype of the proposed water antenna is fabricated as shown in Fig. 5.17. The optimised parameters are L_g = 230 mm, W_g = 130 mm, T_g = 1 mm, L_h = 78 mm, W_h = 45.6 mm, H_h = 11.8 mm, T_h = 1mm, L_w = 76 mm, W_w = 43.6 mm, H_w = 9.8 mm, T_w = 2.5 mm, L_p = 44 mm, L_s = 20 mm, Loc_s = 20 mm, D_g = 1 mm, D_h = 19 mm. The S_{11}, radiation pattern, and realised gain were measured in an anechoic chamber. The radiation efficiency was measured in a reverberation chamber by using the two-antenna approach [17].

Fig. 5.17. Prototype of the water antenna.

The simulated and measured results are compared in Figs. 5.18-5.20. It is evident that the water antenna has a bandwidth from 432 to 900 MHz for S_{11} < -6 dB (a fractional bandwidth of 70%) that is slightly higher than the simulated bandwidth from 410 to 873 MHz. But the overall agreement is good and the two resonant frequencies are shown as expected to cover the desired frequency band. The radiation patterns are plotted at 510 MHz and 710 MHz, respectively, demonstrating that the antenna operates at two different modes in the operating band. Better agreement between the simulated and measured co-polarisation (Co-pol) patterns are observed than the cross-polarisation (X-pol), since the X-pol is more sensitive to the alignment of the antenna in measurements. The radiation efficiency and realised gain are compared, and similar shapes are observed between the simulated and measured results. Due to the time limitation, the realised gain was measured in the direction of $\theta = 90°, \varphi = 45°$. As a reference, the simulated maximum realised gain, a function of the frequency, is added. The measured efficiency is higher than 60% across the required band. The S_{11} and radiation efficiency of the antenna with the pure water and 10% PG were measured, respectively. The performance of the antenna with the pure water and 10% PG are similar, indicating that the water with 10% PG will be a good alternative to pure water in cold climates. The discrepancies between the measurements and simulations are mainly caused by two reasons: 1) the inaccuracy of the antenna fabrication and material properties; 2) the measurement and cabling errors.

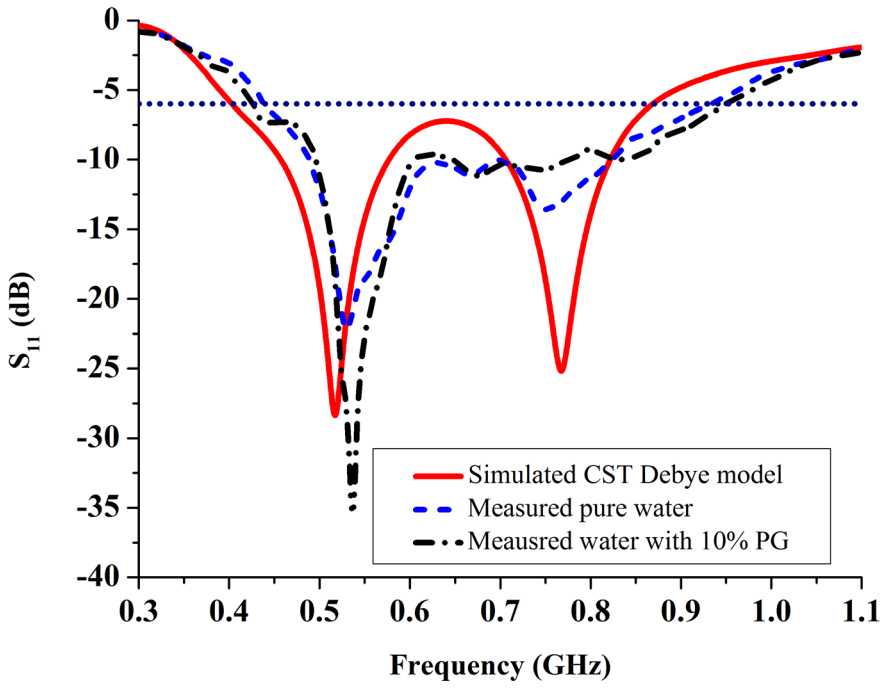

Fig. 5.18. Simulated and measured S_{11} (dB) of the proposed antenna.

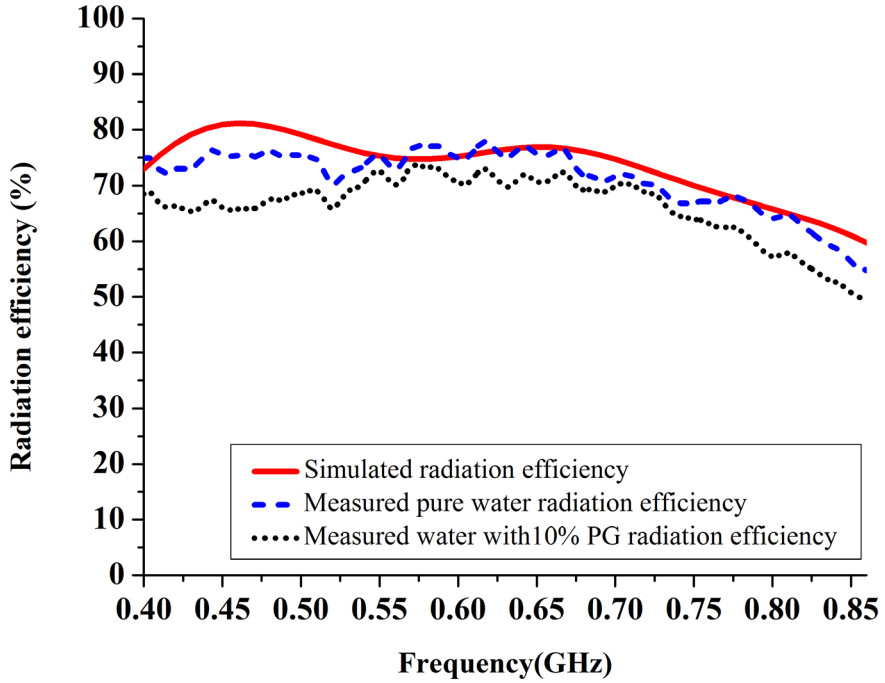

(a)

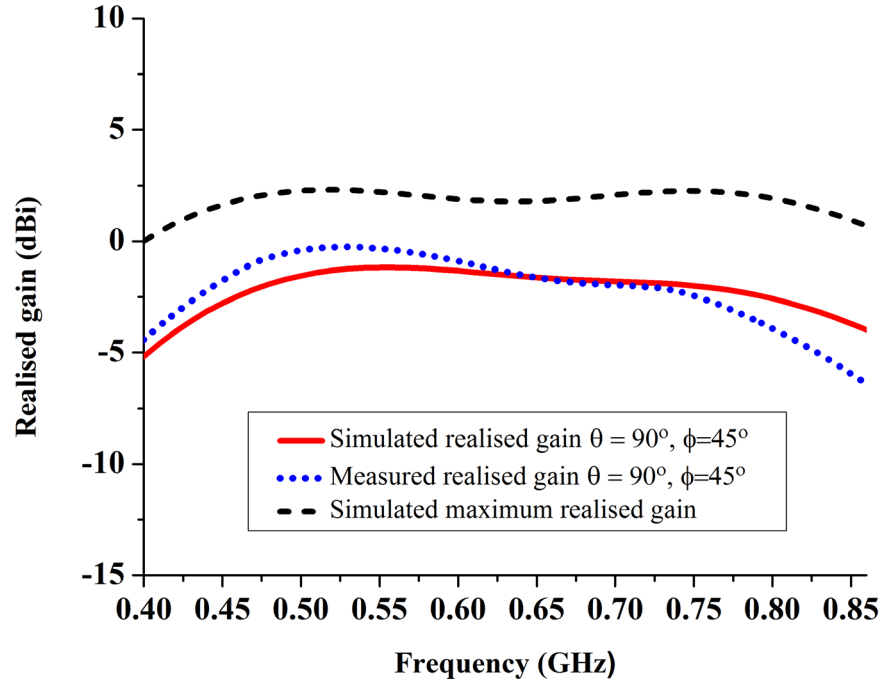

(b)

Fig. 5.19. Simulated and measured comparison of the proposed antenna. (a) Radiation efficiency. (b) Realised gain.

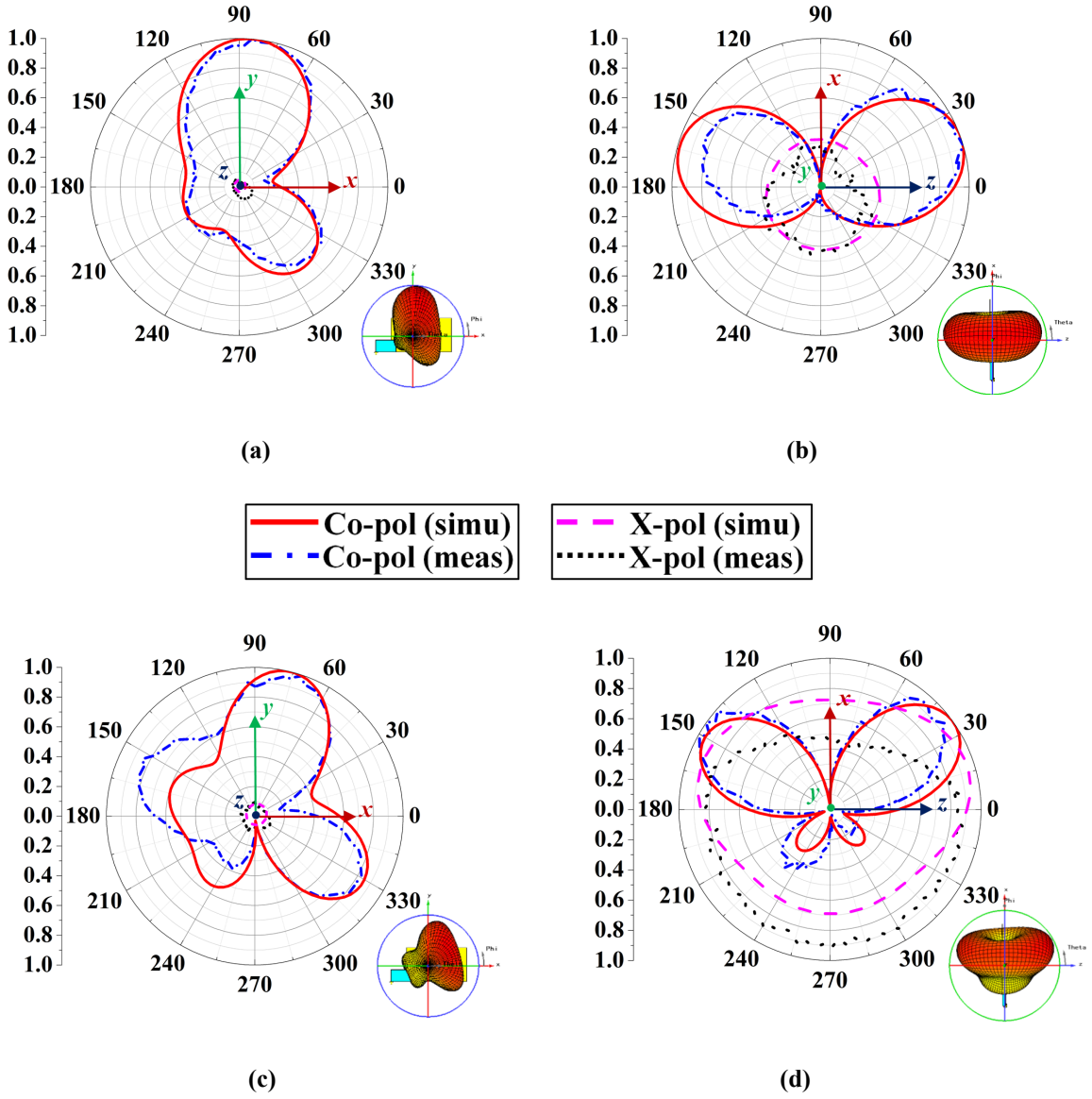

Fig. 5.20. Simulated and measured radiation patterns of the proposed antenna. (a) f = 510 MHz, xoy plane. (b) f = 510 MHz, xoz plane. (c) f = 710 MHz, xoy plane. (d) f = 710 MHz, xoz plane.

Moreover, as the complex permittivity of pure water is a function of tempeture and frequency, the antenna performance will change according to the temperature. To investigate the temperature effects on the antenna performance, the simulated S_{11} and realised gain over different temperatures are compared in Fig. 5.21(a) and (b), where the measured permittivity data at temperatures 5°C, 25°C and 40°C, were used in the simulations.

It is noted that the frequency band slightly shifts upwards when temperature increases from 5°C to 40°C. The realised gain at 5°C is slightly lower than the realised gain at 25°C and 40°C, especially at higher frequencies. Overall, good agreements are obtained, which means for this antenna the temperature will not change the antenna performance significantly.

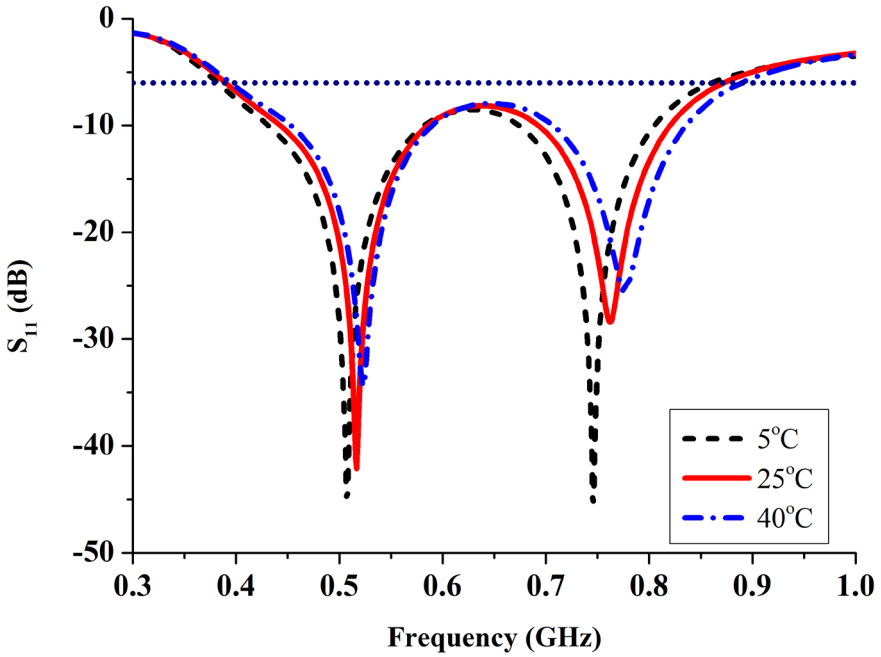

(a)

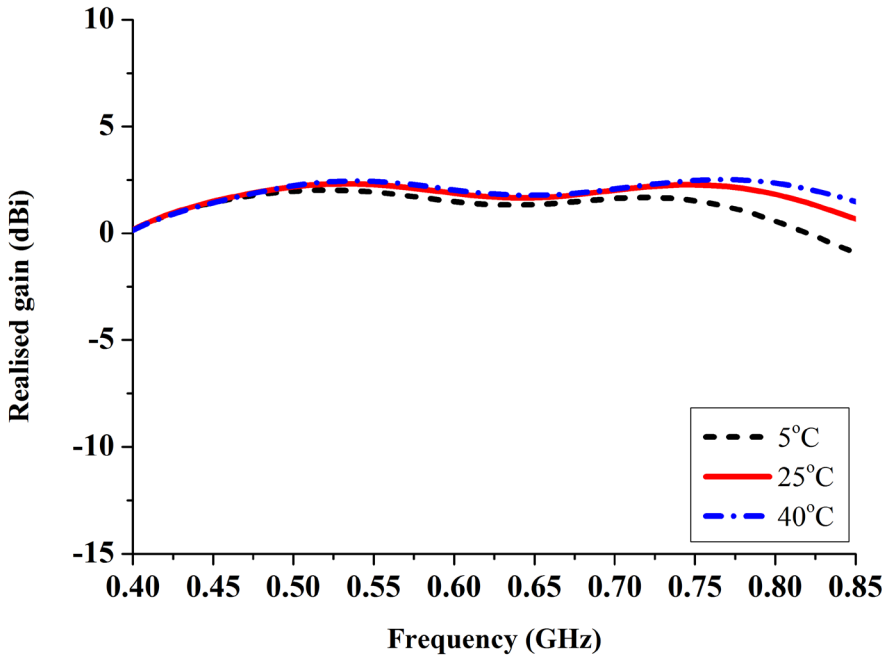

(b)

Fig. 5.21. Performance comparison of the proposed antenna for different temperatures. (a) Simulated S_{11} (in dB). (b) Simulated realised gain.

In this section, a broadband, low profile, hybrid water antenna has been proposed, which has utilised two functions (excitation and radiation) of the feeding probe effectively. The antenna has used the unique features of water in terms of the high permittivity, transparency and convenience/flexibility to embed the complex feeding structures inside the DR. The simulated and measured results have been obtained and they are in good agreement. Also, an antenna with 10% PG has been introduced and demonstrated as a good alternative solution for cold climates. Moreover, the antenna performance over different temperatures has been investigated. It is observed that the temperature will not affect the antenna performance significantly. This work has successfully demonstrated the attractive features of water-based antenna. This proposed design has a wide bandwidth from 432 to 900 MHz (a fractional bandwidth of 70%) with radiation efficiency over 60%.

5.6 A Wideband Hybrid Water Antenna with an F-Shaped Monopole

A new wideband hybrid antenna is proposed in this section. It combines an F-shaped conducting monopole antenna and a water DRA to produce a wideband response. The F-shaped monopole is also used to excite the water DRA which would be difficult for conventional ceramic dielectric materials. Two sides of the water DRA are coated with metal patches to reduce the antenna size. A comprehensive parametric study is conducted to optimise the antenna performance. The final design is made and tested. A good agreement is obtained between the simulation and measurement results. Compared with conventional straight probe, the proposed antenna has a wider bandwidth from 410 to 870 MHz (a fractional bandwidth of 71.8%) for S_{11} < -6 dB, with a compact size (52 × 51.5 × 10 mm^3, roughly 0.071 λ × 0.07 λ × 0.0136λ at 410 MHz).

5.6.1 Antenna Configuration

The geometry of the proposed antenna is shown in Fig. 5.22. It consists of a rectangular water layer with dimensions of $L_w \times W_w \times H_w$ (the dashed blue lines in Fig. 5.22(d)), a holder with dimensions of $L_h \times W_h \times H_h$ and a ground plane with dimensions of $L_g \times W_g \times T_g$ (230 × 130 × 1 mm^3). The substrate (FR4) under the holder is used to support it. The material of the holder is set as acrylic plastic. The rectangular water layer and the holder can form a mixed DRA. An F-shaped feeding probe is inserted in the water layer horizontally to excite the antenna. The F-shaped feeding probe has three parts: the straight part has a length of L_p, the top folded part has a length of L_{pf}, the lower stub part has a length of L_s, a rotated angle of θ, and a location of Loc_s. Two metal patches (made of copper) are attached to the front and left side of the holder, respectively, reducing the resonant

frequency of the DRA. Metal patch 1 in Fig. 5.22(d) has dimensions of $L_{m1} \times (W_{m1} + T_h + H_w)$, where T_h is the thickness of the water holder. Metal patch 2 in Fig. 5.22(c) has dimensions of $L_{m2} \times W_{m2}$. The holder has a displacement of D_h to the left edge of the ground plane.

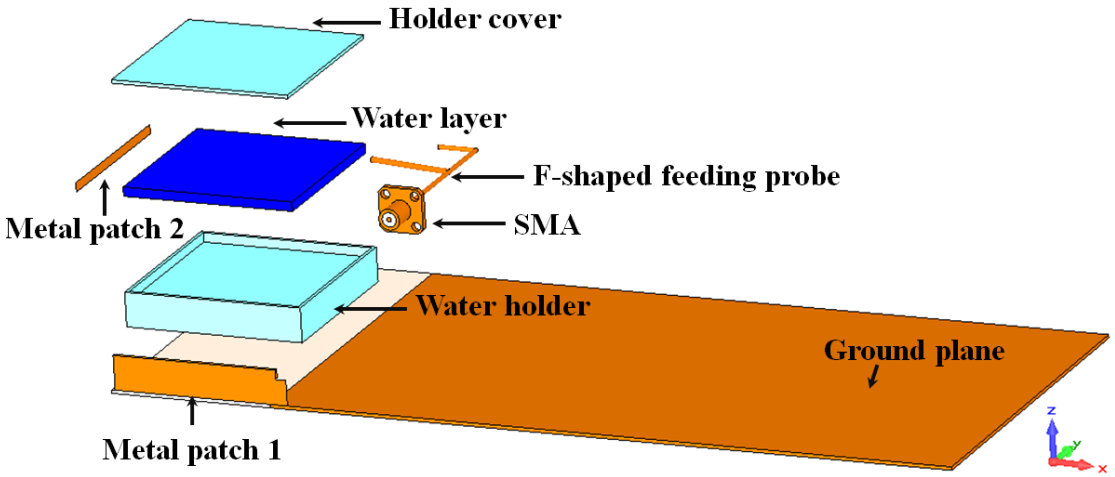

(a)

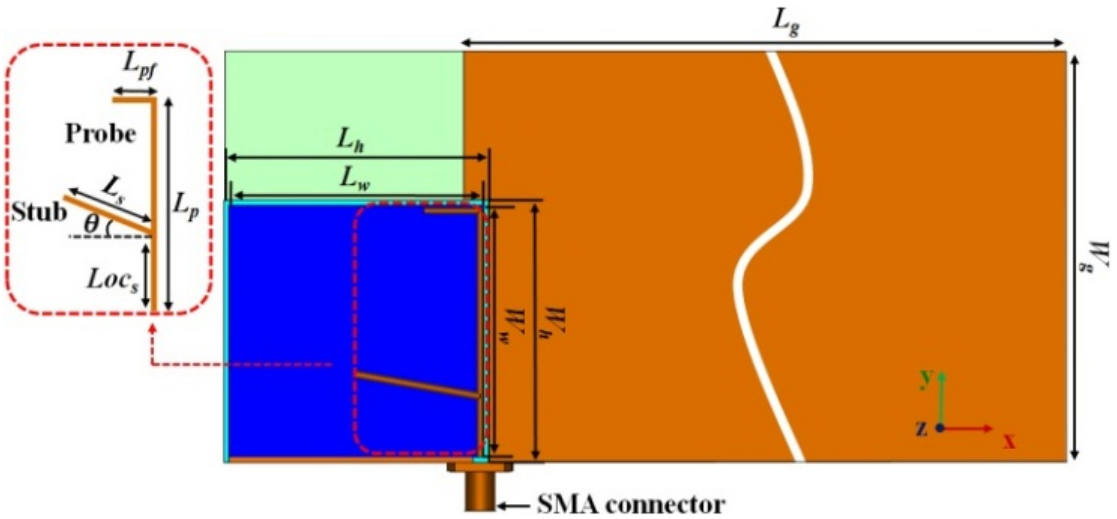

(b)

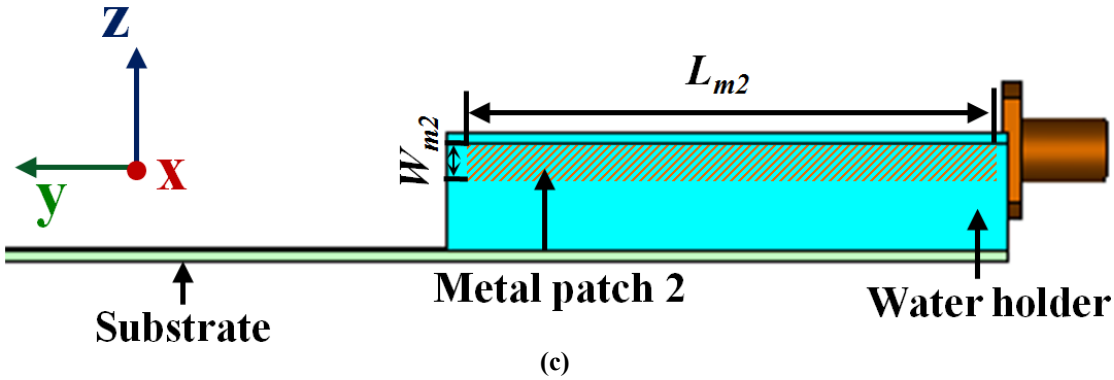

(c)

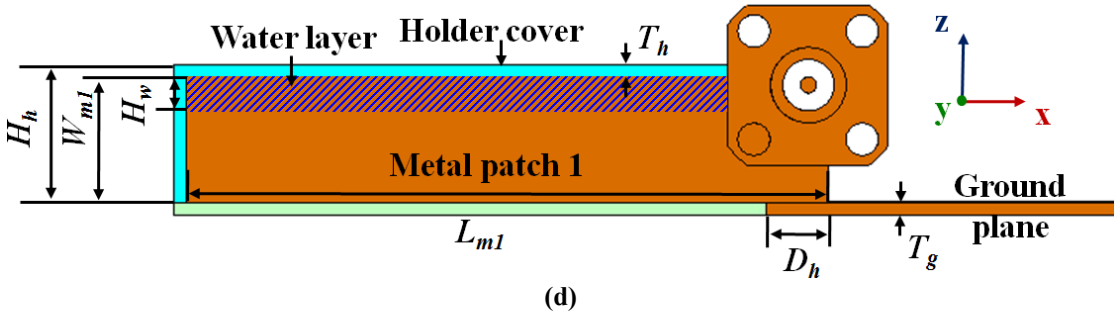

Fig. 5.22. Geometry of the proposed antenna. (a) Exploded view. (b) Xoy plane view (holder cover is hidden). (c) Yoz plane view. (d) Xoz plane view.

5.6.2 Design of Radiating Element

The design procedures of this design are summarised as follows:

1) By properly choosing the ratio (H_h : H_w) of the holder height to the water layer height, an effective permittivity around 20 to 30 can be obtained for the mixed DRA.

2) A metal coated DRA is designed to produce an upper band (i.e. around 850 MHz).

3) A dielectric loaded F-shaped monopole is designed to cover the lower and middle bands (i.e. from 440 to 600 MHz).

A. Metal Coated DRA Mode

For a specific material and frequency, various groups of DRA dimensions can be chosen. The strategy in this section is to fix one dimension at a time, and plot the variations of the resonant frequency and Q factor as a function of the other two dimensions, and select a set of dimensions with the optimised size, desired frequency and Q factor.

The resonant frequency and Q factor of the DRA can be calculated according to the Eqns (5.1-5.9), and shown in Fig. 5.23. It is shown that an increase of the DRA dimensions will decrease the resonant frequency and Q factor. From the plots, it is very convenient to choose the optimised dimensions with estimated resonant frequency and low Q factor. To integrate the DRA inside a hand portable device, we assume that one dimension is 10 mm, in this case, the optimised dimensions of the DRA are a = 10 mm, b = 104 mm, d = 103 mm, f_{res} = 879 MHz, Q factor = 10.27 as shown in Fig. 5.23. According to the E-field distribution of TE^{z}_{111} mode, two metal patches as shown in Fig. 5.22 are placed on two sides of the water DRA (to create electric-walls, alternatively a metallic paint or coating could be used), therefore the antenna size can be reduced to a quarter of the original one at the same frequency. After miniaturisation, the final DRA dimensions are a = 10 mm, b = 52 mm, d = 51.5

mm (f_{res} = 879 MHz is a theoretically estimated frequency when the DRA is placed at the corner of the ground plane, the resonant frequency will be shifted downwards).

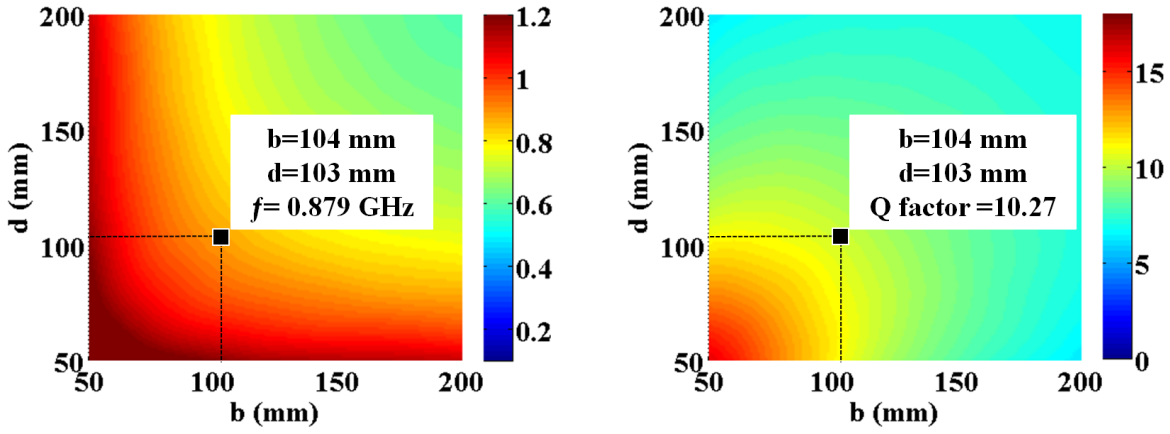

Fig. 5.23. (a) The resonant frequency (as shown by the color in GHz) of TE^z_{111} mode as a function of dimensions b and d. (b) The Q factor (as shown by the color) of TE^z_{111} mode as a function of dimensions b and d.

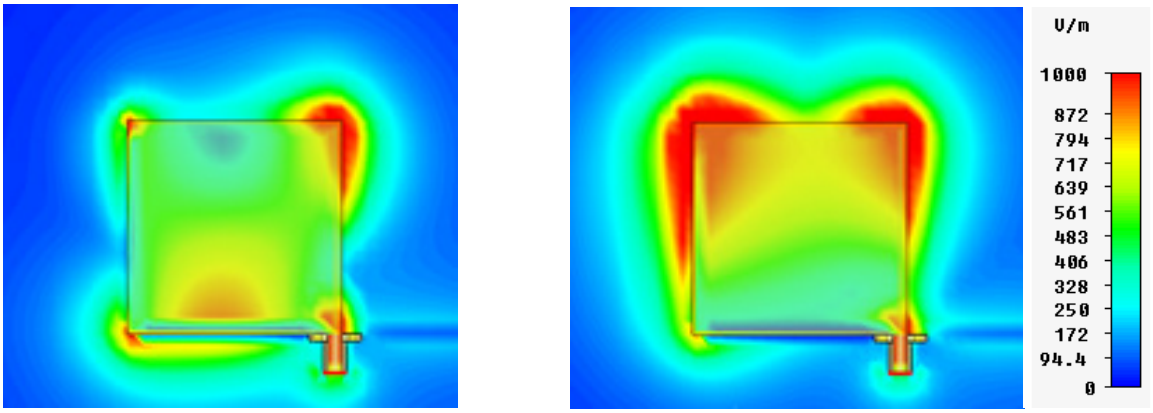

Fig. 5.24. E-field distribution (magnitude) of the proposed antenna (without the stub). (a) 870 MHz. (b) 430 MHz.

Besides the dimensions and ε_r, this mode is also closely linked to the feeding probe. The feeding probe excites the DRA mode and also introduces a perfect electric conducting boundary which will change the field distribution inside the DRA. Without the probe, the desired mode of the DRA cannot be excited properly. The E-field distribution of the probe fed DRA is shown in Fig. 5.24(a). It is noted that the E-field is mainly concentrated inside the DRA and a half cycle TE^z_{111} mode pattern is clearly observed.

B. F-shaped Feeding Probe Mode

To realise a wideband response, a dielectric (mixture of the water and holder) loaded F-shaped monopole is employed to cover the lower and middle bands (i.e. from 440 to 600 MHz), where the feeding probe simultaneously acts as a monopole antenna and the excitation of the DRA.

The lower band is mainly determined by the strong coupling between the feeding probe and metal patch 2. As can be seen in Fig. 5.24(b), there is a power flow propagating from the feeding probe, then coupled to the metal patch 2 (on the left size), and radiated from both the feeding probe and metal patch, which is like a folded monopole antenna. The power flow forms a standing resonant wave with two peaks and one trough and the path of this mode is around one wavelength at 430 MHz. The dielectric loading enhances the coupling considerably, also reduces the antenna size at this band. This coupling is well utilised to overcome the difficulties of achieving 430 MHz band by using compact size antennas.

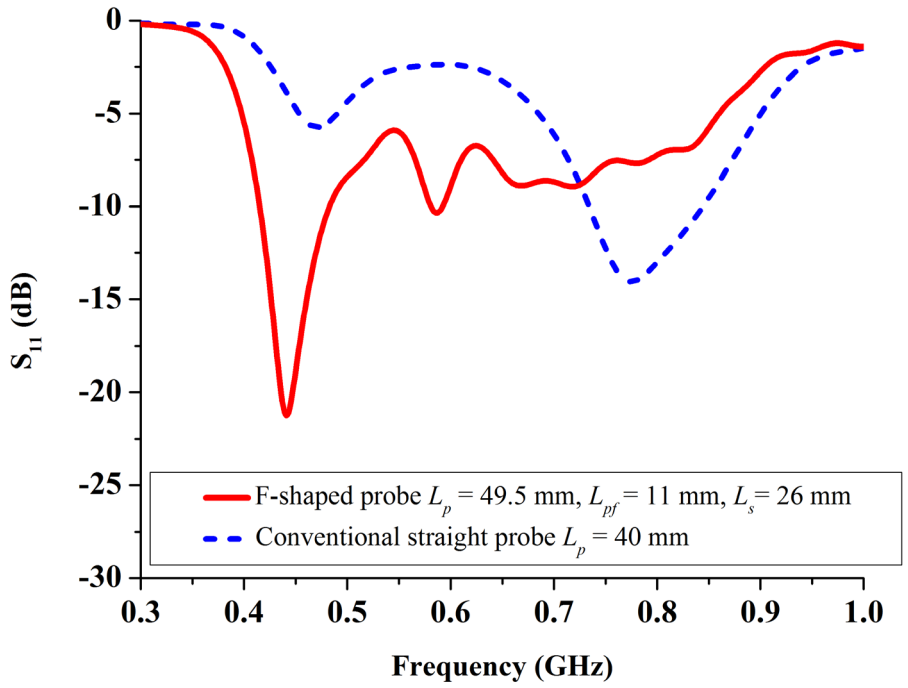

Fig. 5.25. Simulated S_{11} comparison between the antenna with the conventional feeding probe and the proposed F-shaped feeding probe.

To combine the upper and lower bands, a middle band associated with the stub is introduced. A simulated S_{11} comparison of the antenna with a conventional straight feeding probe and the proposed F-shaped feeding probe has been made in Fig. 5.25. It is noted that by using the F-shaped probe, the

lower band and upper band are effectively combined to realise a wide bandwidth and better impedance matching at lower frequencies can be achieved.

It should be mentioned that for whatever mode, the relevant radiator is the main radiator, and the other elements also make contributions to the characteristics of the proposed antenna.

5.6.3 Parametric Study

A number of parameters influence the performance of the hybrid water antenna. These include the water holder offset, the probe length, the stub length, the stub location, the stub rotate angle, and the ground plane dimensions. To investigate the effects of each part, parametric studies are performed. One parameter is changed at a time to observe its effects on the performance while other parameters are kept constant. The initial parameters are: L_g = 230 mm, W_g = 130 mm, T_g = 1mm, L_w = 50 mm, W_w = 49.5 mm, H_w = 2.7 mm, L_h = 52 mm, W_h = 51.5 mm, H_h = 10 mm, L_{m1} = 50 mm, W_{m1} = 10 mm, T_h = 1 mm, L_p = 50 mm, L_{pf} = 11 mm, L_s = 26 mm, θ = 10˚, Loc_s = 12 mm, D_h = 5 mm.

A. Effect of the water holder offset

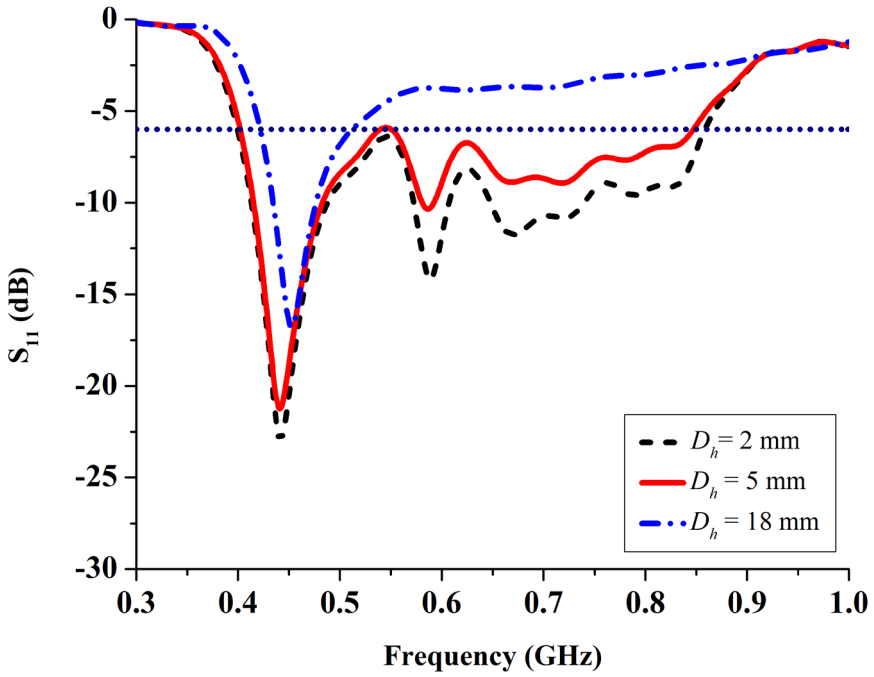

Fig. 5.26. Simulated S_{11} with different values of D_h.

To investigate the effects of the water holder offset, the simulated S_{11} (dB) with different values of D_h are plotted in Fig. 5.26. When the offset D_h is varied from 2 to 18 mm, the lower band around 440

MHz caused by the coupling between the F-shaped feeding probe and metal patch 2 as shown in Fig. 5.24(b) is quite stable while the impedance matching at higher frequencies becomes worse. This is because the matching at higher frequencies (around 800 MHz) is mainly determined by the metal coated DRA. By increasing the value of D_h, the space dielectric resonator (DR) overlapped with the ground plane increases, and this changes the boundary conditions. Decreasing the value of D_h leads to a wider bandwidth response which also increases the difficulty in fabrication. A trade-off between the achievable bandwidth and practical fabrication has been considered by choosing D_h = 5 mm in the final design.

B. Effect of the probe length

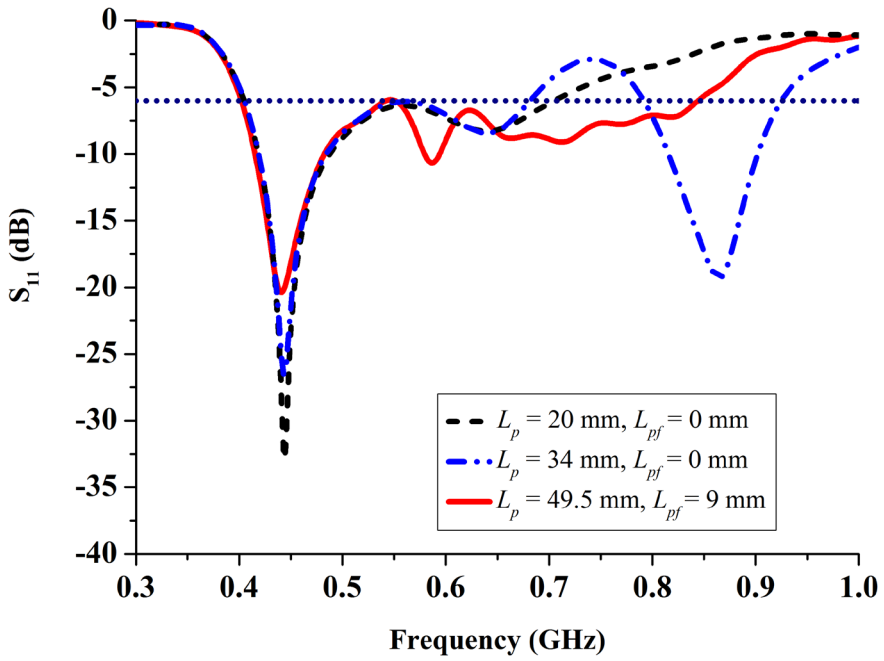

Fig. 5.27. Simulated S_{11} with different values of L_p and L_{pf}.

As a hybrid antenna, the feeding probe has two functions, namely excitation and radiation. To investigate the effects of the probe length, the simulated S_{11} as a function of L_p and L_{pf} is shown in Fig. 5.27. When the probe is short, the metal coated DRA is not properly excited, only two frequency bands are observed (black dash line in Fig. 5.27), one is mainly caused by the coupling between the feeding probe and metal patch 2 (as the stub is quite long, the coupling is not greatly affected by the probe length), the other is from the stub. As the probe length is increased, the metal coated DRA is excited; three separate bands appear (blue dash dot line in Fig. 5.27). By further increasing the probe length, the upper band determined by the metal coated DRA shifts downwards. Thus three bands are

combined and a wide bandwidth can be achieved when L_p = 49.5, L_{pf} = 11 mm (red solid line in Fig. 5.27).

C. Effect of the stub length, location and rotate angle

As water is a liquid dielectric material, a stub can be placed inside the water as shown in Fig. 5.22(b) to tune the impedance matching and also introduce a frequency band. Such a matching circuit is convenient, since no lumped elements are required. To better understand the importance of the stub in achieving a wideband response, the effects of the stub length, location and rotate angle are investigated.

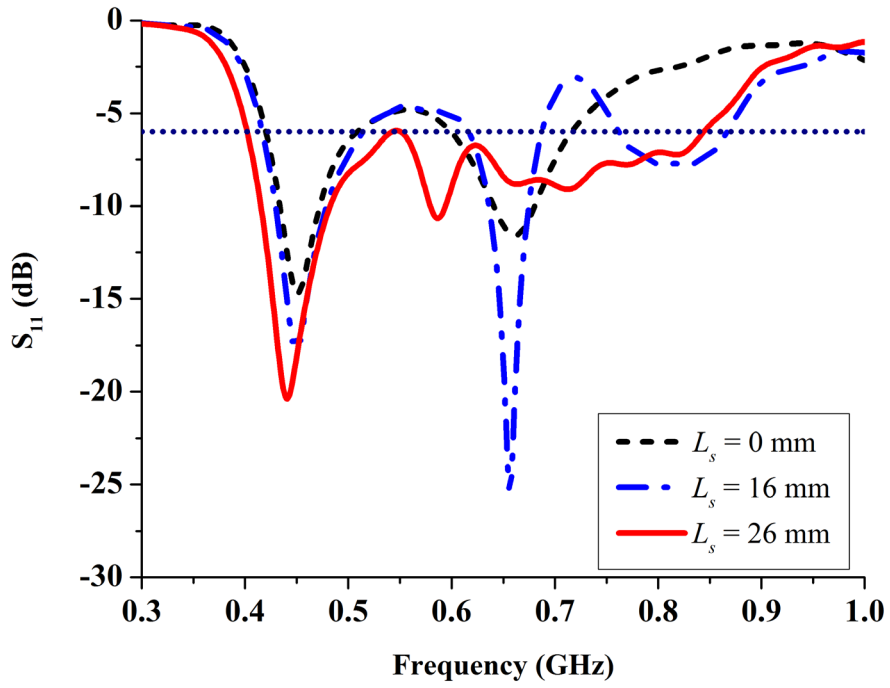

Fig. 5.28. Simulated S_{11} with different values of L_s.

As shown in Fig. 5.28, when L_s = 0 mm, the antenna covers two separate bands, 400 to 500 MHz band and 620 to 720 MHz band for S_{11} < -6 dB, corresponding to two troughs in black dash line in Fig. 5.28. These two bands are associated with coupling between the F-shaped probe and metal patch 2, and the metal coated DRA, respectively. By soldering the stub to the feeding probe, a third frequency band in blue dash dot line from 780 to 880 MHz is introduced. As the value of L_s is increased, the third frequency band is shifted downwards and becomes the middle band. Meanwhile, the frequency band associated with the metal coated DRA shift upwards, since the field inside the water DRA is

disturbed by the changing of the stub length. By combining these three different bands, a maximum -6 dB bandwidth can be achieved when L_s = 26 mm.

Besides the stub length, the stub location is also an important parameter affecting the performance of the antenna. By changing the location of the stub, the field inside the DRA is altered, which affects the impedance matching of the frequency band from 700 to 850 MHz. It is observed in Fig. 5.29, as the value of Loc_s is increased, the lower band caused by the coupling is quite stable; while the frequency band associated the stub and the water DRA is affected (because of the field inside the water is changed) . If the value of Loc_s is further increased, it could lead the bands associated with the stub and the water DRA to be over-merged at Loc_s = 18 mm corresponding to the blue dash dot line in Fig. 5.29. Separating these three bands properly leads to a larger bandwidth.

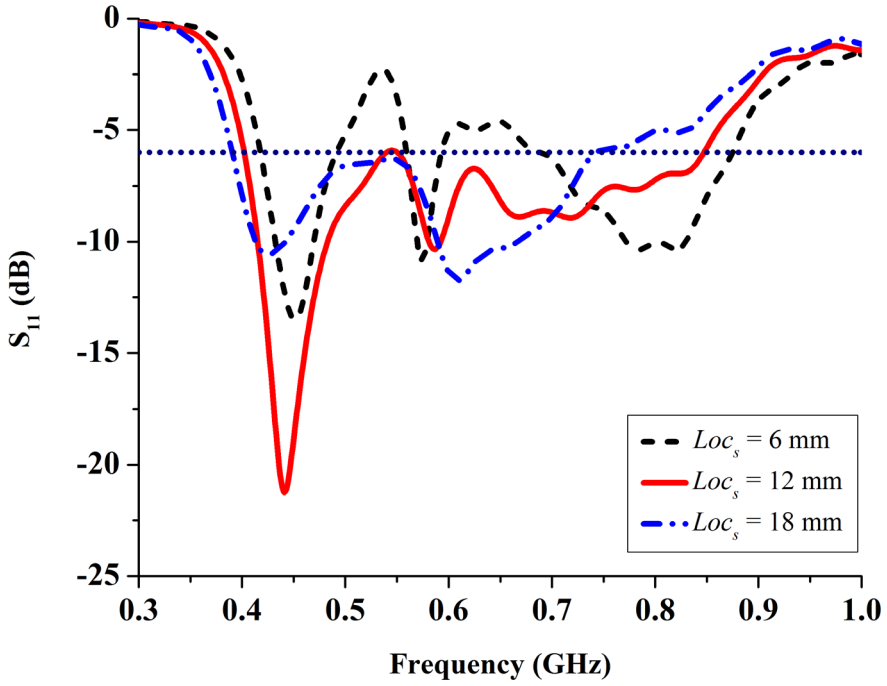

Fig. 5.29. Simulated S_{11} with different values of Loc_s.

Due to the transparency and liquidity of water, the stub can be easily tuned inside the water which provides a degree of control on the impedance matching over a wide band. It is noted in Fig. 5.30, by decreasing θ from 30° to 10°, it mainly affects the middle and higher bands, as the field inside the water will be disturbed and the bands introduced by the stub will be affected. For a smaller value of θ such as θ = -20°, the lower band will also be affected, because the coupling between the F-shaped probe and metal patch 2 will be weaker when θ is negative. When $\theta = 10^{\circ}$, the maximum -6 dB bandwidth can be obtained.

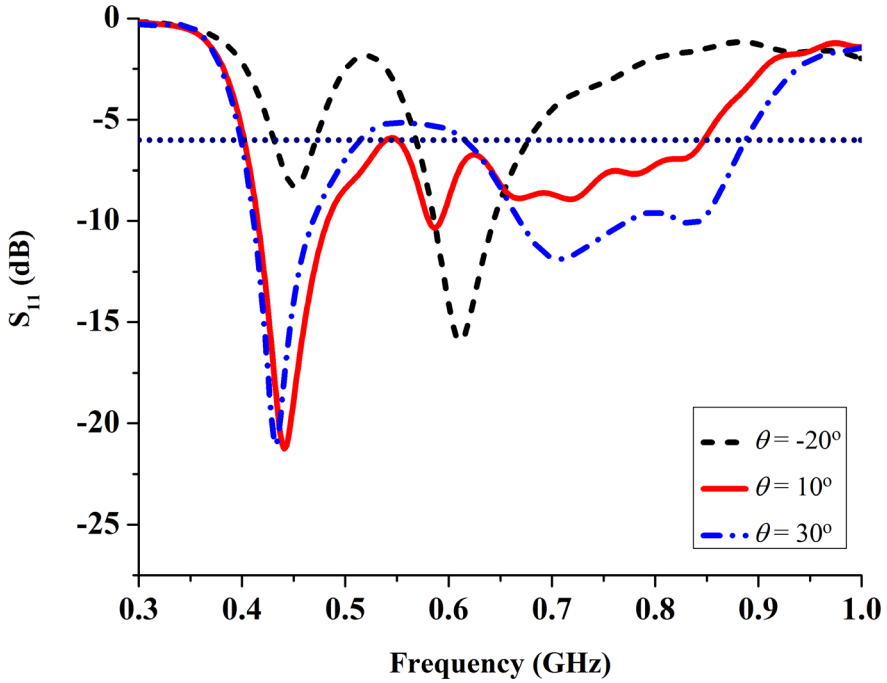

Fig. 5.30. Simulated S_{11} with different values of θ.

D. Effect of the ground plane size

The variations of S_{11} (dB) for different values of L_g have been compared to explore the ground plane effects. Usually, for hand-portable applications such as mobile phones, the ground plane will be part of the radiating element, influencing the input impedance of the antenna. It is observed in Fig. 5.31, for a given ground plane width W_g = 130 mm, the ground plane length affects the impedance matching of the antenna, but its effect on the lower band is bigger. When L_g is decreased from 220 to 100 mm, the impedance matching of the lower band is getting worse (the resistance at 430MHz is increased from 50 to 82 ohm), however, the -6 dB bandwidth across the whole band is stable, which is good for some space limited applications such as mobile phones, the ground plane can be reduced to save more space for other components. When the L_g is further reduced to 100 mm, the impedance matching of the lower band will become worse (the resistance at 430 MHz is 128 ohm), and the lower band gradually separates with other bands. It is necessary to place the metal coated DRA on a ground plane with $L_g \times W_g$=150 mm × 130 mm to promise a wideband performance. Besides the impedance matching, the ground plane size also affects the total efficiency of the antenna, which takes the mismatch into account. Higher total efficiency can be obtained when the antenna is well matched.

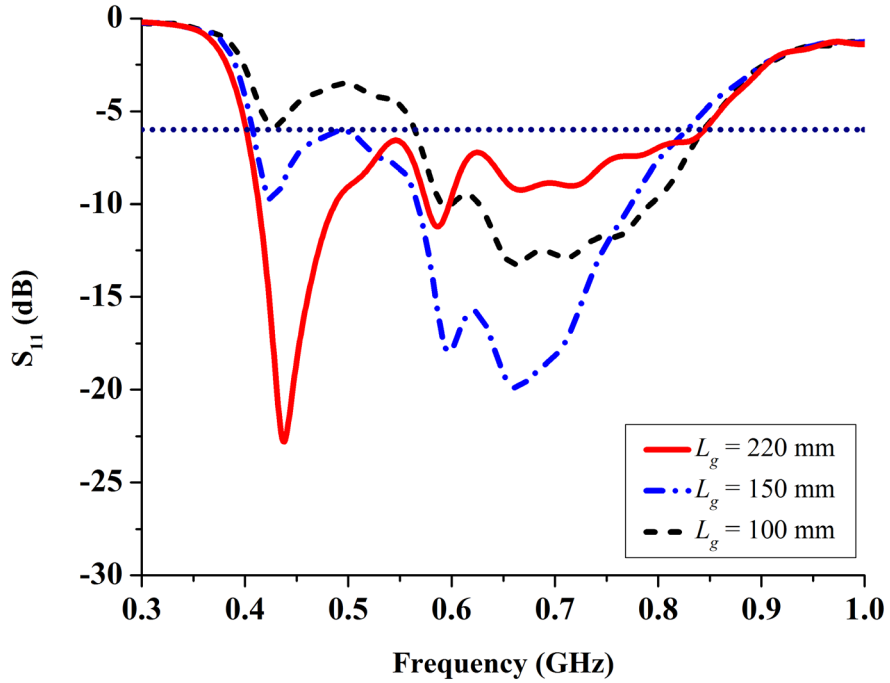

Fig. 5.31. Simulated S_{11} with different values of L_g.

The effects of various parameters on the antenna performance have now been carefully examined. Some interesting conclusions can be summarised as follows:

1) The selection of the water holder offset is very important in achieving the broad bandwidth, as it will affect the impedance matching at higher frequencies. Decreasing the value of D_h leads to a wider bandwidth response but also increases the difficulty in fabrication. A trade-off has to be considered between the achievable bandwidth and practical fabrication.

2) The probe length is also a critical parameter. The DRA mode cannot be properly excited, if the probe is too short. By increasing the length of the probe, the upper band shifts downwards.

3) The stub introduces a new band and also affects the impedance matching, as it will affect the field distribution inside the DRA. At a certain stub length, location and angle, the bandwidth can be maximised.

4) The ground plane size will influence the impedance matching and total efficiency of the antenna, and the effects on the lower band are bigger, especially the real part of the impedance at the lower band will be affected by the variations of ground plane size. In order to obtain a wide bandwidth, it is necessary to place the metal coated DRA on a ground plane with $L_g \times W_g$ =150 × 130 mm^2.

5) As shown in Fig. 5.24(b), a resonant mode is generated near 430 MHz, thus in all results we can see a trough in S_{11} near this frequency.

5.6.4 Measurement Results

To verify the design, an F-shaped probe feed hybrid water antenna was fabricated; the prototype of the proposed antenna is shown in Fig. 5.32(a). The optimal parameters are L_g = 230 mm, W_g = 130 mm, T_g = 1mm, L_w = 50 mm, W_w = 49.5 mm, H_w = 2.7 mm, L_h = 52 mm, W_h = 51.5 mm, H_h = 10 mm, L_{m1} = 50 mm, W_{m1} = 10 mm, T_h = 1 mm, L_p = 49.5 mm, L_{pf} = 11 mm, L_s = 26 mm, θ = 10˚, Loc_s = 12 mm, D_h = 5 mm. The S_{11}, radiation pattern, and realised gain were measured in an anechoic chamber. The radiation efficiency was measured in a reverberation chamber by using the two-antenna approach [17]. The reverberation chamber setup for the antenna efficiency test is shown in Fig. 5.32(b).

(a)

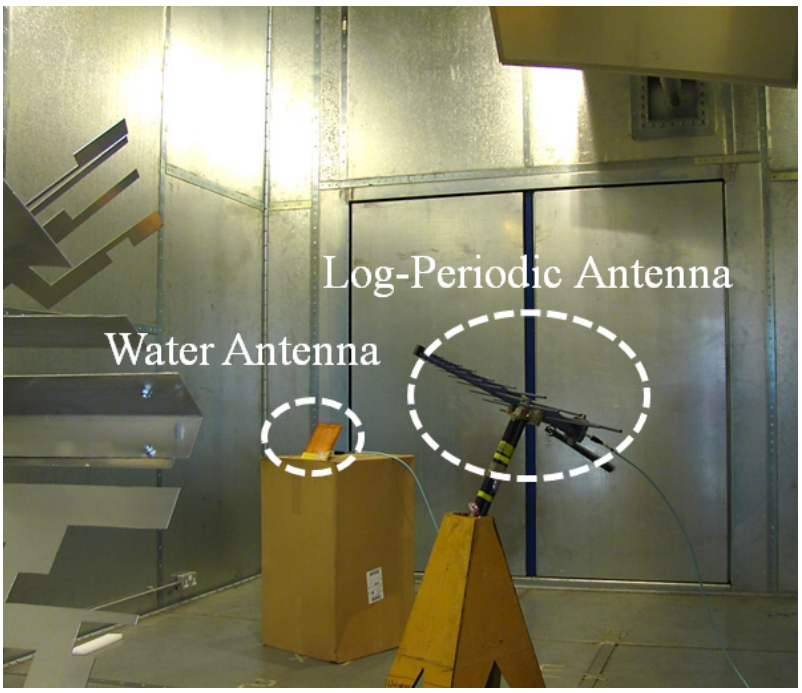

(b)

Fig.5.32. (a) Prototype of the water antenna. (b) Reverberation chamber setup for antenna efficiency test.

The simulated and measured results are compared in terms of S_{11}, radiation efficiency, realised gain as well as radiation pattern as shown in Figs 5.33-5.36. It is evident that the hybrid water antenna has a very broadband from 410 to 870 MHz for S_{11} < -6 dB (the fractional bandwidth > 70%). The radiation patterns corresponding to the polarisations of antenna are plotted at 460 MHz and 700 MHz, respectively. In order to avoid the cable effects, an RF choke was used in the measurement. The realised gain was measured in the direction of $\theta = 90°$, $\varphi = 45°$, again a good agreement is observed. As a reference, the maximum gain (a function of frequency) is added. The discrepancies between the simulations and measurements are mainly caused by two reasons: 1) fabrication error; 2) the material difference. The radiation efficiency of the antenna is larger than 70 % across the whole frequency band, except for the band around 600MHz. The E-field has a strong distribution in the water at the band around 600 MHz, causing more power loss ($\frac{1}{2}\int_V \vec{J} \cdot \vec{E}^* \, dV = \frac{\omega\varepsilon''}{2}\int_V \left|\vec{E}\right|^2 dV$), thus there is a dip in the radiation efficiency plot. Overall, a good agreement is achieved.

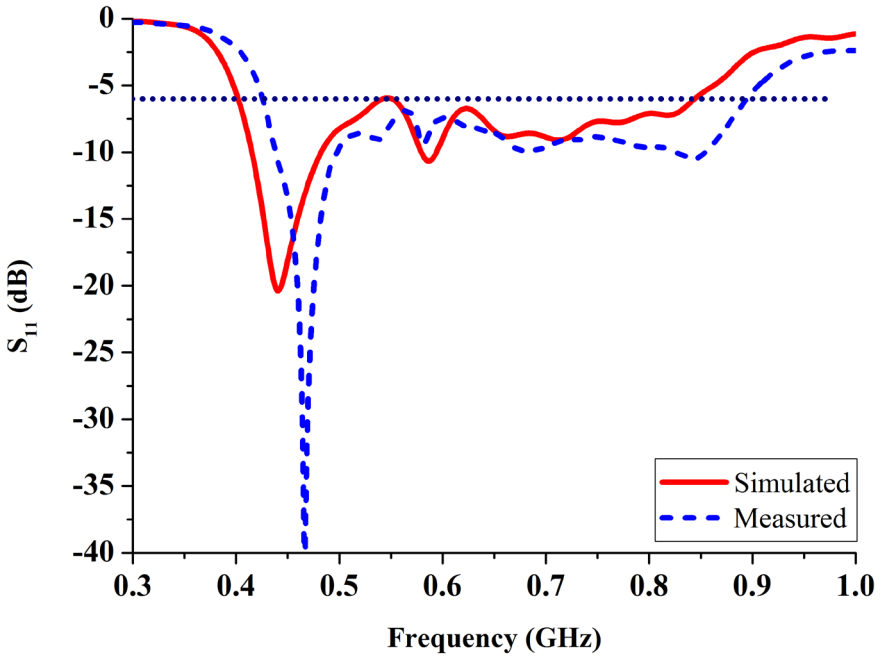

Fig. 5.33. Measured and simulated S_{11} (dB) of the proposed antenna.

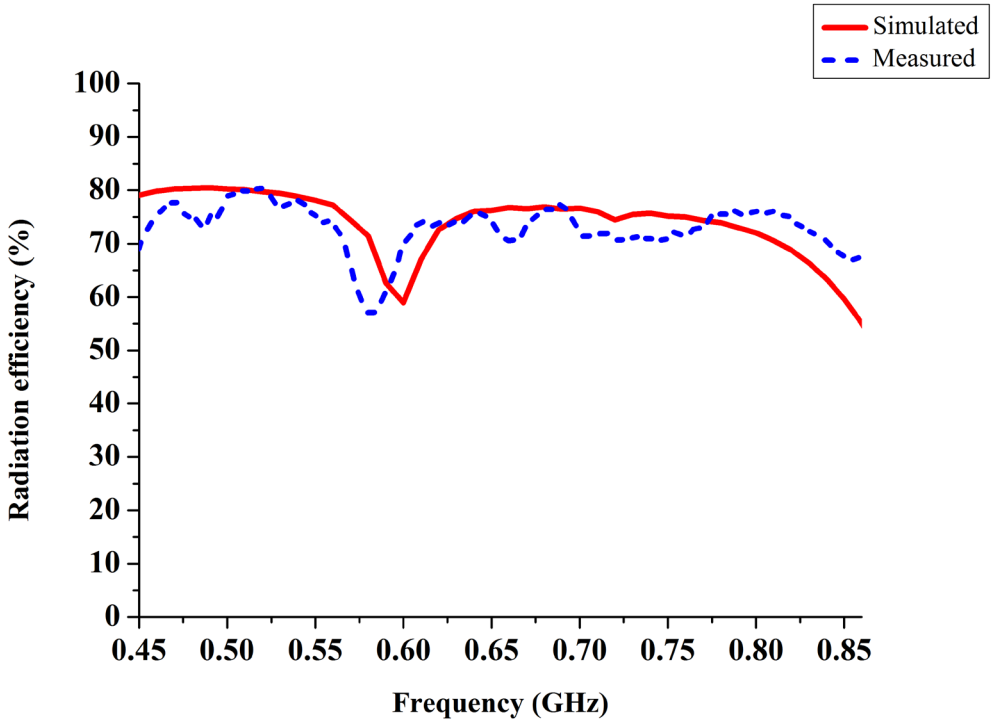

Fig. 5.34. Measured and simulated radiation efficiency of the proposed antenna.

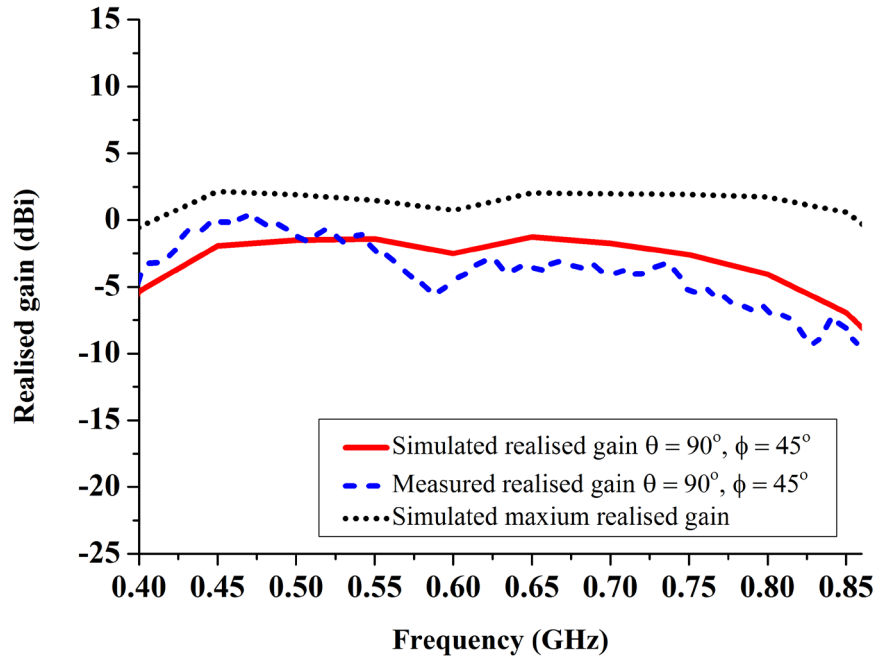

Fig. 5.35. Measured and simulated realised gain at the direction of $\theta = 90^{\circ}$, $\varphi = 45^{\circ}$ of the proposed antenna.

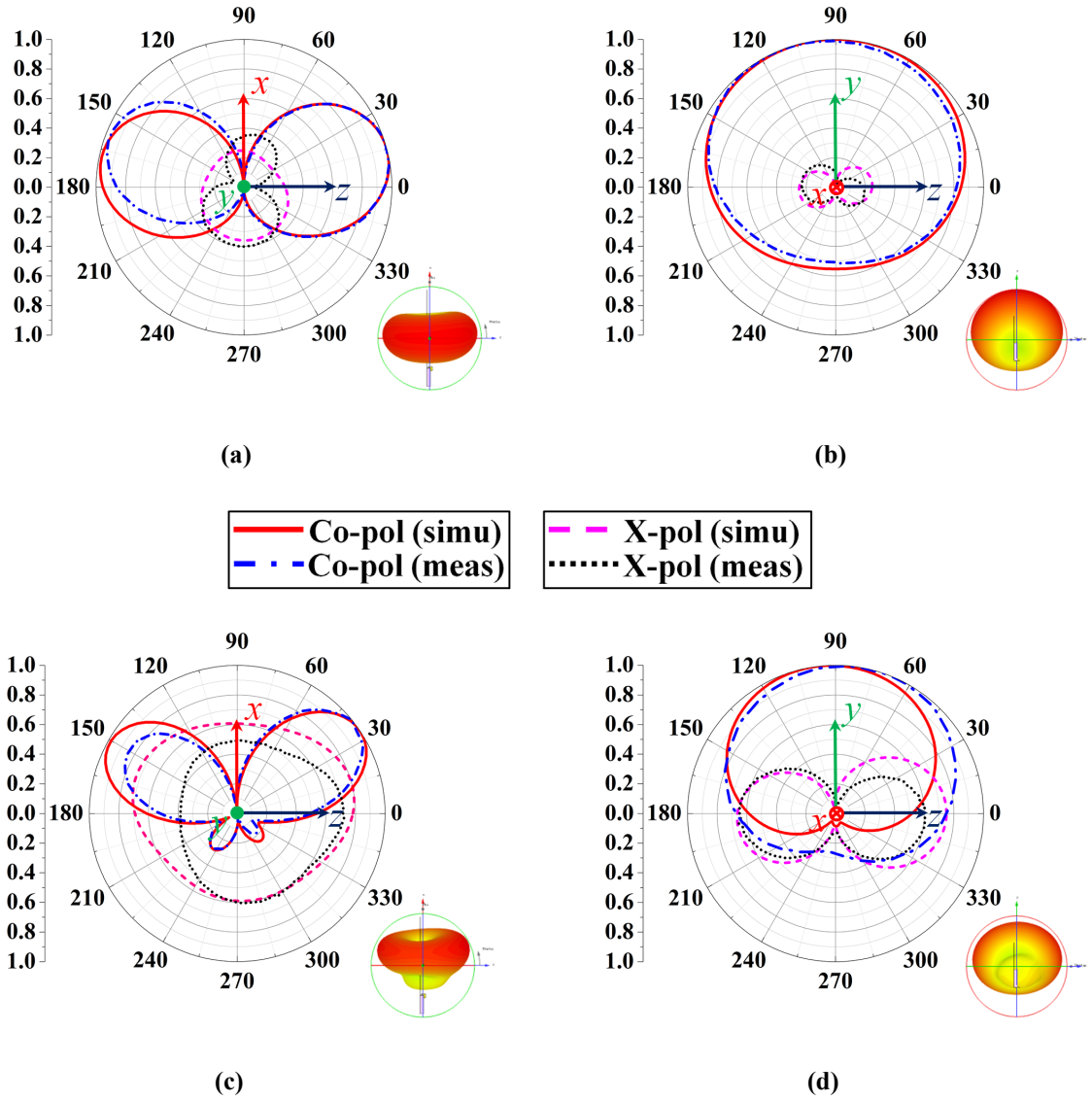

Fig. 5.36. 2D radiation patterns of the proposed antenna. (a) *f* = 460MHz, xoz plane. (b) *f* = 460MHz, yoz plane. (c) *f* = 700MHz, xoz plane. (d) *f* = 700MHz, yoz plane.

In this section, a low profile, wideband hybrid water antenna has been proposed. An F-shaped conducting probe placed inside the water has been designed to efficiently excite the water DRA and also work as a radiating element. Two metal patches have been added to specific faces of the structure to reduce the size of the antenna. The coupling between the feeding probe and the metal patch is well utilised to cover a lower band around 430 MHz, which is very hard to achieve for compact antennas. Three different bands associated with the strong coupling between the feeding probe and metal patches; the stub and the metal coated DRA have been effectively combined to realise a wideband response. A comprehensive parametric study has been performed and the effects of various parameters on the antenna performance have been carefully examined. Measurements have been conducted and the results agree well with the simulations. It has been demonstrated that by using the

F-shaped feeding probe, this hybrid antenna covers a very wide bandwidth from 410 to 870 MHz (a fractional bandwidth of 71.8%) with a compact size (52 × 51.5 × 10 mm^3, roughly 0.071 λ× 0.07 λ × 0.0136λ at 410 MHz) and high radiation efficiency over 60%.

5.7 Summary

In this chapter, three hybrid water antennas have been proposed, designed, optimised, fabricated and measured. The idea of a hybrid resonator antenna technique (HRAT) has been employed, which has combined the resonances of the water DR and the feeding probe. The conducting feeding probe can effectively improve the radiation efficiency of the antenna. Metal patches have been applied to specific faces of the structure, reducing the size of the antenna. The unique features of the water DR namely transparency, reconfigurability, and liquidity, allow complex structures (including the antenna feeding line) to be placed and freely tuned inside water.

The antenna design originated from a rectangular hybrid water antenna; by bending the rectangular water layer to a U-shaped water layer, the radiating element size has been reduced from 90 × 45.6 × 10.6 mm^3 to 78 × 45.6 × 11.8 mm^3. To further reduce the antenna size, the image theory has been implemented by attaching two copper sheets at the front and left side of the holder, the radiating element occupies a compact size of 52 × 51.5 × 10 mm^3 which is about half of the original design. With the size reduction of these designs, the feeding structures have been modified accordingly, from the L-shaped probe feed to the straight probe feed with a parasitic stub then to the F-shaped feeding probe. Although the sizes of the antennas are reduced considerably, bandwidths of these designs are still very wide, with a fractional bandwidth of 74.6% (rectangular hybrid water antenna), 70% (hybrid water antenna with a U-shaped water layer) and 71.8% (hybrid water antenna with an F-shaped monopole) for $S_{11} < -6$ dB.

These designs have successfully demonstrated the attractive features of water-based antenna. The results show that the hybrid structure with a combination of the conducting antenna and DRA is potentially very useful for low frequency, wideband applications. The research is extremely valuable for the water antenna development. The proposed water antennas can be very promising candidates for hand-portable applications such as DVB-H. The designs are not limited to the hand-portable applications; they can also be scaled for other applications.

It should be pointed out that there is a concern on the temperature-dependent performance of water-based antennas. This can be addressed by adding special materials (such as antifreeze), also the applications we are interested are mainly for domestic room temperature. For some extreme cases, this design may not be directly applicable, but the idea of the design is still valid.

5.8 References

[1] Q. Rao, T. A. Denidni, A. R. Sebak, "A hybrid resonator antenna suitable for wireless communication applications at 1.9 and 2.45 GHz," IEEE Antennas Wireless Propag Lett., vol. 4, pp. 341-343, 2005.

[2] Q. Rao, T. A. Denidni, A. R. Sebak, and R. H. Johnston, "Compact independent dual-band hybrid resonator antenna with multifunctional beams," IEEE Antennas Wireless Propag. Lett., vol. 5, pp. 239-242, 2006.

[3] D. Guha, B. Gupta, and Y. M. M. Antar, "New pawn-shaped dielectric ring resonator loaded hybrid monopole antenna for improved ultrawide bandwidth," IEEE Antennas Wireless Propag. Lett., vol. 8, pp. 1178-1181, 2009.

[4] Z. Jiang, M. D. Gregory, and D. H. Werner, "A broadband monopole antenna enabled by an ultrathin anisotropic metamaterial coating," IEEE Antennas Wireless Propag. Lett., vol. 10, pp. 1543-1546, 2011.

[5] L. Huitema, M. Koubeissi, M. Mouhamadou, E. Arnaud, C. Decroze, and T. Monediere, "Compact and multiband dielectric resonator antenna with pattern diversity for multistandard mobile handheld devices," IEEE Trans. Antennas Propag., vol. 59, no. 11, pp. 420-4208, 2011

[6] A. Buerkle, K. Sarabandi, H. Mosallaei, "Compact slot and dielectric resonator antenna with dual-resonance, broadband characteristics," IEEE Trans. Antennas and Propag., vol. 53, no. 3, pp. 1020-1027, 2005.

[7] "DVB-H Implementation Guidelines," ETSI TR 102 377 V1.1.1 (2005 - 02) European Telecommunications Standards Institute.

[8] A. Petosa, A. Ittipiboon, Y. M. M. Antar, D. Roscoe, and M. Cuhaci, "Recent advances in dielectric-resonator antenna technology," IEEE Antennas and Propag. Mag., vol. 40, pp. 35-48, 1998.

[9] A. Petosa, *Dielectric resonator antenna handbook*, Artech House, Inc., 2007.

[10] K. M. Luk and K. W. Leung, *Dielectric resonator antennas*, Research Studies Press Ltd., 2003.

[11] E. A. J. Marcatili, "Dielectric rectangular waveguide and directional coupler for integrated optics," Bell Syst. Tech. J., vol. 43, pp. 2071-2012, 1969.

[12] R. K. Mongia, A. Ittipiboon, "Theoretical and experimental investigations on rectangular dielectric resonator antenna," IEEE Trans. Antenna Propag., vol. 45, no. 9, 1997.

[13] R. K. Mongia, A. Ittipiboon, M. Cuhaci, and D. Roscoe, "Radiation Q-factor of rectangular dielectric resonator antennas-theory and experiment," in Proc. Int. IEEE AP-S Symp., vol. 2, pp. 764-767, 1994.

[14] T. Nakamura, M. Shimizu, H. Kimura and R. Sato, "Effective permittivity of amorphous mixed materials," Electron. Comm. Japan. Pt. I, vol. 88, issue 10, pp. 1-9, 2005.

[15] T. Meissner, F. J. Wentz, "The complex dielectric constant of pure and sea water from microwave satellite observations," IEEE Trans. Geosci. Remote Sens., vol. 42, no. 9, pp.1836-1849, 2004

[16] W. J. Ellison, "Permittivity of pure water, at standard atmospheric pressure, over the frequency range 0-25 THz and the temperature range 0-100˚C," J. Phys. Chem. Ref. Data, vol. 36, no. 1, pp. 1-18, 2007.

[17] C. L. Holloway, H. A. Shah, R. J. Pirkl, W. F. Young, D. A. Hill, and J. Ladbury, "Reverberation chamber techniques for determining the radiation and total efficiency of antennas," IEEE Trans. Antennas Propag., vol. 60, no. 4, pp. 1758-1770, 2012.

Chapter 6: 3D Water Loaded Reconfigurable Antennas for DVB-H Applications

6.1 Introduction

There is a growing interest and demand for compact and broadband antennas for DVB-H (digital video broadcasting-handheld) [1] and also DVB-T2-Lite [2] applications. This is a new standard for delivering broadcast television to a mobile terminal or handheld device, ranging from 470 to 862 MHz [1]. It aims to provide a generic way to serve handheld terminals in various parts of the world. There are two main challenges for the antenna design: 1) The frequency band covers a very wide fractional bandwidth of 59%; 2) The free space wavelength at 470 MHz is about 60 cm, which is very large in comparison with a typical size of a handheld device. A wideband coverage for DVB-H band could be achieved by using conventional approaches, but it would result in either a low efficiency or a large antenna size such as an ultra-wideband DRA with a modified sector shape [3] and a multiband ladder-shaped monopole antenna [4]. Fortunately, a permanent full coverage of the DVB-H band is not needed. Indeed, each channel with a 5 MHz bandwidth is required, and in a typical usage model, only one channel will be selected at one time [1]. Therefore, a frequency tunable narrowband antenna with a high tuning ratio, a small size and low return loss will be a good choice. RF switches and variable capacitors (varactors) are used to integrate with antennas to dynamically tune the resonant frequencies. Each time, a certain portion of the whole DVB-H band is covered, and it is able to provide a full coverage when all working states are combined. For example, a built-in antenna with frequency variability for DVB-H was reported in [5], which consisted of two channel matching networks and a spiral-shaped monopole radiator. By using the matching networks combined with the switches, a wide bandwidth was obtained. A compact varactor-tuned meander line monopole antenna was designed [6]. A continuously tuned operating band from 470 to 702 MHz was realised. A tunable compact printed monopole was proposed in [7], an inductor was loaded to shift the operating frequency from 915 to 470 MHz. To achieve antenna miniaturisation while covering the whole DVB-H frequency band, the use of dielectric material together with the integrated active components were reported [8-11]. In [8], a frequency tunable antenna constructed with a varactor diode and a modified monopole coupled loop antenna was developed. To reduce the size of the antenna, a high permittivity ceramic substrate (ε_r= 20) was used. Part of the DVB-H band is covered. Later, a magneto-dielectric material loaded monopole antenna was developed [9]. A comparison was performed between the

antenna with and without a magneto-dielectric resonator. In [10, 11], two 3D inverted F antennas with magneto-dielectric materials and varactor diodes were presented, where the radiating elements occupied small volumes. The magneto-dielectric material is composed of nanopowder which needs special shaping and appropriate thermal treatments. The magnetic losses increase quickly with the frequency from about 700 MHz [9].

In this chapter, two water loaded 3D reconfigurable antennas are proposed, designed and optimised. Different technologies such as the design of special folded monopole structures, the use of the water and its holder as a transparent dielectric loading, the integration of an active component, are combined to cover a full DVB-H band with an ultra-compact size.

The organisation of this chapter is as follows:

Section 6.2 presents a water loaded reconfigurable 3D folded monopole antenna. The design methodology and the working mechanism behind the design are stated. The characteristics of the varactor diode are presented. The effects of the transparent dielectric loading and ground plane dimensions are discussed. Simulation and measurement results are conducted. By following the same design procedure, a water loaded reconfigurable 3D folded meander line antenna with a smaller size is designed, optimised and measured in section 6.3. A summary is made in section 6.4 to review all findings.

6.2 A Water Loaded Reconfigurable 3D Folded Monopole Antenna

6.2.1 Antenna Configuration

The geometry of the proposed antenna is shown in Fig. 6.1. It consists of a monopole antenna with dimensions of 16 × 9 × 4 mm^3, a holder with dimensions of 10 × 9 × 4 mm^3, a rectangular water layer with dimensions of 8 × 7 × 0.7 mm3, four connecting strips and a 1.57 mm thick double grounded Rogers RT5880 printed circuit board ($\varepsilon_r = 2.2$) with dimensions of 230 × 130 × 1.57 mm^3, corresponding to a standard DVB-H handheld receiver for a tablet PC or portable TV handset. The monopole is folded to form a 3D compact structure, which is convenient to load the dielectric material. A short stub is connected to the starting end of the monopole and soldered to the back of the ground plane as shown in Fig. 6.1(b). The stub is used to tune the impedance matching of the antenna. The optimal length and location of the stub is chosen to obtain a maximal -6 dB bandwidth in the lowest operating band. A capacitor with a value of 100 nF is connected between the short stub and the

ground plane to work as a DC block and RF short, isolating the radiating element to the ground plane. The holder is made of transparent acrylic plastic with relative permittivity around 2.7 ~ 3. The holder and water can form a mixed transparent dielectric loading. Four connecting tips are placed at the corners of the water holder, with one end soldered to the monopole and the other end inserted into the water layer. These connecting tips are utilised to load the water and holder. Without the connecting tips, the water and holder cannot be loaded properly.

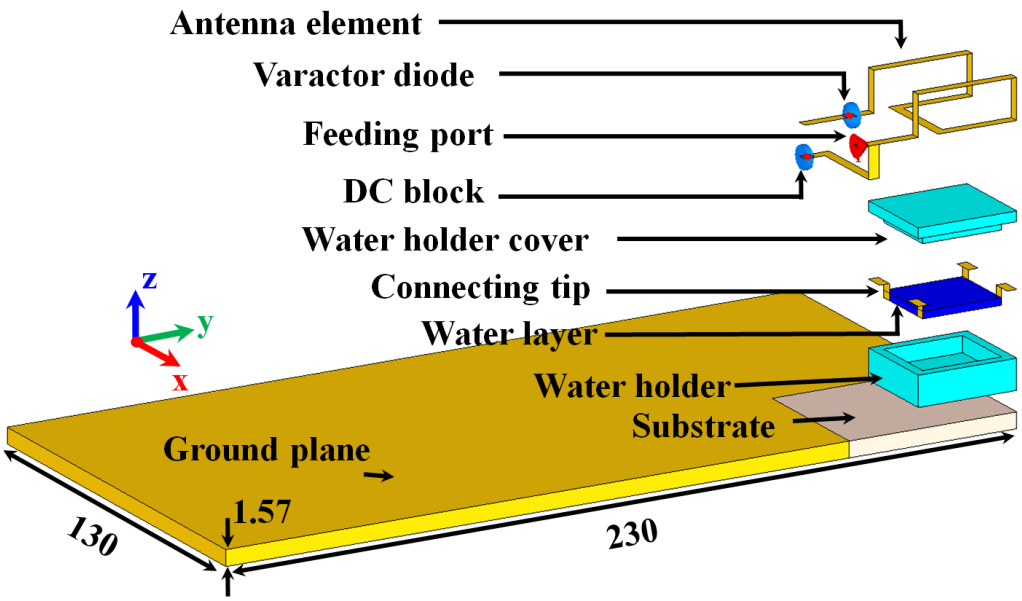

(a)

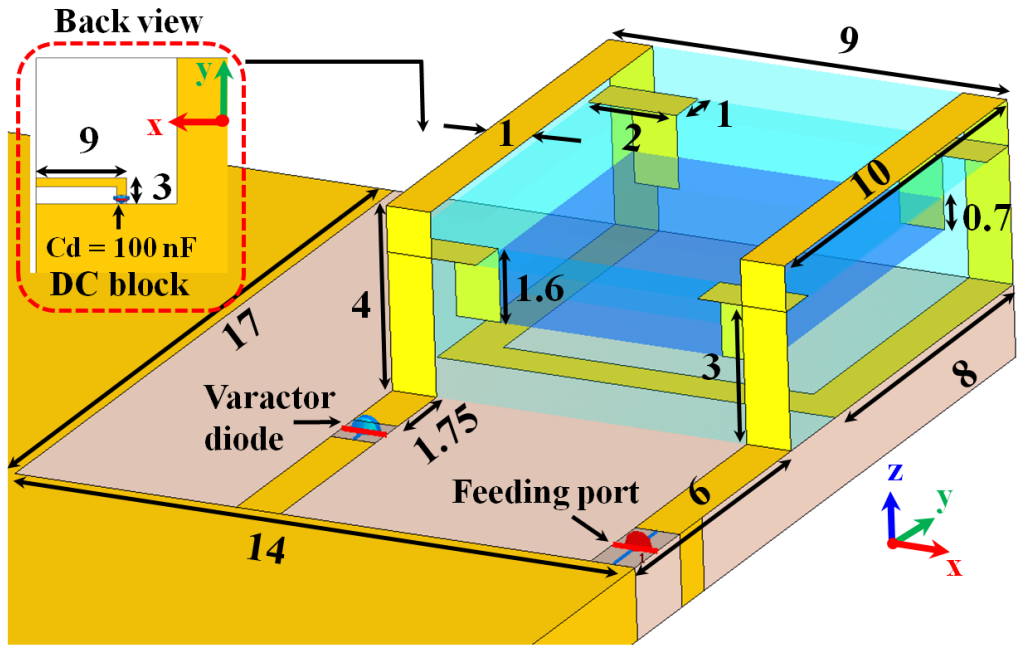

(b)

Fig. 6.1. Geometry of the proposed antenna (unit: mm). (a) Exploded view. (b) Enlarged view.

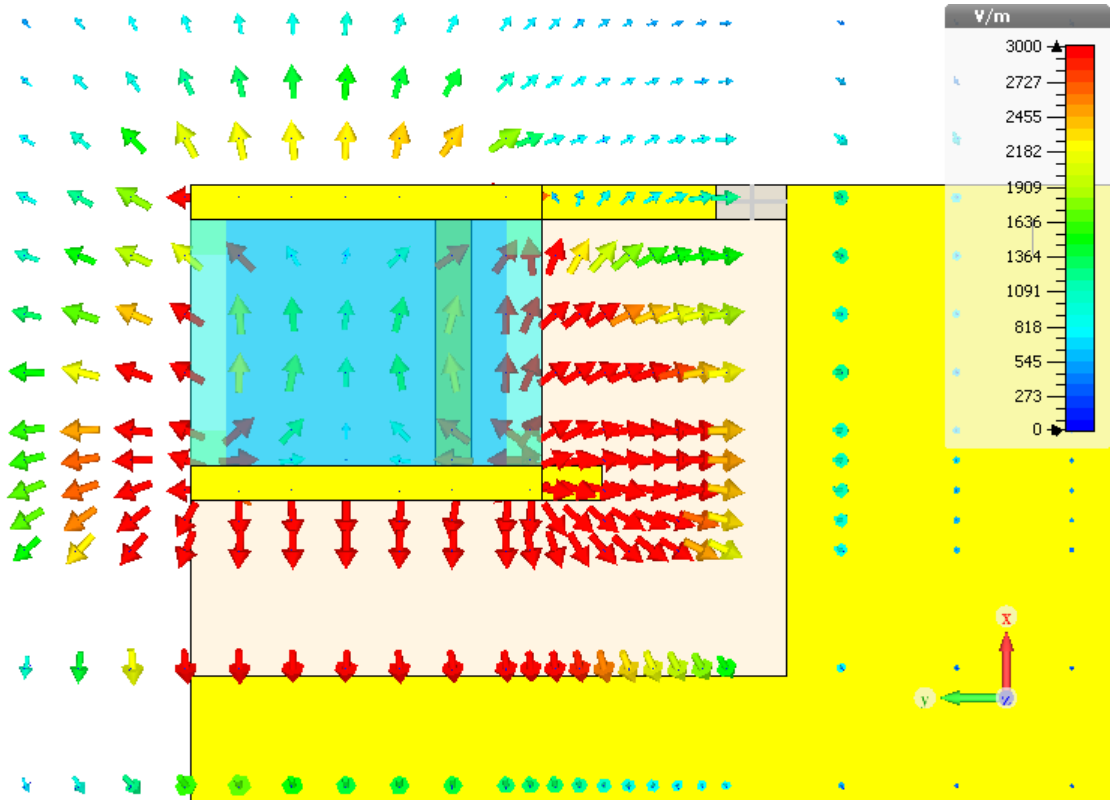

Fig. 6.2. E field distribution of the radiation element.

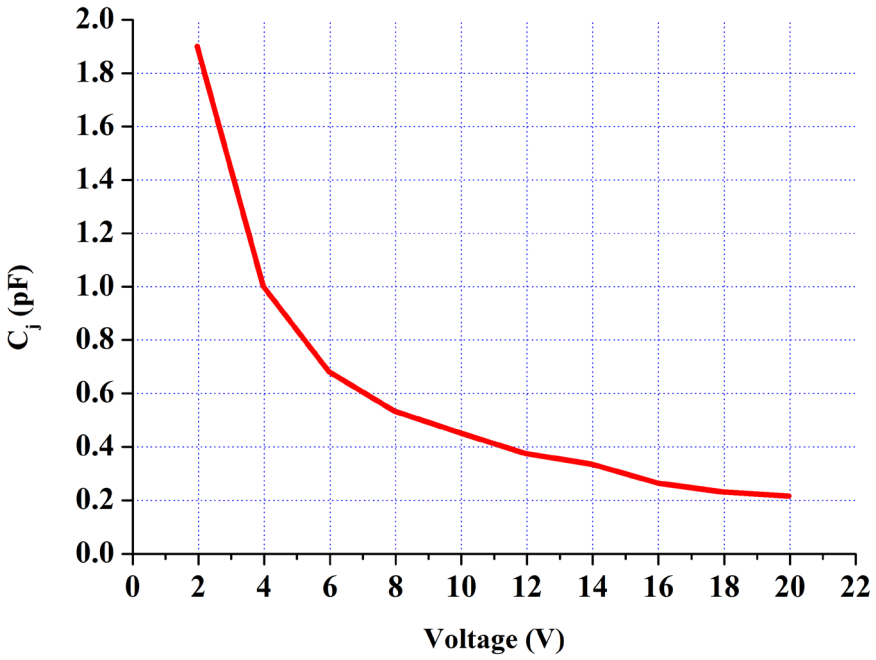

Fig. 6.3. Varactor diode MGV125-22-E28 capacitance value corresponds to the voltage [11].

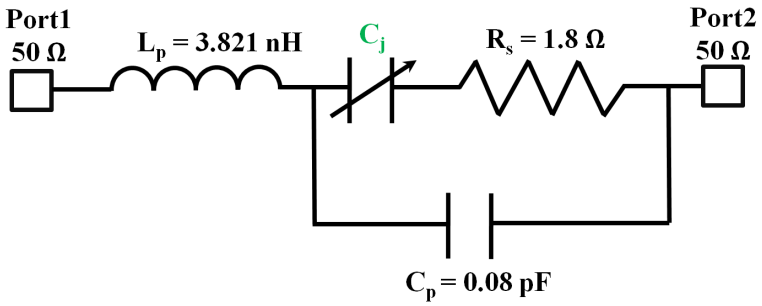

Fig. 6.4. Equivalent circuit of varactor diode MGV125-22-E28 [12].

A surface-mount GaAs varactor diode [12] is placed at the end of the monopole metallic strip. The location of the varactor diode is very important - it should be the place where the E field is maximum which is the end of the radiating element for a monopole as shown in Fig. 6.2. The varactor diode capacitance can be varied from 2 to 0.2 pF, as the biasing voltage is tuned from 0 to 20 V. The variation curve of the capacitance value corresponding to the voltage is presented in Fig. 6.3. The purpose of using the varactor diode is to load the antenna with a voltage-controlled capacitance, artificially increasing its electrical length and decreasing its resonant frequency. The equivalent circuit of the diode is shown in Fig. 6.4. The varactor diode is chosen for two reasons: 1) a small resistance R_s, which will not affect the efficiency of the antenna significantly; 2) a wide tuning range.

6.2.2 Transparent Dielectric Loading

Water is a high permittivity material and used as a dielectric loading in this chapter. It has many attractive features such as low-cost, transparent and readily accessible. However, water is not considered as a good loading, because: 1) the loss of water normally increases with the frequency; 2) the high permittivity may make the bandwidth of the antenna narrow; 3) its property is a function of temperature. For our application, the frequency is below 1 GHz, thus the loss is low and the temperature is room temperature (also antifreeze can be used for lower temperature environment [13]). By mixing the high permittivity material (water) with low permittivity material (water holder), the effective permittivity of the mixture will be reduced to improve the bandwidth [14]. By tuning the height ratio of the water layer to water holder, different values of effective permittivity can be obtained, which is a convenient way to obtain any desired permittivity. The loss of the combined case is lower than one with just water loading of the same antenna size.

In this section, the effects of the transparent dielectric loading to the antenna performance are examined in two aspects: 1) the performances of the antenna with and without the dielectric loading are compared; 2) the variations of the antenna bandwidth and total efficiency corresponding to the

water layer thickness are checked, while other parameters are kept unchanged. In the simulation, the water layer thickness and C_j is set as 0.7 mm and 0.2 pF, respectively. Water (CST Debye model) is used in the simulation, which agrees with the measured complex permittivity of pure water used in the experiment [15].

The simulated S_{11} and total efficiency of the proposed antenna with and without dielectric loading are shown in Fig. 6.5. The proposed antenna with and without dielectric loading work at the same resonant frequency (around 880 MHz), but with different dimensions. The antenna with dielectric loading has dimensions of 16 × 9 × 4 mm^3, while the antenna without dielectric loading has dimensions of 16 × 9 × 6.8 mm^3. After loading the water and holder, the bandwidth is slightly reduced (Fig. 6.5(a)), the total efficiency is decreased from 90% to 70% (Fig. 6.5(b)) at the peak frequency (880 MHz), which is acceptable for a DVB-H receiving antenna. However, 30% of the antenna volume reduction is achieved.

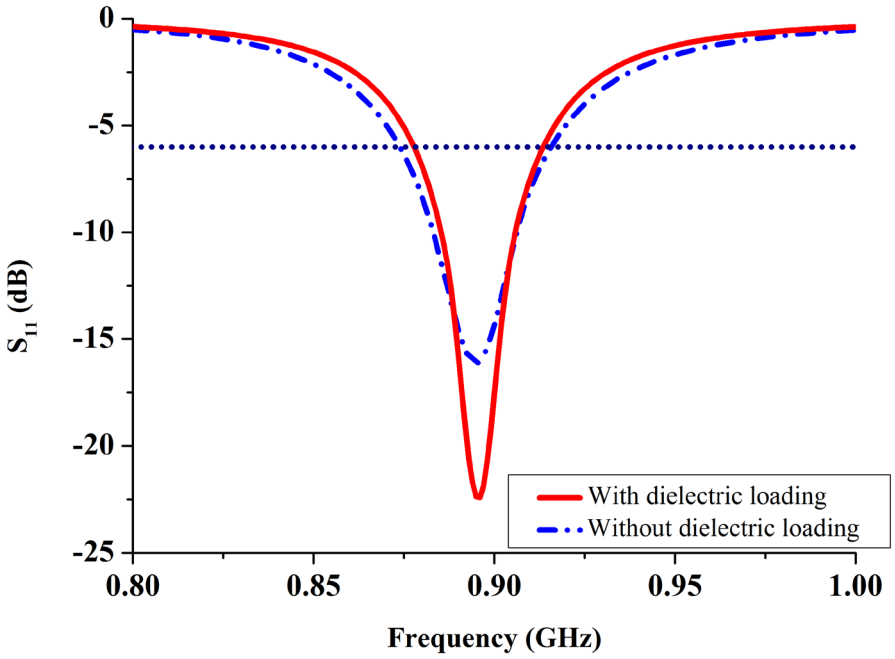

(a)

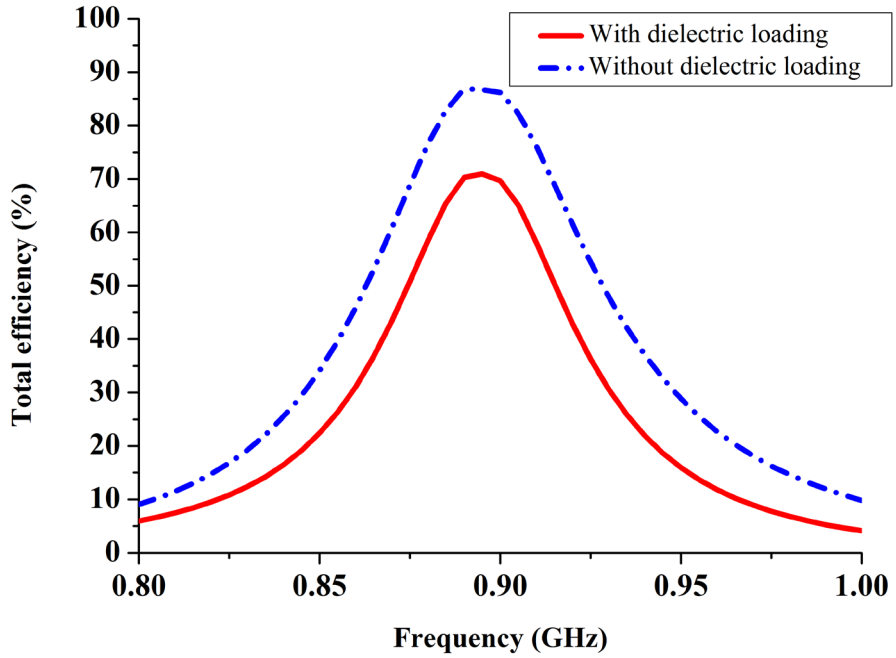

(b)

Fig. 6.5. Comparison of the proposed antenna with and without dielectric loading. (a) S_{11}. (b) Total efficiency.

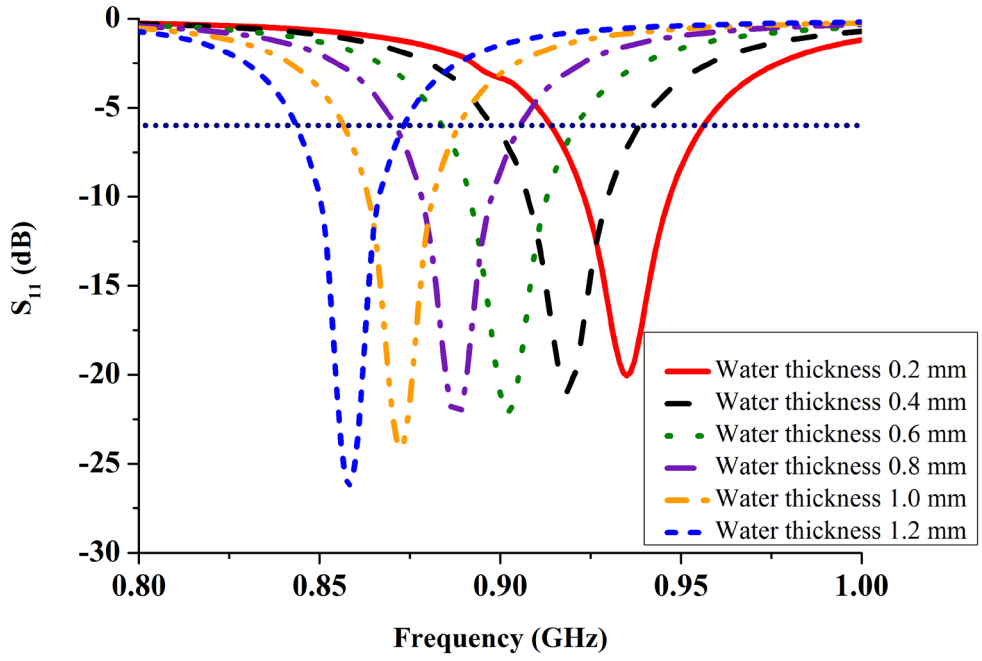

(a)

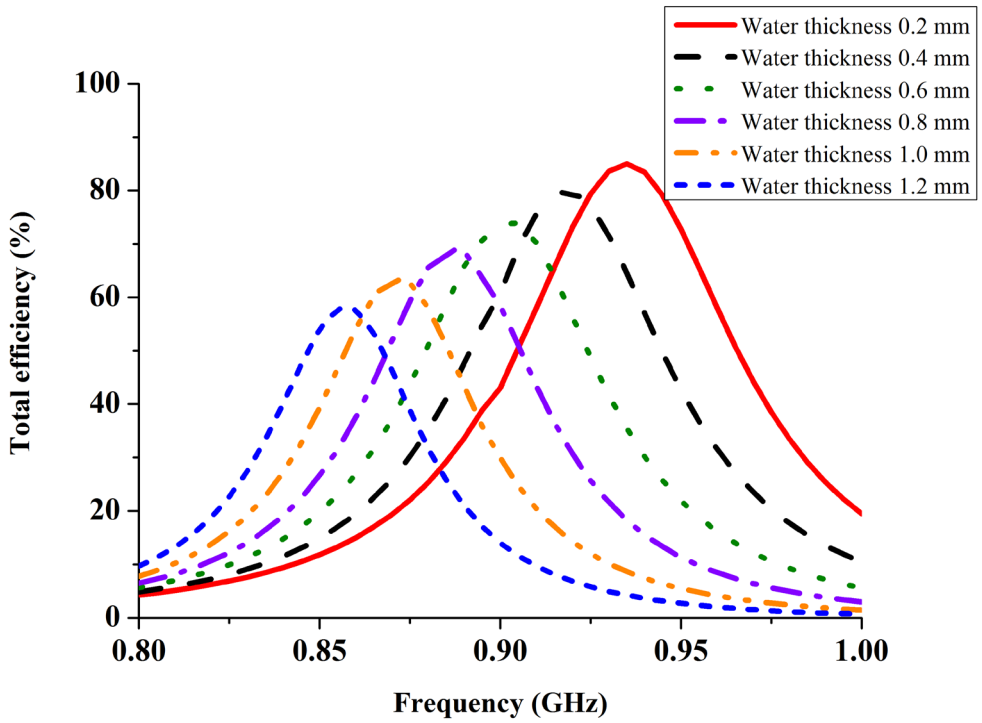

(b)

Fig. 6.6. Comparison of the proposed antenna with different water layer thickness values. (a) S_{11}. (b) Total efficiency.

The effects of the water layer thickness are investigated and shown in Fig. 6.6. It is observed that, for a fixed antenna height, by increasing the water thickness, the working frequency is shifted downwards as expected; and the total efficiency is decreased simultaneously. There exists a trade-off between the size and total efficiency. If a thick water layer is used, a low working frequency can be obtained. However, the total efficiency will be low. By choosing a proper water layer thickness, the antenna can have a relatively small size, acceptable bandwidth and high total efficiency.

6.2.3 Ground Plane Effects

For antennas designed for hand-portable applications, ground plane is a part of the radiating element, which affects the impedance matching of the antenna. As observed in section 6.2.2, the water layer thickness and C_j is set as 0.7 mm and 0.2 pF, respectively. In this section, the effects of ground plane dimensions are investigated. Two scenarios are considered. For a given ground plane width W_g = 130 mm, the simulated S_{11} with different values of L_g are compared in Fig. 6.7(a). It is observed that, by reducing the values of L_g, the S_{11} does not change significantly, indicating that for some applications, the ground plane length can be reduced to save some space. While for a given ground plane length L_g

= 130 mm, as shown in Fig. 6.7(b), by reducing the values of W_g, the impedance matching of S_{11} becomes worse, and the bandwidth becomes narrow. The reason is that when the value of W_g is changed from 130 to 30 mm, the resistance at 880MHz is increased from 106 to 196 ohm, which makes the antenna hard to be matched.

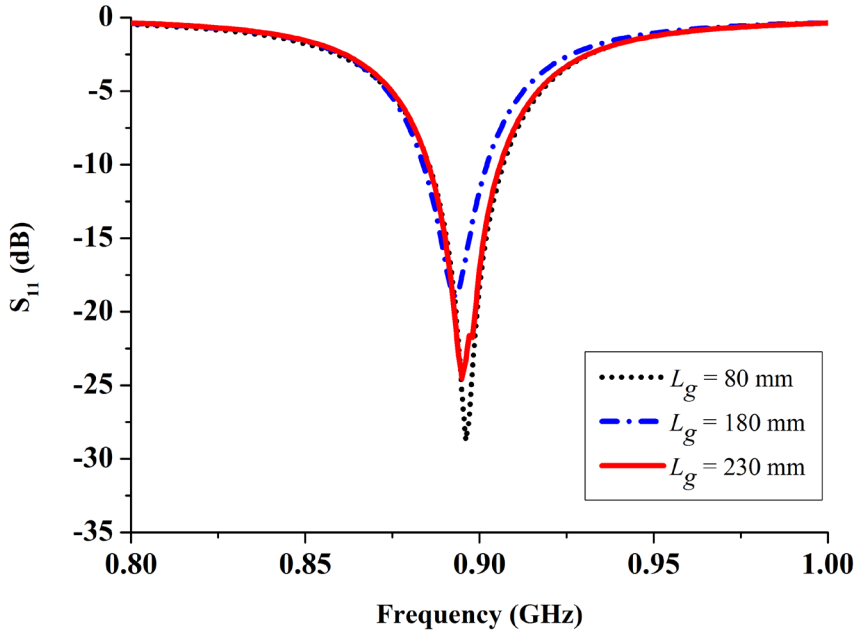

(a)

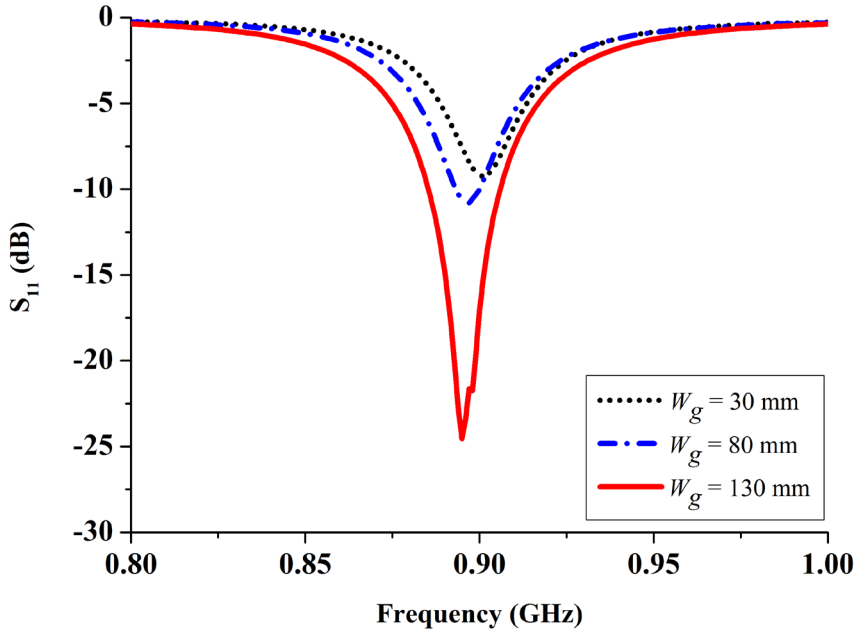

(b)

Fig. 6.7. (a) Simulated S_{11} with different values of L_g. (b) Simulated S_{11} with different values of W_g.

6.2.4 Temperature Effects

The complex permittivity of pure water is temperature dependent, and the antenna performance will be affected by the temperature. In this section, the temperature effects on the water loaded reconfigurable 3D folded monople antenna performance are investigated, the water layer thickness and C_j is set as 0.7 mm and 0.2 pF, respectively. The simulated S_{11} and total efficiency over different temperatures are compared in Fig. 6.8(a) and (b), where the measured permittivity data at temperatures 5°C, 25°C and 40°C were used in the simulations.

It is seen that by increasing the temperature from 5°C to 40°C , the resonant frequency of the antenna slightly shifts upwards, and the total efficiency increases. This is because, for pure water, in the frequency band of 0 to 1 GHz, ε' and ε'' decreases with the temperature. Overall, very similar shapes are observed.

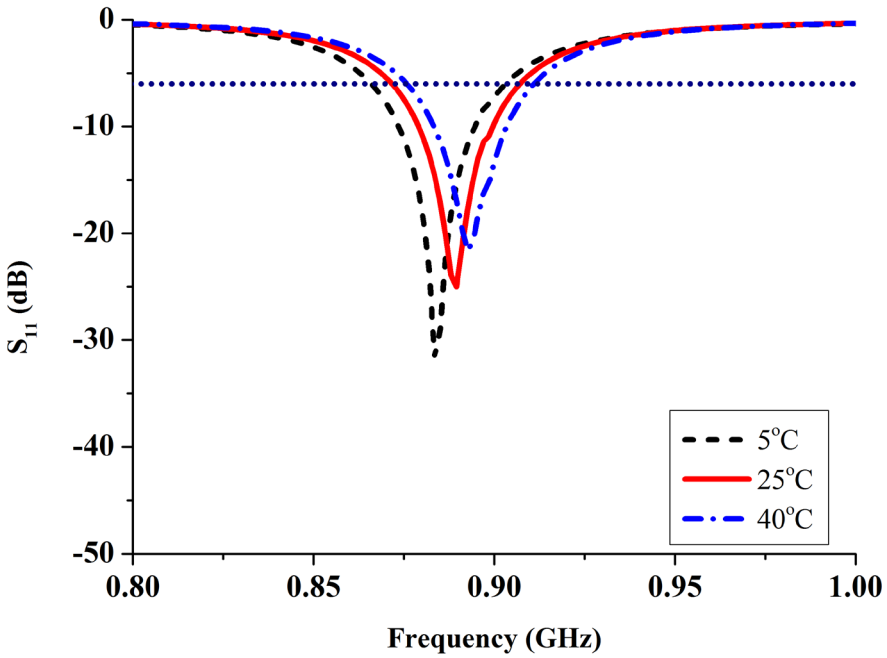

(a)

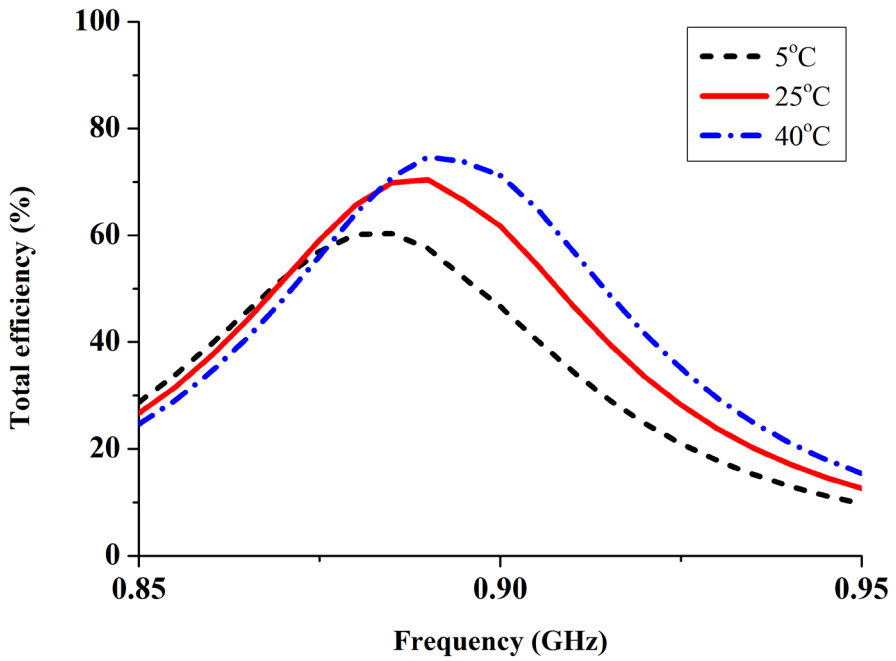

(b)

Fig. 6.8. Performance comparison of the proposed antenna for different temperatures. (a) Simulated S_{11} (in dB). (b) Simulated total efficiency.

6.2.5 Antenna Performance

To validate the design, the antenna with optimised dimensions has been fabricated and the prototype is shown in Fig. 6.9. The results are presented in terms of S_{11}, total efficiency and radiation patterns in Figs. 6.10 - 6.12. The complex permittivity of pure water used in the measurements can be found in [15]. The dielectric constant and loss tangent of pure water at 900 MHz and room temperature 25°C are ε_r = 78, $tan\delta$ = 0.045. The loss tangent of pure water is far less than that of the magneto-dielectric materials used in [9]. A bias Tee was connected between the antenna and VNA to supply a DC voltage to the varactor diode during the measurement.

Fig. 6.9. Prototype of the fabricated antenna.

For integrated antennas in handheld terminals, DVB-H implementation guidelines have requirements for the bandwidth and realised gain. The DVB-H standard splits the whole frequency band (from 470 to 862 MHz) in several channels. For each channel, 5 MHz channel bandwidths are necessary. The estimated antenna gain would be in the order of -10 dBi at the lowest UHF-band frequencies increasing to -5 dBi at the end of UHF-band, the antenna gain between these frequencies can be obtained by linear interpolation, that is -10 dBi at 474 MHz (channel 21), -7 dBi at 698 MHz (channel 49) and -5 dBi at 858 MHz (channel 69) [1].

As shown in Fig. 6.10, by tuning the voltage values from 1 to 20 V, the operating frequency can be continuously tuned from 419 to 883 MHz. The narrowest bandwidth for S_{11} < -6 dB is 9 MHz at 423MHz. The widest bandwidth is 43 MHz at 863 MHz, well satisfying the DVB-H bandwidth criteria (5 MHz).

The total efficiency (defined as the ratio of the power radiated to the power available at the antenna port, which is the radiation efficiency multiplied by the impedance mismatch loss of the antenna) was measured in a reverberation chamber by using the approach described in [16]. For different DC voltage values, the total efficiency was measured and the envelope is recorded in Fig. 6.11. As a reference, the total efficiency of an omnidirectional antenna with required DVB-H realised gain [1] is given. It is observed the total efficiency of the proposed antenna is higher than that of an omnidirectional antenna with DVB-H specifications. According to the relationship of the efficiency, gain and directivity ($G_{realised} = \eta_{total} \cdot D$), it can be concluded that the realised gain of the proposed antenna is higher than the DVB-H specifications, as both the directivity and the total efficiency are higher than that of an omnidirectional antenna with the required DVB-H realised gain, thus the proposed design fulfills the DVB-H requirement.

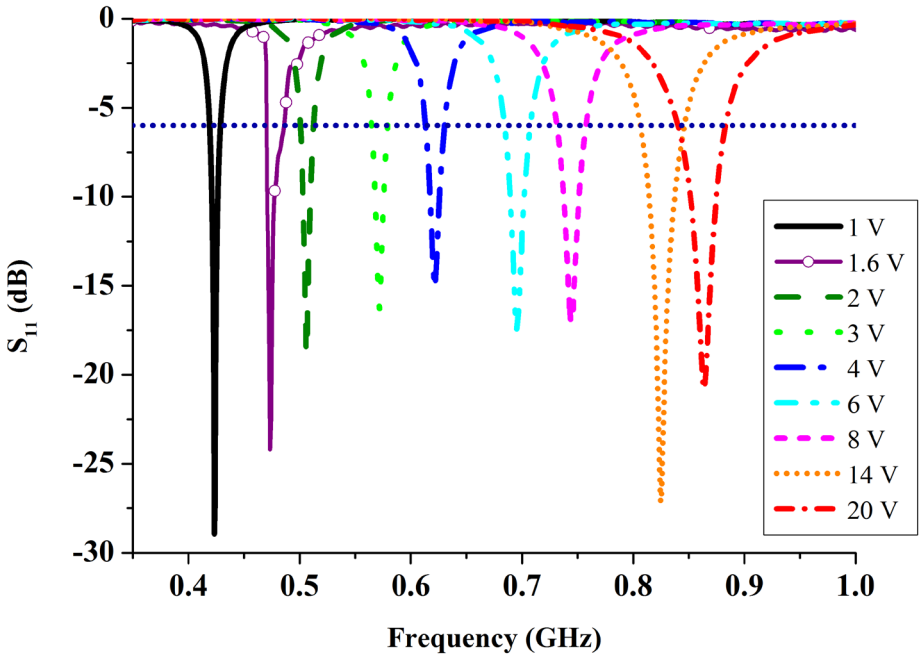

Fig. 6.10. Measured S_{11} (dB) of the proposed antenna.

The radiation patterns were measured in an anechoic chamber. Both simulated and measured radiation patterns (dual polarisations) have been shown in Fig. 6.12 at 622 MHz and 880 MHz, respectively. Overall, good agreements are achieved.

In this section, a compact folded monopole with a transparent dielectric loading has been proposed, designed, optimised and measured. The antenna has realised a very wide tuning band from 419 to 883 MHz, with a narrowest bandwidth 9 MHz at 423MHz and a widest bandwidth is 43 MHz at 863 MHz for S_{11} < -6 dB, which is apparently larger than the required 5 MHz for each channel. The antenna has high total efficiency especially at higher frequencies, meeting the efficiency requirements for a DVB-H receiving antenna. By integrating a transparent dielectric loading, 30% of the antenna volume is reduced. The measurement results demonstrate that this antenna has fulfilled the DVB-H requirements and is a very promising candidate for DVB-H applications. In future, more work will be done to further improve the total efficienty in the lower frequencies.

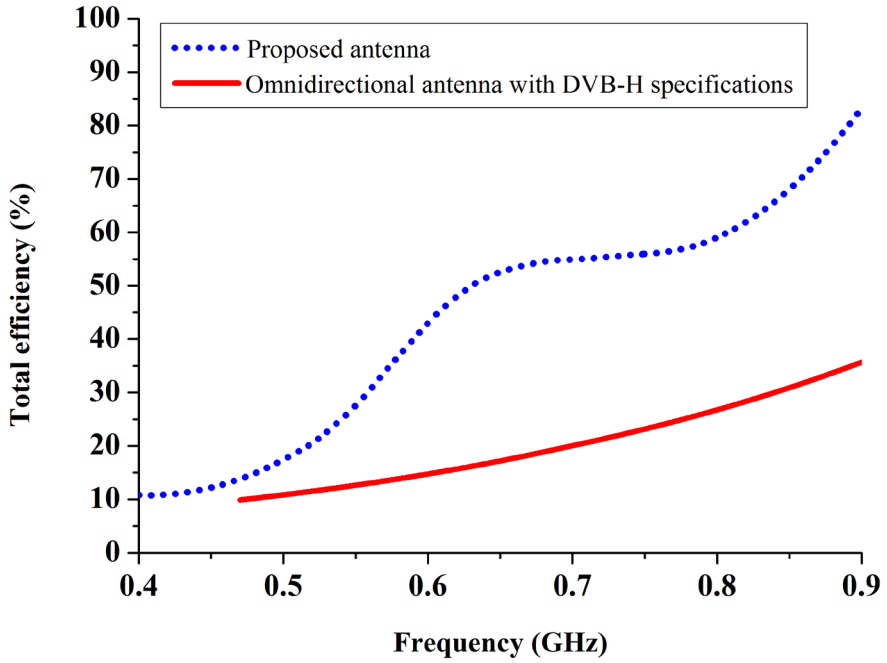

Fig. 6.11. Measured total efficiency of the proposed antenna.

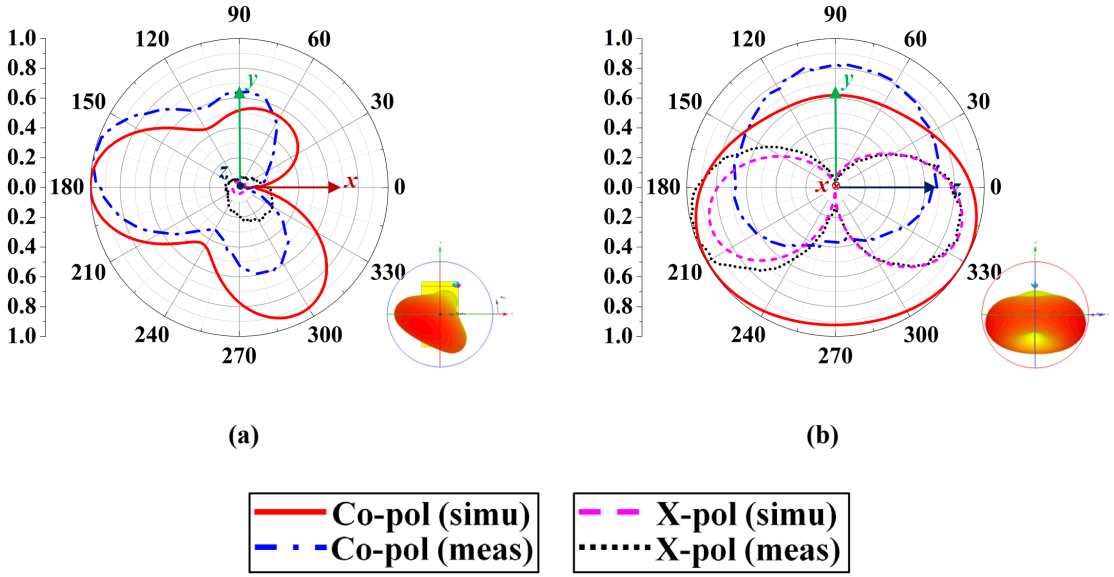

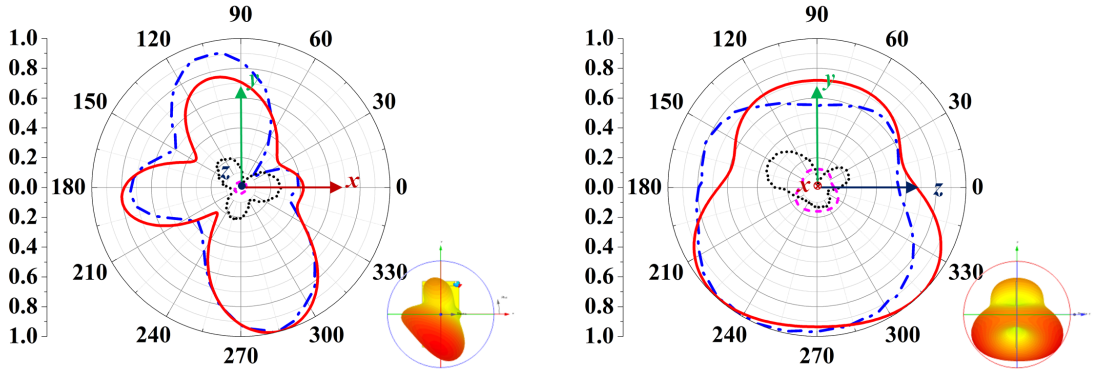

(c) (d)

Fig. 6.12. Measured and simulated radiation pattern of the proposed antenna. (a) Xoy plane at 622MHz. (b) Yoz plane at 622MHz. (c) Xoy plane at 880MHz. (d) Yoz plane at 880MHz.

6.3 A Water Loaded Reconfigurable 3D Folded Meander Line Antenna

6.3.1 Antenna Configuration

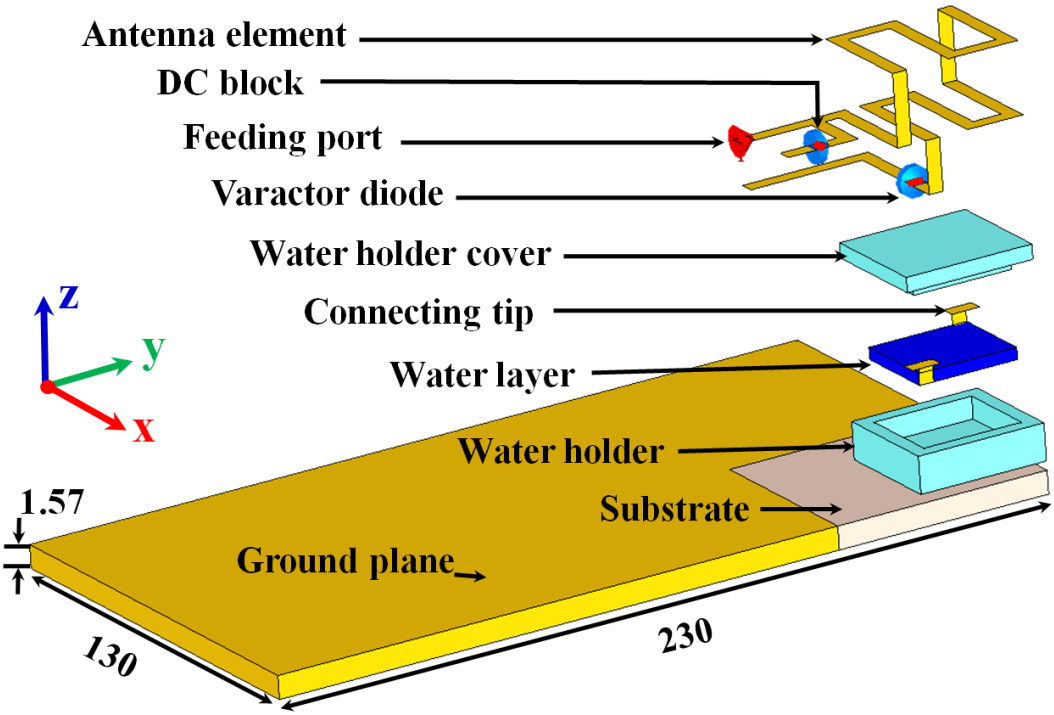

(a)

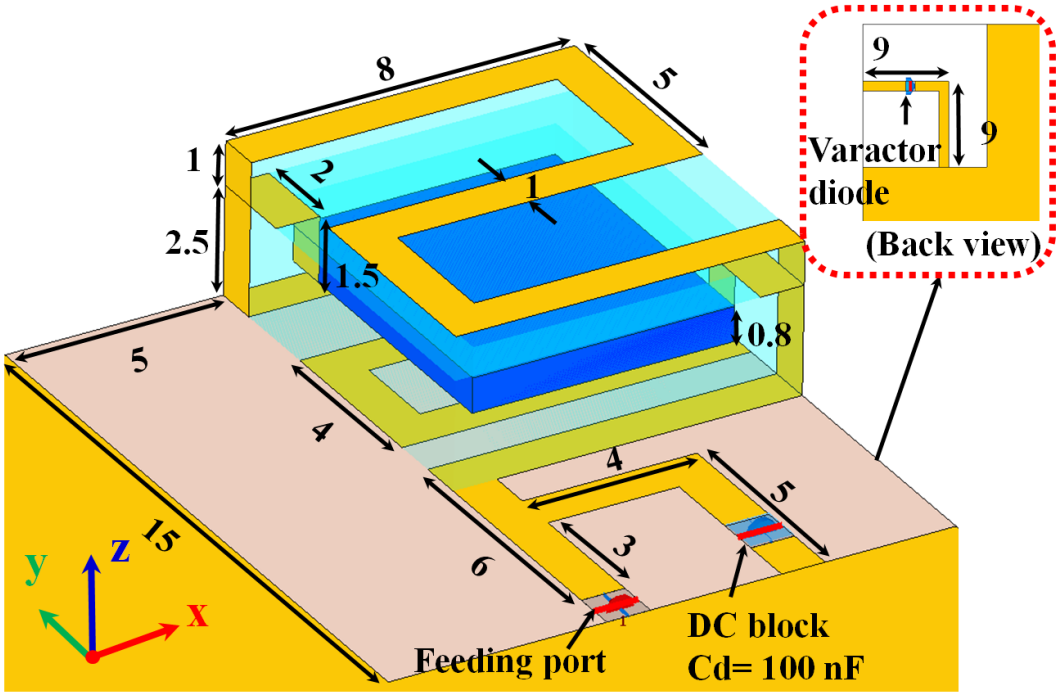

(b)

(c)

Fig. 6.13. Geometry of the proposed antenna (unit: mm). (a) Exploded view. (b) Enlarged view. (c) Fabricated antenna.

Based on the previous section, the special 3D folded meander line structure is employed to further reduce the antenna dimensions.

The configuration of the proposed antenna is shown in Fig. 6.13. It consists of a 3D folded meander line monopole antenna with dimensions of 8 × 15 × 3.5 mm^3, a rectangular water holder with dimensions of 8 × 10 × 3.5 mm^3, a rectangular water layer with dimensions of 6 × 8 × 0.8 mm^3 inside the holder, and a ground plane (made of Rogers RT5880 printed circuit board) with dimensions of 230 × 130 × 1.57 mm^3. The water holder is made of acrylic plastic as the previous design. The 3D folded

monopole includes three parts: the 3D meander line, a strip line connected to the feeding port and the L-shape short matching stub. The strip line with a length of 5 mm is to improve the impedance of the antenna (resistive part), as when the radiating element is too close to the ground plane, the resistance could be too small. The short matching stub is to tune the impedance matching across the frequency band of interest. A capacitor with a value of 100 nF is inserted in the matching stub to act as a DC block and an RF short. The height ratio of the water layer to water holder is 0.8 : 3.5, giving an effective relative permittivity around 20. Two connecting tips are used, with one end soldered to the meander line strip and the other end inserted into the water layer. After loading the water and holder, the volume of the antenna is reduced by half to 8 × 10 × 3.5 mm^3 (folded monopole with water and holder loading). The total metallic strip length is roughly 90 mm, which is around a quarter wavelength at 862 MHz (the higher bound of DVB-H band).

6.3.2 Antenna Performance

The measured S_{11} results with the bias voltages from 1.5 to 20 V are presented in Fig. 6.14. The DC voltage is added over the varactor diode by connecting a bias Tee between the antenna and VNA. It can be seen that the operating frequency can be continuously tuned from 463 to 900 MHz. The narrowest bandwidth for S_{11} < -6 dB is 9 MHz at 466MHz. The widest bandwidth is 18 MHz at 886 MHz which well meets the required channel width criteria for DVB-H reception (5 MHz).

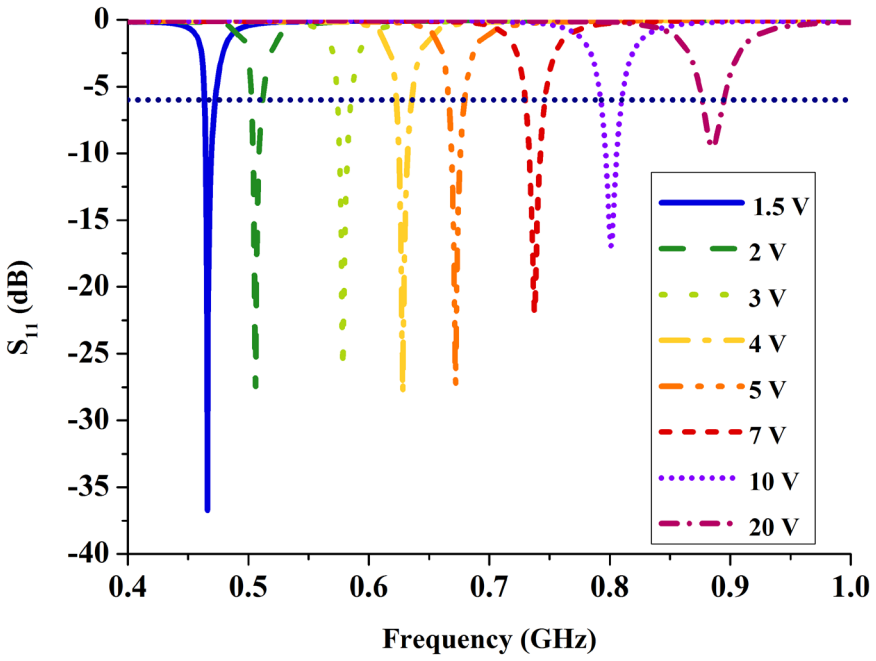

Fig. 6.14. Measured S_{11} (dB) of the proposed antenna with different bias voltages.

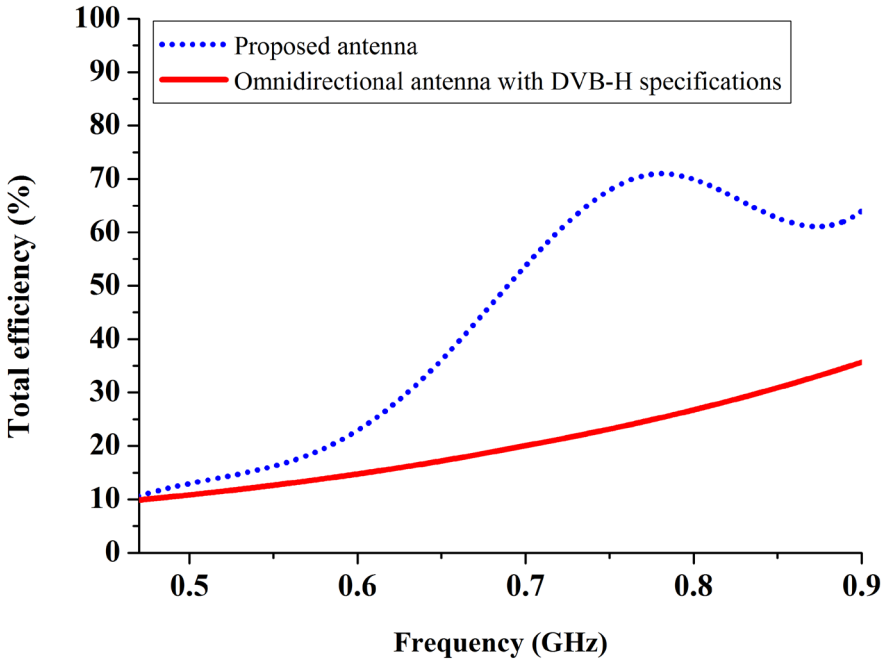

Fig. 6.15. Measured total efficiency.

The antenna efficiency measurement was performed in a reverberation chamber and the result is shown in Fig. 6.15. Compared with published designs [9-11], the total efficiency of this new antenna is much higher, especially at high frequencies. The total efficiency of an omnidirectional antenna with required maximum DVB-H realised gain [1] is plotted as a reference. In Fig. 6.15, the total efficiency of the proposed antenna is larger than the total efficiency of an omnidirectional antenna with the required realised gain, and the maximum directivity of the proposed antenna will be higher than 1 (omnidirectional antenna), thus the realised gain of the proposed antenna will certainly be higher than the DVB-H standard [1], indicating that the proposed antenna satisfies the DVB-H requirements.

The radiation patterns (dual polarisations) at 640 MHz and 890 MHz were measured in an anechoic chamber, respectively. The comparisons between the measurement and simulation results are displayed in Fig. 6.16. The simulated 3D patterns at the same frequency are presented. Good agreements are observed.

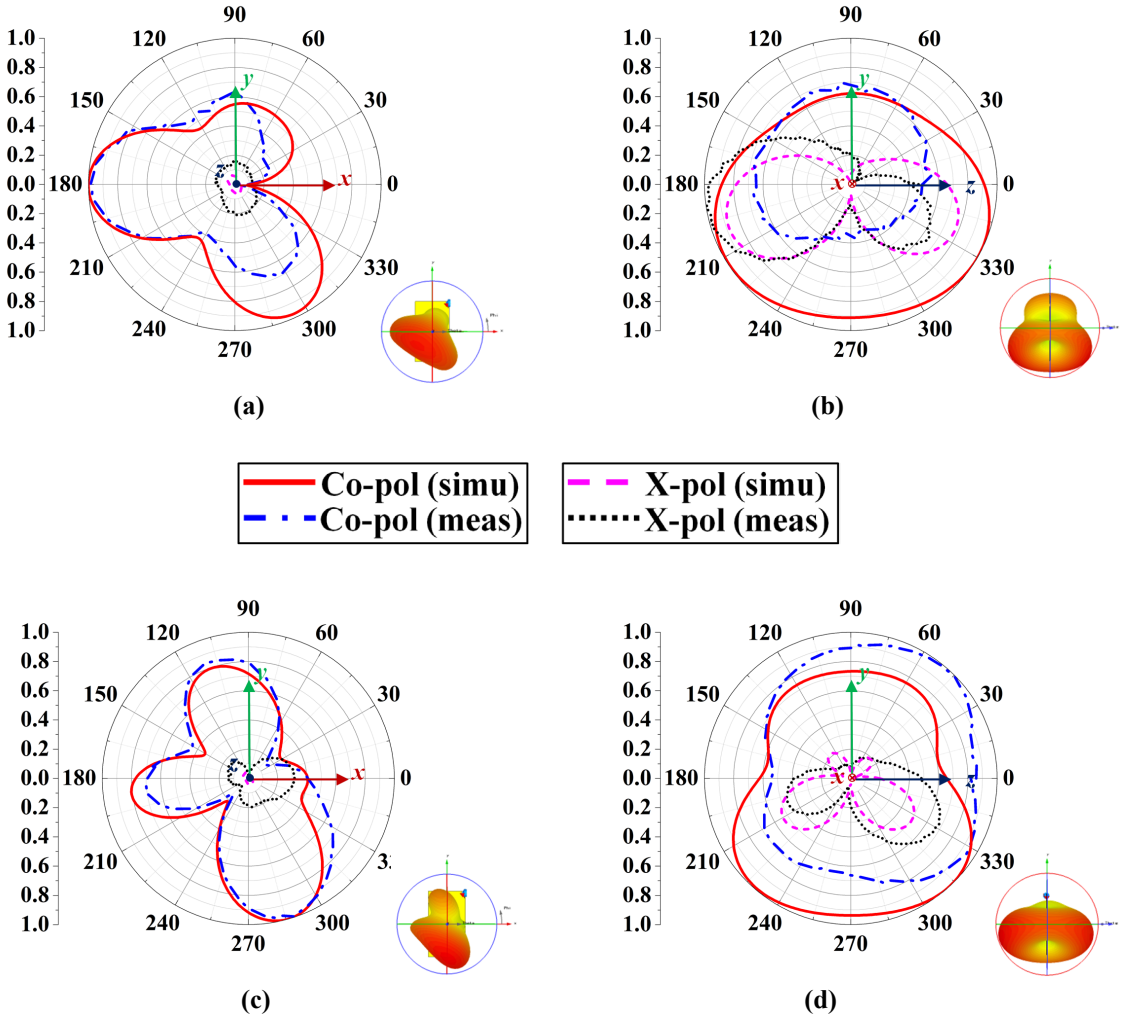

Fig. 6.16. Measured and simulated radiation pattern of the proposed antenna. (a) Xoy plane at 640MHz. (b) Yoz plane at 640MHz. (c) Xoy plane at 890MHz. (d) Yoz plane at 890MHz.

In this section, a water loaded 3D meander line folded monopole antenna has been proposed. The antenna covers a wide frequency band from 463 to 900 MHz with an ultra-compact size (0.013λ × 0.016λ × 0.005λ at 470 MHz). By loading the antenna with a mixture of water and holder, half of the antenna size is saved, with a good bandwidth and high total efficiency. It is demonstrated that this antenna could be a promising candidate for internal antenna solutions for DVB-H and other UHF applications.

Table 6.1 Comparison of the proposed design and other designs

Ref.	Structure	Frequency band (MHz)	Dimensions (mm^3)	Measured total efficiency (%) @ lower bound of the operating frequency (MHz)	Measured total efficiency (%) @ higher bound of the operating frequency (MHz)
[9]	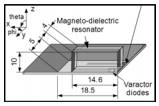	470 - 862	584	5.28% @ 470	21.9% @ 860
[10]	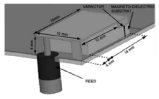	470 - 862	640	16% @ 470	18% @ 862
[11]	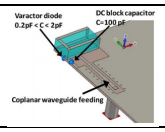	460 - 875	696.6	10% @ 470	32% @ 850
Proposed Str 1	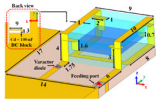	419 - 883	576	12% @ 419 (14% @ 470)	75% @ 880 (71.2% @ 862)
Proposed Str 2	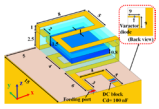	463 - 900	420	10% @ 460 (12% @ 470)	65% @ 900 (61.5% @ 862)

* Proposed Str 1refers to the water loaded reconfigurable 3D folded monopole antenna. Proposed Str 2 refers to the water loaded reconfigurable 3D folded meander line antenna. As a reference, the measured total efficiency of the proposed designs at lower and higher bound of DVB-H band is also listed.

6.4 Summary

In this chapter, two water loaded reconfigurable antennas have been proposed, designed, optimised, made and measured. The idea of effective relative permittivity has been applied. A transparent dielectric loading has been used for the first time to effectively reduce the antenna size while maintaining a reasonable bandwidth and high efficiency. The varactor diode is integrated in the design to continuously tune the operation frequency.

The antenna design originated from a 3D water loaded monopole. To improve the antenna performance, a 3D folded meander line monopole with a smaller size has been developed. A wide frequency tuning range has been achieved for both designs. The bandwidth and efficiency of these two designs meet the requirements of the DVB-H standard.

A comparison between our designs and published related designs is given in Table 6.1. It is apparent that this work provides a wider tuning range and higher efficiency especially at higher frequencies.The dimensions of designs produced in this work are smaller than most of the previous

designs in terms of volume, while exhibiting eqvivalent or significantly superior bandwidths and efficiency.

Between the proposed two designs, the Str1 has a wider frequency tuning range and higher efficiency, while the Str2 has a smaller size. However, both designs have successfully demonstrated the attractive features of water loaded antenna, showing the great potential of water in compact antennas. The knowledge gained in these two designs is not limited to the DVB-H band; it can also be generalised to other bands for various applications.

6.5 References

[1] 'DVB-H implementation guidelines', ETSI TR 102 377 V1.4.1 (2009-06) European Telecommunications Standards Institute.

[2] https://www.dvb.org/resources/public/factsheets/dvb-t2_factsheet.pdf

[3] L. Huitema, M. Koubeissi, C. Decroze, T. Monediere, "Ultrawideband dielectric resonator antenna for DVB-H and GSM applications," IEEE Antennas Wireless Propag. Lett., vol. 8, pp. 1021-1027, 2009.

[4] W. Liu, D. Huang, "Multiband ladder-shaped monopole antenna for digital television and wireless communications," Microw. Opt. Technol. Lett., vol. 51, no. 9, pp. 2124-2127, 2009.

[5] D. H. Choi, Y. T. Im, Y. J. Cho, S. O. Park, "A Tunable Antenna for DVB-H Applications," IEEE Antennas Wireless Propag. Lett., vol. 6, pp. 515-517, 2007.

[6] M. Komulainen, M. Berg, H. Jantunen, E. Salonen, "Compact varactor-tuned meander line monopole antenna for DVB-H signal reception," Electron. Lett., vol. 43, no. 24, pp. 1324-1326, 2007.

[7] X. L. Bao, M. J. Ammann, S. V. Shynu, "Design of a tunable compact antenna for digital video broadcasting handheld terminals," in Proc. Loughborough Antennas & Propag. Conf., 2009, pp. 461-464,

[8] M. Abdallah, F. Colombel, G. Le Ray, and M. Himdi, "Frequency tunable antenna for digital video broadcasting hand-held application," Prog. Electromagn. Res. Lett., vol. 24, pp. 1-8, 2011.

[9] F. Ferrero, A. Chevalier, J. M. Ribero, R. Staraj, J. L. Mattei, Y. Queffelec, "A new magneto-dielectric material loaded, tunable UHF antenna for handheld devices," IEEE Antennas Wireless Propag. Lett., vol. 10, pp. 951-954, 2011.

[10] F. Canneva, F. Ferrero, A. Chevalier, J. M. Ribero, J. L. Mattei, P. Queffelec and R. Staraj, "Miniature reconfigurable antenna with magneto dielectric substrate for DVB-H band," Microw. Opt. Technol. Lett., vol. 55, no. 9, pp. 2007-2011, 2013.

[11] L. Huitema, T. Reveyrand, J. L. Mattei, E. Arnaud, C. Decroze, T. Monediere, "Frequency Tunable Antenna Using a Magneto-Dielectric Material for DVB-H Application," IEEE Trans. Antennas Propagat., vol. 61, no. 9, pp. 4456-4466, 2013.

[12] Aeroflex Metelics Datasheet, [Online]. Available: http://www.aeroflex.com/AMS/Metelics/pdfiles/MGV_Series_Hyperabrupt_A17041.pdf.

[13] L. Xing, Y. Huang, Q. Xu, S. Aljaafreh, T. Liu, "A Broadband hybrid water antenna for hand-portable applications," IEEE Antennas Wireless Propag. Lett., 2015, [Online].Available: http://ieeexplore.ieee.org/stamp/stamp.jsp?tp=&arnumber=7112462

[14] T. Nakamura, M. Shimizu, H. Kimura, R. Sato, "Effective permittivity of amorphous mixed materials," Electron. Comm. Japan. Pt. I, vol. 88, no. 10, pp. 1-9, 2005.

[15] L. Xing, Y. Huang, Q. Xu, and S. Alja'afreh, "A wideband hybrid water antenna with an F-shaped monopole," IEEE Access, vol. 3, pp. 1179-1187, 2015

[16] Q. Xu, Y. Huang, X. Zhu, L. Xing, Z. Tian, C. Song, "A modified two-Antenna method to measure the radiation efficiency of antennas in a reverberation chamber," IEEE Antennas and Wireless Propag. Lett., 2015. [Online].Available: http://ieeexplore.ieee.org/stamp/stamp.jsp?tp=&arnumber=712223.

Chapter 7: Future Work and Contributions

7.1 Summary

To summarise the content of this thesis, it has demonstrated that the water-based liquid antennas are excellent alternatives to traditional antennas and have attractive features and great potential. Over the last two decades, major progress has been made in various aspects of water-based liquid antenna technology, as evidenced by many popular designs, valuable patents and high quality papers. These investigations have shown that the water-based liquid antennas are versatile, efficient, flexible. Thus they are promising candidates for future wireless communications.

Due to the lack of knowledge on water-based liquids and the inherited views of water being a lossy material, the development of water-based liquid antennas has been limited. Actually, water-based liquids have many favourable characteristics and a lot of room for improvement. Several key challenges should be tackled:

1) The complex permittivity of water-based liquids is temperature, frequency and substance concentration dependent. A precise knowledge of permittivity variations on temperature, frequency and substance concentrations is essential. Regarding to a particular application (frequency band), properly choosing the suitable liquid with a specific substance concentration for antenna design is very critical, which will influence the radiation efficiency and bandwidth of the antenna.
2) Pure water will be frozen at 0^{o}C, which affects the performance of the water-based liquid antennas. Solutions have to be found to lower the freezing point of water, without changing the antenna performance significantly.
3) Like the traditional antenna designs, bandwidth enhancement is required. Techniques have to be applied to water-based liquid antennas to enhance the operational bandwidth beyond what can be achieved by the original designs.
4) In existing water antenna designs reported in the published papers, the use of the resonance of water itself will result in either low efficiency or narrow bandwidth. To design a wideband water-based liquid antenna with high efficiency will be challenging.
5) Dielectric materials with high permittivity are frequently used in the compact antenna designs, and water is one of them. The transparency and liquidity make water a very good dielectric loading. However, the high permittivity of water will narrow the bandwidth. To design a compact water loaded antenna with a reasonable bandwidth and high efficiency is very tricky.

Thus, this thesis tries to solve these issues and overcome the design limits with good solutions.

In Chapter 2, an overview of the water-based liquid antennas has been presented and the current state of the art of water-based liquid antenna technology is carefully reviewed. The work has been summarised in chronological order. This chapter looks at the development of water-based liquid antennas from very beginning to the present, which covers nearly all the published prototypes, wideband designs, hybrid techniques, reconfigurable configurations. The knowledge provided in Chapter 2 should be very valuable for researchers who are currently working on this topic or going to start the research in this area.

The investigations on water-based liquid antennas are carried out in two aspects: water-based liquids analysis and water-based liquid antennas design, which is a natural and logical way to explore a new type of antennas, that is from the materials used to the design created.

In Chapter 3, three water-based liquids, namely pure water, salty water and water with antifreeze (propylene glycol), have been carefully studied. Pure water and salty water are frequently used in the liquid antenna designs. Intensive studies on complex permittivity of pure water and salty water have been carried out over decades. In this chapter, pure water and salty water have been analysed from antenna design point of view. New knowledge has been learned to properly choose pure water and salty water for different applications. Water with antifreeze (PG) is first time proposed as an alternative candidate for pure water in cold climates. It has been demonstrated that the performance of antenna will not be changed significantly by using water with antifreeze.

From Chapter 4 to Chapter 6, water-based liquid antennas according to different working mechanisms have been proposed. By using water differently, such as tuning the salt concentration, integrating the feeding structure or using water as a dielectric loading, the water-based liquid antenna can be either a conducting antenna, a hybrid antenna or a water loaded antenna.

In Chapter 4, a monopole water antenna with a dielectric layer has been designed and studied. Salty water is used to replace the conducting material (usually copper is used) in traditional designs. The antenna works very similar to the conducting monopole antenna. But in some aspects, it is different from the traditional conductor monopole. Furthermore, it has some extra features that traditional copper monopole cannot achieve, such as a very wide bandwidth, reconfigurability, transparency and low cost.

In Chapter 5, the idea of HRAT has been implemented and three hybrid water antennas have been produced. By combining the resonance of the feeding structure and the resonance of the water DR, a wideband response can be achieved. The designs have low profiles and high efficiency, overcoming

the limits for the existing water antennas, i.e. low efficiency and narrow bandwidths. The liquidity and transparency of the water have been perfectly utilised; complex feeding structures have been integrated to improve the antenna bandwidth and impedance matching.

Chapter 6 discloses new compact water loaded reconfigurable designs for DVB-H application. By using the idea of effective permittivity method, water works as a transparent dielectric loading in the designs. It has been shown that the transparent dielectric loading can reduce the volume of the 3D folded antennas with reasonable efficiency while not narrow the bandwidth significantly. The designs are not limited to DVB-H applications; they can also be scaled for higher or lower bands.

7.2 Key Contributions

This work has provided a thorough study on water-based liquid antennas, both in liquid characteristics and antenna designs. 7 journal papers and 4 conference publications are produced to report the contributions of this work in [1-11].

The key contributions to new knowledge are detailed as follows:

1. Chapter 2 Overview of Water-Based Liquid Antennas

A comprehensive literature review has been presented to illustrate the development of the water-based liquid antennas and provides a clear evolution picture of the water-based liquid antennas history. Some of the published designs have been summarised and reported in [1]

2. Chapter 3 Complex Permittivity of Water-Based Liquids for Liquid Antennas

New knowledge has been obtained for three promising candidates for liquid antennas (namely water with PG, pure water and salty water). The nonlinear least-squares fitting routines are employed to derive new formulae. Both measurement and numerical simulation approaches have been carried out. A liquid permittivity measurement software package has been developed to record the liquid permittivity data under different temperatures automatically. New fits with lower orders and fewer parameters are derived for pure water and salty water, which are simple and convenient to use. New knowledge has been obtained for water with PG, which is proposed as an alternative candidate for water antenna designs for cold climates. The information gained for water with PG is a big progress in water-based liquid antenna development, which provides a good solution to water-based liquid antenna designs under low temperatures. It has been shown that the new fits proposed in this chapter can accurately describe the complex permittivity, when $0< f \leq 18$ GHz, $0 < T \leq 70^{o}$C (for pure water and salty water) and $-10^{o}\text{C} < T \leq 70^{o}\text{C}$ (for water with PG), $0 \leq PG\ concentration \leq 70\%$, 0

$\leq Salinity \leq$ 50 ppt. The findings investigated in this chapter have reported in [2]. The methods and system used in this research can be generalised to deal with other types of liquids.

3. Chapter 4 A Monopole Water Antenna

A close relationship between conductivity and antenna radiation efficiency for a specific antenna configuration has been explored. The radiation efficiency of an antenna varies with the salinity of the salty water. A monopole water antenna with a dielectric layer between the water and the ground plane has been developed. A comprehensive parametric study has been performed. A water monopole with Teflon base has been fabricated, it has a broad bandwidth (the fractional bandwidth > 70% for S_{11} < -10 dB) and total efficiency up to 62%. The monopole water antenna with a dielectric layer is superior to the conventional antenna in the following aspects: 1) a broad bandwidth with reasonable efficiency, 2) low cost, 3) transparent, 4) frequency and conductivity reconfigurable characteristics. The work has been published in [3, 4].

4. Chapter 5 Hybrid Water Antennas

The work in Chapter 5 concentrates on developing low profile, hybrid water antennas for wideband responses. The designs combine the resonance of the feeding structure and the resonance from the water DRA to effectively broaden the bandwidth of the antenna. Three designs have been proposed.

- **A Rectangular Hybrid Water Antenna Design**

  The hybrid structure combines a rectangular DRA and a monopole antenna (formed by the feeding probe) to effectively double the available bandwidth without compromising other characteristics. The proposed antenna has a 75% bandwidth for S_{11}< -6 dB and radiation efficiency > 60% across the whole working frequency band from 470 to 862 MHz. The water DR occupies a compact size of 90 × 45.6 × 10.6 mm^3 (0.15λ × 0.072 λ × 0.017 λ, at lowest frequency 470 MHz). The design has been published in [5].

- **A U-shaped Hybrid Water Antenna Design**

  Based on the rectangular hybrid antenna design, an improved U-shaped hybrid water antenna has been reported, as published in [6, 7]. A U-shaped water layer has been used to reduce the antenna size and a parasitic stub has been glued to the feeding probe to improve the impedance matching. A parametric study has been performed to achieve the optimal performance. This proposed design has a wide bandwidth from 432 to 900 MHz (a fractional bandwidth of 70%) with radiation efficiency over 60%. Moreover, the experiments in terms of S_{11} and radiation efficiency for the antenna with pure water and water with 10% PG have been carried out, the antenna

performances are similar in both cases, indicating that the water with 10% PG will be a good alternative to pure water in cold climates.

- **A Wideband Hybrid Water Antenna with an F-shaped Monopole**

  To further reduce the antenna size and improve the antenna performance, a wideband hybrid antenna with an F-shaped monopole has been designed and published in [8]. The F-shaped feeding probe simultaneously acts as a monopole antenna and the excitation of the water DRA. The antenna size is reduced by attaching two metal patches (copper sheet) to the bottom and left side faces of the water DRA. Three different bands corresponding to the strong coupling between the feeding probe and metal patches, the stub, and the metal coated water DRA have been combined to realise a wideband response. The hybrid antenna has a very wide bandwidth from 410 to 870 MHz (a fractional bandwidth of 71.8%) with a compact size ($52 \times 51.5 \times 10$ mm^3, roughly $0.071\,\lambda \times 0.07\,\lambda \times 0.0136\lambda$ at 410 MHz) and high radiation efficiency over 60%.

The studies and the disclosed results serve to validate the excellent performances and great potential for the use of the hybrid structures in water antenna designs.

5. Chapter 6 Water Loaded Reconfigurable Antennas

Two water loaded reconfigurable antennas have been developed to cover the DVB-H band (from 470 to 862 MHz) [9, 10, 11], which is one of the most challenging bands for antenna designs. Different technologies are applied in the reconfigurable designs such as the special folded 3D monopole structure, the use of water and its holder as a transparent dielectric loading, and the integration of an active component. By tuning the height ratio of the water layer to its holder, different values of effective permittivity can be obtained, which is a smart way to obtain any desired permittivity. And the loss of the transparent dielectric loading is smaller than the only water loading of the same size.

- **A Water Loaded Reconfigurable 3D Folded Monopole Antenna**

  A compact, frequency tunable antenna with a wide tuning range have been designed [9, 10]. By controlling the DC voltage over the varactor diode, a continuously tuned operating frequency band from 419 to 883 MHz has been realised, with a reasonable bandwidth. The effects of ground plane dimensions are studied. The results show that by reducing the ground plane length, the S_{11} does not change significantly. However, by reducing the ground plane width, the impedance matching of the antenna will become worse. The effects of the transparent dielectric loading and water layer thickness to the antenna performance have been carefully examined. With the aid of the transparent dielectric loading, 30% of the antenna volume reduction is realised. It is proved that the mixed transparent dielectric loading can effectively reduce the antenna size with a reasonable bandwidth, which is superior to the traditional ceramics and

magneto dielectric material. It is demonstrated that this design has fulfilled the DVB-H requirements and is a very promising candidate for DVB-H applications.

- **A Water Loaded Reconfigurable 3D Folded Meander Line Antenna**
  A water loaded reconfigurable antenna with 3D folded meaner line antenna has been developed and published in [11]. It covers a wide frequency band from 463 to 900 MHz with an ultra-compact size ($0.013\lambda \times 0.016\lambda \times 0.005\lambda$ at 470 MHz). The working mechanism is similar to the first water loaded reconfigurable antenna design; however, a special 3D folded meander line structure is used to further reduce the antenna size. With the transparent dielectric loading, half of the antenna size has been saved, with a good bandwidth and high total efficiency.

7.3 Future Work

Based upon the conclusions above and considering the limitations of the work existed, future research could be carried out in the following areas.

- The complex permittivity estimations of water-based liquids in Chapter 3 have been validated in the temperature range from 0 to 70^{o}C (for pure water and salty water) and -10^{o}C to 70^{o}C (for water with PG). Further investigations can be carried out to extend the lower bound of temperature range for both salty water and water with PG.
- There are many kinds of nontoxic antifreeze on the market, such as PG. In future research, other antifreeze such as ethanol can be tried and studied for liquid antenna designs at extremely low temperature environment. The initial measurement results in Fig. 7.1 show that, for a specific solution of ethanol and PG (5% Ethanol, 10% Ethanol, 5% PG, 10% PG), the relative permittivity and conductivity for pure water, water with ethanol and water with PG are very similar, which means water with ethanol is also a good alternative to pure water in cold climates.
- According to Chapter 4, the performance of the salty water monopole antenna is very similar to the traditional monopole made of metal. In this case, salty water can be considered as a conducting material. The knowledge gained in Chapter 4 can be applied to different designs of conducting antennas. In particular, the working frequency of the antennas can be shifted to lower bands such as HF and VHF band to reduce the water loss.
- Further, in the existing designs, most of water monopole antennas are static-type. A plastic tube is usually used to hold the water. The working frequency is tuned by adding water manually. There are some limitations, such as the water evaporates very quickly when the temperature is high. The use of water pump could be advantageous. The real-time reconfigurability can be realised.

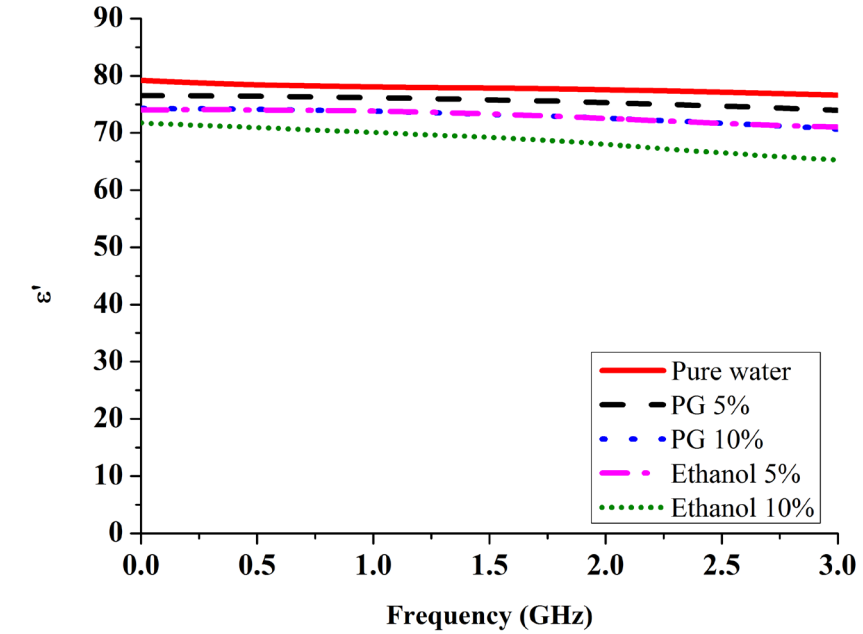

(a)

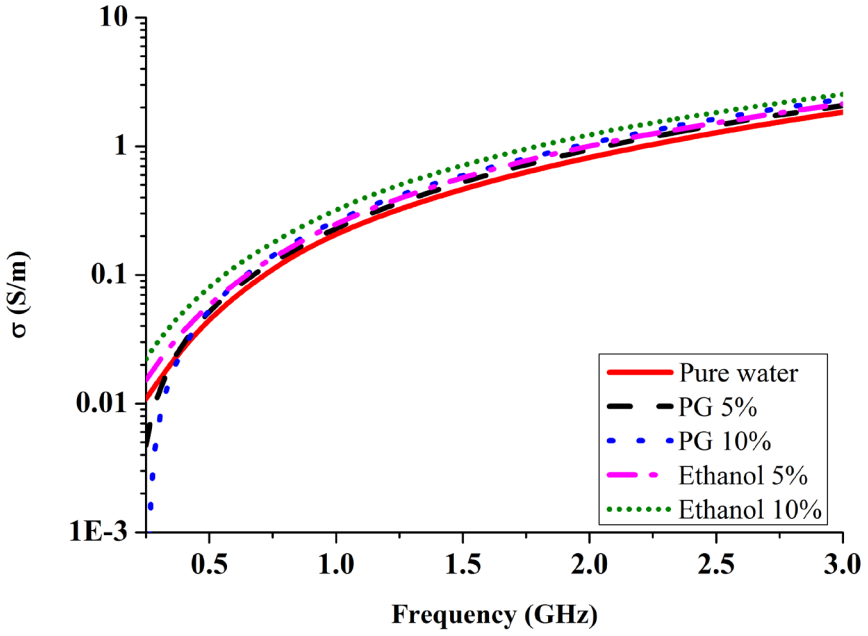

(b)

Fig. 7.1. (a) Measured real part of the permittivity of the pure water, water with 5% PG, 10% PG, 5% Ethanol, 10% Ethanol at 25°C over the frequency of interest. (b) Measured conductivity of the pure water, water with 5% PG, 10% PG, 5% Ethanol, 10% Ethanol at 25°C over the frequency of interest.

- In terms of hybrid water antennas in Chapter 5, the scope can be extended in two aspects: 1) combine the water DRA with some planar feeding structures such as microstrip feed or aperture feed to achieve low profiles; 2) combine the water DRA with other types of conducting antennas. The transparent conductive sheet as shown in Fig. 7.2 [12] can be used together with the water DRA to realise the total transparent antenna designs, which is very promising in future wireless communications.

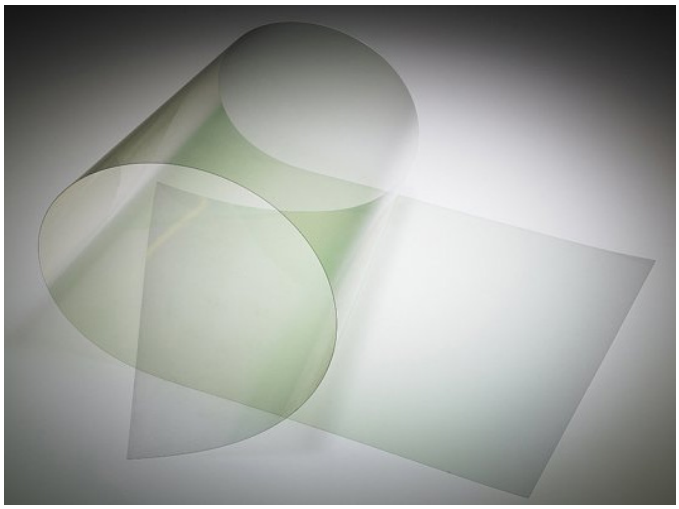

Fig. 7.2. Conductive silver coated films AgHT [12].

- From Chapter 6, the technique of the water loaded reconfigurable antenna for DVB-H applications has been validated and provided good performances. Further work to be shifted the frequency to higher bands such as LTE700 (698 - 787 MHz), LTE2300 (2300 - 2400 MHz), LTE2500 (2500 - 2690 MHz), would be expected to yield even better performances. The transparent conductive sheet can be used to form the conducting antenna structure which will be a very good candidate for transparent mobile phone antenna designs.
- Further, as water is a transparent liquid, by using a transparent elastomeric holder (e.g., polydimethylsiloxane, PDMS), a conformal water antenna can be realised. It can be either a conducting antenna by using salty water or a DRA by using pure water or a hybrid antenna. The conformal water antenna would be beneficial for many wearable applications. More importantly, it is low cost and eco-friendly.

7.4 References

[1] L. Xing, Y. Huang, Q. Xu, S. Aljaafreh, "Overview of water antenna designs for wireless communications," in Proc. IEEE Asia-Pacific Conf. on Antennas and Propag., 2015, pp. 242-243.

[2] L. Xing, Y. Huang, Q. Xu, S. Aljaafreh, T. Liu, "Complex permittivity of water-based liquids for liquid antennas," IEEE Antennas Wireless Propag. Lett. (In Revision)

[3] L. Xing, Y. Huang, S. Alja'afreh, and S. J. Boyes, "A monopole water antenna," in Proc. Loughborough Antennas Propag. Conf., 2012, pp. 1-4.

[4] L. Xing, Y. Huang, Y. Shen, S. Alja'afreh, Q. Xu, R. Alrawashdeh, "Further investigation on water antennas," IET Microw., Antennas Propag., vol. 9, no. 8, pp. 735-741, 2015.

[5] L. Xing, Y. Huang, Q. Xu, S. Aljaafreh, "Wideband, hybrid rectangular water antenna for DVB-H applications," Microw. Opt. Technol. Lett., vol. 59, no. 9, pp. 2160-2164, 2015.

[6] L. Xing, Y. Huang, Y. Shen, S. Alja'afreh, Q. Xu, R. Alrawashdeh, "Broadband U-shaped water antenna for DVB-H applications," in Proc. IEEE Int. Symp. on Antennas and Propag., 2014, pp. 1930-19311.

[7] L. Xing, Y. Huang, Q. Xu, S. Aljaafreh, T. Liu, "A broadband hybrid water antenna for hand-portable applications," IEEE Antennas Wireless Propag. Lett. [Online]. Available: http://ieeexplore.ieee.org/stamp/stamp.jsp?tp=&arnumber=7112462.

[8] L. Xing, Y. Huang, Q. Xu, S. Alja'afreh, "A wideband hybrid water antenna with an F-shaped monopole," IEEE Access, vol. 3, pp. 1179-1187, 2015.

[9] L. Xing, Y. Huang, S. Alja'afreh, Q. Xu, M. Kod, C. Y. Song, "Reconfigurable 3D folded monopole antenna design for DVB-H applications," in Proc. Loughborough Antennas Propag. Conf., 2014, pp. 530-532.

[10] L. Xing, Y. Huang, Q. Xu and S. Alja'afreh, "A transparent dielectric loaded reconfigurable antenna with a wide tuning range," submitted to IEEE Antennas Wireless Propag. Lett..

[11] L. Xing, Y. Huang, Q. Xu and S. Alja'afreh, "A compact water loaded reconfigurable antenna for DVB-H applications" Electron. Lett. to be published.

[12] http://www.instrumentplastics.co.uk/perch/resources/data-sheets/cfds-7.pdf

Appendix A1

The purpose of this appendix is to detail the complete derivation procedure as to how a TE mode can be calculated in an isolated rectangular DRA by using the conventional waveguide model (CWGM). This technique can be used to analysis the field distribution inside the dielectric resonator antenna and also to predict the resonant frequency and Q factor of the dielectric resonator antenna.

Since the systematic study of dielectric resonators as radiating elements was first explored by Long *et al* in 1980s [1], significant progress has been made in various aspects of DRA technology. Various numerical techniques such as the method of moments (MoM) or the finite difference time domain (FDTD) method have been used to solve the fields inside the DRA, but these techniques are time consuming, memory intensive. In order to aid with the design of DRAs, several relatively simple models such as the conventional waveguide model (CWGM) [2], the modified waveguide model (MWGM) [3] and effective dielectric constant (EDC) model [4] have been developed to estimate the resonant frequency and Q factor.

As stated in [5], the lowest order TM modes were never observed experimentally, the existence of TM modes appears to be doubtful. However, the existence of lower order TE modes is well known. And the lowest order TE mode (also known as $TE_{11\delta}$) has also been employed in various circuit applications. Therefore, in this part, we discuss TE modes only.

CWGM method and magnetic wall model (MWM) are combined to predict the resonant frequency of an isolated rectangular DRA as shown in Fig. A1.1, which has a width 2*w* in x direction, a height 2*h* in y direction and a length 2*l* in z direction. TE^z mode is used as an example to illustrate the derivation process (TE^x and TE^y mode can be derived in a similar way).

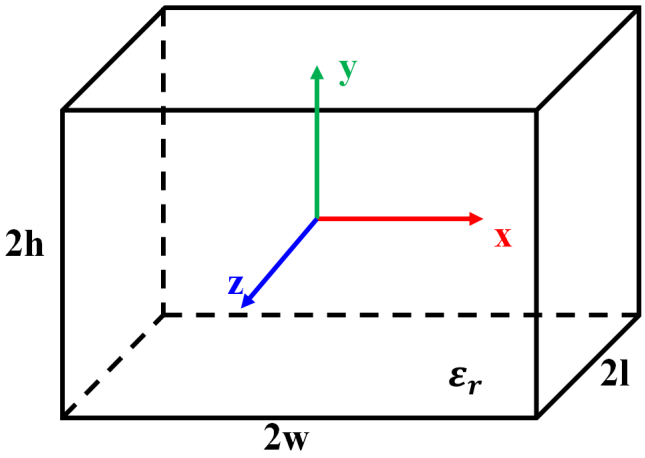

Fig. A1.1. Isolated rectangular dielectric resonator antenna.

For an arbitrarily shaped DR of very high permittivity, modes of a DR can be a confined or non-confined type. For both confined and non-confined modes, the following condition is satisfied at all the surfaces of the resonator [6, 7]:

$$\vec{E} \cdot \vec{n} = 0 \qquad (A1.1a)$$

Where $\vec{E}$ denotes the electric-field intensity and $\vec{n}$ denotes the normal to the surface of the resonator. Equation (A1.1a) is one of the conditions that fields are satisfied at a magnetic wall. The other magnetic wall condition is

$$\vec{n} \times \vec{H} = 0 \qquad (A1.1b)$$

is not necessarily satisfied at all the surfaces of the DR by all the modes. The confined modes are those modes of a DR satisfy both (A1.1a) and (A1.1b), and the non-confined modes are those who satisfy (A1.1a) only. It has been shown by Van Bladel that confined modes can be supported by dielectric bodies of revolution only, such as spherical and cylindrical. As a rectangular DR is not a body of revolution, it can only support non-confined modes [6].

The derivation of TE^z modes starts from the magnetic vector potential $\vec{A}$ and electric vector potential $\vec{F}$, which are frequently used as aids in obtaining solutions for electrical $\vec{E}$ and magnetic fields $\vec{F}$.

In a source-free region, the $\vec{E}$ and $\vec{F}$ fields in terms of vector potentials $\vec{A}$ and $\vec{F}$ can be presented as [8]:

$$\vec{E} = \overrightarrow{E_A} + \overrightarrow{E_F} = -j\omega\vec{A} - \frac{j}{\omega\mu\varepsilon}\nabla\left(\nabla \cdot \vec{A}\right) - \frac{1}{\varepsilon}\nabla \times \vec{F} \qquad (A1.2a)$$

$$\vec{H} = \overrightarrow{H_A} + \overrightarrow{H_F} = \frac{1}{\mu}\nabla \times \vec{A} - j\omega\vec{F} - \frac{j}{\omega\mu\varepsilon}\nabla\left(\nabla \cdot \vec{F}\right) \tag{A1.2b}$$

For a TE^z rectangular coordinate system, let [8]:

$$\vec{A} = 0 \tag{A1.3a}$$

$$\vec{F} = \vec{a}_z F_z(x, y, z) \tag{A1.3b}$$

Then

$$E_x = -\frac{1}{\varepsilon}\frac{\partial F_z}{\partial y} \qquad H_x = -\frac{j}{\omega\mu\varepsilon}\frac{\partial^2 F_z}{\partial x \partial z}$$

$$E_y = \frac{1}{\varepsilon}\frac{\partial F_z}{\partial x} \qquad H_y = -\frac{j}{\omega\mu\varepsilon}\frac{\partial^2 F_z}{\partial y \partial z}$$

$$E_z = 0 \qquad H_z = -\frac{j}{\omega\mu\varepsilon}\left(\frac{\partial^2}{\partial z^2} + \beta^2\right)F_z \tag{A1.4}$$

According to the equations above, once the F_z is known, the $\vec{E}$ and $\vec{F}$ fields can be obtained correspondingly. We divided the isolated DRA into 7 different areas, and the cross-section views are shown in Fig. A1.2. For a well-guided modes, most of the power travels in Area 1 (inside DRA), a small part travels in Areas 2, 3, 4, 5, 6, 7 (outside DRA), and even less travels in the shaded areas [9]. The fields within the DRA are assumed to vary sinusoidally, while the fields outside the guide are assumed to decay exponentially [9]. In order to simplify the analysis, the fields in the shaded regions of Fig. A1.2 are assumed to be zero [9].

The field components in Area 1 vary sinusoidally in the x, y and z directions. Those in Area 2 and 3 vary sinuasoidally along y and z directions, and exponentially along x direction. Those in Area 4 and 5 vary sinuasoidally along x and z directions, and exponentially along y direction. Those in Area 6 and 7 vary sinuasoidally along x and y directions, and exponentially along z direction. The wave numbers β_{yd} and β_{zd} along y and z directions in Area 1, 2, 3, are identical. Similarly, the wave numbers β_{xd} and β_{zd} along x and z directions in Area 1, 4, 5 are identical. The wave numbers β_{xd} and β_{yd} along x and y directions in Areal 1, 6, 7, are identical. The attenuation constants in the x, y and z directions are α_{x0}, α_{y0} and α_{z0}, respectively.

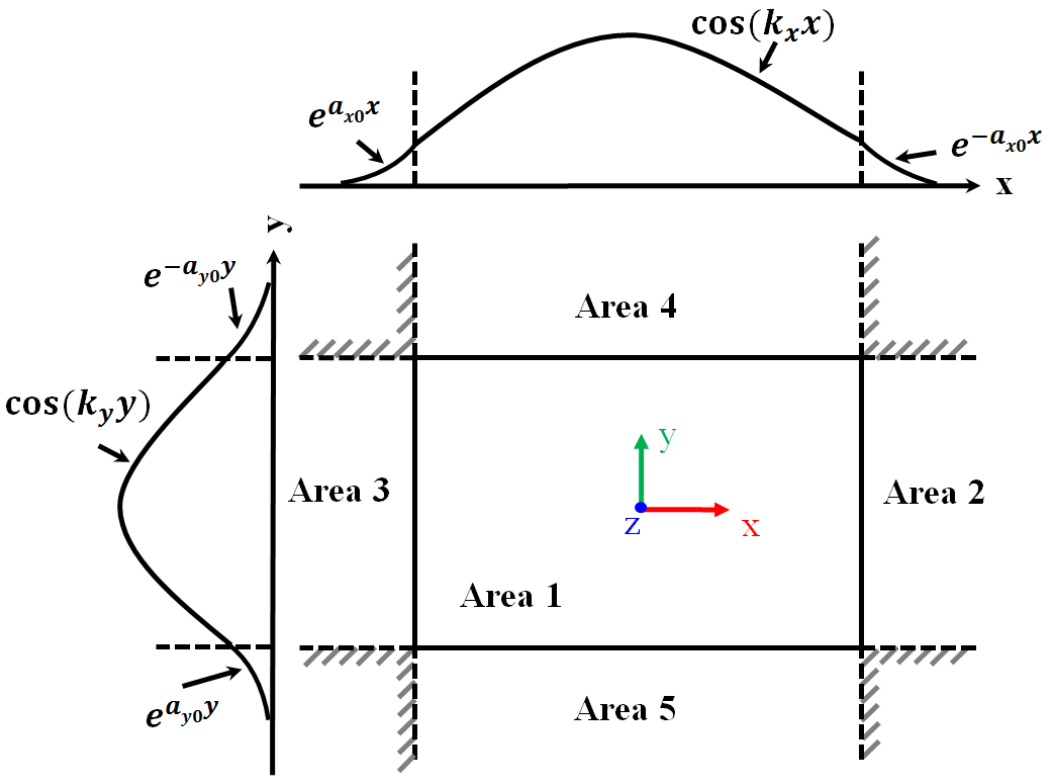

(a)

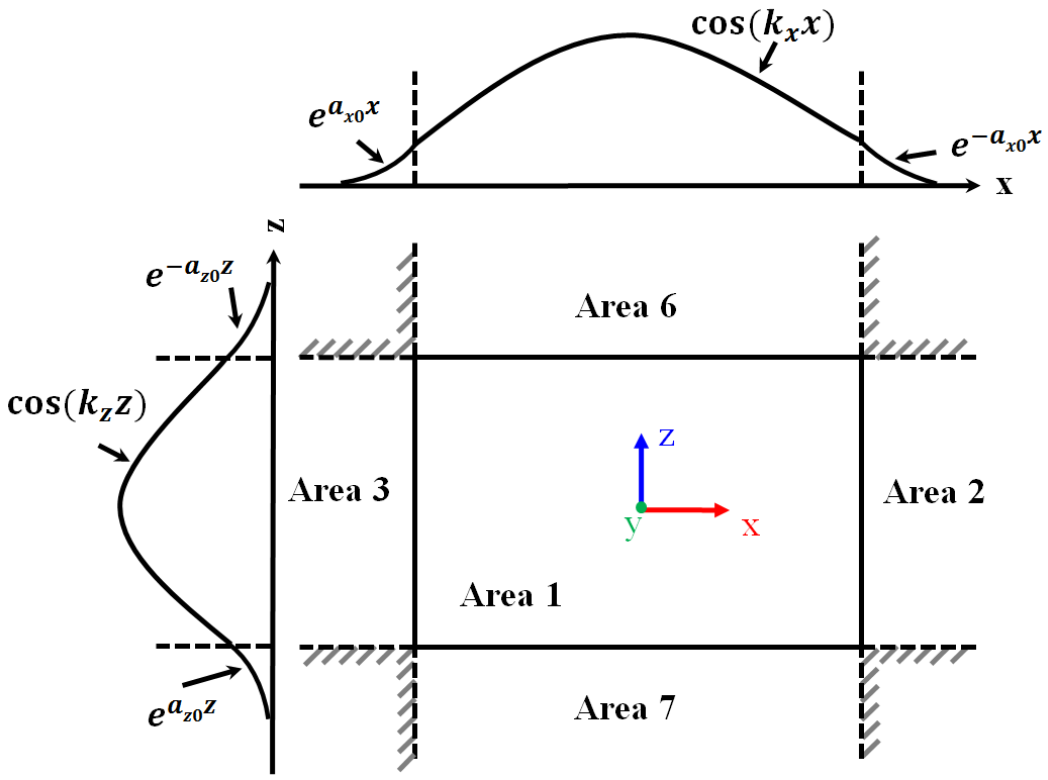

(b)

Fig. A1.2. Cross section of the rectangular dielectric resonator antenna. (a) Xoy plane. (b) Xoz plane.

To simplify the derivation process, we assume that *Fz* has only even mode in *x*, *y* direction, and the coefficients C_d, C_{posx}, C_{posy}, C_{negx}, C_{negy}, C_{posz}, $C_{negz} \neq 0$

Area 1 ($-w \leq x \leq w$, $-h \leq y \leq h$, $-l \leq z \leq l$): the vector potentials F_{zd} can be expressed as:

$$F_{zd} = C_d \cos(\beta_{xd}x) \cos(\beta_{yd}y) \left(C_1 e^{-j\beta_{zd}z} + C_2 e^{j\beta_{zd}z}\right) \qquad (A1.5a)$$

Area 2 ($w \leq x$, $-h \leq y \leq h$, $-l \leq z \leq l$): the vector potentials F_{zposx} can be expressed as:

$$F_{zposx} = C_{posx}\, e^{-\alpha_{x0}x} \cos(\beta_{yd}y) \left(C_1 e^{-j\beta_{zd}z} + C_2 e^{j\beta_{zd}z}\right) \qquad (A1.5b)$$

Area 3 ($x \leq -w$, $-h \leq y \leq h$, $-l \leq z \leq l$): the vector potentials F_{znegx} can be expressed as:

$$F_{znegx} = C_{negx}\, e^{\alpha_{x0}x} \cos(\beta_{yd}y) \left(C_1 e^{-j\beta_{zd}z} + C_2 e^{j\beta_{zd}z}\right) \qquad (A1.5c)$$

Area 4 ($-w \leq x \leq w$, $y \geq h$, $-l \leq z \leq l$): the vector potentials F_{zposy} can be expressed as:

$$F_{zposy} = C_{posy} \cos(\beta_{xd}x)\, e^{-\alpha_{y0}y} \left(C_1 e^{-j\beta_{zd}z} + C_2 e^{j\beta_{zd}z}\right) \qquad (A1.5d)$$

Area 5 ($-w \leq x \leq w$, $y \leq -h$, $-l \leq z \leq l$): the vector potentials F_{znegy} can be expressed as:

$$F_{znegy} = C_{negy} \cos(\beta_{xd}x)\, e^{\alpha_{y0}y} \left(C_1 e^{-j\beta_{zd}z} + C_{21} e^{j\beta_{zd}z}\right) \qquad (A1.5e)$$

Area 6 ($-w \leq x \leq w$, $-h \leq y \leq h$, $l \leq z$): the vector potentials F_{zposz} can be expressed as:

$$F_{zposz} = C_{posz} \cos(\beta_{xd}x) \cos(\beta_{yd}y)\, e^{-\alpha_{z0}z} \qquad (A1.5f)$$

Area 7 ($-w \leq x \leq w$, $-h \leq y \leq h$, $z \leq -l$): the vector potentials F_{znegz} can be expressed as:

$$F_{znegz} = C_{negz} \cos(\beta_{xd}x) \cos(\beta_{yd}y)\, e^{\alpha_{z0}z} \qquad (A1.5g)$$

In a source-free region, the vector potential $\vec{F}$ satisfies the Laplace equation:

$$\nabla^2 \vec{F} + \beta^2 \vec{F} = 0 \quad \text{where} \quad \beta^2 = \omega^2 \mu\varepsilon \qquad (A1.6)$$

By implementing the vector potential $\vec{F}$ of Areal 1 to Areal 7 into Laplace equation, we can get:

$$-\omega^2 \varepsilon_0 \varepsilon_d \mu_d + \beta_{xd}^2 + \beta_{yd}^2 + \beta_{zd}^2 = 0 \qquad (A1.7a)$$

$$-\omega^2 \varepsilon_0 \mu_0 - \alpha_{x0}^2 + \beta_{yd}^2 + \beta_{zd}^2 = 0 \qquad (A1.7b)$$

$$-\omega^2 \varepsilon_0 \mu_0 - \alpha_{y0}^2 + \beta_{xd}^2 + \beta_{zd}^2 = 0 \qquad (A1.7b)$$

$$-\omega^2\varepsilon_0\mu_0 - \alpha_{z0}^2 + \beta_{xd}^2 + \beta_{yd}^2 = 0 \qquad (A1.7d)$$

The $\vec{E}$and $\vec{F}$ fields are obtained according to equation (A1.4):

1. Area 1 ($-w \le x \le w$, $-h \le y \le h$, $-l \le z \le l$):

$$\overrightarrow{E_d} = \left(\frac{C_d\, cos(\beta_{xd}x)\, sin(\beta_{yd}y)\, \beta_{yd}\left(C_1e^{-j\beta_{zd}z} + C_2e^{j\beta_{zd}z}\right)}{\varepsilon_d}\right)\overrightarrow{a_x} + \left(-\frac{C_d\, sin(\beta_{xd}x)\beta_{xd}\, cos(\beta_{yd}y)\left(C_1e^{-j\beta_{zd}z} + C_2e^{j\beta_{zd}z}\right)}{\varepsilon_d}\right)\overrightarrow{a_y} \qquad (A1.8a)$$

$$\overrightarrow{H_d} = \left(\frac{jC_d\, sin(\beta_{xd}x)\, \beta_{xd}cos(\beta_{yd}y)\left(-jC_1\beta_{zd}e^{-j\beta_{zd}z} + jC_2\beta_{zd}e^{j\beta_{zd}z}\right)}{\omega\mu_d\varepsilon_d}\right)\overrightarrow{a_x} + \left(\frac{jC_d\, cos(\beta_{xd}x)\, sin(\beta_{yd}y)\beta_{yd}\left(-jC_1\beta_{zd}e^{-j\beta_{zd}z} + jC_2\beta_{zd}e^{j\beta_{zd}z}\right)}{\omega\mu_d\varepsilon_d}\right)\overrightarrow{a_y} + \left(-j\omega C_d\, cos(\beta_{xd}x)\, cos(\beta_{yd}y)\left(C_1e^{-j\beta_{zd}z} + C_2e^{j\beta_{zd}z}\right) - \frac{jC_d\, cos(\beta_{xd}x)\, cos(\beta_{yd}y)\left(-C_1{\beta_{zd}}^2e^{-j\beta_{zd}z} - C_2{\beta_{zd}}^2e^{j\beta_{zd}z}\right)}{\omega\mu_d\varepsilon_d}\right)\overrightarrow{a_z} \qquad (A1.8b)$$

2. Area 2 ($w \le x$, $-h \le y \le h$, $-l \le z \le l$):

$$\overrightarrow{E_{posx}} = \left(\frac{C_{posx}e^{-\alpha_{x0}x}\, sin(\beta_{yd}y)\, \beta_{yd}\left(C_1e^{-j\beta_{zd}z} + C_2e^{j\beta_{zd}z}\right)}{\varepsilon_0}\right)\overrightarrow{a_x} + \left(-\frac{C_{posx}\alpha_{x0}e^{-\alpha_{x0}x}\, cos(\beta_{yd}y)\left(C_1e^{-j\beta_{zd}z} + C_2e^{j\beta_{zd}z}\right)}{\varepsilon_0}\right)\overrightarrow{a_y} \qquad (A1.9a)$$

$$\overrightarrow{H_{posx}} = \left(\frac{jC_{posx}\alpha_{x0}e^{-\alpha_{x0}x}\, cos(\beta_{yd}y)\left(-jC_1\beta_{zd}e^{-j\beta_{zd}z} + jC_2\beta_{zd}e^{j\beta_{zd}z}\right)}{\omega\mu_0\varepsilon_0}\right)\overrightarrow{a_x} + \left(\frac{jC_{posx}e^{-\alpha_{x0}x}\, sin(\beta_{yd}y)\beta_{yd}\left(-jC_1\beta_{zd}e^{-j\beta_{zd}z} + jC_2\beta_{zd}e^{j\beta_{zd}z}\right)}{\omega\mu_0\varepsilon_0}\right)\overrightarrow{a_y} + \left(-j\omega C_{posx}e^{-\alpha_{x0}x}\, cos(\beta_{yd}y)\left(C_1e^{-j\beta_{zd}z} + C_2e^{j\beta_{zd}z}\right) - \frac{jC_{posx}e^{-\alpha_{x0}x}\, cos(\beta_{yd}y)\left(-C_1{\beta_{zd}}^2e^{-j\beta_{zd}z} - C_2{\beta_{zd}}^2e^{j\beta_{zd}z}\right)}{\omega\mu_0\varepsilon_0}\right)\overrightarrow{a_z} \qquad (A1.9b)$$

3. Area 3 ($x \le -w$, $-h \le y \le h$, $-l \le z \le l$):

$$\overrightarrow{E_{negx}} = \left(\frac{C_{negx} e^{\alpha_{x0} x} \sin(\beta_{yd} y)\, \beta_{yd} \left(C_1 e^{-j\beta_{zd} z} + C_2 e^{j\beta_{zd} z}\right)}{\varepsilon_0}\right)\overrightarrow{a_x} + \left(\frac{C_{negx} \alpha_{x0} e^{\alpha_{x0} x} \cos(\beta_{yd} y) \left(C_1 e^{-j\beta_{zd} z} + C_2 e^{j\beta_{zd} z}\right)}{\varepsilon_0}\right)\overrightarrow{a_y} \quad (A1.10a)$$

$$\overrightarrow{H_{negx}} = \left(-\frac{jC_{negx} \alpha_{x0} e^{\alpha_{x0} x} \cos(\beta_{yd} y) \left(-jC_1 \beta_{zd} e^{-j\beta_{zd} z} + jC_2 \beta_{zd} e^{j\beta_{zd} z}\right)}{\omega \mu_0 \varepsilon_0}\right)\overrightarrow{a_x} + \left(\frac{jC_{negx} e^{\alpha_{x0} x} \sin(\beta_{yd} y) \beta_{yd} \left(-jC_1 \beta_{zd} e^{-j\beta_{zd} z} + jC_2 \beta_{zd} e^{j\beta_{zd} z}\right)}{\omega \mu_0 \varepsilon_0}\right)\overrightarrow{a_y} + \left(-j\omega C_{negx} e^{\alpha_{x0} x} \cos(\beta_{yd} y) \left(C_1 e^{-j\beta_{zd} z} + C_2 e^{j\beta_{zd} z}\right) - \frac{jC_{negx} e^{\alpha_{x0} x} \cos(\beta_{yd} y) \left(-C_1 {\beta_{zd}}^2 e^{-j\beta_{zd} z} - C_2 {\beta_{zd}}^2 e^{j\beta_{zd} z}\right)}{\omega \mu_0 \varepsilon_0}\right)\overrightarrow{a_z} \quad (A1.10b)$$

4. Area 4 ($-w \le x \le w$, $y \ge h$, $-l \le z \le l$):

$$\overrightarrow{E_{posy}} = \left(\frac{C_{posy} \cos(\beta_{xd} x) \alpha_{y0} e^{-\alpha_{y0} y} \left(C_1 e^{-j\beta_{zd} z} + C_2 e^{j\beta_{zd} z}\right)}{\varepsilon_0}\right)\overrightarrow{a_x} + \left(-\frac{C_{posy} \sin(\beta_{xd} x) \beta_{xd}\, e^{-\alpha_{y0} y} \left(C_1 e^{-j\beta_{zd} z} + C_2 e^{j\beta_{zd} z}\right)}{\varepsilon_0}\right)\overrightarrow{a_y} \quad (A1.11a)$$

$$\overrightarrow{H_{posy}} = \left(\frac{jC_{posy} \sin(\beta_{xd} x) \beta_{xd} e^{-\alpha_{y0} y} \left(-jC_1 \beta_{zd} e^{-j\beta_{zd} z} + jC_2 \beta_{zd} e^{j\beta_{zd} z}\right)}{\omega \mu_0 \varepsilon_0}\right)\overrightarrow{a_x} + \left(\frac{jC_{posy} \cos(\beta_{xd} x) \alpha_{y0} e^{-\alpha_{y0} y} \left(-jC_1 \beta_{zd} e^{-j\beta_{zd} z} + jC_2 \beta_{zd} e^{j\beta_{zd} z}\right)}{\omega \mu_0 \varepsilon_0}\right)\overrightarrow{a_y} + \left(-j\omega C_{posy} \cos(\beta_{xd} x) e^{-\alpha_{y0} y} \left(C_1 e^{-j\beta_{zd} z} + C_2 e^{j\beta_{zd} z}\right) - \frac{jC_{posy} \cos(\beta_{xd} x) e^{-\alpha_{y0} y} \left(-C_1 {\beta_{zd}}^2 e^{-j\beta_{zd} z} - C_2 {\beta_{zd}}^2 e^{j\beta_{zd} z}\right)}{\omega \mu_0 \varepsilon_0}\right)\overrightarrow{a_z} \quad (A1.11b)$$

5. Area 5 ($-w \le x \le w$, $y \le -h$, $-l \le z \le l$):

$$\overrightarrow{E_{negy}}$$
$$= \left(-\frac{C_{negy}\, cos(\beta_{xd}x)\alpha_{y0}e^{\alpha_{y0}y}\left(C_1e^{-j\beta_{zd}z} + C_2e^{j\beta_{zd}z}\right)}{\varepsilon_0} \right)\overrightarrow{a_x}$$
$$+ \left(-\frac{C_{negy}\, sin(\beta_{xd}x)\beta_{xd}\, e^{\alpha_{y0}y}\left(C_1e^{-j\beta_{zd}z} + C_2e^{j\beta_{zd}z}\right)}{\varepsilon_0} \right)\overrightarrow{a_y} \qquad (A1.12a)$$

$$\overrightarrow{H_{negy}}$$
$$= \left(\frac{jC_{negy}\, sin(\beta_{xd}x)\beta_{xd}e^{\alpha_{y0}y}\left(-jC_1\beta_{zd}e^{-j\beta_{zd}z} + jC_2\beta_{zd}e^{j\beta_{zd}z}\right)}{\omega\mu_0\varepsilon_0} \right)\overrightarrow{a_x}$$
$$+ \left(-\frac{jC_{negy}\, cos(\beta_{xd}x)\alpha_{y0}e^{\alpha_{y0}y}\left(-jC_1\beta_{zd}e^{-j\beta_{zd}z} + jC_2\beta_{zd}e^{j\beta_{zd}z}\right)}{\omega\mu_0\varepsilon_0} \right)\overrightarrow{a_y}$$
$$+ \Bigg(-j\omega C_{negy}\, cos(\beta_{xd}x)e^{\alpha_{y0}y}\left(C_1e^{-j\beta_{zd}z} + C_2e^{j\beta_{zd}z}\right)$$
$$- \frac{jC_{negy}\, cos(\beta_{xd}x)e^{\alpha_{y0}y}\left(-C_1{\beta_{zd}}^2e^{-j\beta_{zd}z} - C_2{\beta_{zd}}^2e^{j\beta_{zd}z}\right)}{\omega\mu_0\varepsilon_0} \Bigg)\overrightarrow{a_z} \qquad (A1.12b)$$

6. Area 6 ($-w \le x \le w$, $-h \le y \le h$, $l \le z$)

$$\overrightarrow{E_{posz}}$$
$$= \left(\frac{C_{posz}\, cos(\beta_{xd}x)sin(\beta_{yd}y)\beta_{yd}\, e^{-\alpha_{z0}z}}{\varepsilon_0} \right)\overrightarrow{a_x}$$
$$+ \left(-\frac{C_{posz}\, sin(\beta_{xd}x)\beta_{xd}cos(\beta_{yd}y)\, e^{-\alpha_{z0}z}}{\varepsilon_0} \right)\overrightarrow{a_y} \qquad (A1.13a)$$

$$\overrightarrow{H_{posz}}$$
$$= \left(-\frac{jC_{posz}\, sin(\beta_{xd}x)\beta_{xd}cos(\beta_{yd}y)\alpha_{z0}e^{-\alpha_{z0}z}}{\omega\mu_0\varepsilon_0} \right)\overrightarrow{a_x}$$
$$+ \left(-\frac{jC_{posz}\, cos(\beta_{xd}x)sin(\beta_{yd}y)\beta_{yd}\alpha_{z0}e^{-\alpha_{z0}z}}{\omega\mu_0\varepsilon_0} \right)\overrightarrow{a_y}$$
$$+ \Bigg(-j\omega C_{posz}\, cos(\beta_{xd}x)cos(\beta_{yd}y)e^{-\alpha_{z0}z}$$
$$- \frac{jC_{posz}\, cos(\beta_{xd}x)cos(\beta_{yd}y){\alpha_{z0}}^2e^{-\alpha_{z0}z}}{\omega\mu_0\varepsilon_0} \Bigg)\overrightarrow{a_z} \qquad (A1.13b)$$

7. Area 7 ($-w \le x \le w, -h \le y \le h, z \le -l$)

$$\overrightarrow{E_{negz}} = \left(\frac{C_{negz}\, cos(\beta_{xd}x) sin(\beta_{yd}y)\beta_{yd}\, e^{\alpha_{z0}z}}{\varepsilon_0}\right)\overrightarrow{a_x} + \left(-\frac{C_{negz}\, sin(\beta_{xd}x)\beta_{xd} cos(\beta_{yd}y)\, e^{\alpha_{z0}z}}{\varepsilon_0}\right)\overrightarrow{a_y} \quad (A1.14a)$$

$$\overrightarrow{H_{negz}} = \left(\frac{jC_{negz}\, sin(\beta_{xd}x)\beta_{xd} cos(\beta_{yd}y)\alpha_{z0} e^{\alpha_{z0}z}}{\omega\mu_0\varepsilon_0}\right)\overrightarrow{a_x} + \left(\frac{jC_{negz}\, cos(\beta_{xd}x) sin(\beta_{yd}y)\beta_{yd}\alpha_{z0} e^{\alpha_{z0}z}}{\omega\mu_0\varepsilon_0}\right)\overrightarrow{a_y} + \left(-j\omega C_{negz}\, cos(\beta_{xd}x) cos(\beta_{yd}y) e^{\alpha_{z0}z} - \frac{jC_{negz}\, cos(\beta_{xd}x) cos(\beta_{yd}y)\alpha_{z0}{}^2 e^{\alpha_{z0}z}}{\omega\mu_0\varepsilon_0}\right)\overrightarrow{a_z} \quad (A1.14b)$$

Applying the magnetic wall boundary condition (A1.1a) at the surfaces of the DRA, i. e. at $|x| = w$ and $|y| = h$, the following equations are obtained for the wave numbers β_{xd} and β_{yd}:

$$\beta_{xd} = \frac{m\pi}{2w}\,;\, \beta_{yd} = \frac{n\pi}{2h} \quad (A1.15)$$

where *m* and *n* represent the number of peaks along the x, and y directions, respectively.

Applying the tangential components of the $\vec{E}$ and $\vec{F}$ fields continuous across the two surfaces, perpendicular to the direction of propagation, i.e. $|z| = l$, the following equation is achieved [10]:

$$\beta_{zd}\, tan(\beta_{zd} l) = \alpha_{z0} \quad (A1.16)$$

Substitute (A1. 7a) and (A1. 7d) into (A1. 16),

$$\beta_{zd}\, tan(\beta_{zd} l) = \sqrt{\beta_0^2(\varepsilon_d - 1) - \beta_{zd}^2} \quad (A1.17)$$

By calculating the equations (A1.17), (A1.15) and (A1. 7a), the resonant frequency of a specific TE^z mode can be obtained.

References

[1] A. Petosa, A. Ittipiboon, Y. M. M. Antar, D. Roscoe, and M. Cuhaci, "Recent advances in dielectric-resonator antenna technology," IEEE Antennas and Propag. Mag., vol. 40, pp. 35-48, 1998.

[2] E. A. J. Marcatili, "Dielectric rectangular waveguide and directional coupler for integrated optics," Bell Syst. Tech. J., vol. 43, pp. 2071-2012, 1969.

[3] Y. M. M. Antar, D. Cheng, G. Seguin, B. Henry, and M. G. Keller, "Modified waveguide model (MWGM) for rectangular dielectric resonator antenna (DRA)," Microw. Opt. Technol. Lett., vol. 19, no. 2, 1998.

[4] R. K. Mongia, "Theoretical and experimental resonant frequencies of rectangular dielectric resonators," Proc. Inst. Elcci, Eng., vol. 139, pp. 98-104, 1992.

[5] R. K. Mongia, A. Ittipiboon, "Theoretical and experimental investigations on rectangular dielectric resonator antenna," IEEE Trans. Antenna Propag., vol. 45, no. 9, 1997.

[6] J. Van.Bladel, "On the resonances of a dielectric resonator of very high permittivity," IEEE Trans. Microw. Theory Tech., vol. MTT-25, pp. 199-208, 1975.

[7] J. Van.Bladel, "The excitation of dielectric resonators of very high permittivity," IEEE Trans. Microw. Theory Tech., vol. MTT-23, pp. 208-215, 1975.

[8] C. A. Balanis, *Antenna theory analysis and design*, John Wiley & Sons, Inc., 2005.

[9] K. M. Luk, K. W. Leung, *Dielectric resonator antennas*, Research Studies Press Ltd, 2003.

[10] A. Petosa, *Dielectric resonator antenna handbook*, Artech House, Inc., 2007.

Appendix A2

The purpose of this appendix is to provide a briefly introduction to different dielectric property measurement techniques. The strengths and limitations of each technique are illustrated and compared. There are mainly six types of measurement techniques currently used to obtain the dielectric properties, namely coaxial probe method, transmission line method, free space method, resonant cavity method, parallel plate method, and inductance measurement method [1].

A. Coaxial Probe Method

A typical measurement system using a coaxial probe method is shown in Fig. A2.1, including a VNA, software to calculate permittivity, a coaxial probe, probe stand and connecting cables. The material under test (MUT) is measured by immersing the probe into a liquid or touching it to the flat face of the material [2]. The S_{11} can be measured, and ε can be derived according to the S_{11}. The coaxial probe technique is a simple and convenient, broadband permittivity measurement method for liquids and semi-solid materials. When the experiment is performed, special attention should be taken to aspects such as: 1) Avoid air gaps between the sample and the probe. For solid materials, the surface should be flat. For liquids, the air gap should be removed. 2) The sample should be thick enough to appear "infinite" to the probe. The limitations of this method are the accuracy under some conditions when compared with other methods (the transmission line, free space or resonant cavity method) [3].

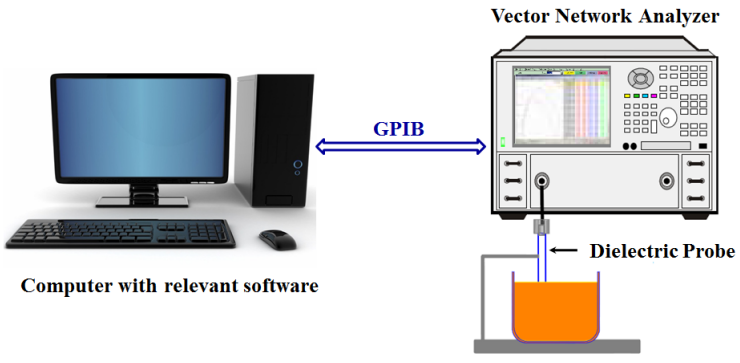

Fig. A2.1. Coaxial probe method measurement system [3].

B. Transmission Line Method

A typical measurement system using the transmission line method includes a VNA, a coaxial or waveguide transmission line and relevant software to calculate ε and μ. The MUT is placed inside a portion of an enclosed transmission line. This method is an ideal solution for hard solid materials.

However, the limitations for this method is that it must fill the cross-section of the transmission line (coaxial or rectangular), sample preparation is also more difficult and time consuming [1], and large samples are needed for low frequencies and small samples are required for high frequencies.

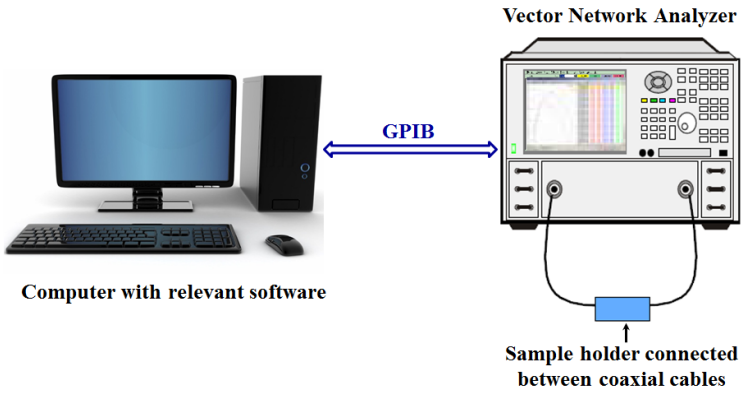

Fig. A2.2. Transmission line method measurement system [2].

C. Free Space Method

Fig. A2.3 shows a typical free space system consisting of a VNA, two antennas facing each other with a sample holder between them. This technique is grouped under non-destructive and contact less measuring methods, which is ideal for remote sensing [1]. It is particularly suitable for materials at high temperature applications. The limitations for this method are: 1) the samples need flat parallel faces; 2) very large samples are required at low frequencies [4].

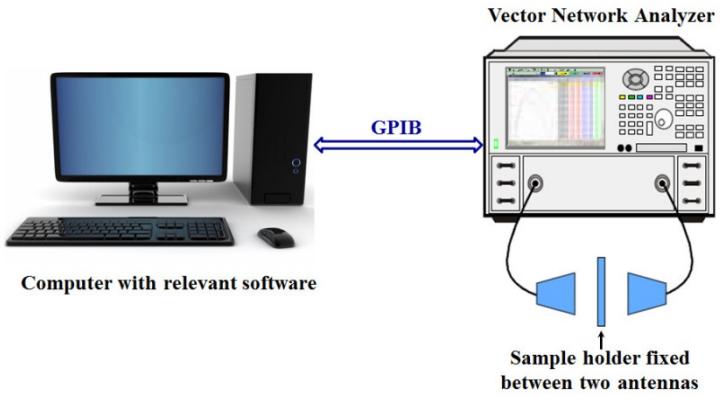

Fig. A2.3. Free space method measurement system [4].

D. Resonant Cavity Method

The resonant cavity method as shown in Fig. A2.4 can obtain the ε of the material under test by comparing the resonant frequency (f) and Q factor of the cavity with and without the sample material at a single frequency. It is more accurate than broadband measurement techniques [1].

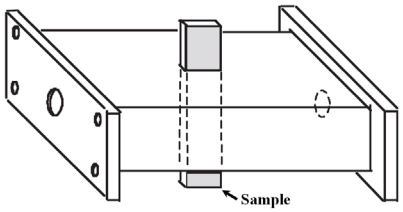

Fig. A2.4. Resonant cavity method [8].

E. Parallel Plate Method

In parallel plate method measurement set up, a thin sheet of material or liquid under test is sandwiched between two electrodes to for a capacitor as shown in Fig. A2.5. And the permittivity of the material is calculated according to the obtained capacitance. This method is ideal for accurate, low frequency measurements of thin sheets or liquids.

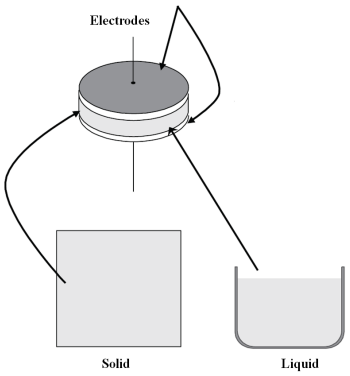

Fig. A2.5. Parallel plate method [3].

F. Inductance Measurement Method

The relative permeability of magnetic material can be derived by measuring the inductance of the material (toroidal core). The idea is to wind some wire around material under test and evaluate the inductance with respect to the ends of the wire. Fig. A2.6 shows a magnetic material test fixture from Keysight.

Fig. A2.6. Magnetic material test fixture from Keysight [5].

Regarding to the stated measurement techniques, to select the most appropriate measurement technique for a specific material, some factors need to be considered [1]: 1) frequency range; 2) expected values of ε_r and μ_r; 3) required measurement accuracy; 4) material properties (i.e., homogeneous, isotropic); 5) form of material (i.e. liquid, powder, solid, sheet); 6) sample size restrictions; 7) destructive or non-destructive; 8) contacting or non-contacting; 9) temperature; 10) cost. Fig. A2.7 provides a comparison between different techniques.

Coaxial Probe ε_r		Broadband. Convenient, non-destructive. Best for lossy MUTs, liquids and semi-solids.
Transmission Line ε_r and μ_r	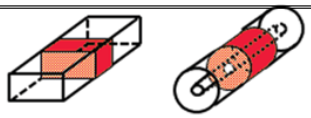	Broadband. Best for lossy MUTs.
Free Space ε_r and μ_r	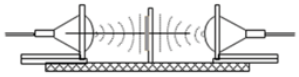	Broadband; Non-contacting Best for flats sheet, powders and high temperature.
Resonant Cavity ε_r	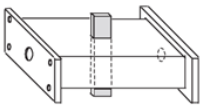	Single frequency; Accurate; Best for low loss MUTs. Small samples
Parallel Plate ε_r	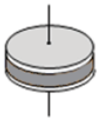	Accurate; Best for low frequencies; Thin, flat sheets samples
Inductance Measurement μ_r		Accurate; Simple measurement; A toroidal core structure is required

Fig. A2.7. Summary of the measurement techniques [1].

References

[1] M. S. Venkatesh, G.S.V. Raghavan, "An overview of dielectric properties measuring techniques," Canadian Biosystems Engineering, vol. 47, pp. 7.15-7.30, 2005.

[2] D. V. Blackham, R. D. Pollard, "An improved technique for permittivity measurements using a coaxial probe," IEEE Trans. Instrum. Meas, vol. 46, no. 5, pp. 1093-1099, 1997.

[3] "Basics of measuring the dielectric properties of materials," Keysight literature number 5989-2589EN, 2015.

[4] "Measuring dielectric properties using Keysight's materials measurement solutions," Keysight literature number 5991-2171EN, 2015.

[5] http://keysight.medexpert.hu/tudastar/cikkek/anyagtudomanyi-meresek-a-keysight-technologies-eszkozeivel